The Development of a Multi-Contrast Chest X-ray Radiography (MC-CXR) Prototype System for the Diagnosis of Lung Disease

by

Daniel Bushe

A dissertation submitted in partial fulfillment of
the requirements for the degree of

Doctor of Philosophy
(Medical Physics)

at the
University of Wisconsin–Madison
2023

Date of final oral examination: May 22nd, 2023

The dissertation is approved by the following members of the Final Oral Committee:

Guang-Hong Chen, Professor, Medical Physics
Ke Li, Associate Professor, Medical Physics
Michael A. Speidel, Associate Professor, Medical Physics
John Garrett, Assistant Professor, Radiology
Ran Zhang, Assistant Professor, Radiology

Acknowledgements

I have been incredibly fortunate to have been surrounded by truly remarkable individuals and communities throughout my life and time in Madison. My career in medical physics and the completion of this dissertation owe a great deal to the many people who have supported my personal, educational, and professional growth. I would like to take this opportunity to express my gratitude to several of these individuals.

First and foremost, I would like to extend my heartfelt thanks to my advisor, Dr. Guang-Hong Chen, for his unwavering guidance and mentorship. It is an honor to have had the privilege of studying under such a brilliant and passionate teacher. I will always be grateful for his tireless efforts towards my development as a medical physicist and as a well-rounded individual. Dr. Chen's dedication to the field of medical physics, as well as his commitment to the fundamental principles of physics, mathematics, statistics, and medicine, have been a constant source of inspiration. I will carry his many teachings with me throughout my career and life.

I would also like to my gratitude to the members of my dissertation committee: Dr. Ke Li, Dr. Michael Speidel, Dr. John Garrett, and Dr. Ran Zhang. Throughout my graduate studies, Dr. Li served as my second advisor and I want to sincerely thank him for his unwavering support, guidance, and patience. Beyond the scope of this dissertation, Dr. Li has provided me with invaluable opportunities relating to clinical CT, interventional X-ray, and photon counting detector CT imaging. I am eternally grateful for his commitment to my development and his mentorship. I extend my thanks to Dr. Michael Speidel for his genuine interest in my educational growth and for his valuable insights into this dissertation. His perspectives on this project and the broader field of medical imaging have proven invaluable in shaping my work. To Dr. John Garrett, I am deeply indebted for his instrumental role in my involvement with the X-ray/CT research group. From the time I met Dr. Garrett, he has gone above and beyond to support me. His passion for the field, selflessness, and work ethic will continue to serve as inspirations to me. I am truly grateful to have had the opportunity to work with someone of the quality and character of Dr. Ran Zhang. The contribution of Dr. Ran Zhang to this thesis work cannot be overstated. He played a pivotal role in teaching me the intricacies of X-ray grating interferometry, multi-contrast imaging, and hardware engineering. Dr. Zhang generously devoted countless hours to answering my questions with patience, kindness, and intuition. His expertise across all facets of medical imaging has been a

constant source of inspiration, and I am immensely thankful for the opportunity to learn from him. Additionally, I would like to extend my appreciation to Dr. Xu Ji for his efforts in the construction and image reconstruction of the prototype system. I have always admired Dr. Ji's dedication, intelligence, and work ethic.

I would like to give a special thank you to Dalton Griner, Chengzhu Zhang, and Kevin Treb for their friendship and endless support. Going through this degree alongside each of you has been an incredible pleasure, and I look forward to seeing your continued success in this field. I am also deeply grateful to the alumni and current students of the X-ray/CT research group, including Yinsheng Li, John Hayes, Juan Pablo Cruz Batisda, Juan Montoya, Adam Budde, Evan Harvey, Mango Feng, Joe Whitehead, Ethan Nikou, Christian De Caro, Xin Tie, Nikou Lei, and Linying Zhan. Their support and engaging conversations have been instrumental in my academic journey, and I appreciate their contributions immensely.

To Olivia Robertson, words cannot adequately express my gratitude to you. Throughout my highest highs and lowest lows, you have remained my greatest source of happiness and support. I am forever indebted to you for the countless sacrifices you have made in support of my career. Your strength, perseverance, and selflessness are truly inspiring and reflect the truly remarkable person that you are. I am incredibly grateful to have had you by my side for the past 4 years. Without your unconditional support, I could not have finished this dissertation. You have made a challenging time in my life easier just by knowing I got to come home to you and Blu at the end of every day. Thank you sunshine.

To my parents, I have always considered myself the luckiest person alive because I had the privilege of being raised by both of you. Throughout my entire life, I have had the two greatest role models by my side, which is why it comes as no surprise that I decided to pursue a career in the same field as both of you. Mom, you have been my rock for as long as I can remember. Your brilliance, intuition, and kindness have always provided me with guidance through any hardship I have faced. The most valuable lessons I have learned in my life have been taught by you, and for that, I am eternally grateful. Pops, I hold a deep admiration for your resilience, work ethic, loyalty, and unwavering dedication to our family. If I can one day become even half the person you are, I will consider myself a great man. To my sister Catie, my greatest achievement has always been and will always be being your brother. Thank you for your unending support and the countless moments of laughter we have shared.

Lastly, but certainly not least, I want to express my gratitude to the UW Medical Physics and the Worcester communities. I will never take for granted the support and opportunities that these communities have provided me with.

— Daniel Bushe (2023)

Abstract

Chest X-ray radiography (CXR) has long served as the frontline imaging modality deployed for the detection of pulmonary disorders. Despite the modality's widespread clinical utility, the diagnostic efficacy of radiography for the detection and diagnosis of pulmonary diseases is severely hindered by the intrinsic physical limitation of the X-ray absorption contrast mechanism. The early manifestation of many pulmonary disorders involves the destruction, damage, or filling of the alveoli with fluids, immunological agents, and lesions prior to the onset of clinical symptoms. These underlying structural and physiological changes to the pulmonary anatomy result in an increase of X-ray attenuation by only a few percent. The low contrast generated between diseased and healthy pulmonary tissue can be easily obfuscated by the presence of anatomical noise or the superimposition of other anatomical structures along the X-ray beam direction.

The aim of this thesis is to construct, optimize, and evaluate a novel multi-contrast chest X-ray radiography prototype system to address the limitations associated with conventional X-ray radiography. Multi-contrast X-ray imaging leverages the wave nature of X-rays to simultaneously generate information regarding the absorption, refraction, and small-angle scattering of X-rays. The small-angle scattering mechanism has demonstrated the capacity to probe the microstructures of the lungs and generate a strong image signal of alveolar air interfaces. However, when the alveoli become filled, damaged, or destroyed, the small-angle scattering signal is extinguished. It is for this reason that multi-contrast X-ray imaging is hypothesized to enhance the utility of X-ray radiography. The first key topic of this thesis work is the design and construction of a clinically compatible multi-contrast prototype system. Following the system construction, a fast scanning beam acquisition scheme is implemented to enable imaging of the entire chest within a single breath-hold. The interferometric and clinical imaging performances are then optimized for a variety of clinical imaging scenarios. To conclude this thesis, the potential for multi-contrast imaging to enhance the diagnostic efficacy of X-ray radiography is evaluated through phantom and animal imaging studies.

Contents

Tables

Figures

Chapter *1*

Introduction

This thesis builds upon decades of prior research on the topics of pulmonary disease, medical X-ray imaging, and multi-contrast X-ray imaging. This chapter serves as a review of the pre-existing literature to place this thesis work in the appropriate historical context.

1.1 Clinical Background

Diseases of the respiratory system impose a significant global health burden, serving as leading causes of mortality and chronic morbidity[1,2]. In 2019, respiratory diseases constituted three of the ten leading causes of death globally, culminating in over 7 million deaths[2]. In the third edition of *The Global Impact of Respiratory Disease* Report, The Forum of International Respiratory Societies (FIRS) identified five diseases that are the predominant contributors to the substantial mortality and morbidity associated with pulmonary disorders: chronic obstructive pulmonary disease (COPD), lung cancer, tuberculosis (TB), acute lower respiratory tract infections, and asthma[1].

1.1.1 Chronic Obstructive Pulmonary Disease (COPD)

Chronic obstructive pulmonary disease, or COPD, is the third most common cause of death worldwide[1]. It is estimated that there are over 200 million individuals, or 4% of the global population, with COPD, resulting in 3.2 million annual deaths on average[7–9]. COPD refers to a group of progressive diseases characterized by chronic inflammation and damage to the structural and functional components of the bronchi, bronchioles, pulmonary vasculature, and lung parenchyma[10]. Chronic inflammation and the potential destruction of parenchymal tissue have

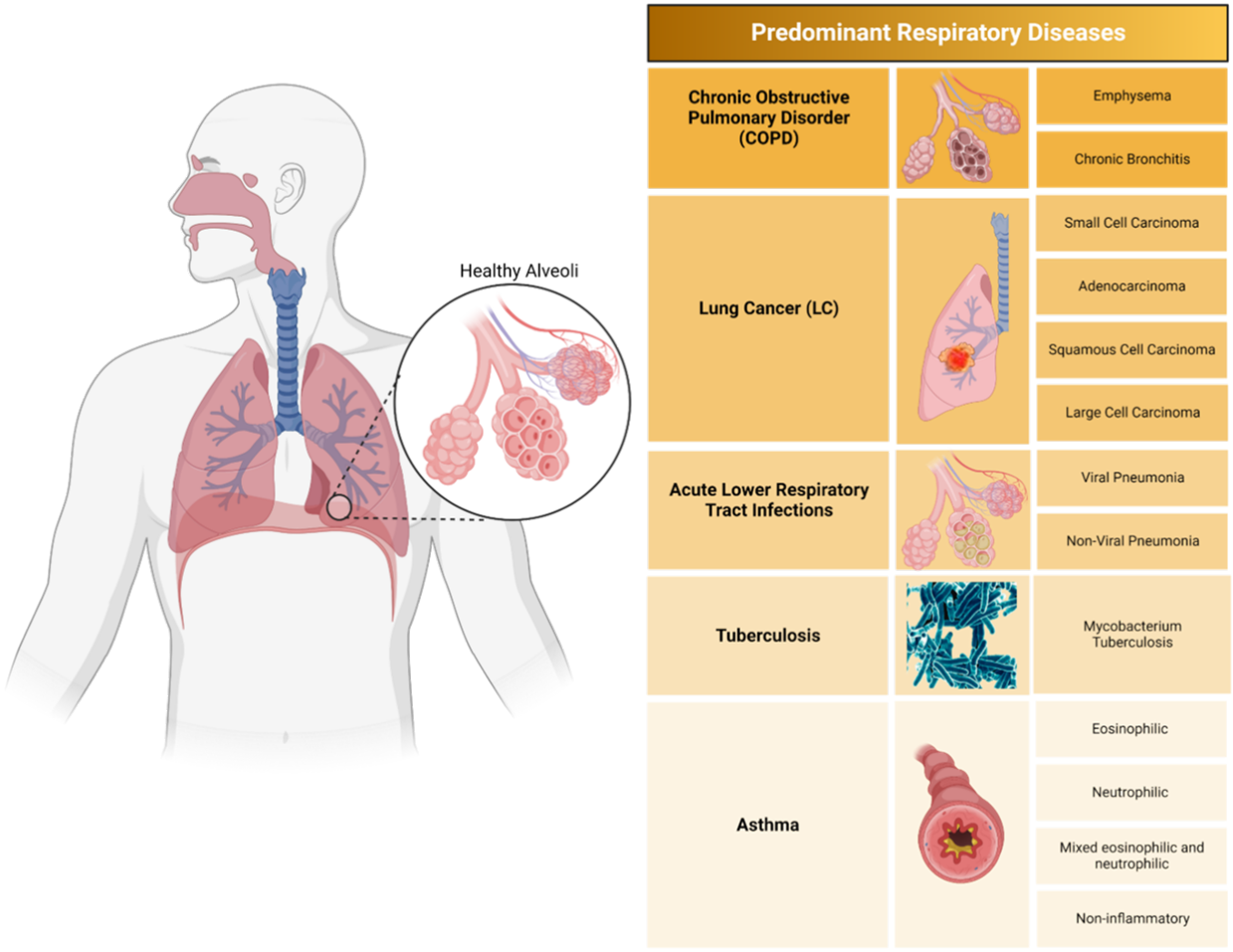

Figure 1.1: (Left) Healthy lungs and alveoli (Right) The five predominant respiratory diseases according to The Forum of International Respiratory Societies.[1] (Created in Biorender)

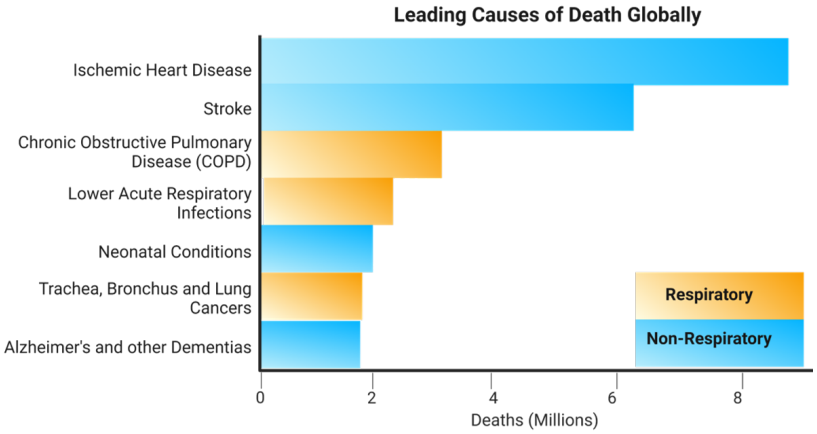

Figure 1.2: (Left) Estimates for the leading causes of death globally in 2019, according to the World Health Organization.[2] (Created in Biorender)

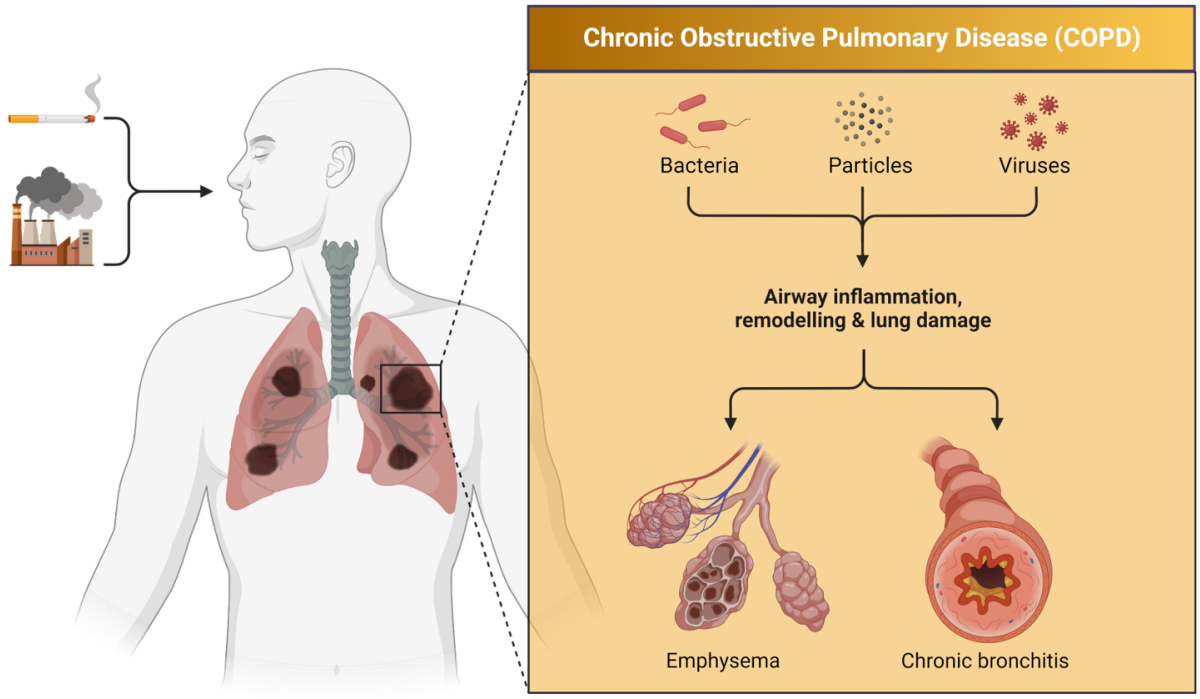

Figure 1.3: A depiction of the factors that cause COPD, the early progression of the disease, and the main conditions associated with it. (Created in Biorender)

been shown to culminate in the narrowing of airways, which may result in irreversible airflow limitations and reductions in gas exchanges and lung elasticity[11]. The two most common conditions of COPD are emphysema and chronic bronchitis. Emphysema is characterized by the enlargement of the alveolar airspaces, the weakening of the epithelial cells lining the alveoli, and a loss in lung parenchyma elasticity[12]. Enlargement of the alveolar airspaces can be caused by the collapse of the epithelial cells lining the alveoli or by structural rearrangements[13]. A loss of alveolar surface area results in a reduction in the underlying gas exchange processes. In contrast to emphysema, chronic bronchitis is the chronic inflammation of the major airways, including the bronchi and bronchioles, rather than the alveolar air spaces[13]. Chronic bronchitis is characterized by excessive mucus secretions along the lung's major airways resulting in airflow limitations to the distal branches of the respiratory system.

1.1.2 Lung Cancer

Lung cancer is the primary cause of cancer-related death in the United States and worldwide. Based on the 2020 Global Cancer Observatory's (GCO) annual cancer burden report, there were

an estimated 2.2 million new cases and 1.8 million deaths associated with lung cancer worldwide. This corresponds to 11.4% of all new cancer cases and 18% of all cancer-related deaths[14,15]. Despite advancements in the development of effective treatment modalities, the prognosis for lung cancer patients remains among the worst of all cancers, with a 5-year survival rate of just 21%[16].

The high mortality associated with lung cancer can be ascribed to delays in diagnosis, a lack of effective treatment options for advanced-stage or metastatic disease, and the highly heterogeneous nature of the disease's clinical presentation and histopathology. Delays in diagnosis are frequently the result of clinical symptoms not presenting until the advanced stages of disease progression. Reports demonstrate that roughly 80% of lung cancer patients have developed stage III or IV disease at the time of presentation, thus excluding them from the potentially curative surgical resection that can be performed at earlier disease stages[17]. To compound upon the challenges in diagnosis, lung cancer can present with a vast range of symptoms that are largely non-specific and may coincide with symptoms of pre-existing respiratory conditions, such as chronic obstructive pulmonary disease (COPD)[18,19].

Significant progress has been made in developing an understanding of the highly heterogeneous biological and histopathological characteristics of lung cancer. Recognizing the heterogeneity of lung cancer is essential for the development of effective diagnostic and treatment modalities. Traditionally, lung cancer has been classified into two primary histologic categories: non-small cell lung cancer (NSCLC) and small cell lung cancer (SCLC). SCLC accounts for 13%-15% of all new lung cancer cases[20]. The limited stage of SCLC refers to a disease that is confined to the thorax, specifically, the lungs, central airways, and lymph nodes. The extensive SCLC denomination is characterized by the spread of disease beyond the thorax with the most common metastatic sites being the liver, brain, and bones[21,22]. The SCLC sub-classification is highly metastatic and associated with extreme lethality due to the disease's fast metabolic function, rapid growth rate, proclivity for early metastasis, and aggressive nature[23]. In addition to the disease's rapid development, SCLC has exhibited a strong resistance to lung cancer treatments[24]. As a result, 85% of patients present with extensive SCLC at the time of diagnosis, and the overall 5-year survival rate is just 6.4%[25]. NSCLC is further sub-categorized into adenocarcinoma, squamous cell carcinoma (SqCC), and large cell carcinoma[23]. Adenocarcinoma of the lung is the most common histologic classification of lung cancer, accounting for 40% of all cases and 70% of NSCLC cases[26]. By definition, adenocarcinoma

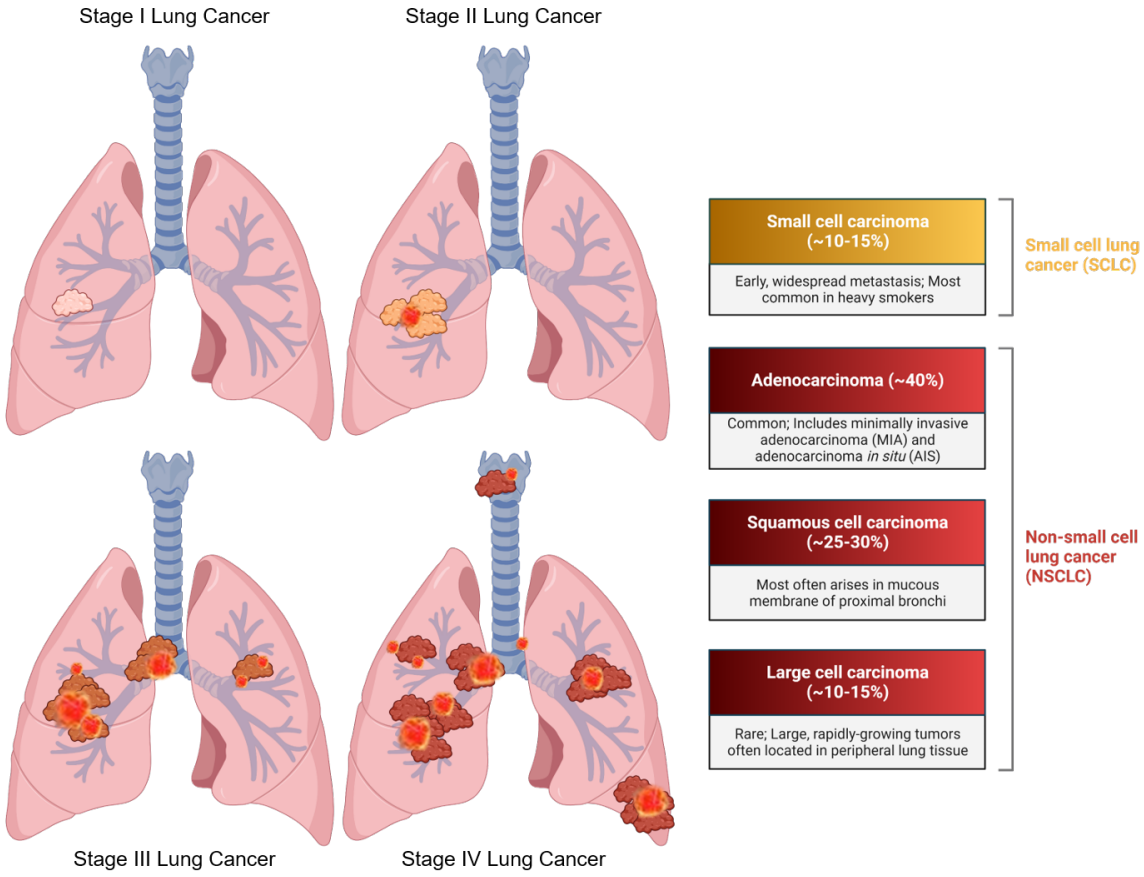

Figure 1.4: (Left) Illustration of the four stages of lung cancer. (Right) Description of the four major lung cancer sub-classifications. (Created in Biorender)

refers to a malignant epithelial mass that exhibits glandular involvement or mucin production. Adenocarcinoma of the lung is also accompanied by a variety of histologic sub-classifications.

Squamous cell carcinoma accounts for 20% of lung cancer cases. The majority of SqCCs express along the central portion of the lungs, most commonly arising in the bronchi and other major airways[27]. SqCC is more strongly associated with smoking and chronic inflammation when compared to other NSCLC histologic classifications[28]. In contrast to adenocarcinoma, SqCC of the peripheral lung is more expansive, demonstrating initial filling of alveolar spaces and the displacement of normal pulmonary structures[29]. Large cell carcinomas are the most infrequent lung cancer. Large cell carcinomas appear as bulky necrotic tumors that are primarily found along the peripheral lung with limited presentation in the central region. Large cell carcinoma is associated with significant displacement of the underlying pulmonary anatomy[27].

1.1.3 Acute Lower Respiratory Tract Infections

Acute lower respiratory tract infections account for over 2.4 million deaths annually and remain the leading cause of death for children under 5 and individuals over the age of 65[1]. Lower respiratory infections refer to a group of immunological responses in the lower respiratory tract, including the bronchi, bronchioles, and alveoli. The clinical presentation and underlying etiological agents associated with acute lower respiratory tract infections are complex and widely vary.

Pneumonia is an inflammatory immunological response primarily pertaining to the alveoli and interstitial spaces. Determining the etiological agent for a given case of pneumonia is crucial in assessing an effective course of treatment.

1.1.4 Tuberculosis

Mycobacterium tuberculosis which is the causative bacteria in TB, is one of the primary causes of pneumonia and severe respiratory disease. In 2019, Tuberculosis was responsible for 1.4 million deaths and 10 million new cases[1]. Tuberculosis is transmitted by small airborne droplets that typically settle throughout the upper tracts of the respiratory system once inhaled. As such, the majority of TB-infected individuals have a latent disease. Clinical symptoms and the onset of pneumonia do not begin unless the bacteria reaches the alveoli[30].

1.1.5 Asthma

The final major respiratory disease identified by FIRS is asthma, which has become an increasingly prevalent disease over the past three decades, impacting over 350 million people and causing over 500,000 deaths each year[31,32]. Asthma is a disease of chronic bronchial inflammation characterized by hyperresponsiveness of the major airways. The cause of asthma is complex and generally relates to environmental stimuli and genetics.

1.1.6 2019 Novel Coronavirus

The burden associated with pulmonary diseases has been exacerbated by the emergence of the 2019 novel coronavirus pandemic. In December 2019, several patients presented with cases of severe pneumonia of unknown etiology in the Hubei province of China[33]. This event was subsequently

determined to be the initial outbreak of the 2019 novel coronavirus disease (COVID-19). COVID-19 rapidly reached pandemic levels due to its prompt proliferation and substantial mortality, having since infected over 350 million individuals resulting in 5.6 million deaths as of 2022[34,35].

SARS-CoV-2 (Severe Acute Respiratory Syndrome-Coronavirus 2), which was identified as the causative agent of the COVID-19 outbreak, is an enveloped positive-stranded RNA virus that utilizes angiotensin-converting enzyme 2 (ACE2) as a source for cellular entry. ACE2 is primarily expressed in tissues along the respiratory tract including in alveolar cells, bronchial epithelium, and vascular endothelial cells[33,36–39]. Compared with previous outbreaks of coronaviruses including SARS-CoV (severe acute respiratory syndrome-coronavirus) and MERS-CoV (Middle East respiratory syndrome-coronavirus), SARS-CoV-2 is highly contagious and transmissible[40,41]. The early immunological response to SARS-CoV-2 is the inflammation and filling of the small air chambers, known as the alveoli, with mucus, proteinaceous exudates, alveolar macrophages, and other infiltrates prior to the onset of clinical symptoms or severe disease[36,42,43].

The most common outcome for patients experiencing severe disease is acute respiratory distress syndrome (ARDS) characterized by bilateral diffuse alveolar damage (DAD), the destruction of alveoli epithelial cells, hyaline membrane formation, and eventual intracapillary thrombosis[36,42,44–53]. A prompt diagnosis, adequate initial management, and early treatment are crucial to improve patient prognosis and mitigate negative health outcomes for individuals suffering from COVID-19.

1.2 Chest X-ray Radiography for the Diagnosis of Lung Disease

Efforts have been made to develop effective diagnostic tools and treatment methods to address the significant burden of respiratory diseases. Medical imaging is crucial in the diagnosis and management of lung diseases, with chest X-ray radiography (CXR), computed tomography (CT), positron emission tomography (PET), and magnetic resonance imaging (MRI) being the primary imaging modalities used to provide detailed functional and structural information on pulmonary anatomy for improved diagnosis and monitoring of lung diseases. CXR, in particular, is often the first-line imaging modality used to detect many pulmonary abnormalities.

Chest radiography is a rapid, simple, and inexpensive method for evaluating the heart, lungs, major airways, blood vessels, and osseous structures related to the thoracic cavity. It is widely

used to screen for and diagnose lung cancer, tuberculosis, asthma, viral and non-viral pneumonia, COPD, diffuse parenchymal lung disease (DPLD), and pneumothorax. Compared to other imaging modalities, radiography is advantageous due to its reduced system/exam cost, high spatial resolution, increased throughput, and widespread availability[54–59]. In fact, planar radiography is the most common imaging procedure performed in medicine, as almost all urban and rural clinics, emergency rooms, urgent care facilities, and hospitals are equipped with stationary and mobile CXR units.

1.2.1 History of X-rays in Medicine

Since their initial description, X-rays have been used as a tool to visualize the internal structures of the human anatomy. Wilhelm Roentgen was the first to describe the existence of X-rays in 1895. The accidental observation came when Roentgen was using a Crooke's tube to study "cathode rays". During an experiment, Roentgen observed fluorescence on a barium platinocyanide screen across the room, despite the tube being covered. Roentgen quickly recognized this as a distinct phenomenon from the "cathode rays" he had been studying, as these new rays could penetrate through thick materials and still be seen at distances far greater than that of the "cathode rays"[60]. In one of his early experiments, Roentgen captured the first medical X-ray image by placing his wife, Anna Bertha Ludwig, hand in between the Crooke's tube and a film, as shown in Fig. **??**[5].

For the first time, X-rays allowed for medical professionals to non-invasively observe the internal structures of the human body. X-rays were being used in a clinical setting within one year of their initial description[60–63]. By the 1920s, X-rays had changed the landscape of modern medicine. Hardware advancements allowed for the widespread adoption of medical X-ray imaging. The Coolidge tube allowed for increased output, improved stability, and greater flexibility compared to the Crooke's tube[64]. Advancements in intensifying screens allowed for film to replace the bulky glass plates that were common practice in the early days of X-ray imaging[63]. By 1951, it was estimated that 42% of all patients admitted to the hospital would receive at least one X-ray examination[63]. Since the 1960s, CXR has been the most common X-ray imaging examination[63,65]. CXR was being evaluated as a potential screening tool for lung cancer as early as the 1950s[66–69]. Despite the emergence of tomographic imaging modalities including CT and MRI, planar X-ray imaging remains the primary workhorse in modern medicine.

1.2.2 Limitations of Conventional X-ray Radiography

The intrinsic limitations of CXR have severely limited the capacity of the modality to detect or differentiate the structural and functional changes associated with various pulmonary abnormalities. For instance, multi-institutional studies have found that the sensitivity of conventional CXR to COVID-19 ranges from 33% to 73%[70–72], with sensitivity being poorest in the early stages of disease[73]. The sensitivity of CXR to COPD has been found to be roughly 35%[55]. The National Lung Screening Trial (NLST) at Johns Hopkins[74], the Mayo Clinic[75], and Meomrial-Sloan Kettering Cancer Center[76] concluded that CXR had a statistically insignificant impact on overall mortality, did not result in a stage shift in detected cancers, and may have lead to an overdiagnosis of lesions that could be considered not clinically relevant[77–82]. Similarly, the Prostate-Lung-Colorectal-Ovary (PLCO) screening trial also found that CXR imaging did not have an impact on the cumulative lung cancer mortality of patients[83].

The poor diagnostic performance of CXR can be attributed to the nature and underlying physics that governs planar X-ray imaging and the biological and histological characteristics of the respiratory system and pulmonary diseases. Another inherent limitation of planar radiography is the superimposition of anatomical structures along the X-ray beam direction. This inherent limitation is pronounced for chest imaging due to the presence of highly attenuating structures such as the ribs, clavicles, and spine, in conjunction with the highly complex and heterogeneous anatomy associated with the hilar and peri-hilar regions. Several comprehensive reviews have found that location plays an important role in the capacity for radiologists to detect lesions and abnormalities in CXR images[84–91].

In conjunction with the modality's planar nature, the major limitation of CXR relates to using X-ray absorption as the primary mechanism to generate contrast between diseased and healthy pulmonary tissues. The attenuation coefficient is roughly proportional to the fourth power of the effective atomic number, Z_{eff} for a given image object. As such, materials composed of low Z elements, such as the soft tissues in the human body, become difficult to distinguish in absorption imaging. In their early manifestations, pulmonary diseases directly impact the microscopic structural anatomy of the lungs. For instance, the alveoli become filled with mucus, immunological agents, and other liquids during the early stages of pneumonia, even prior to the onset of ARDS and

DAD[36,42,43]. The culmination of these minuscule air spaces becoming filled with water-equivalent material is an increase in X-ray absorption by only a few percent. Similarly, the destruction of epithelial cells and enlargement of the alveolar air spaces during emphysema results in significant functional changes. However, these microscopic changes have little impact on the absorption of X-rays when compared to the absorption of X-rays in healthy lung tissue[55]. Early-stage lung cancers typically present as small, low-density lesions with ill-defined margins, resulting in limited contrast in a conventional radiographic image[29,87,89,92,93]. Thus, the limited contrast generated by the underlying pathophysiology associated with respiratory diseases can become easily obfuscated by image noise or the superimposition of other anatomical structures in conventional radiographic images.

1.3 Multi-Contrast X-ray Imaging

Despite significant advancements in our understanding of the nature of X-rays, the underlying contrast mechanism in medical X-ray imaging has remained entirely unchanged since Roentgen's initial discovery in 1895. As such, medical imaging has been unable to access a fundamental aspect of X-rays - their wave nature. The wave properties of X-rays become distorted as the X-ray wavefront interacts with matter through physical processes such as X-ray refraction and X-ray small-angle scattering (SAS)[94–96].

Information about the microstructure, distribution of scatterers, and material composition of the interacting medium is encoded in the distortions of the X-ray wavefront. X-ray refraction occurs when X-rays interact with the orbital electrons of a medium through elastic scattering, which alters the direction of X-ray wave propagation. The degree of change in the wave propagation direction depends on the local electron density of the material. Consequently, information on the electron density distributions of an object is intrinsically encoded in the local changes in the phase of the X-rays as they leave the object.

X-ray small-angle scattering is the diffraction of X-rays into a narrow forward propagating cone caused by scatterers that are much larger than the wavelength of the X-rays. Thus, small-angle scattering events will be generated by scatterers ranging in size from hundreds of micrometers to tens of nanometers for X-rays in the diagnostic energy range. The likelihood of an X-ray small-angle

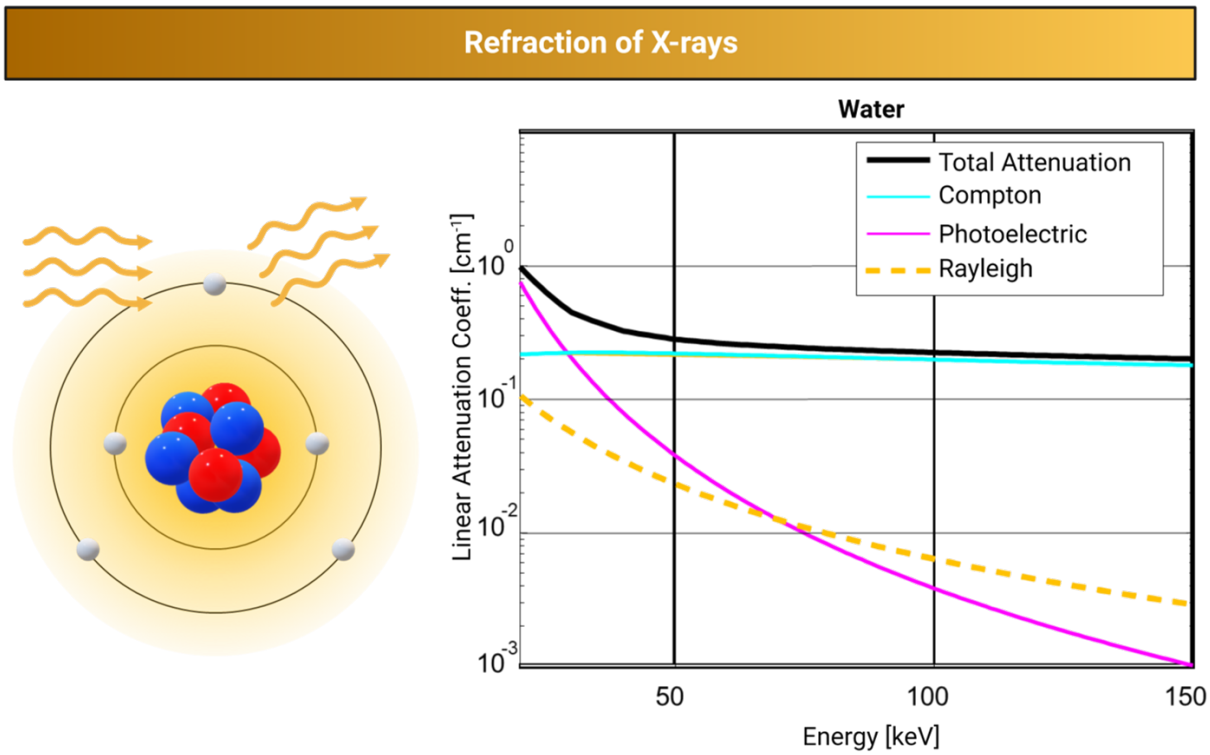

Figure 1.5: (Left) Alteration of the X-ray wave propagation direction through refraction (Right) Contribution of Rayleigh scatter, Photoelectric absorption, and Compton scatter on the linear attenuation coefficient of water in the diagnostic energy range. (Created in Biorender)

scattering event occurring is not dependent on the physical density, but rather on the spatial density correlation coefficient of a given object[97,98]. To be more specific, the small-angle scattering cross section is related to the density spatial correlation coefficient, ρ_{cor} by $\sigma_{SAS} = 1 - \rho_{cor}$. As a result, regions of uniform density will generate no small-angle scattering events, while regions of heterogenous density will be associated with a strong scattering signal. By detecting X-ray wave distortions resulting from small-angle scattering events, valuable information on the microstructure and spatial density distributions of a given object can be extracted.

There have been various techniques developed to extract the rich material-specific information encoded through the interactions of X-ray refraction and X-ray small-angle scattering. X-ray phase contrast and X-ray dark-field imaging are imaging modalities that respectively utilize X-ray refraction and X-ray small-angle scattering mechanisms to generate image contrast. The simultaneous generation of X-ray absorption, X-ray phase, and X-ray dark-field images is known as multi-contrast X-ray (MCXR) imaging. Over the past three decades, the medical imaging community

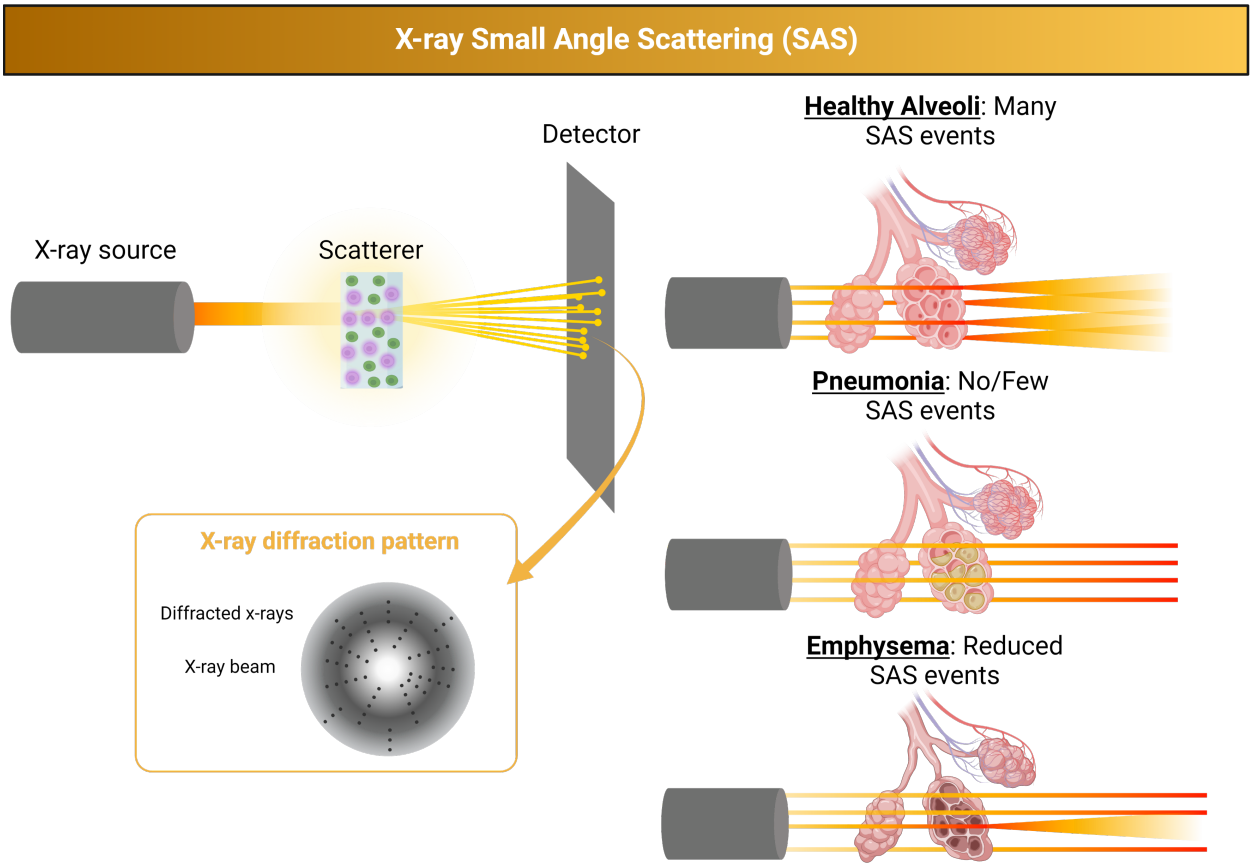

Figure 1.6: (Left) Depiction of X-ray small-angle scattering event and the subsequent diffraction pattern generated. (Right) Demonstration of small-angle scattering events in healthy alveoli, alveoli with pneumonia, and emphysemic alveoli. (Created in Biorender)

has made significant efforts to explore the potential of multi-contrast X-ray imaging to overcome the limitations of conventional X-ray imaging methods[99–123,123–128].

1.3.1 Multi-Contrast Chest X-ray Imaging

For the detection of respiratory diseases, it is the fundamental physics and imaging principles governing multi-contrast X-ray imaging that encompass the potential for it to improve upon the diagnostic performance of chest radiography. In specific, analysis of the dark-field image signal may provide a powerful tool for the detection of lung abnormalities. When healthy, the hundreds of millions of microscopic balloon-shaped alveoli will provide a strong X-ray dark-field signal. First, the size of the alveoli, roughly 200-500 μm, are on the order of particulate small-angle scatterers for X-rays in the diagnostic energy range. Second, the density gradient between the alveolar membrane and the air compartment for given alveoli will reduce the density spatial correlation coefficient in

healthy lungs. The reduction of the density spatial correlation coefficient results in a sharp increase in the probability of small-angle scattering to occur. For many pulmonary disorders, the structural and physiological manifestations of the disease are related to the inflammation and/or destruction of the alveoli. These underlying changes will result in an increase in density homogeneity across the impacted region. As a consequence, the density spatial correlation coefficient will approach unity, thus decreasing the overall dark-field signal for infected alveoli and lesions. The discrepancy between the dark-field signal generated in diseased and healthy alveoli is hypothesized to be the key to improving the diagnosis of lung diseases via chest radiography. It is for this reason that dark-field lung imaging has been a special interest in the scientific community for the past decade[111,112,129–142].

To further compound upon the benefits of MC-CXR imaging, the X-ray phase contrast signal has also demonstrated utility in the medical imaging domain. First, the X-ray phase contrast signal exhibited the capacity to provide superior contrast resolution for certain types of soft tissues and cancers[99,106,113,114,143**?** ,144]. In addition, the quantitative electron density, ρ_e, information encoded in the X-ray phase contrast signal can be leveraged to effectively generate soft tissue-only images[145]. Similar to dual-energy radiography, soft-tissue-only images can suppress the overlapping bony structures in the absorption images for improved detection of low contrast lesions[109,110,146–148].

1.3.2 Review of Multi-Contrast X-ray Imaging Methods

The physical and mathematical foundation of multi-contrast X-ray imaging is presented in Chapter 2 of this thesis. The remainder of this chapter is dedicated to reviewing the major multi-contrast X-ray imaging techniques that have been investigated by the scientific community. The potential advantages and disadvantages of each method are discussed within the context of creating a human-compatible multi-contrast X-ray imaging system that adheres to the constraints of a clinical setting. Clinical compatibility requires that a proposed prototype system be compatible with currently employed x-ray hardware systems. That is to say, the prototype system must match or resemble the geometry, field-of-view (FOV), dosimetric characteristics, and acquisition times associated with conventional chest radiography

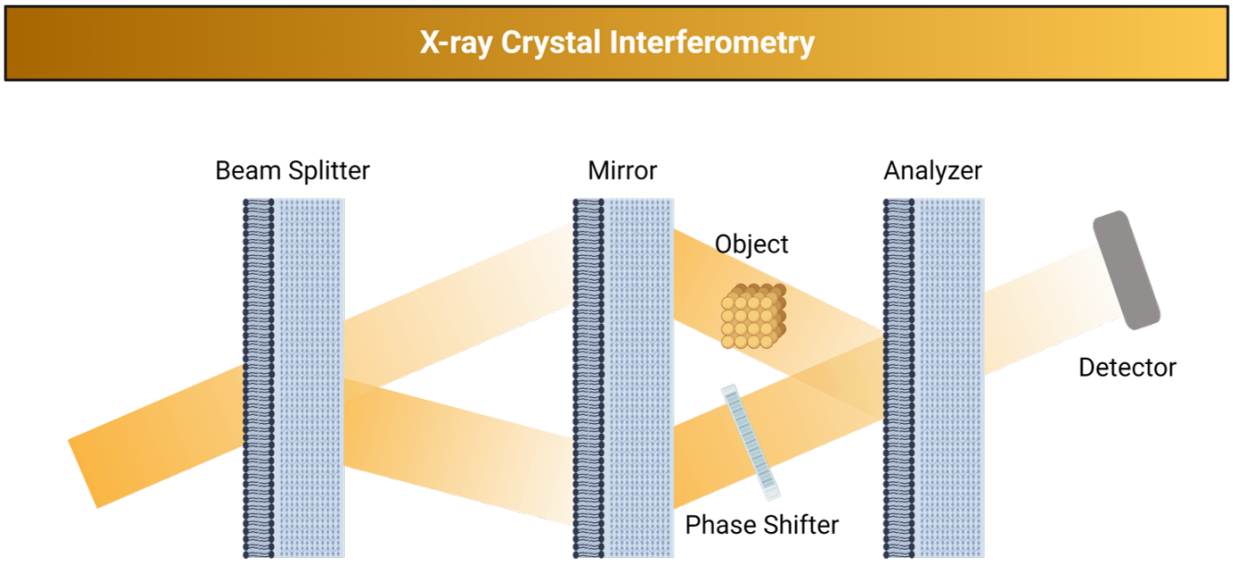

Figure 1.7: X-ray crystal interferometer with three silicon crystals serving as a beam splitter, a mirror, and an analyzer. Interference patterns are generated at the detector to detect phase shifts produced by the object in one of the beam paths. (Created in Biorender)

1.3.2.1 X-ray Crystal Interferometry

X-ray interferometry exploits the interference of X-ray waves to extract the information encoded through the X-ray refraction and small-angle scattering processes. In specific, the interference of X-rays is used to generate detectable interference patterns, otherwise known as interferograms. Analyzing changes in the interferogram caused by an image object can reveal the structural and compositional information discussed previously. The concept of X-ray interferometry was first introduced in 1965 by U. Bonse and M. Hart[95]. They created an interferometer using three nearly perfect silicon crystal plates, as illustrated in Figure 1.7. In this setup, a monochromatic X-ray beam is directed at the first silicon crystal at a non-perpendicular angle. The first crystal acts as a beam splitter, diffracting a portion of the beam and allowing the other portion to continue along the original angle of incidence. The second crystal serves as a mirror, reflecting the diffracted portion of the beam back towards an analyzer silicon crystal.

The image object is positioned between the mirror and analyzer crystals, obstructing one of the beams and causing a phase shift while the other beam remains unaffected. The spatially separated beams then interfere as they reach the third analyzer crystal. This interference is then detected downstream of the third crystal as an interference pattern across a detector. The interference at the detector can be modeled as a sinusoidal function with oscillating intensity. A phase splitter can

also be added to the unmodulated beam to resolve the relative phase shift introduced by the image object. This process is referred to as phase stepping and is discussed in more detail in Chapter 2.

Crystal interferometry has been explored for small animal imaging applications. The first investigation for biological imaging was conducted by Momose and Fukuda in 1995[143]. In the subsequent two decades, crystal interferometry was investigated for imaging of the brain, liver, and blood vessels of small animals[103,149–152]. The clinical potential of crystal-based interferometry techniques is limited by several inherent aspects. One of the challenges is that crystal interferometry requires a monochromatic X-ray source, which is difficult to achieve in the clinical environment. Synchrotron sources are associated with significant system costs, are not compatible with standard radiography suites, and are not widely available in clinical practice. Other monochromatic X-ray sources do not provide adequate flux to enable clinical imaging within a reasonable time. Another limitation is the stability associated with crystal interferometers.

The high sensitivity of crystal interferometers also comes at the cost of being highly sensitive to external disturbances. This sensitivity has resulted in substantial stability issues with crystal interferometry[97]. Finally, crystal-based phase imaging methods are limited to a field of view of only a few centimeters due to their dependency on crystal size and uniformity. As a result of these limitations, crystal-based interferometry is not a viable candidate for clinical lung imaging.

1.3.2.2 Diffraction-Enchanced X-ray Imaging

Diffraction Enhanced Imaging (DEI) or analyzer-based imaging is a technique that uses an analyzer crystal to detect changes in the phase of monochromatic X-rays. After a monochromatic beam of X-rays interacts with matter, the refracted and unrefracted components of the beam will have different directions of propagation. As such, if an analyzer crystal is placed after the image object, then the two components of the beam will be incident on the crystal at different angles. The analyzer crystal will diffract X-rays with a narrow range of incidence angles toward a detector. Deviations from the Bragg angle introduced by refraction will result in changes in the measured intensity at the detector plane.

The working principles of DEI and the method to generate the phase and absorption signals were established by Chapman et al. in 1996[153,154]. The underlying mechanism to extract the phase contrast in DEI is to measure rocking curves at the detector with and without an image object

present. A rocking curve is generated by introducing slight angular variations from the Bragg angle to the analyzer crystal. Angular deviations from the Bragg angle will cause a gradual decrease in the intensity measured at the detector. The rocking curve is therefore measured as a plot of the intensity as a function of the introduced angular deviation. The rocking curve becomes shifted when X-ray refraction in an image object causes a change to the angle of incidence onto the analyzer crystal. This shift in the rocking curve is a direct measure of the angle of refraction induced by the image object. As shown in Chapter 2, the angle of refraction is proportional to the differential phase shift introduced by the image object. In addition to the phase and absorption information, dark-field image signals can also be generated through the rejection of small-angle scattered X-rays by the analyzer crystal[155].

DEI has been investigated for medical imaging applications including mammography, lung imaging, and joint imaging[156]. Improved soft tissue imaging associated with DEI phase imaging has demonstrated utility in improved contrast between diseased and healthy breast tissue[157,158] and the evaluation of cartilage and synovial tissues in joints[159,160]. Dark imaging via the extinction of the X-ray small-angle scattering signal has also demonstrated utility for the visualization of the lungs for small animal imaging[111,112]. Despite the modalities demonstrated success, the clinical adoption of DEI for clinical pulmonary imaging is impeded. Similar to crystal interferometry, the challenges associated with DEI include the requirements for monochromatic X-rays and the limited field of view resulting from crystal fabrication. As a result of these impedances, DEI is not considered a viable candidate for a human-compatible multi-contrast imaging system.

1.3.2.3 Propagation-Based X-ray Imaging

Propagation-based X-ray imaging (PBI) techniques are based on observing the Fresnel or near-field diffraction of spatially coherent X-rays. Refracted components of these X-rays begin to interfere downstream from the image object, and this interference can be detected as local variations in brightness and darkness by introducing a distance between the object and the detector plane. For PBI imaging, the intensity across the detector, $I(x, y)$ can be modeled in the following manner:

$$I(x,y) = \frac{I0(x,y)T(x,y)}{M^2}\left(1 - \frac{\lambda\, d}{2\pi}\nabla_{\perp}^{2}\phi(x,y)\right) \tag{1.1}$$

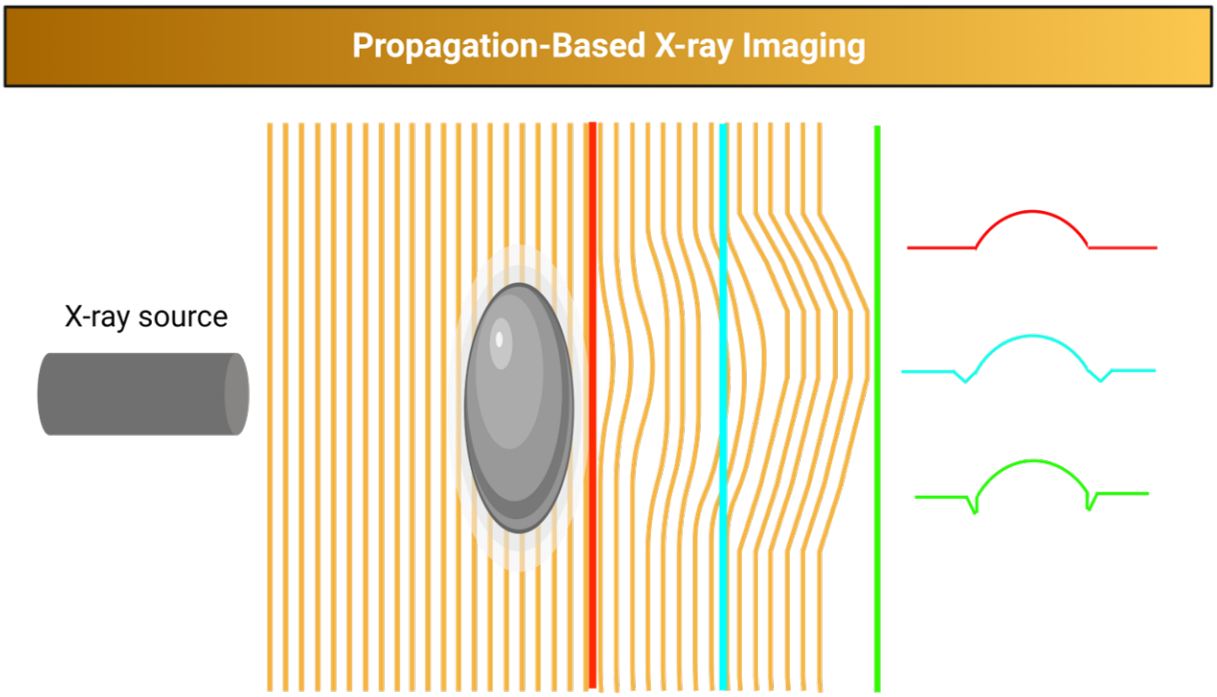

Figure 1.8: Visualization of the underlying principle governing propagation-based X-ray phase contrast imaging methods. Distortions to the X-ray wavefront will interfere at distances downstream from the sample. (Created in Biorender)

In this model, $I0(x, y)$ is the measured intensity in the absence of an image object, $T(x, y)$ is the transmission of the X-rays through the image object, M is the magnification, λ is the wavelength of the X-rays, d is the defocusing distance or the distance between the object and detector divided by the magnification, $\nabla_{\perp}^{2}$ is the Laplacian operator that is perpendicular to the $x - y$ plane, and $\phi(x, y)$ is the phase shift[161]. Equation 1.1 shows that the phase contrast is directly related to the distance between the object and the detector plane. Greater defocusing distances lead to an increased contribution from the phase component of the signal while decreasing the defocusing distance provides conventional absorption imaging. The phase signal in PBI is proportional to the Laplacian of the local phase shift.

The PBI method was first introduced by Snigirev et al.[144] and Wilkins et al.[100] in the mid-1990s. Soon after the initial investigations, phase retrieval methods were developed to decouple the contributions from the absorption and phase contrast mechanisms. This has been typically accomplished by utilizing the Transport of Intensity equation (TIE) and collecting images at two or more source-to-detector distances or by assuming little absorption of the X-rays[162–164].

In the medical imaging domain, PBI has demonstrated promising results in mammography[120–123]

and lung imaging[123–128]. For mammography, PBI has primarily been used for tomographic imaging (PBI-CT). The phase component of PBI-CT provides superior soft tissue contrast resolution compared to absorption imaging. Recently, Gureyev et al. also demonstrated the potential utility of dark-field PBI-CT for breast imaging[165]. In relation to pulmonary imaging, PBI has been utilized to perform edge enhancement for planar imaging by leveraging the second-order differential nature of the phase component[125,128]. Similarly, high-resolution PBI-CT lung imaging using synchrotron sources has been investigated[127].

One of the major benefits of PBI with respect to clinical applicability is that PBI does not require any additional hardware components apart from the X-ray source and detector. PBI has therefore been considered the simplest method for achieving multi-contrast imaging. Additional benefits when compared to crystal interferometry include that PBI does not require monochromatic X-rays and the field of view is not limited to a few centimeters. The only strict requirements are a high degree of spatial coherence and appropriate distances between the object and detector planes. To achieve adequate levels of spatial coherence, one must either use a large source-to-object distance and/or an X-ray source with a focal spot on the order of a few microns. Herein lies the major limitation of the PBI technique when considering potential clinical adoption. First, synchrotron sources or microfocus X-ray tubes must be used to adhere to clinically acceptable source-to-object distances. As mentioned previously, synchrotron sources are not clinically feasible at this time. Microfocus X-ray tubes are suitable for small animal imaging but do not provide the necessary flux to achieve human imaging within a reasonable imaging time. Even with synchrotron sources or microfocus X-ray sources, the source-to-detector distances required to achieve large animal imaging with PBI are too great to adhere to the constraints of standard radiography suites[127,128].

1.3.2.4 Grating-Based Multi-Contrast Imaging

In the past three decades, grating-based multi-contrast X-ray imaging methods and their CT counterparts have been employed and extensively investigated for use in an array of applications, revealing enhanced contrast resolution and the ability to detect abnormalities or diseases that are not apparent in traditional attenuation images.[103–110,113–119,166–168]. Similar to crystal interferometry, the fundamental principle in grating-based multi-contrast imaging is to harvest the phase and dark-field information from interference patterns generated at the detector. Gratings are periodic

structures that can act as diffractive optical elements. When sufficiently coherent X-rays interact with a set of gratings, the X-rays will be diffracted by each individual grating element. The diffracted X-ray wavefront from a single grating can then interfere with the diffracted wavefronts from the adjacent grating elements. This phenomenon was first demonstrated with light in 1836 by Henry Talbot. Talbot found that the interference of the light generated repeated images of the gratings at regular distances downstream from the gratings. This phenomenon, otherwise known as the Talbot self-image effect, was eventually replicated with X-rays in 1997 by Cloetens et al[166].

The spatial period of the interference patterns generated from a single grating interferometer is too high to be resolved with conventional X-ray detectors. However, a second grating or crystal analyzer can be added in front of the detector to resolve the interference pattern. This second optical element with the same pitch as the interference pattern at the detector is capable of generating a resolvable interference pattern[167]. The generated interference pattern can be modeled as a sinusoidal function. Distortions to the X-ray wave field arising from absorption, refraction, or small-angle scattering interactions are encoded into changes in the interference pattern. Absorption events will cause an overall reduction in the intensity of the interference pattern. Refraction will generate a lateral shift in the interference fringes. In other words, refraction introduces a phase shift to the sinusoidal function. Small-angle scattering events result in a reduction in the amplitude of the sinusoidal function or a blurring of the interference fringes.

A procedure known as phase stepping was developed in 2005 to analyze the changes to the interference pattern[168]. Phase stepping is performed by translating one of the X-ray gratings along the lateral direction to generate a shift in the interference pattern. An image is acquired at each phase step such that the intensity variation for a single pixel can be tracked. The intensity variation for a single pixel can also be modeled as a sinusoidal function, such that the three contrast mechanisms can be simultaneously extracted from changes to the intensity, amplitude, and phase of the sinusoidal function for each image pixel.

Grating-based X-ray imaging has been widely studied for quantitative CT imaging[117,169–171], breast imaging[38,172–174] and lung imaging. In specific, grating-based techniques have demonstrated great promise for clinical lung imaging. Dark field imaging from the grating-based technique has been studied for emphysema, lung cancer, COVID-19 pneumonia, and pneumothoraces for both animal and human subjects[119,130–142,175,176].

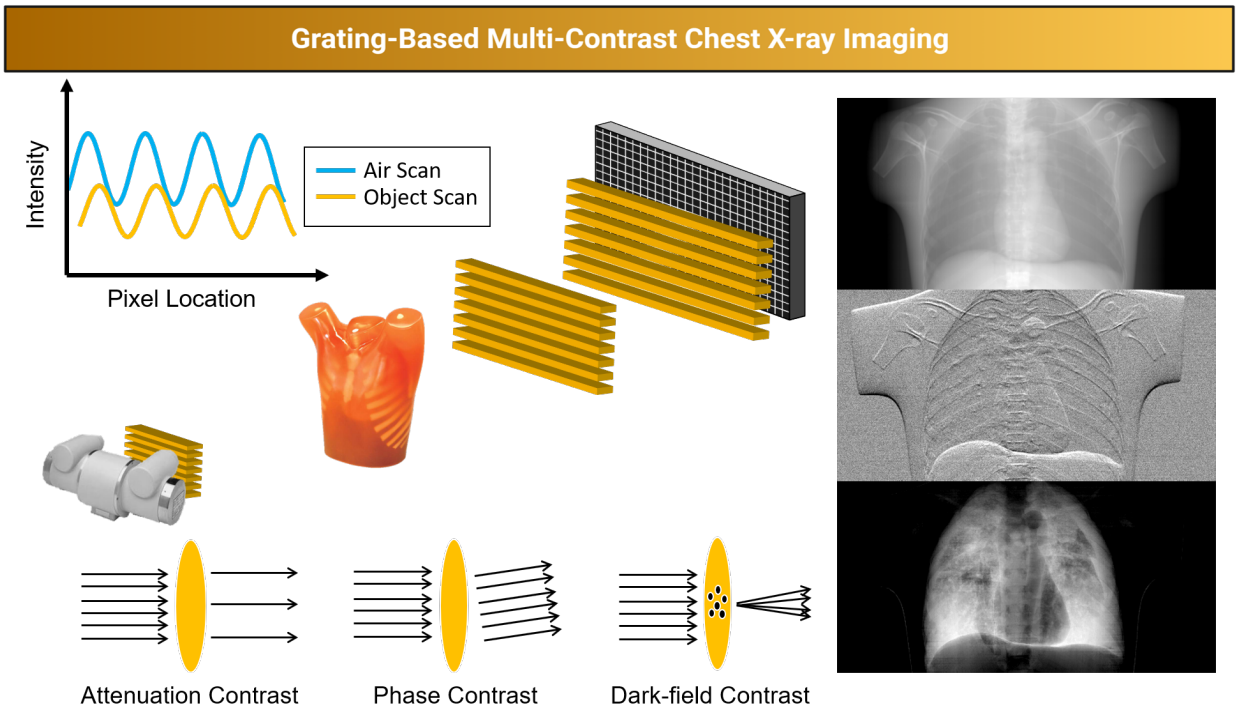

Figure 1.9: Illustration of a grating-based multi-contrast chest X-ray imaging including a grating interferometer, a model for the interference at the detector, and simulated absorption, differential phase, and dark-field images of a chest. (Created in Biorender)

1.4 Outline of the Thesis work

In this thesis work, a novel prototype MC-CXR imaging system is developed to meet the constraints imposed by clinical chest radiography. Towards enabling a seamless clinical translation, the proposed prototype system will adopt the grating-based approach for achieving MCXR imaging. In addition to the success of clinically compatible grating-based multi-contrast imaging systems, there are several distinct advantages associated with the grating-based technique when compared to other multi-contrast imaging methods. First, current grating-based imaging methods are compatible with medical-grade X-ray sources. The grating-based approach relaxes the spatial coherency requirements, enabling the use of polychromatic, square millimeter-sized x-ray sources for MCXR imaging[105]. Additionally, the grating-based approach allows for a compact prototype system to be designed to match the geometry of clinical chest radiography systems.

The purpose of this thesis work is to construct, optimize, and evaluate a novel multi-contrast chest X-ray imaging prototype system to determine the potential clinical efficacy of MC-CXR imaging. The remainder of this thesis was organized as follows:

Chapter 2 reviews the fundamental imaging physics and principles governing grating-based multi-contrast X-ray imaging.

Chapter 3 presents the design, construction, and characteristics of the novel prototype system. A comprehensive multi-contrast image correction framework is detailed and the novel fast-scanning imaging signal formation and reconstruction methods are outlined.

In Chapter 4, the prototype system constructed in Chapter 3 is optimized and evaluated through a series of phantom imaging studies.

Chapter 5 of this thesis work examines the challenges associated with the beam hardening effect in dark field imaging of the chest.

Chapter 6 presents imaging studies for a series of *in-vivo* and *ex-vivo* large animal studies to realize the potential for MC-CXR imaging.

Finally, Chapter 7 summarizes the key results of this thesis work and provides a discussion regarding the outlook of future works.

Chapter 2

Principles of Multi-Contrast X-ray Imaging

The focus of this chapter is the physical principles governing grating-based multi-contrast X-ray imaging. To begin, a theoretical foundation for the propagation of electromagnetic waves is established through the use of the Maxwell equations in vacuum. This discussion is extended to the propagation of electromagnetic waves in medium to introduce the refractive index and complex index of refraction. The complex index of refraction is then related to the phase shift induced by a medium to establish the physical foundation for phase contrast imaging. The next goal of this chapter is to introduce the fundamental principles governing grating interferometry. Such principles include the Talbot effect, the Lau effect, and the signal formation theory for grating interferometers.

To guide the design of the novel prototype system presented in this thesis work, a unified grating interferometer design framework is presented based on the Fresnel diffraction theory. This framework is then utilized to evaluate the theoretical performance of different grating interferometer configurations.

2.1 Electromagnetic Wave Propagation

2.1.1 Electromagnetic Waves in Vacuum

James C. Maxwell provided the first comprehensive description of the relationship between electric fields, $\vec{E}$, and magnetic fields, $\vec{B}$, in his book *A Dynamical Theory of The Electromagnetic Field*[177]. The four fundamental equations stemming from this book provide the basis for the spatial and temporal

propagation of X-rays. In vacuum, the Maxwell equations are provided as follows:

$$\nabla \cdot \vec{E} = 0 \tag{2.1}$$

$$\nabla \cdot \vec{B} = 0 \tag{2.2}$$

$$\nabla \times \vec{E} = -\frac{\partial \vec{B}}{\partial t} \tag{2.3}$$

$$\nabla \times \vec{B} = \mu_0 \epsilon_0 \frac{\mathrm{d}\partial E}{\partial t} \tag{2.4}$$

In the above equations, ∇ is the three-dimensional spatial gradient, ϵ_0 is the permittivity of free space, μ_0 is the permeability of free space, and c is the speed of light in vacuum. Eq. (2.1) is Gauss' Law for electric fields which states that the electric flux through any enclosed surface is proportional to the total electric charge enclosed within the surface. With no enclosed charges, the electric flux is 0 in vacuum. Similarly, Equation (2.2) is Gauss's Law for magnetic fields, which is zero for all circumstances as magnetic monopoles do not exist. Faraday's Law of Induction (Equation 2.3) asserts that a changing magnetic field induces an electric field. Finally, Equation 2.4 is Ampere's equation in vacuum, which states that an oscillating electric field will induce a magnetic field[177].

By taking the curl of Faraday's and Ampere's laws and applying Maxwell's equations, one can derive the wave equation.

$$\left(\mu_0 \epsilon_0 \frac{\partial^2}{\partial t^2} - \nabla^2\right) \vec{E} \quad = 0 \tag{2.5}$$

$$\left(\mu_0 \epsilon_0 \frac{\partial^2}{\partial t^2} - \nabla^2\right) \vec{B} \quad = 0 \tag{2.6}$$

Considering the above wave equations are identical for the electric and magnetic fields, only the electric field will be considered in the subsequent formulations. Equation 2.5 permits many solutions, one of which is the plane wave. The plane wave can be used to model the behavior of electromagnetic waves in vacumm and in homogeneous medium. Assuming a time-harmonic plane wave, the spatial and temporal components of the electric field are separable. That is to say, the electric field can be represented as:

$$\vec{E}(\vec{r}, t) = \qquad \vec{E_0} \sin(\vec{k} \cdot \vec{r} - \omega t) \tag{2.7}$$

$$\vec{E}(\vec{r},t) = \quad \vec{E_0}\exp(\vec{k}\cdot\vec{r} - \exp(i\omega t). \tag{2.8}$$

Here, $\vec{E_0}$ is the amplitude of the electric field, ω is the angular frequency, $\vec{k}$ is the wave vector, $\vec{r}$ is the position vector. Substituting Equation 2.8 into Equation 2.5, we obtain:

$$\mu_0\epsilon_0\frac{\partial^2\vec{E}(\vec{r},t)}{\partial t^2} - \nabla^2\vec{E}(\vec{r},t) = 0 \tag{2.9}$$

$$\mu_0\epsilon_0\left(i\omega\right)^2\vec{E}(\vec{r}) - \nabla^2\vec{E}(\vec{r}) = 0 \tag{2.10}$$

$$\mu_0\epsilon_0\omega^2\vec{E}(\vec{r}) + \nabla^2\vec{E}(\vec{r}) = 0 \tag{2.11}$$

This result is a form of the Helmholtz equation where the wave number k can be defined as $k = \sqrt{\mu_0\epsilon_0}\omega$. Based on the dispersion relation, the phase velocity is therefore defined as

$$c = \frac{1}{\sqrt{\mu_0\epsilon_0}} \tag{2.12}$$

such that

$$\left(\frac{\omega}{c}\right)^2\vec{E}(\vec{r}) + \nabla^2\vec{E}(\vec{r}) = 0 \tag{2.13}$$

$$\left(k^2 + \nabla^2\right)\vec{E}(\vec{r}) = 0 \tag{2.14}$$

This derivation can also be performed for the magnetic field vector and for all scalar components of both the electric and magnetic fields. As such, a single scalar wave-field can be employed to describe the behavior of both the electric and magnetic field as

$$U(\vec{r},t) = U_0\exp(i\vec{k}\cdot\vec{r})\exp(-i\omega t). \tag{2.15}$$

The separability of the scalar wave equation can once again be used to formulate the Helmholtz equation.

$$\left(k^2 + \nabla^2\right)\vec{U}(\vec{r}) = 0 \tag{2.16}$$

2.1.2 Electromagnetic Waves in Medium

We can now extend the prior discussion to the case of electromagnetic wave propagation in medium. To establish a foundation, a simplified model is used in which the medium is assumed to be time-invariant and linear. To begin, the Maxwell equations are reintroduced.

$$\nabla \cdot \vec{E} = \frac{\rho(x,y,z)}{\epsilon(x,y,z)} \tag{2.17}$$

$$\nabla \cdot \vec{B} = 0 \tag{2.18}$$

$$\nabla \times \vec{E} = -\frac{\partial \vec{B}}{\partial t} \tag{2.19}$$

$$\nabla \times \vec{B} = \mu(x,y,z)\left(\vec{J} + \epsilon(x,y,z)\frac{\partial D}{\partial t}\right) \tag{2.20}$$

In the above formulation, ρ is the charge density, ϵ is the electric permittivity, μ is the magnetic permeability, and $\vec{J}$ is defined as the current density of the medium. Assuming a non-magnetic material, the magnetic permeability can simply be represented as μ_0. The wave equation for electromagnetic waves in medium can be recovered by applying a similar procedure to that done in the previous section. For the electric field, it can be found that:

$$\left(\mu_0\epsilon(x,y,z)\frac{\partial^2}{\partial t^2} - \nabla^2\right)\vec{E} \quad = 0, \tag{2.21}$$

$$\tag{2.22}$$

such that the wave equation for the plane wave presented in Equation 2.8 is

$$\left(\mu_0\epsilon(x,y,z)\omega^2 + \nabla^2\right)\vec{E} \quad = 0 \tag{2.23}$$

Applying the dispersion relation, the phase velocity of the wave in medium is:

$$v = \frac{1}{\sqrt{\mu_0\epsilon(x,y,z)}}. \tag{2.24}$$

As expected, the phase velocity of electromagnetic fields is changed in medium. The well-known refractive index can be presented to compare the phase velocity of electromagnetic waves in medium

to that in vacuum. The refractive index is given as $n = c/v$, or

$$n(x, y, z) = \frac{c}{\sqrt{\mu_0 \epsilon(x, y, z)}} = \sqrt{\frac{\epsilon(x, y, z)}{\epsilon_0}} \tag{2.25}$$

The refractive index, as the name implies, is essential for understanding the refraction of electromagnetic waves. When a wave passes from one medium to another there will be a change in the propagation direction of the wave arising from the change in the phase velocity of the wave. The refractive index provides the degree to which the wave will be refracted. A more comprehensive quantity can be introduced to describe the propagation of X-rays when the X-rays are absorbed or scattered in the medium. This quantity is called the complex index of refraction and describes the absorptive and dispersive properties of X-rays in medium.

$$n(x, y, z) = 1 - \delta(x, y, z) + i\beta(x, y, z) \tag{2.26}$$

Here, β describes the imaginary component of the refractive index. The imaginary component of the refractive index relates to the absorption of X-rays in a given material. For instance, the imaginary component is related to the linear attenuation coefficient of X-rays as

$$\beta = \frac{\mu\lambda}{4\pi}, \tag{2.27}$$

where λ is the wavelength of the X-rays[97]. The other term in Equation 2.26, δ, is the real part of the refractive index. The real part of the refractive index is related to the refraction-induced phase shift to the wave-field.

$$\phi(x, y) = \frac{2\pi}{\lambda} \int_l \delta(x, y, z) dl, \tag{2.28}$$

From a physical perspective, the real part of the refractive index is directly proportional to the electron density ρ_e of the interacting medium by

$$\delta(x, y, z) = \frac{\rho_e r_0 h^2 c^2}{2\pi E^2}. \tag{2.29}$$

With the physical foundation for the propagation of X-rays in vacuum and medium established, we can now begin a discussion on how grating interferometry can be leveraged to generate multi-contrast X-ray images.

2.2 Principles of Grating-Based Multi-Contrast X-ray Imaging

2.2.1 Spatial Coherence Requirement

Sufficient spatial coherence of the incident X-ray wave-field is required to generate the diffraction of X-rays in a grating interferometer. Spatial coherence relates to the degree of correlation of the wave properties for a given X-ray wave or between multiple waves. Spatially coherent X-rays have well-defined relationships between the phases of different components of the wavefield or between wavefields. The degree of spatial coherence is dependent on the wavelength, size of the source fs, and propagation distance z, and can be characterized by a quantity known as the spatial coherence length L_{coh}. The spatial coherence length is defined as follows.

$$L_{coh} = \frac{\lambda z}{fs} \tag{2.30}$$

As such, spatial coherence can be increased by decreasing the size of the X-ray source or by increasing the distance between the source and grating for a given X-ray energy. From a clinical imaging perspective, medical-grade X-ray tubes do not meet sufficient beam coherence to perform grating-based X-ray imaging. However, a technique has been developed to enable the use of medical grade X-ray sources for grating interferometry[106]. The working principle of this technique is to introduce an absorption grating close to the X-ray source to split the beam into an array of independent beamlets. From a physical perspective, each individual beamlet essentially acts as a new X-ray source. As such, the coherence length no longer depends on the size of the source, but rather on the width of the openings in the gratings.

2.2.2 Diffraction and the Talbot Effect

As mentioned in Chapter 1, the working principle in grating-interferometry is to generate the interference of X-rays by using a diffracting optical element called a grating. This interference can

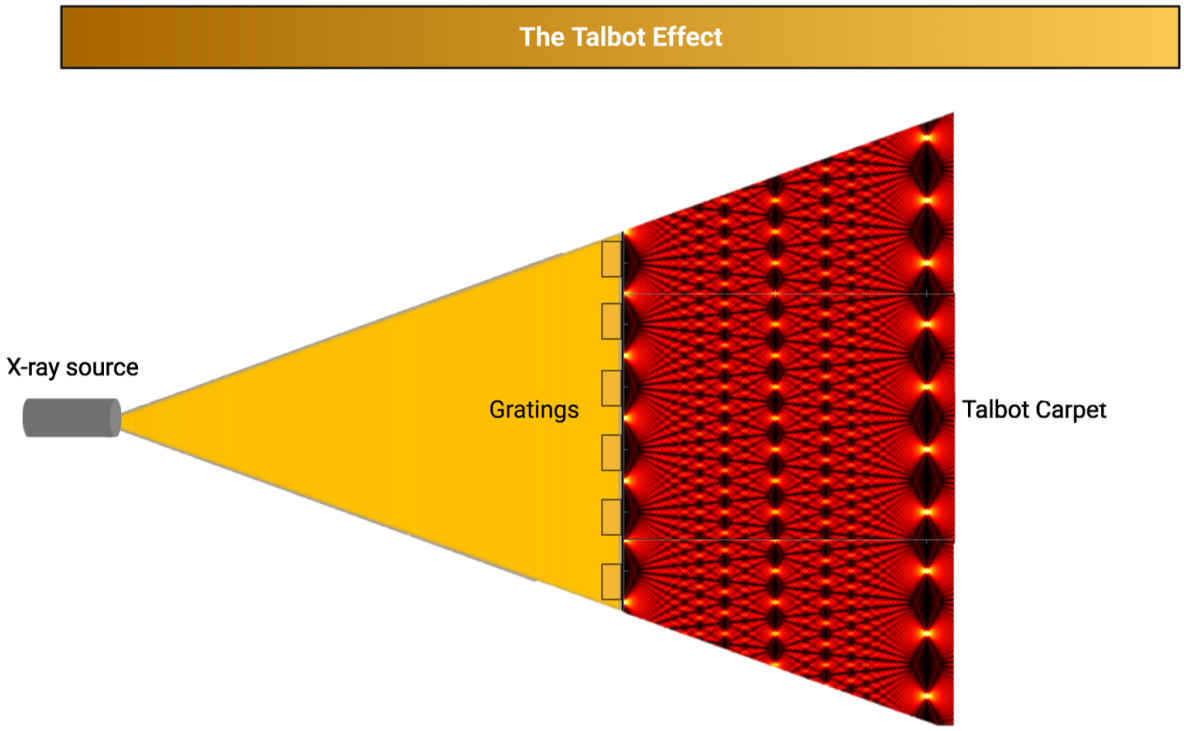

Figure 2.1: Visualization of the interference pattern generated downstream from a grating from a simulated Talbot carpet. (Created in Biorender)

then be detected as a periodic intensity modulation at distances downstream from the grating itself. Based on the Talbot effect, at certain distances from the gratings, the intensity modulation will resemble a self-image of the gratings. The Talbot distance, Z_T, at which this self-image occurs for a π phase shift grating is dependent on the wavelength of the X-rays and the pitch of the grating, p. This relationship is given as

$$Z_T = \frac{2p^2}{\lambda} \tag{2.31}$$

Although the Talbot distance provides a self-image of the gratings, it can be seen from Figure 2.1 that the periodic intensity modulations can be detected at various distances downstream from the gratings. The highest contrast in the detected intensity of the interference pattern can be found at fractional Talbot distances, defined by

$$d = \frac{2m-1}{16} Z_T \tag{2.32}$$

where m is a real positive valued integer.

2.2.3 The Lau Effect

With the interference generated, the next natural questions are: (1) how is the interference detected, and (2) how are the physical contrast mechanisms encoded into changes in the detected intensity? To address the first question, we can introduce the Lau effect. The rationale behind introducing the Lau effect is that the interference pattern generated from a single grating cannot be resolved by conventional X-ray equipment used for medical imaging applications.

The Lau effect, named after Ernst Lau[178], is a diffraction phenomenon that occurs when two gratings are placed near each other to form an interferometer. The interference pattern generated by the first grating interferes with the diffraction generated by the second grating. When the period of the second grating is matched to the period of the intensity pattern at the plane of the second grating, the superimposition of the two periodic interference patterns results in the generation of a moiré pattern. The benefit of the Lau effect for X-ray grating interferometry is that the generated moiré pattern can be resolved with clinically compatible X-ray detectors[179]. Equipping an analyzer grating to a Talbot interferometer with a source grating to provide sufficient spatial coherence is known as a Talbot-Lau interferometer. The Talbot-Lau interferometer is compatible with X-ray sources and detectors currently employed in clinical practice and provides a compact solution to multi-contrast X-ray imaging. For these reasons, the principles of Talbot-Lau interferometry are exploited in this thesis to construct a modified grating interferometer that is compact and compatible with the hardware components currently used in radiography. A framework for optimizing the design of this modified interferometer is presented in the next section.

2.2.4 Signal Extraction and Image Formation

Before discussing the design considerations for the prototype interferometer developed in this work, it is important to first establish the relationship between the interference patterns generated by the interferometer and the absorption, phase, and dark-field contrast mechanisms. The goal of this sub-section is to provide a model for the interference pattern detected at the detector plane and how it can be exploited to generate multi-contrast projection images. The intensity of the

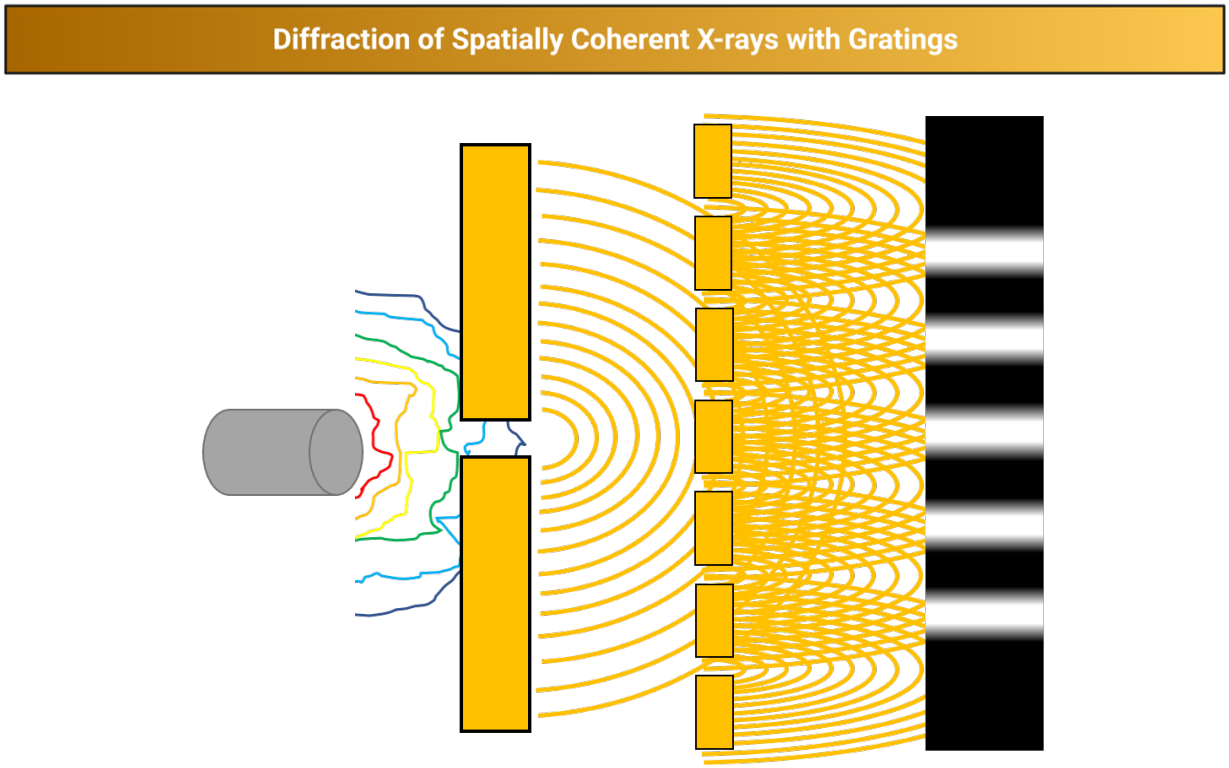

Figure 2.2: Talbot interferometry from incoherent polychromatic X-rays. (Created in Biorender)

interference pattern at the detector plane in the absence of an image object can be modeled as a sinusoidal function:

$$I(x,y) = I_0(x,y) + I_1(x,y)\cos\left[\phi_0(x,y)\right] \tag{2.33}$$

where $I_0(x,y)$ is related to the overall intensity of the pattern, $I_1(x,y)$ is the amplitude of the sinusodial intensity, and $\phi(x,y)$ is the phase of the interference patten. The absorption of X-rays will result in a decrease to the overall intensity of the interference pattern at the detector and is therefore directly related to I_0. Refraction will induce a phase shift to ϕ, while small-angle scattering will cause a blurring of the interference fringes resulting in a decrease to the amplitude I_1 of the sinusoidal function. To avoid an ill-posed problem, three or more measurements should be made to solve for the three unknowns of I_0, I_1, and ϕ. Traditionally, this has been accomplished through the phase-stepping approach introduced in Chapter 1. Phase modulation can be introduced to the interference pattern by incrementally shifting one of the gratings laterally. The shift of the grating is equivalent to the pitch of the grating divided by the total number of phase steps used in the

acquisition. For an M step acquisition, the intensity at the detector for the k-th phase step can be modeled as:

$$I^{(k)}(x,y) = I_0(x,y) + I_1(x,y)\cos\left[\frac{2\pi k}{M} + \phi_0(x,y)\right]. \tag{2.34}$$

The three unknowns from the set of M phase step equations can be solved in the following manner.

$$I_0(x,y) = \tfrac{1}{M}\textstyle\sum_{k=1}^{M} I^{(k)}(x,y) \tag{2.35}$$

$$I_1(x,y) = \tfrac{2}{M}\sqrt{\left(\textstyle\sum_{k=1}^{M} I^{(k)}(x,y)\sin\left[\frac{2\pi k}{M}\right]\right)^2 + \left(\textstyle\sum_{k=1}^{M} I^{(k)}(x,y)\cos\left[\frac{2\pi k}{M}\right]\right)^2} \tag{2.36}$$

$$\phi(x,y) = \tan^{-1}\left(-\frac{\sum_{k=1}^{M} I^{(k)}(x,y)\sin(\frac{2\pi k}{M})}{\sum_{k=1}^{M} I^{(k)}(x,y)\cos(\frac{2\pi k}{M})}\right) \tag{2.37}$$

The phase stepping procedure is performed for an air scan and an object scan to generate the absorption, phase, and dark-field images. The formulation for the absorption and phase contrast images is:

$$A(x,y) = \ln\frac{I_0^{(air)}(x,y)}{I_0^{(obj)}(x,y)} = \int_z \mu(x,y,z)dz \tag{2.38}$$

$$P(x,y) = \phi^{(obj)}(x,y) - \phi_0(x,y) = \frac{2\pi}{\lambda}\frac{\partial}{\partial x}\int_z \delta(x,y,z)dz, \tag{2.39}$$

For the dark field signal, we can first introduce a concept known as visibility. The visibility is defined as the ratio of the overall intensity with respect to the amplitude of the cosine function. Therefore, the visibility for the object scan is defined as follows:

$$v^{(obj)}(x,y) = \frac{I_1^{(obj)}(x,y)}{I_0^{(obj)}(x,y)} \tag{2.40}$$

The dark field signal is then defined as the log of the ratio of the air scan visibility and the object scan visibility.

$$D(x,y) = \ln(\frac{v^{(air)}(x,y)}{v^{(obj)}(x,y)} = \int \sigma_{DF}(x,y,z)[1 - G(\zeta)]dl \tag{2.41}$$

Here, σ_{DF} is the small-angle scattering cross section, ζ is the autocorrelation length of the interferometer, and G is the density spatial correlation function.

2.3 Grating Interferometer Design Optimization Framework

There are several considerations that must be taken into account when designing an X-ray grating interferometer. For instance, one must select the number of gratings, the type of gratings, the thickness of materials used in the grating design, etc. At this time, there have been several grating configurations that have been employed for multi-contrast imaging. The Talbot-Lau interferometer and the far-field interferometer represent two extremes in interferometer design, where either absorption gratings or phase gratings are used (for the first and the third gratings). Given the two extremes of a general absorption-phase grating setup, it is natural to develop a theory using general gratings, such that all available setups can be seen as particular examples of the general interferometer. In this section, a unified theory is introduced to demonstrate how information about the object is encoded as the X-rays propagates through a general X-ray grating interferometer consisting of one, two, or three mixed absorption-phase gratings. Using the derived fringe intensity expressions, one can calculate the fringe visibility and phase sensitivity factor. From here, the dependence on characteristic parameters of the system such as the number of gratings, type of gratings, detector pixel size, x-ray focal spot size, and the location of the image object. Using this unified theoretical framework, one can determine the optimal grating design for a given set of constraints.

System geometries with one, two, and three gratings are shown in Fig. 2.3. For each grating interferometer setup, image objects can be placed at various locations downstream of the source. The example shown in Fig. 2.3(c) will be referred to as the configuration III-1, where III indicates a three-grating system and 1 indicates that the object is placed behind the G_0 grating. Note that the configuration III-0 will indicate that the object is placed between the source and the G_0 grating.

The wave field is modulated by the object and gratings via complex transmission functions as it propagates through the system. In addition, the wave-field will also propagate in free space, which can be expressed in terms of a convolution with the Fresnel propagator. Information encoding is accomplished through these cascaded steps of wave-field modulation and free propagation. Intensity expressions can then be calculated at the detector for a given wave-field. Calculations of the intensity at the detector are similar for all configurations. However, the complexity of the calculations increases with an increasing number of gratings. As such, the following subsection

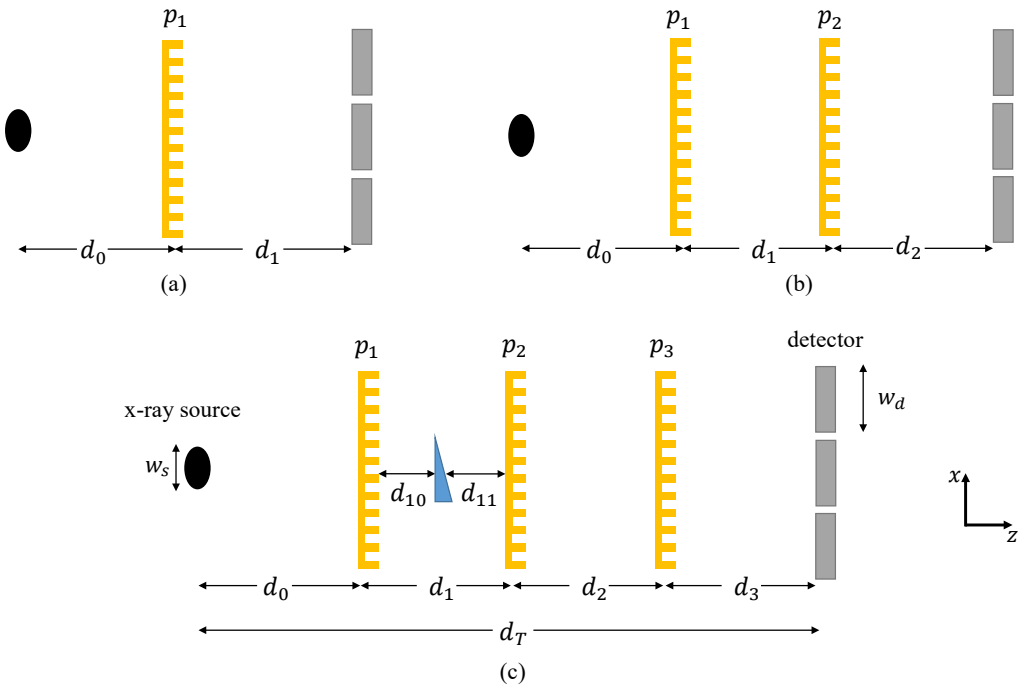

Figure 2.3: System geometries considered in this unified framework. The primary distance variables, d_0, d_1, d_2, d_3, are labeled in each sub-figure. The total distance from the X-ray source to the detector is given as d_T. The period of the i-th grating is p_i. To define image object position within distance d_i, d_{i0}/d_{i1} is used for the pre/post-object distance. Sizes of the x-ray focal spot and detector pixel are w_s and w_d, respectively.

will use the III-1 configuration to demonstrate the fringe intensity calculation. Through this example, a framework will be established by which the fringe intensity calculations for other grating configurations can be calculated.

2.3.1 Fringe Intensity Calculation for a Three Grating Interferometer with a Monochromatic Source

To begin, the fringe intensity will be calculated for the III-1 configuration under the condition of a monochromatic X-ray source. The next subsection will extend these calculations to the polychromatic case. The well-known Fresnel propagator[180] is used to model the free-space propagation from one element of the system to the next.

$$P_d(x) = \frac{\exp\left(\frac{i2\pi d}{\lambda}\right)}{\sqrt{i\lambda d}} \exp\left(\frac{i\pi x^2}{\lambda d}\right), \tag{2.42}$$

where d is the propagation distance, x is the transverse distance from the optical axis and λ is the wavelength. The use of the paraxial approximation in the Fresnel propagator can be justified as long as the cone angle is small, which is usually the case due to the small size of the gratings. Note that in the following calculations, only the phase term $\exp[(i\pi x^2)/(\lambda d)]$ of the propagator is used. The constant phase factor $\exp(i2\pi d/\lambda)$ is ignored because it will be canceled out during the intensity calculation. The normalization constant $1/\sqrt{i\lambda d}$ is ignored because it only affects the absolute intensity.

Assuming a unit-intensity monochromatic point source located at $x = x_0$. After a propagation distance of d_0, the wave-field at the entrance plane of the first grating (denoted by G_0^-) can be calculated as follows:

$$U_{G_0^-}(x) = \delta(x - x_0) * \exp\left(\frac{i\pi x^2}{\lambda d_0}\right) = \exp\left[\frac{i\pi(x - x_0)^2}{\lambda d_0}\right], \tag{2.43}$$

where the convolution operation is denoted by the asterisk sign $*$. g

The wave-field at the exit plane of the G_0 grating (denoted by G_0^+) can be written as

$$U_{G_0^+}(x) \quad = \quad U_{G_0^-}(x) T_{G_0}(x), \tag{2.44}$$

where $T_{G_0}(x)$ is the complex transmission function of the G_0 grating. In this paper, the complex transmission function of the grating is modeled by the following general form:

$$T_G(x) = \begin{cases} t_b \exp(-i\varphi_b) & x \in [0, cp] \\ t_s \exp(-i\varphi_s) & x \in (cp, p] \end{cases} \tag{2.45}$$

where t, φ determine the amplitude and phase modulation of the grating, respectively. The subscripts b and s indicate the grating bars and slits. The duty cycle c is defined as the width of the grating bars divided by the grating period p. To facilitate the discussion, the complex transmission function of the grating can be conveniently written as the Fourier series:

$$T_G(x) = \sum_{m=-\infty}^{\infty} a_m \exp\left(\frac{i2\pi m x}{p}\right). \tag{2.46}$$

In the remainder of the paper, the Fourier coefficients for G_0, G_1 and G_2 are denoted as a_m, b_n, c_r respectively. Using Eqs. (2.44) and (2.46), the wave-field right after the first grating can be calculated as follows:

$$\begin{aligned} U_{G_0^+}(x) &= U_{G_0^-}(x) T_{G_0}(x) \\ &= \sum_{m=-\infty}^{\infty} a_m \exp\left(\frac{i2\pi m x}{p_1}\right) \exp\left[\frac{i\pi(x-x_0)^2}{\lambda d_0}\right]. \end{aligned} \tag{2.47}$$

After a propagation distance of d_{10}, the wave-field right before the image object, $U_{O^-}(x)$, can be written as:

$$\begin{aligned} U_{O^-}(x) &= U_{G_0^+}(x) * P_{d_{10}}(x) \\ &= \sum_{m=-\infty}^{\infty} a_m \int_{-\infty}^{\infty} \exp\left(\frac{i2\pi m x'}{p_1}\right) \exp\left[\frac{i\pi(x'-x_0)^2}{\lambda d_0}\right] \exp\left[\frac{i\pi(x-x')^2}{\lambda d_{10}}\right] dx'. \end{aligned} \tag{2.48}$$

The integral is the standard type of Gaussian integral, using the corollary in Appendix A, one can carry out the integral to obtain the following result:

$$\begin{aligned} U_{O^-}(x) &= \sum_{m=-\infty}^{\infty} a_m \exp\left(\frac{-i\pi\lambda m^2}{p_1^2} \frac{d_0 d_{10}}{d_0 + d_{10}}\right) \exp\left(\frac{i2\pi m x_0}{p_1} \frac{d_{10}}{d_0 + d_{10}}\right) \\ &\times \exp\left(\frac{i2\pi m x}{p_1} \frac{d_0}{d_0 + d_{10}}\right) \exp\left[\frac{i\pi(x-x_0)^2}{\lambda(d_0 + d_{10})}\right]. \end{aligned} \tag{2.49}$$

The wave-field after the image object (denoted by U_{O^+}) can be written as:

$$U_{O^+}(x) = U_{O^-}(x) T_O(x), \tag{2.50}$$

where $T_O(x) = \exp[-i\varphi_O(x)]$ is the complex transmission function of the object. Under the projection approximation[181], $\varphi_O(x)$ can be written as:

$$\phi_O(x) = \frac{2\pi}{\lambda} \int [\delta(x,z) - i\beta(x,z)] dz. \tag{2.51}$$

where $\delta(x,z)$ is the decrement of the real part of the complex refractive index and and $\beta(x,z)$ is the imaginary part of the complex refractive index. The wave-field $U_{O^+}(x)$ that carries the information

of the object will be further propagated by a distance of d_{11}. Then, the wave-field at the surface plane of the G_1 grating can be calculated as follows:

$$\begin{aligned} U_{G_1^-}(x) &= U_{O^+}(x) * P_{d_{11}}(x) \\ &= \sum_{m=-\infty}^{\infty} a_m \exp\left(\frac{-i\pi\lambda m^2}{p_1^2}\frac{d_0 d_{10}}{d_0+d_{10}}\right)\exp\left(\frac{i2\pi m x_0}{p_1}\frac{d_{10}}{d_0+d_{10}}\right) \\ &\times \int_{\infty}^{\infty}\exp\left(\frac{i2\pi m x'}{p_1}\frac{d_0}{d_0+d_{10}}\right)\exp\left[\frac{i\pi(x'-x_0)^2}{\lambda(d_0+d_{10})}\right]\exp[-i\phi_O(x')] \\ &\quad \exp\left[\frac{i\pi(x-x')^2}{\lambda d_{11}}\right]dx'. \end{aligned} \tag{2.52}$$

Under the smooth approximation condition of the phase information $\phi_O(x)$, the stationary phase approximation shown in Appendix A can be directly used to calculate the integral in above equation. The result is given as follows:

$$\begin{aligned} U_{G_1^-}(x) &= \sum_{m=-\infty}^{\infty} a_m \exp\left(\frac{-i\pi\lambda m^2}{p_1^2}\frac{d_0 d_1}{d_0+d_1}\right)\exp\left(\frac{i2\pi m x_0}{p_1}\frac{d_1}{d_0+d_1}\right) \\ &\times \exp\left(\frac{i2\pi m x}{p_1}\frac{d_0}{d_0+d_1}\right)\exp\left[\frac{i\pi(x-x_0)^2}{\lambda(d_0+d_1)}\right] \\ &\times \exp\left[-i\phi_O\left(x\frac{d_0+d_{10}}{d_0+d_1}+x_0\frac{d_{11}}{d_0+d_1}-\frac{\lambda m}{p_1}\frac{d_0 d_{11}}{d_0+d_1}\right)\right]. \end{aligned}$$

From the above result, one can observe that the phase information of the image object $\phi_O(x)$ has been encoded into the phase change of the wave-field as follows:

$$\phi_O(x) \to \phi_O\left(x\frac{d_0+d_{10}}{d_0+d_1}+x_0\frac{d_{11}}{d_0+d_1}-\frac{\lambda m}{p_1}\frac{d_0 d_{11}}{d_0+d_1}\right). \tag{2.53}$$

The first two terms in the argument represent a geometrical projection of a point from the image object onto the surface of the G_1 grating with a shift that depends on the source location x_0 and the third term is used to characterize the impact of the grating G_0. These direct product and convolution operations are repeated to generate the ultimate wave-field at the detector plane as follows:

$$\begin{aligned} U_{G_1^+}(x) &= U_{G_1^-}(x)T_{G_1}(x), \\ U_{G_2^-}(x) &= U_{G_1^+}(x) * P_{d_2}(x), \end{aligned}$$

$$
\begin{aligned}
U_{G_2^+}(x) &= U_{G_2^-}(x) T_{G_2}(x), \\
U_{det}(x) &= U_{G_2^+}(x) * P_{d_3}(x).
\end{aligned} \tag{2.54}
$$

Using the methods presented in this section, one can readily carry out the rest of the information encoding steps shown in Eqs. (2.54) to obtain the wave-field at the detector plane $U_{det}(x)$. For brevity, these calculations will not be repeated here. The final result is given as follows:

$$
\begin{aligned}
& U_{det}(x) \\
&= \sum_{m,n,r=-\infty}^{\infty} a_m b_n c_r \\
&\times \exp\left[\frac{-i\pi\lambda}{d_T} S_1(m,n,r) + \frac{i2\pi x_0}{d_T} S_2(m,n,r) + \frac{i2\pi x}{d_T} S_3(m,n,r) + \frac{i\pi(x-x_0)^2}{\lambda d_T}\right] \\
&\times \exp\left\{-i\phi_O\left[x\frac{d_0+d_{10}}{d_T} + x_0\frac{d_{11}+d_2+d_3}{d_T} - \frac{\lambda}{d_T} S_4(m,n,r)\right]\right\},
\end{aligned} \tag{2.55}
$$

where m, n, r are integers. The functions $S_1(m,n,r)$, $S_2(m,n,r)$, $S_3(m,n,r)$, and $S_4(m,n,r)$ are defined as follows:

$$
\begin{aligned}
S_1(m,n,r) &= m^2 \frac{d_0(d_1+d_2+d_3)}{d_T p_1^2} + n^2 \frac{(d_0+d_1)(d_2+d_3)}{d_T p_2^2} + r^2 \frac{d_3(d_0+d_1+d_2)}{d_T p_3^2} \\
&+ 2mn \frac{d_0(d_2+d_3)}{d_T p_1 p_2} + 2mr \frac{d_0 d_3}{d_T p_1 p_3} + 2nr \frac{d_3(d_0+d_1)}{d_T p_2 p_3}, \\
S_2(m,n,r) &= m\frac{d_1+d_2+d_3}{p_1} + n\frac{d_2+d_3}{p_2} + r\frac{d_3}{p_3}, \\
S_3(m,n,r) &= m\frac{d_0}{p_1} + n\frac{d_0+d_1}{p_2} + r\frac{d_0+d_1+d_2}{p_3}, \\
S_4(m,n,r) &= m\frac{d_0(d_{11}+d_2+d_3)}{p_1} + n\frac{(d_2+d_3)(d_0+d_{10})}{p_2} + r\frac{d_3(d_0+d_{10})}{p_3}.
\end{aligned} \tag{2.56}
$$

Since $\phi_O(x)$ is a slowly varying function over a length scale of $\frac{\lambda S_4}{d_T}$, which is usually about several micrometers, we can approximate it using the first order Taylor expansion:

$$
\begin{aligned}
\phi_O\left[x\frac{d_0+d_{10}}{d_T} + x_0\frac{d_{11}+d_2+d_3}{d_T} - \frac{\lambda}{d_T} S_4(m,n,r)\right] &\approx \\
\phi_O\left(x\frac{d_0+d_{10}}{d_T} + x_0\frac{d_{11}+d_2+d_3}{d_T}\right)&
\end{aligned}
$$

$$-\frac{\lambda}{d_T}S_4(m,n,r)\times\phi'_O\left(x\frac{d_0+d_{10}}{d_T}+x_0\frac{d_{11}+d_2+d_3}{d_T}\right). \tag{2.57}$$

Once the wave-field expression is obtained, the intensity on the detector plane can be calculated by taking the modular square of $U_{det}(x)$. Using Eqs. (2.51), (2.55) and (2.57), the intensity can be finally written as

$$\begin{aligned} I(x;x_0,E) &\approx \sum_{s=-\infty}^{\infty}\sum_{t=-\infty}^{\infty}\sum_{q=-\infty}^{\infty}A(s)B(t)C(q)\exp\left(\frac{i2\pi x_0}{p_s}\right)\exp\left(\frac{i2\pi x}{p_f}\right) \\ &\times \exp\left[-\int\mu\left(x\frac{1}{M}+x_0\frac{M-1}{M}\right)dz\right] \\ &\times \exp\left[-i2\pi\eta\frac{d}{dx}\int\delta\left(x\frac{1}{M}+x_0\frac{M-1}{M}\right)dz\right]. \end{aligned} \tag{2.58}$$

In this equation, definition of the phase function ϕ_O in Eq. (2.51) has been used to separate the contribution of decrement δ and β in the complex refractive index, where $\mu=4\pi\lambda/\beta$. The geometrical magnification of the object is defined as $M=d_T/(d_0+d_{10})$. Other parameters are defined as follows:

$$\begin{aligned} \frac{1}{p_f} &= \frac{s}{p_1}\frac{d_0}{d_T}+\frac{t}{p_2}\frac{d_0+d_1}{d_T}+\frac{q}{p_3}\frac{d_0+d_1+d_2}{d_T}, \\ \frac{1}{p_s} &= \frac{s}{p_1}\frac{d_1+d_2+d_3}{d_T}+\frac{t}{p_2}\frac{d_2+d_3}{d_T}+\frac{q}{p_3}\frac{d_3}{d_T}, \\ \eta &= \frac{s}{p_1}\frac{d_0(d_{11}+d_2+d_3)}{d_T}+\frac{t}{p_2}\frac{(d_0+d_{10})(d_2+d_3)}{d_T}+\frac{q}{p_3}\frac{d_3(d_0+d_{10})}{d_T}. \end{aligned} \tag{2.59}$$

Here, the period of the interference fringe is given by $|p_f|$. For a given grating interferometer, the required focal spot size is determined by the source period $|p_s|$, which will be further discussed in section 3. The last two exponential terms in Eq. (2.58) represent the mean fringe intensity reduction and fringe phase shift caused by the object. For a given x-ray refraction angle (i.e. $\frac{d}{dx}\int\delta dz$), the sensitivity factor η determines the phase shift of the interference fringe. The attenuation information, in contrast, is independent of the interferometer parameters.

Also note that the following equation is always valid:

$$\frac{s}{p_1}+\frac{t}{p_2}+\frac{q}{p_3}=\frac{1}{p_f}+\frac{1}{p_s}. \tag{2.60}$$

In addition to the above parameters, the coefficients $A(s)$, $B(t)$ and $C(q)$ in Eq. (2.58) are defined as follows:

$$\begin{aligned} A(s) &= \sum_{m=-\infty}^{+\infty} a_m a_{m-s}^* \exp\left[-i2\pi\gamma_1(m-s/2)\right], \\ B(t) &= \sum_{n=-\infty}^{+\infty} b_n b_{n-t}^* \exp\left[-i2\pi\gamma_2(n-t/2)\right], \\ C(q) &= \sum_{r=-\infty}^{+\infty} c_r c_{r-q}^* \exp\left[-i2\pi\gamma_3(r-q/2)\right], \end{aligned} \tag{2.61}$$

where $\gamma_1 = \frac{\lambda d_0}{p_1 p_s}$,$\gamma_2 = \frac{\lambda}{p_2}(\frac{d_2+d_3}{p_f} - q\frac{d_2}{p_3})$,$\gamma_3 = \frac{\lambda d_3}{p_3 p_f}$. Note that for gratings with rectangular profiles, the infinite summations in $A(s)$, $B(t)$ and $C(q)$ can be carried out explicitly, as shown in Appendix B. These coefficients can be rewritten as:

$$\begin{aligned} A(s) &= \exp(i\pi s\gamma_1)F_1(s,\bar{\gamma}_1), \\ B(t) &= \exp(i\pi t\gamma_2)F_2(t,\bar{\gamma}_2), \\ C(q) &= \exp(i\pi q\gamma_3)F_3(q,\bar{\gamma}_3), \end{aligned} \tag{2.62}$$

where F_1, F_2 and F_3 are the characteristic functions of the gratings. The parameter $\bar{\gamma}$ is defined as $\bar{\gamma} = \gamma - \lfloor\gamma\rfloor$.

Here we want to emphasize that p_f, p_s and η in Eq.(2.58) all depend on the choices of integers s, t and q. This means that the intensity on the detector plane consists of infinitely many harmonics with different amplitude and period. However, for a practical system, only certain choices of s, t and q need to be considered due to two reasons: First, the coefficients $A(s), B(t)$ and $C(q)$ drop at higher orders. Second, due to the finite detector spatial resolution and the finite focal spot size, only a few leading terms which correspond to proper fringe period and source period can be observed, this will be discussed in section 3.3.

2.3.2 Fringe Intensity Calculation for a Three Grating Interferometer with a Polychromatic Source

The intensity expression shown in Eq. (2.58) corresponds to the case of a monochromatic point source. When an extended monochromatic source is considered, assuming the source consists of

infinite point source which generates x-rays independently, the intensity can be written as:

$$I\left(x;E\right)=\int W\left(x_0\right)I\left(x;x_0,E\right)dx_0, \tag{2.63}$$

where $W(x_0)$ is the intensity distribution of the x-ray source.

One can further extend the above result to the polychromatic case by integrating the contributions from each given wavelength.

$$I(x)=\int \Omega(E)I(x;E)dE, \tag{2.64}$$

where $\Omega(E)$ is the spectrum of the x-ray source.

2.3.3 Fringe Intensity for Different Grating Configurations

Using the method provided in section 2, the calculations for the other configurations shown in Fig. 2.3 can be done similarly. Results are summarized in this section.

2.3.3.1 Monochromatic fringe intensity: One-grating system

For a monochromatic extended x-ray source, the pre-sampled fringe intensity (intensity at the detector entrance plane) for the one-grating system can be expressed as:

$$\begin{aligned} I\left(x\right) &= \sum_s A(s)\exp\left(\frac{i2\pi x}{p_f}\right)\int W(x_0)\exp\left(\frac{i2\pi x_0}{p_s}\right)dx_0 \\ &= \sum_s A(s)\exp\left(\frac{i2\pi x}{p_f}\right)\tilde{W}(-\frac{1}{p_s}) \end{aligned} \tag{2.65}$$

where $\tilde{W}(-\frac{1}{p_s})$ is the Fourier transform of the x-ray source intensity distribution sampled at frequency $1/p_s$, i.e. $\tilde{W}(-\frac{1}{p_s})=\int dx_0 W(x_0)\exp\left(\frac{-i2\pi x_0}{p_s}\right)$. Assuming the intensity distribution of the x-ray source can be modeled by a box function whose width is the focal spot size w_s. In this case, $\tilde{W}(-\frac{1}{p_s})$, can be calculated to be $\tilde{W}(\frac{1}{p_s})=\mathrm{sinc}(\frac{w_s}{p_s})$. The parameters p_s and p_f are given by:

$$\begin{aligned} \frac{1}{p_s} &= \frac{s}{p_1}\frac{d_1}{d_0+d_1}, \\ \frac{1}{p_f} &= \frac{s}{p_1}\frac{d_0}{d_0+d_1}. \end{aligned} \tag{2.66}$$

The coefficient, $A(s)$ in Eq. (2.65) is defined as:

$$A(s) = \exp(i\pi s\gamma_1)F_1(s,\bar{\gamma}_1), \tag{2.67}$$

where $\gamma_1 = \frac{\lambda d_0}{p_1 p_s}$. Note that the following equation is always satisfied:

$$\frac{s}{p_1} = \frac{1}{p_f} + \frac{1}{p_s}. \tag{2.68}$$

2.3.3.2 Monochromatic fringe intensity: Two-grating system

For the two-grating system, the intensity can be calculated to be:

$$I(x) = \sum_{s,t} A(s)B(t)\exp\left(\frac{i2\pi x}{p_f}\right)\tilde{W}(-\frac{1}{p_s}). \tag{2.69}$$

where the parameters p_s and p_f are given as below:

$$\begin{aligned}\frac{1}{p_s} &= \frac{s}{p_1}\frac{d_1+d_2}{d_0+d_1+d_2} + \frac{t}{p_2}\frac{d_2}{d_0+d_1+d_2},\\ \frac{1}{p_f} &= \frac{s}{p_1}\frac{d_0}{d_0+d_1+d_2} + \frac{t}{p_2}\frac{d_0+d_1}{d_0+d_1+d_2},\end{aligned} \tag{2.70}$$

with

$$\frac{s}{p_1} + \frac{t}{p_2} = \frac{1}{p_f} + \frac{1}{p_s}. \tag{2.71}$$

The coefficients $A(s)$ and $B(t)$ for the two-grating systems are defined as follows:

$$\begin{aligned}A(s) &= \exp(i\pi s\gamma_1)F_1(s,\bar{\gamma}_1),\\ B(t) &= \exp(i\pi t\gamma_2)F_2(t,\bar{\gamma}_2),\end{aligned} \tag{2.72}$$

where $\gamma_1 = \frac{\lambda d_0}{p_1 p_s}$, $\gamma_2 = \frac{\lambda d_2}{p_2 p_f}$.

Table 2.1: A summary of sensitivity factors for all configurations

Configuration	η	Maximum value of η
I-0	$\frac{d_{00}}{p_s}$	$\frac{d_0}{p_s}$
I-1	$\frac{d_{11}}{p_f}$	$\frac{d_1}{p_f}$
II-0	$\frac{d_{00}}{p_s}$	$\frac{d_0}{p_s}$
II-1	$\frac{s}{p_1}\frac{d_0(d_{11}+d_2)}{d_T} + \frac{t}{p_2}\frac{d_2(d_0+d_{10})}{d_T}$	$\max(\frac{d_0}{p_s}, \frac{d_2}{p_f})$
II-2	$\frac{d_{21}}{p_f}$	$\frac{d_2}{p_f}$
III-0	$\frac{d_{00}}{p_s}$	$\frac{d_0}{p_s}$
III-1	$\frac{s}{p_1}\frac{d_0(d_{11}+d_2+d_3)}{d_T} + \frac{t}{p_2}\frac{(d_0+d_{10})(d_2+d_3)}{d_T} + \frac{q}{p_3}\frac{d_3(d_0+d_{10})}{d_T}$	$\max(\frac{d_0}{p_s}, \frac{d_2+d_3}{p_f} - q\frac{d_2}{p_3})$
III-2	$\frac{s}{p_1}\frac{d_0(d_{21}+d_3)}{d_T} + \frac{t}{p_2}\frac{(d_0+d_1)(d_{21}+d_3)}{d_T} + \frac{q}{p_3}\frac{d_3(d_0+d_1+d_{20})}{d_T}$	$\max(\frac{d_3}{p_f}, \frac{d_2+d_3}{p_f} - q\frac{d_2}{p_3})$
III-3	$\frac{d_{31}}{p_f}$	$\frac{d_3}{p_f}$

2.3.3.3 Monochromatic fringe intensity: Three-grating system

For the three-grating system, the intensity can be expressed as:

$$I(x) = \sum_{s,t,q} A(s)B(t)C(q)\exp\left(\frac{i2\pi x}{p_f}\right)\tilde{W}(-\frac{1}{p_s}), \tag{2.73}$$

where the parameters are defined in Eqs. (2.59) and (2.62).

2.3.3.4 Phase sensitivity

The sensitivity factors for all configurations shown in Fig. 2.3 are summarized in Table. 2.1. Note that the maximum value of η for each configuration can be achieved when the object is placed close to one of the gratings. For example, in configuration II-2, the maximum value of η is obtained when $d_{21} = d_2$, where the object is close to the G_1 grating.

2.3.3.5 Monochromatic Fringe visibility

Using the derived fringe intensity expression, the fringe visibility can be readily calculated. Once again, we will use the three-grating system as an example to illustrate the analysis. In theory, the intensity fringe consists of infinite s, t, q terms. However, given the size of the x-ray focal spot and

the size of the detector pixel, only a given choice of s,t and q $(s,t,q \neq 0)$ can generate intensity fringes with large amplitude. The other terms don't have significant contributions to the final detected intensity. Also note that $A(0)B(0)C(0)$ corresponds to the mean intensity of the fringe, denoted as I_0; the terms (s,t,q) and $(-s,-t,-q)$ are conjugate to each other and will always appear together. Consider a monochromatic extended x-ray source with a size of w_s. The fringe intensity corresponding to a given choices of s,t, and q $(s,t,q \neq 0)$ can be generally written as:

$$\begin{aligned} I_{mono}(x) &= A(0)B(0)C(0) \\ &+ \operatorname{sinc}\left(\frac{w_s}{p_s}\right)\left[A(s)B(t)C(q)\exp\left(\frac{i2\pi x}{p_f}\right) + A(-s)B(-t)C(-q)\exp\left(-\frac{i2\pi x}{p_f}\right)\right]. \\ &= I_0 + 2\times\operatorname{sinc}\left(\frac{w_s}{p_s}\right)|A(s)B(t)C(q)|\cos\left(\frac{2\pi x}{p_f}+\alpha\right), \end{aligned} \tag{2.74}$$

where $\alpha = \operatorname{Arg}[A(s)B(t)C(q)]$. When the finite detector pixel size is taken into consideration, another term $\operatorname{sinc}(\frac{w_d}{p_f})$ should be similarly introduced, and the fringe intensity becomes:

$$I_{mono}(x) = I_0 + 2\times\operatorname{sinc}\left(\frac{w_s}{p_s}\right)\operatorname{sinc}\left(\frac{w_d}{p_f}\right)|A(s)B(t)C(q)|\cos\left(\frac{2\pi x}{p_f}+\alpha\right). \tag{2.75}$$

Using the definitions of $A(s)$, $B(t)$ and $C(q)$, the fringe visibility corresponding to a monochromatic x-ray source can be expressed as:

$$\begin{aligned} V_{mono} &= 2\times\operatorname{sinc}\left(\frac{w_d}{p_f}\right)\operatorname{sinc}\left(\frac{w_s}{p_s}\right)\times\left|\frac{A(s,\gamma_1)}{A(0,0)}\frac{B(t,\gamma_2)}{B(0,0)}\frac{C(q,\gamma_3)}{C(0,0)}\right| \\ &= 2\times\operatorname{sinc}\left(\frac{w_d}{p_f}\right)\operatorname{sinc}\left(\frac{w_s}{p_s}\right)\times\left|\frac{F_1(s,\bar{\gamma}_1)}{c_1t_1^2+1-c_1}\frac{B(t,\bar{\gamma}_2)}{c_2t_2^2+1-c_2}\frac{C(q,\bar{\gamma}_3)}{c_3t_3^2+1-c_3}\right|, \end{aligned} \tag{2.76}$$

where $t_i = t_b/t_s$ is the transmission of the grating bars relative to the slits.

2.3.3.6 Polychromatic fringe visibility

Using Eqs. 2.64 and 2.75, the polychromatic fringe intensity can be calculated as follows:

$$\begin{aligned} I_{poly}(x) &= \int\Omega(E)I_0(E)dE \\ &+ 2\times\operatorname{sinc}\left(\frac{w_d}{p_f}\right)\int\operatorname{sinc}\left(\frac{w_s}{p_s}\right)\int\Omega(E)|A(s)B(t)C(q)|\cos\left(\frac{2\pi x}{p_f}+\alpha\right)dE. \end{aligned} \tag{2.77}$$

As x-ray energy changes, α may also change. However, it can be easily seen from Appendix B that α will only add $\pm\pi$ as energy changes, which means the polychromatic fringe intensity can be written as:

$$\begin{aligned} I_{poly}(x) &= \int \Omega(E) I_0(E) dE \\ &+ 2 \times \mathrm{sinc}\left(\frac{w_d}{p_f}\right) \int \mathrm{sinc}\left(\frac{w_s}{p_s}\right) \int \Omega(E) |A(s)B(t)C(q)| (\pm 1) dE \cos\left(\frac{2\pi x}{p_f}\right), \end{aligned} \quad (2.78)$$

where the energy-independent constant in the cosine function can be neglected. The (± 1) term accounts for the $\pm\pi$ fringe phase shift for different monochromatic fringes, which causes annihilation.

The resulting fringe visibility is:

$$V_{poly} = \int \Omega_0(E) V_{mono}(E) (\pm 1) dE, \quad (2.79)$$

where

$$\Omega_0(E) = \frac{\Omega(E) I_0(E)}{\int \Omega_0(E) I_0(E) dE} \quad (2.80)$$

is the normalized x-ray spectrum received at the detector plane.

2.3.4 Universal Conclusions for Grating Interometer Design

Using results presented above, it is possible to retrieve several universal conclusions regarding the design of x-ray grating interferometers. These conclusions serve as general guidelines when designing the system, as they don't rely on any specific type of x-ray grating interferometers.

2.3.4.1 Number of Gratings

The first question to be asked when designing a x-ray grating interferometer is: how many gratings should be used? As briefly mentioned in section 1, the SNR of the phase contrast information is determined by the fringe visibility and the phase sensitivity of the grating interferomter. From Eq. (2.76), to achieve high fringe visibility, the fringe period $|p_f|$ needs to be at least 4 times larger than the detector pixel size w_d and the source period p_s needs to be 4 times larger than the source size w_s,

such that the two sinc terms are close to 1. For conventional x-ray imaging systems, both w_d and w_s are on the order of several tens to several hundreds micrometers.

However, as shown in the Table. 1, to achieve high phase sensitivity, one always require smaller p_f or p_s values, with an exception of the three-grating interferometer where the object is placed close to the second grating (configurations III-1 and III-2). In this case, the phase sensitivity factor can be written as $\eta = \frac{d_2+d_3}{p_f} - q\frac{d_2}{p_3}$. Since the period of the third grating p_3 can be much smaller than $|p_f|$, the phase sensitivity factor can be approximately written as $\eta \approx q\frac{d_2}{p_3}$. As a result, η is decoupled from the source-related term p_s and the detector-related term p_f.

This leads to the first universal conclusion regarding the design of x-ray grating interferometers: **Only the three-grating interferometer can achieve high phase sensitivity with conventional x-ray source and detector.**

For the one-grating interferometer, p_f and p_s are tightly coupled, since $d_0/p_s = d_1/p_f$. To achieve high SNR, the one-grating interferometer must be used with both very small x-ray focal spot AND very high resolution detector. Therefore it is only reasonable to use a one-grating interferometer with the synchrotron x-ray source.

For the two-grating interferometer, as the coupling of p_f and p_s becomes loose, it is possible to achieve high SNR by using a small x-ray focal spot OR a high resolution detector. Two of the possible configurations are shown in Fig. 2.4.

In the first configuration shown in Fig. 2.4 (a)., assuming $d_2 \approx 0$ and the image object is close to the first grating. If the intensity is primarily determined by $(s,t) = (1,-1),(-1,1)$, the fringe period can be expressed as:

$$p_f = \frac{d_0+d_1}{d_0}\frac{p_1 p_2}{p_2 - p_1\frac{d_0+d_1}{d_0}}. \tag{2.81}$$

It's easy to find that when $p_2 = p_1\frac{d_0+d_1}{d_0}$, the fringe period can be infinitely large and a high resolution detector is not required. The source period and the sensitivity factor can be further calculated as:

$$\begin{aligned} p_s &= p_1\frac{d_0+d_1}{d_1}, \\ \eta &= \frac{d_0}{p_s} = \frac{d_1}{p_2}. \end{aligned} \tag{2.82}$$

Note that the Talbot interferometer with an analyzer grating[103] is one specific example of the setup shown in Fig. 2.4 (a), the phase sensitivity factor $\eta = d_1/p_2$ is well studied for this setup. However, if we only look at the expression d_1/p_2, it is not easy to directly see why the phase sensitivity is limited by the source.

In the second configuration shown in Fig. 2.4 (b)., assuming $d_0 \approx 0$ and the image object is close to the second grating. If the intensity is primarily determined by $(s,t) = (1,-1),(-1,1)$, the source period can be expressed as:

$$p_s = \frac{d_1 + d_2}{d_2} \frac{p_1 p_2}{p_2 \frac{d_1+d_2}{d_2} - p_1}. \tag{2.83}$$

When $p_1 = p_2 \frac{d_1+d_2}{d_2}$, the source period can be infinitely large and a x-ray tube with large focal spot can be used. The fringe period and the sensitivity factor can be further calculated as:

$$\begin{aligned} p_f &= p_2 \frac{d_1 + d_2}{d_1}, \\ \eta &= \frac{d_2}{p_f} = \frac{d_1}{p_1}. \end{aligned} \tag{2.84}$$

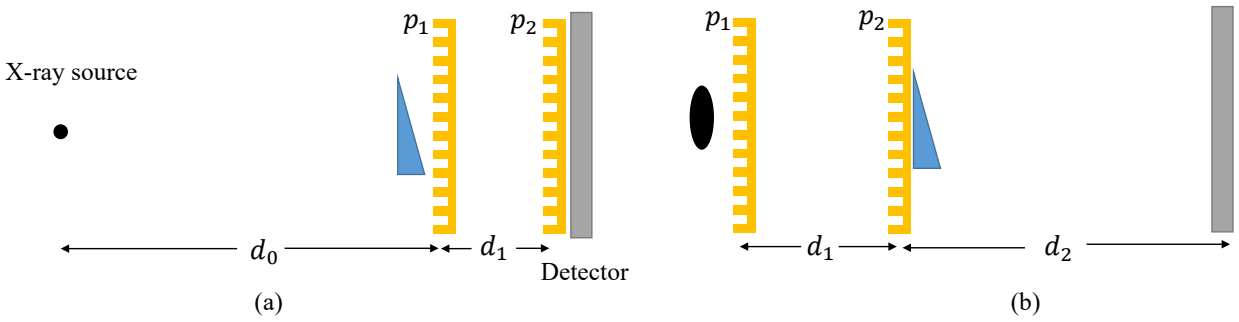

Figure 2.4: Two possible configurations of the two-grating interferometer.

In this case, the phase sensitivity of the system is limited by the detector.

As can be seen from the above results, if we exchange the position of the x-ray tube and the dectector in Fig. 2.4 (b), then it becomes identical to Fig. 2.4 (a). Therefore, it is known as the inverse geometry setup[182,183].

2.3.4.2 Type of Grating

When the number of gratings is determined, the next question to be asked is: how to determine the type of each grating? It's well known that the phase grating has some advantages over the absorption grating: it has better flux efficiency and dose efficiency; for the same grating period, it has much lower aspect ratio, therefore easier to fabricate. Since the grating type has noting to do with the phase sensitivity factor, the constraint of choosing the grating type comes from the fringe visibility, particularly, from the third term in Eq. (2.76). With the introduction of the three dimensionless quantities (γ_1,γ_2,γ_3) and the characteristic functions of the gratings (F_1, F_2, F_3), the influences of each grating on the visibility can be separated. Moreover, they share the same functional form, as shown below.

$$V_G = \frac{|F(s,\bar{\gamma})|}{ct^2 + 1 - c}. \tag{2.85}$$

For $c = 0.5$, $s = 1$ and $\bar{\gamma} \in (0, 0.5)$, V_G can be written as:

$$V_G = \frac{2}{\pi}\left|\frac{\cos(\pi\bar{\gamma})(1-t^2) + 2t\sin(\pi\bar{\gamma})\sin(\varphi)}{1+t^2}\right|. \tag{2.86}$$

(1) When ideal absorption grating is used, i.e. $t = 0$:

$$V_G \approx \frac{2}{\pi}|\cos(\pi\bar{\gamma})|. \tag{2.87}$$

In this case, the phase modulation of the grating (φ) becomes irrelevant. To achieve high fringe visibility, one needs to select system parameters such that $\bar{\gamma}$ is close to either 0 or 1.

(2) When ideal phase grating is used, i.e. $t = 1$:

$$V_G = \frac{2}{\pi}|\sin(\pi\bar{\gamma})\sin(\varphi)|. \tag{2.88}$$

In this case, a $\varphi = \pi/2$ phase grating should be used and system parameters should be selected such that $\bar{\gamma}$ is close to 0.5.

For $c = 0.5$, $s = 2$, and $\bar{\gamma} \in (0, 0.5)$, V_G can be written as:

$$V_G = \frac{1}{\pi} \left| \frac{(t^2+1)\sin(2\pi\bar{\gamma}) - 2t\sin(2\pi\bar{\gamma})\cos(\varphi)}{1+t^2} \right|. \tag{2.89}$$

(3) When ideal phase grating is used, i.e. $t = 1$:

$$V_G = \frac{2}{\pi} \left| \frac{\sin(2\pi\bar{\gamma})[1-\cos(\varphi)]}{2} \right|. \tag{2.90}$$

In this case, the maximum visibility of $2/\pi$ is achieved when $\varphi = \pi$, $\bar{\gamma} = 0.25$.

From the above examples, we can see that the choice of the grating type is directly related to $\bar{\gamma}$. For the Talbot-Lau interferometer, $\bar{\gamma}_1 = \gamma_1 = \frac{\lambda d_0}{p_s p_1}$ is very close to 0, therefore, G_0 has to be absorption grating, similarly for G_2. However, when d_0/p_1 can be increased such that $\frac{\lambda d_0}{p_s p_1} = 0.25$, then a π phase grating can be used for G_0.

This leads to the second universal conclusion regarding the design of x-ray grating interferometers: **For conventional x-ray source and detector, absorption grating should be used for G_0 and G_2 unless d/p is sufficiently high.** Note that this conclusion also applies to the one-grating or two-grating interferometers.

For realistic gratings, the phase and amplitude modulations are not independent, they are totally determined by the material and thickness of the grating. For grating made of Au, Fig. 2.5 shows how V_G changes with s, $\bar{\gamma}$ and c, assuming an x-ray energy of 28 keV.

Fig. 2.5 (a) to (c) show how V_G change with the thickness of Au and $\bar{\gamma}$ for $s = 1, 2$ and 3, respectively. The duty cycle is fixed to 0.5. Several conclusions can be drawn from these results: First, we can see that only $s = 1$ and $s = 2$ need to be considered, as higher order terms can't generate high visibility fringes. Second, for $s = 1$, one should use a $\pi/2$ phase grating (2.7 μm Au thickness) with $\bar{\gamma} = 0.5$, or the absorption grating (on the lower right corner of the map) with $\bar{\gamma}$ close to 0 or 1. For $s = 2$, π phase grating (5.4 μm Au thickness) with $\bar{\gamma} = 0.25$ or 0.75 generates the highest visibility.

Fig. 2.5 (d) to (f) show the impact of duty cycle on V_G. The $\bar{\gamma} = 0.01$ case correspond to the absorption grating, as can be seen from Fig. 2.5 (d), increasing the duty cycle of the absorption grating and the thickness of the material will improve the visibility. Both $\bar{\gamma} = 0.25$ and $\bar{\gamma} = 0.5$

correspond to the case of phase grating. Fig. 2.5 (e) and (f) show the standard case of π phase grating and $\pi/2$ phase grating. For both cases, the optimal duty cycle of the grating is around 0.5.

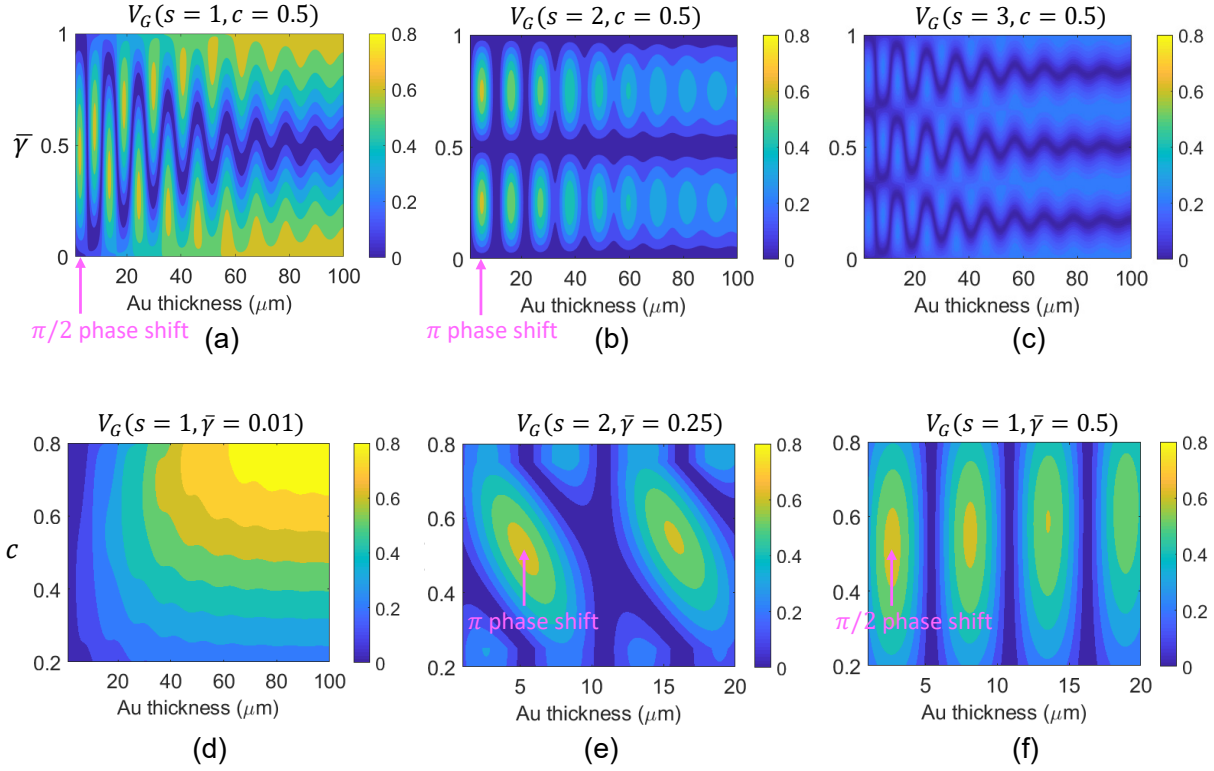

Figure 2.5: V_G changes with system parameters.

2.3.5 Polychromatic performance

Design of x-ray grating interferometers always starts with a design energy, with which the system parameters are determined. However, in practice, the x-ray source is almost always polychromatic. As discussed in Section 3.3.2, the decrease of fringe visibility due to the use of polychromatic source is two-fold: one is the decrease of monochromatic fringe visibility when the x-ray energy is deviated from the design energy; the other is the possible $\pm\pi$ fringe phase shift of the monochromatic fringes, due to the change of α with x-ray energy. Note that α can be also separated into the contribution of each grating, similar to the case of V_G. Using the following relationship: $\gamma(E) = \gamma(E_0)(E_0/E)$, where E_0 is the design energy. We can analyze V_G and $\mathrm{Arg}(A)$ as a function of x-ray energy.

Fig. 2.6(a)-(c) show the case of the $\pi/2$ phase grating (Au thickness of 2.7 μm, E_0 = 28 keV, $c = 0.5$) with three different $\gamma(E_0)$ values. Using $\gamma(E_0)$ higher than one is required to increase the

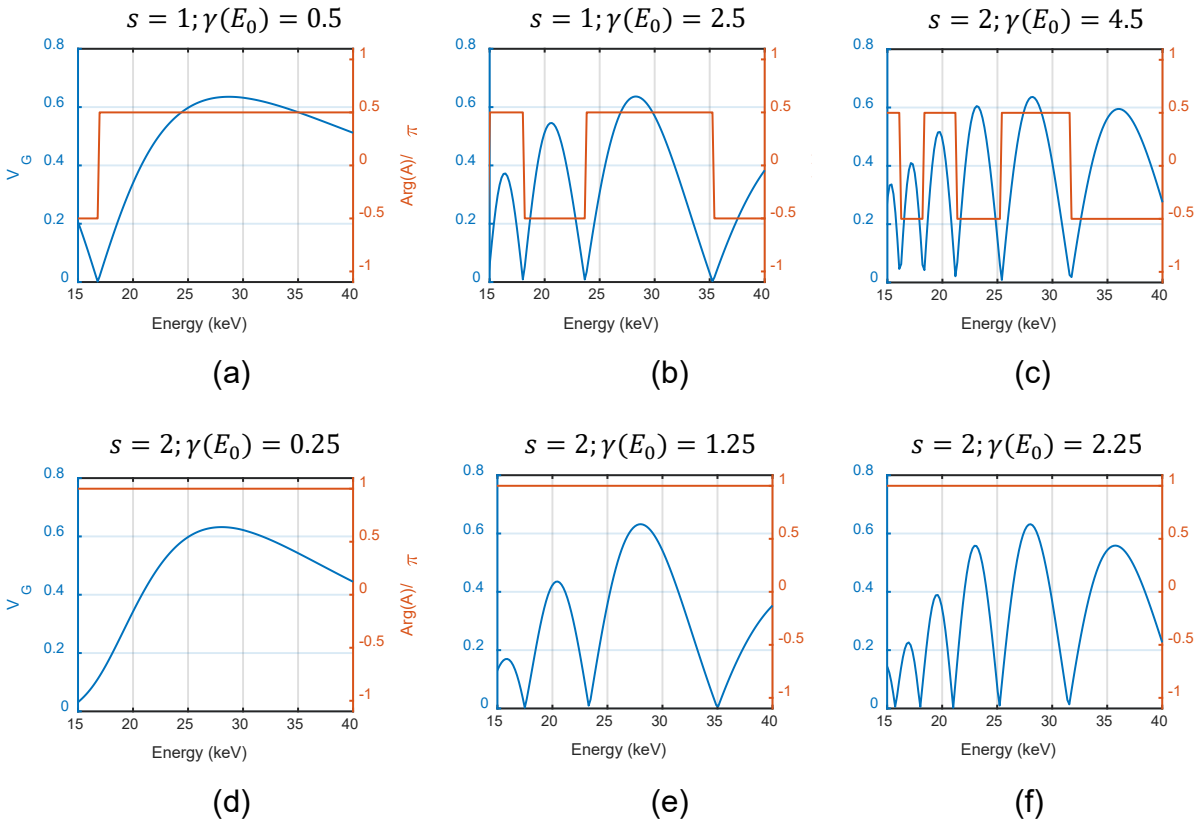

Figure 2.6: V_G changes with x-ray energy for (a) absorption grating. (b) $\pi/2$ phase grating. (c) π phase grating.

phase sensitivity of the system. For example, for the G_1 grating in a three-grating setup, $\gamma_2 = \lambda\eta/p_2$ is directly related to the phase sensitivity of the system. Fig. 2.6(d)-(f) show the case of the π phase grating (Au thickness of 5.4 μm, E_0 = 28 keV, $c = 0.5$) with three different $\gamma(E_0)$ values.

By comparing the results in Fig. 2.6, the following observations can be made: (1) When x-ray energy is deviated from the design energy, the monochromatic fringe visibility (V_G) for both $\pi/2$ phase grating system and π phase grating system will decrease in a similar manner: as $\gamma(E_0)$ increases, more oscillations start to appear. (2) For the π phase grating system, all monochromatic fringes are perfectly in phase as $\mathrm{Arg(A)}$ doesn't change with energy; for the $\pi/2$ phase grating system, $\pm\pi$ phase shift of the monochromatic fringes will happen especially when higher phase sensitivity is required, i.e. $\gamma(E_0) > 1$.

This leads to the third universal conclusion regarding the design of x-ray grating interferometers:

When designing system with phase sensitivity with a polychromatic x-ray source, π phase grating should be used.

Chapter *3*

Design, Construction, and Image Reconstruction for a Novel MC-CXR Prototype System

3.1 Introduction

Chapter 1 of this thesis work has highlighted the potential of grating-based multi-contrast X-ray imaging to improve upon the diagnostic accuracy of conventional chest radiography, a field that has been extensively investigated in the past decade[119,130–142,175,176]. Building on these promising results, the development of a pre-clinical prototype system is a logical next step toward the clinical translation of this technology. The absence of commercially available grating-based multi-contrast systems has motivated the design and construction of the novel prototype developed in this thesis. This chapter presents the key design components, construction, calibration, image reconstruction algorithm, and image correction framework for the prototype system.

3.2 Prototype Design

Designing a prototype system requires careful consideration of several clinical requirements. To begin, the system must be compatible with medical-grade X-ray tubes and standard flat panel detectors (FPDs). The use of the advanced source or detector technologies can significantly increase the overall cost of a system and necessitates that all currently employed clinical systems be modified or upgraded. The next major requirement is that the radiation dose to the patient should be matched or reduced when compared to CXR. One of the major benefits of chest radiography is the low dose associated with the modality. Failing to do match the dosimetric performance of CXR would

compromise the overall clinical efficacy of multi-contrast imaging. An additional consideration is that the X-ray energy used in the prototype system should not deviate significantly from the energies utilized in clinical practice. Traditionally, 110-120 kVp is used for the imaging of the lungs, 70-90 kVp is used for imaging of the bones in the thoracic cavity, and 60-140 kVp can be used for spectral imaging applications[184,185]. Furthermore, the grating interferometer should exhibit no stability issues to ensure the reliability of the system. Finally, a prototype system must be able to image the entire field of view (FOV) of the thoracic cavity within a single breath-hold, or within 10 seconds[186]. The typical FOV for lung imaging is 40 cm $\times$ 30 cm.

3.2.1 The Major Barriers to Clinical Adoption

As discussed in Chapter 1, the capacity for grating-based X-ray imaging to meet these aforementioned clinical requirements is hindered by several technical challenges associated with grating interferometry. First, the FOV of grating-based X-ray imaging is determined by the size of the gratings, which is typically 4-6 cm for a single grating wafer. Consequently, several grating tiles would need to be stitched together to cover the entire thoracic cavity. The requirement for many grating tiles significantly increases the overall cost of the imaging system, especially when considering that this must be done for both the diffracting/modulation grating (G1) and the analyzer grating (G2). Furthermore, achieving uniform interferometric performance over the entire FOV becomes a new challenge. This issue worsens when considering the typical energies used in chest radiography. The use of higher X-ray energies places increased demands on the fabrication of gratings. Specifically, the aspect ratio, or ratio of grating material height to period, must be increased to accommodate for higher X-ray energies. As such, the fabrication of high energy and large FOV gratings becomes increasingly challenging.

The next major challenge is the long acquisition time associated with traditional grating-based imaging methods. Although the phase-stepping approach provides a reliable method for signal retrieval, the acceleration, deceleration, and stabilization of each phase step contributes to incompatible imaging times for clinical studies. This problem becomes exacerbated when considering the small FOV associated with gratings, as several phase stepping procedures would need to be performed to image the entire chest. The scientific community has made several attempts to address this limitation, including slit-scanning techniques in mammography[187,188] and single-shot

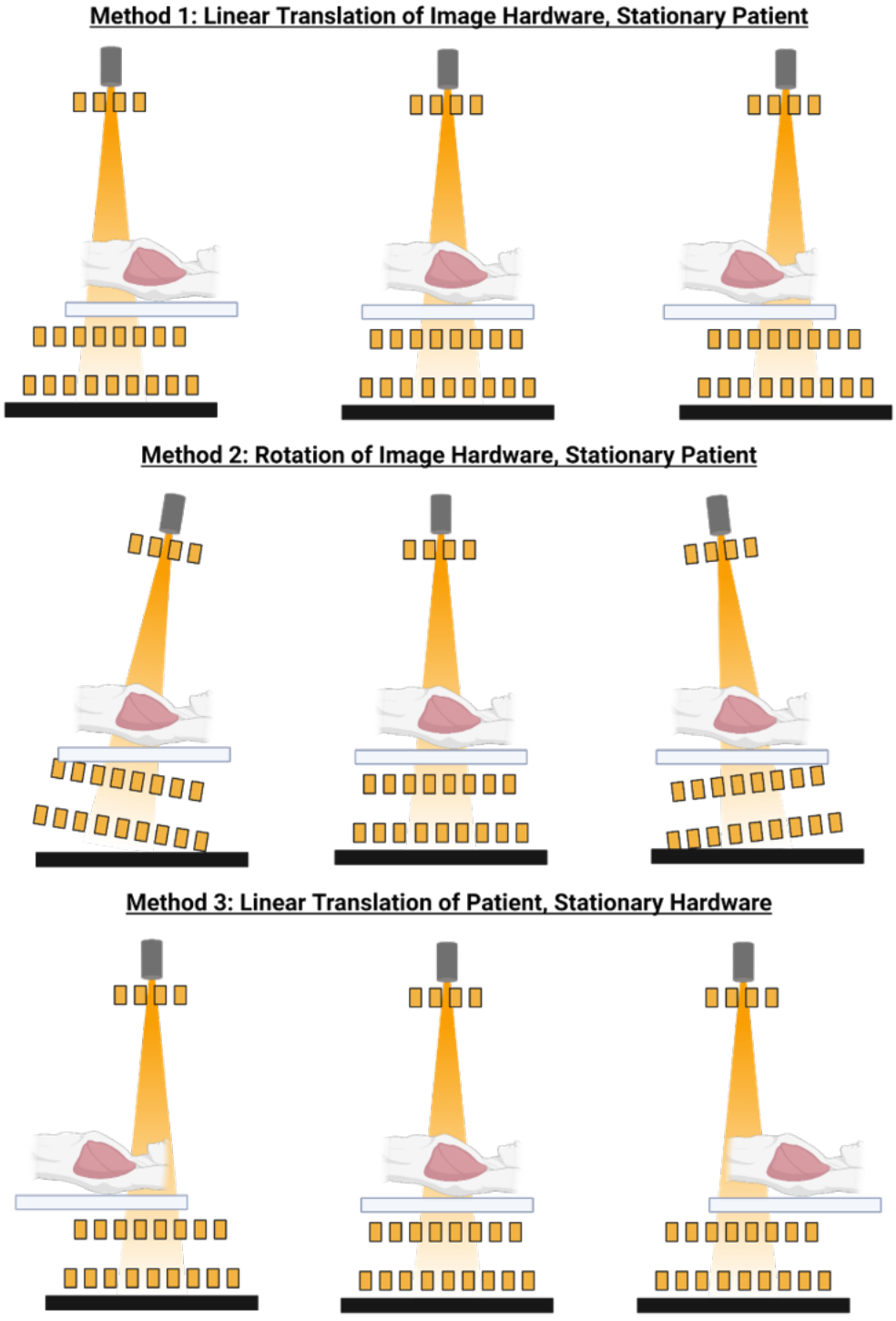

Figure 3.1: The three methods to achieve the modified fast scanning acquisition scheme. (Top) The gratings, X-ray tube, and detector are translated along the superior-inferior direction while the patient remains stationary. (Middle) The gratings and X-ray tube are slightly rotated about a central pivot point. (Bottom) The patient is translated along the superior-inferior direction while the hardware components of the system remain stationary. This is the method that is employed in the prototype MC-CXR imaging system presented in this thesis work. (Created in Biorender)

extraction methods[170,189,190]. However, slit-scanning techniques are still associated with acquisition times that are too long for clinical chest radiography due to the narrow beam collimation, and the assumptions made in single-shot retrieval methods are often violated in practice[118].

3.2.2 Modified Fast Scanning Acquisiton

The prototype system developed in this work was designed to address these two major limitations while providing a compact, cost-effective, and clinically compatible solution to MC-CXR imaging. To overcome the aforementioned limitations associated with MCXR and achieve imaging of the entire thorax within a feasible acquisition time, a modified fast acquisition with a seamless patient translation was adapted and implemented for the prototype system[118,191,192]. The proposed acquisition technique replaces the interleaved grating motion used in phase-stepping procedures with a continuous translation of a patient table. This method leverages the periodicity of the moiré pattern such that each point on the patient will be imaged at a series of different moiré positions by a rapid train of X-ray pulses throughout a single scan. The scanning procedure reduces the small FOV limitation to a single dimension. To address the other dimension, the prototype employs two wide FOV X-ray gratings. This approach significantly reduces the cost compared to a full FOV interferometer and mitigates challenges in uniformity.

3.2.3 Design of the Gratings and Interferometer

Three different approaches can be considered to image the patient at a series of different moiré positions. Figure 3.1 presents each of these three approaches. First, the gratings, source, and detector can be linearly translated along the superior-inferior (SI) while the patient remains stationary. However, there are several practical challenges associated with this approach. To translate the source, gratings, and detector, all three components must be attached to a single gantry. One problem with this configuration is that medical-grade X-ray tubes are known to produce significant vibrations due to the rotating anode tube. These vibrations may cause disturbances to the interference patterns that could significantly deteriorate the MC-CXR imaging performance by introducing inconsistencies between frames. If multiple gantries are used with multiple linear stages, then synchronization between the translation of each component and the cost of the system

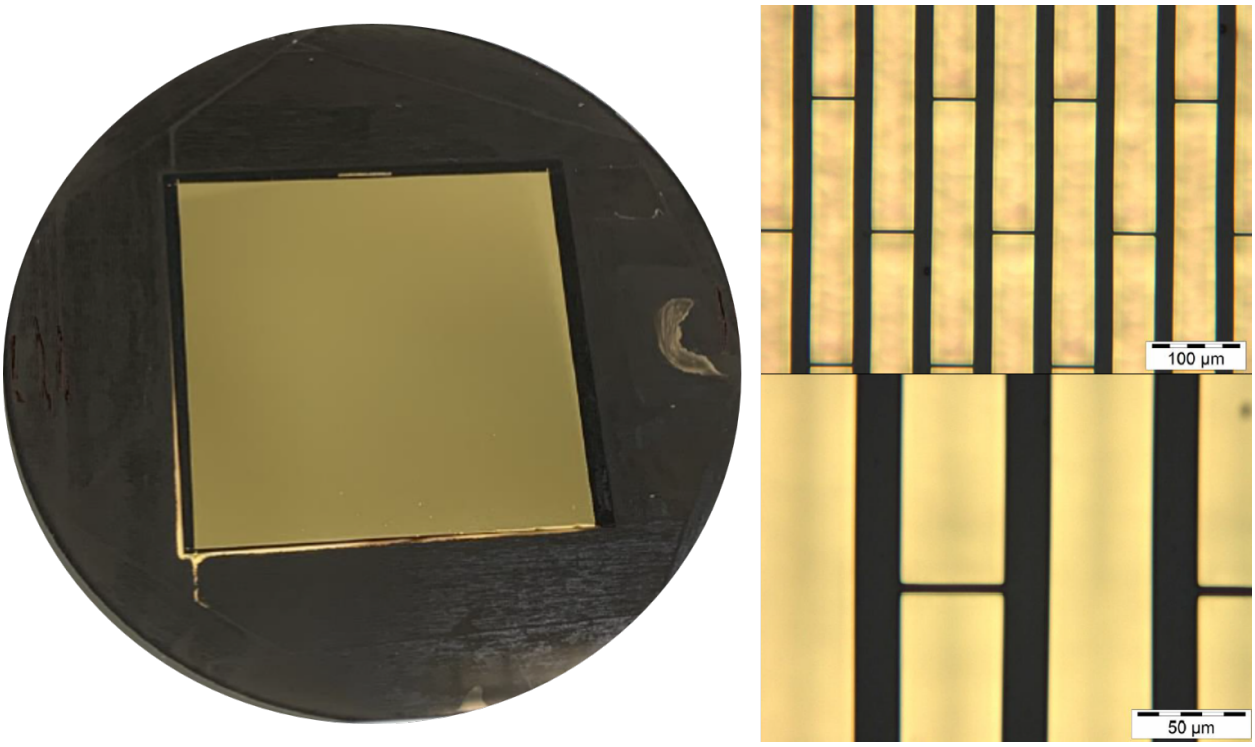

Figure 3.2: (Left) The source grating G_0. (Right) Magnified images of the individual grating tiles.

become new challenges. Furthermore, if a cone-beam source is used then geometric inconsistencies arise as the projection direction through the patient slightly changes as the object is translated

In the second approach, the patient and detector remain stationary while the gratings and source are rotated about a fixed axis. This approach does not require the source and gratings to be connected by a single gantry and overcomes the geometric inconsistency associated with the first approach. The major challenge with this method is that it still requires the grating interferometer to be placed in motion. It is not desirable to have the interferometer in motion, as it is the component that is most susceptible to mechanical disturbances.

The third approach involves the linear translation of the patient while all hardware components of the system remain stationary. The major benefits of this approach include not requiring that the interferometer be put in motion, relaxing mechanical precision requirements, and enabling the use of multiple decoupled gantries. However, the projection ray inconsistency is still an issue and the translation of the image object results in an inherent blurring of the spatial resolution along the table translation direction. Given the benefits of the third approach, it was selected for the prototype system developed in this thesis. To overcome the projection ray inconsistency issue, the

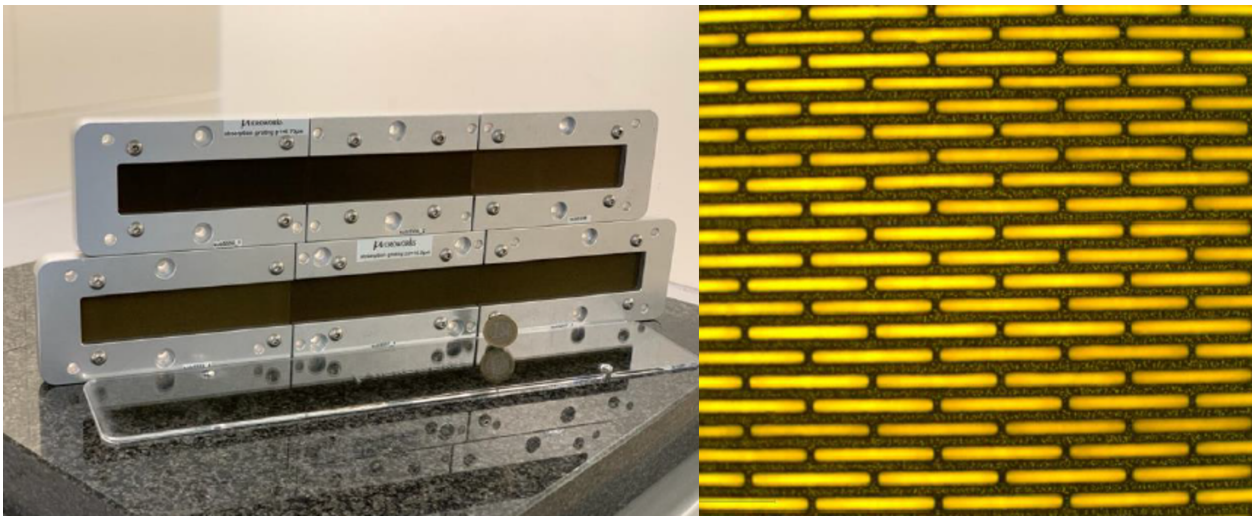

Figure 3.3: (Left) The wide FOV G_1 and G_2 gratings. (Right) Magnified image of one of the G_1 grating tiles.

cone-beam source can be collimated such that it can be approximated by a fan beam. The inherent blurring caused by the translation of the image object is addressed with a regularized deconvolution approach that is outlined later in this chapter.

Based on the universal conclusion drawn from the grating design optimization framework in Section 2.3.4.1, the grating interferometer will be comprised of three gratings. Assuming a mean X-ray energy between 45-80 keV in the diagnostic energy range, the Talbot distance and fractional Talbot distances are too great to enable a compact imaging system. However, the use of an absorption grating for G_1 and placing G_1 after the image object allows for the generation of a moiré pattern with a small distance between G_1 and G_2. The intensity modulation generated by the G_1 absorption grating projects onto the intensity modulation generated at G_2 to generate the necessary interference fringes at the detector plane. Based on this approach and the universal conclusion drawn in Section 2.3.4.2, all three gratings used to form the interferometer for this prototype system are absorption gratings. MicroWorks GmbH fabricated the three gratings using X-ray lithography and electroplating.

The first grating, G_0, is shown in Figure 3.2. As discussed in Chapter 2, G_0 is an absorption grating designed to split the source radiation into an array of periodically repeating line sources to satisfy the spatial coherence requirements for grating-based X-ray imaging. The G_0 grating consists of a 0.5 mm silicon substrate with a gold thickness of 200 µm. The pitch of the grating is 68.7 µm, resulting in an aspect ratio of 4.2. The area of the grating is 5 cm^2.

Table 3.1: Grating Specifications

	Gratings		
	G0	G1	G2
Pitch (μm)	68.7	8.73	10
Duty Cycle (%)	70	50	55
Au thickness (μm)	200	200	200
Aspect Ratio	4.2	45.8	36.4
Area (cm^2)	5	35×3	40×3
Substrate	0.5 mm Si	1 mm graphite	1 mm graphite

The G_1 grating serves as a modulation grating to generate a "shadow" of the grating downstream at G_2. To widen the field of view of the G_1 grating, three individual grating wafers were tiled together. The total size of the G_1 grating is 35 cm along the lateral direction and 3 cm along the longitudinal direction. This grating consists of a 1 mm graphite substrate with 200 µm of gold plating. The grating was fabricated at a high aspect ratio of 45.8 and with a pitch of 8.73 µm. The duty cycle for the G_1 grating is 50%. The G_1 grating is depicted in Figure 3.3.

The analyzer grating, or G_2, generates a resolvable moiré pattern at the detector from the interference generated at G_1. Similar to the G_1 grating, the G_2 grating consists of three individual grating wafers. The total FOV of the grating is 40 cm along the lateral direction and 3 cm along the longitudinal axis. The analyzer grating also consists of a 1 mm graphite substrate with 200 μ of gold. The pitch of G_2 is 10 μm resulting in an aspect ratio of 36.4. Finally, the duty cycle is 55%. The details of the gratings are summarized in Table 3.1.

Given that the modified fast scanning method utilized in this prototype system necessitates the translation of the patient, the interferometer was aligned vertically to accommodate a translatable patient couch. The gratings were fixed to a separate gantry (Gantry B) to prevent potential mechanical disturbances, such as vibrations from the rotating X-ray tube, from affecting the system. The gantry was built in-house using aluminum frames. The dimensions of the gantry include a height of 228 cm, an inner width of 89 cm, and an outer width of 102 cm. The distances between G_0 and G_1, G_1 and G_2, and G_2 and the detector are 171 cm, 26 cm, and 1 cm, respectively. Rubber padding is added to the bottom of Gantry B to further ensure decoupling from potential mechanical disturbances. The interferometer's dimensions are summarized in Table 3.2, while Figure 3.4 shows the design and dimensions of Gantry B.

Table 3.2: System dimensions

System Dimensions	
	Distance (cm)
Source to G0	32
Source to Object	187
G0 to G1	171
G1 to G2	26
Source to Detector	238

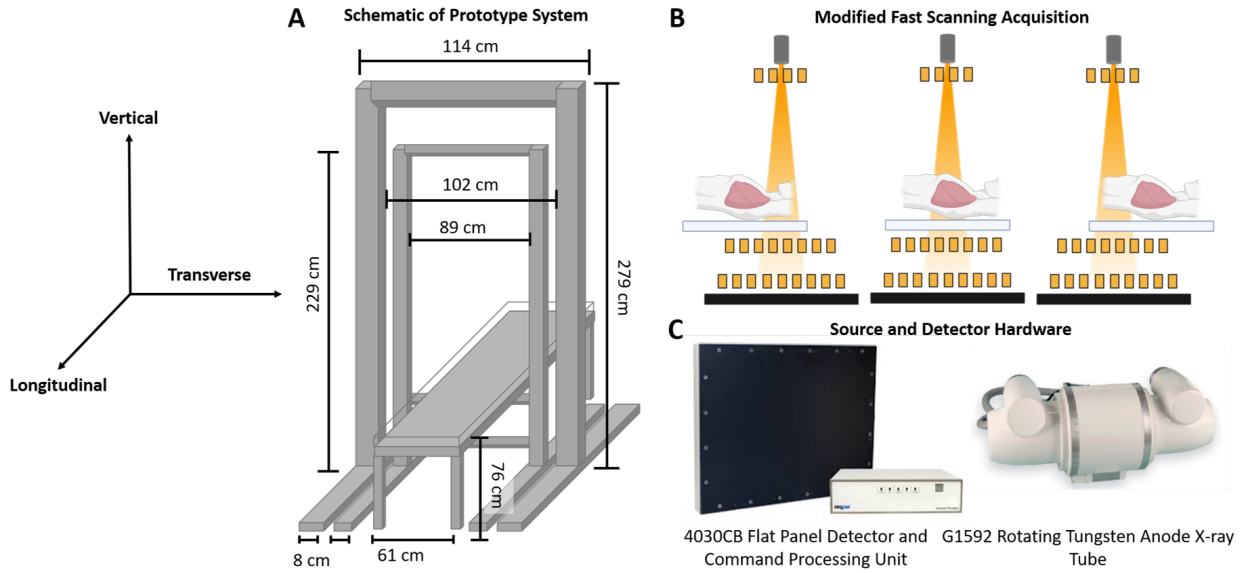

Figure 3.4: (A) Schematic and dimensions of the two gantries and patient table for the prototype system. (B) Illustration of modified fast scanning acquisition via patient table translation. (C) The source and detector hardware components.

3.2.4 Design of the X-ray Imaging System

In addition to the interferometer, the prototype must be equipped with the hardware components of a conventional chest radiography system. A conventional CXR system was constructed from scratch to avoid the added cost of purchasing an existing CXR system and allow for increased design flexibility/customization.

The X-ray tube used in this prototype is the G-1592 medical-grade rotating tungsten anode X-ray tube with B-180H housing from Varian Medical Systems Inc. (Figure 3.4C). The tube has two nominal focal spot sizes (0.6 and 1.2 mm), with nominal anode input powers of 47 kW and 112 kW for the small and large focal spots, respectively. The maximal anode heat content is 1.5 MHU. The Indico100 high-frequency generator from CPI Inc., with an output voltage of 40-125 kV, was used.

To collimate the cone-beam source to a quasi-fan-beam in order to avoid ray projection inconsistency for the modified scanning acquisition, the R221/A DHS square-field X-ray collimator from Ralco Inc. was attached to the exit window of the X-ray tube. The radiation field was collimated to a field size of 30 cm x 2.5 cm at the object plane.

The 4030CB FPD from Varian Medical Systems Inc. was used as the detector for this prototype system (Figure 3.4C). The detector is a CsI:Tl-based FPD with a native pixel size of 198 μm. However, the detector is operated in fluoroscopy mode, such that a 2×2 binning of the pixels is employed, resulting in an effective pixel size of 388 μm at a maximal frame rate of 30 fps. The parameters of the detector used in this study are comparable to those of detectors used in clinical practice. To enable the modified scanning acquisition, the X-ray tube, and the detector are operated in the pulsed fluoroscopic mode. The pulse rate of the X-rays and the frame rate of the detector are matched at 30 pulses/frames per second. Synchronization between the tube and detector was achieved to ensure optimal dose efficiency.

The X-ray tube and detector are mounted on a second gantry, Gantry A. Gantry A was also constructed in-house using aluminum frames. The dimensions of Gantry A include a height of 279 cm, an inner width of 107 cm, and an outer width of 114 cm (Figure 3.4A). The source-to-detector distance for the system is 238 cm, and the source-to G_0 distance is 32 cm due to the presence of the collimator at the exit window of the tube.

One design consideration that was taken into account was the weight of the X-ray tube. Several safety precautions were taken to ensure that the weight of the tube could be supported and that the gantry would not experience significant mechanical distortions when the anode was rotating. First, Gantry A was connected to a 9 cm thick aluminum frame through four clearance holes at the ends of Gantry A and four threaded holes at the ends of the aluminum frame. Four 5/16”-36” screws were used to ensure this connection. The aluminum frame was then connected to the X-ray tube with a custom aluminum adapter and four screws connecting the aluminum frame to the adapter, and an additional four screws connecting the adapter to the tube. An additional safety measure was also taken, in which two safety railings were added to the end of the collimator as a fail-safe measure. Stabilization of the base of Gantry A was accomplished with two 140 cm longitudinal base frames. The base frames were connected to the vertical component through three distinct connections. The first was a set of two clearance holes in the base frames that lead to threaded

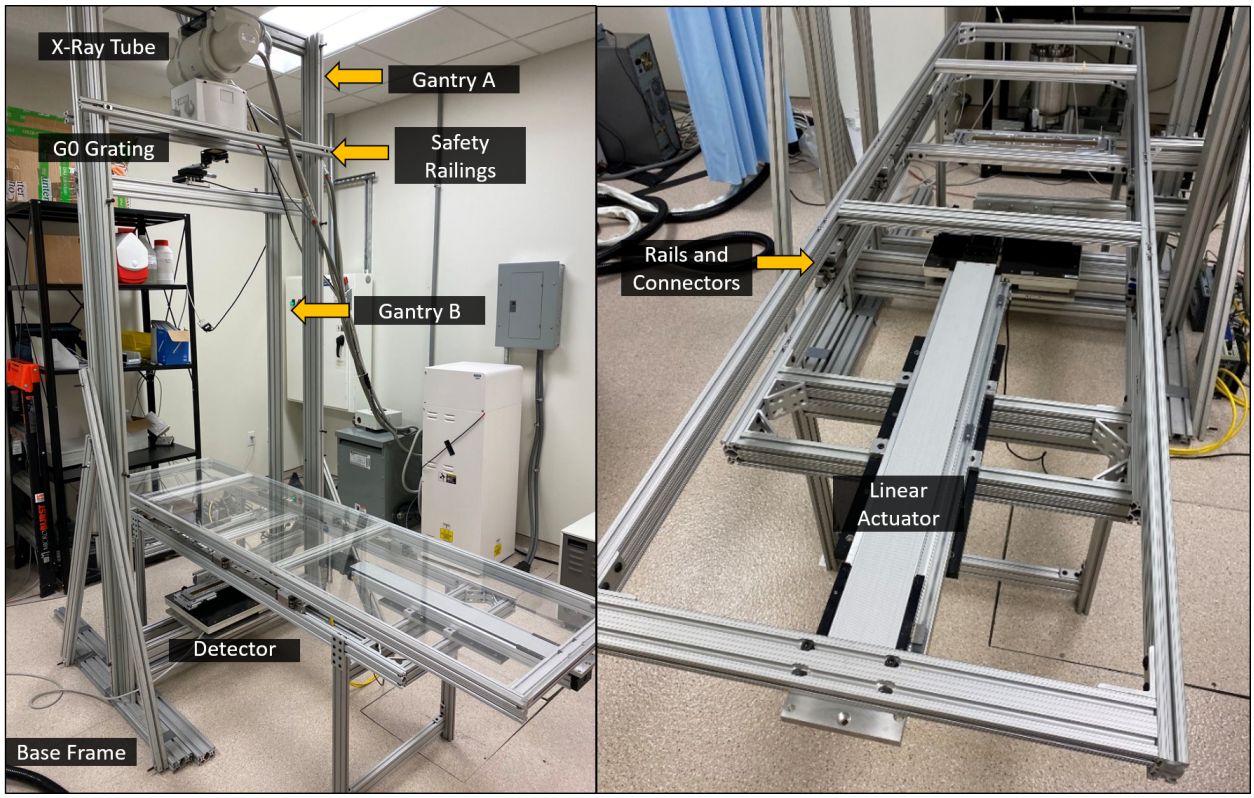

Figure 3.5: (Left) Image of the constructed prototype system including the two gantries, the grating interferometer, the detector, and the patient table. (Right) The constructed patient table includes the linear actuator used to translate the table and the rails/connectors that connect the stationary and mobile components of the table.

holes in the vertical component of the gantry. The other two connections come from two additional aluminum frames that are attached at the ends of both base frames to form a triangle at the vertical component of the gantry. These additional features are shown in Figure 3.5.

3.2.5 Construction of the Patient Table

A patient table was constructed to enable the modified fast-scanning image acquisition scheme. The patient table consists of two primary components: a stationary component and a translatable component. The stationary component was constructed with aluminum frames consisting of four table legs connected to a rectangular aluminum base. The base frame is 66 cm off the ground with a width of 61 cm and a longitudinal length of 183 cm. The base component is designed to support the patient and stabilize the table translation procedure. Each side of the base frame is connected to two stationary rails that act as linear guides for the patient table. Two ball-bearing carriers are placed on the rails and connected to the translatable component of the patient table through four

custom adapters. The translatable component of the table consists of another rectangular frame and a patient bed made of 2 cm thick acrylic sheets. The rectangular frame is 76 cm from the ground and both the frame and PMMA slabs have a width of 61 cm and a longitudinal length of 224 cm. With this configuration, the source-to-table surface distance is 178 cm.

The last major component of the patient table is a linear actuator that drives the translation of the table. The linear actuator used for the prototype system is the Parker 404XE with a precision ground ballscrew. The actuator enables table translation of 45", has a load capacity of 270 lbs, and a precision and repeatability of less than $\pm$ 0.1 mm. The patient table is shown in Figure 3.5.

3.2.6 Construction of Grating Housing Units

There are several aspects of the gratings that must be aligned to generate a moiré pattern at the detector plane. First, high precision in the inter-grating distances must be achieved. Coarse adjustment of the distance is achieved by three rectangular aluminum frames that are attached to Gantry B. These frames are oriented in the transverse plane and can be moved along the vertical direction of Gantry B to position the gratings. Fine adjustment of the inter-grating distance is achieved with micro-adjustment linear stages for each of the three gratings.

Three rotational directions must be sufficiently aligned: tilt, tip, and in-plane rotation. These three rotational orientations are demonstrated in Figure 3.6. The G_0 grating is held by a commercially available housing unit that allows for fine adjustment of all three rotations. However, no such housing units existed for the G_1 and G_2. As such, two new grating housings were constructed to enable the rotation of the grating along all three rotational directions. Housing units were placed below the gratings such that only the edges of the gratings were in contact with the housing unit. In other words, only the outer metallic shell of the grating unit was placed onto the housing unit as shown in Figure 3.6. A clearance hole was then drilled through the housing unit and the metallic shell of the grating in one of the corners. In this corner, the grating does not directly rest on the housing unit, but rather a hemispherical plastic ball with a clearance hole is placed between the two. A screw then connects the housing unit, ball, and grating. This configuration allows for this corner of the grating to act as a pivot point for the system. Two screws are then placed on the opposing end of the housing unit to allow for tilt rotation to be accomplished.

The in-plane and tip rotations of the grating are achieved by placing two additional screws at

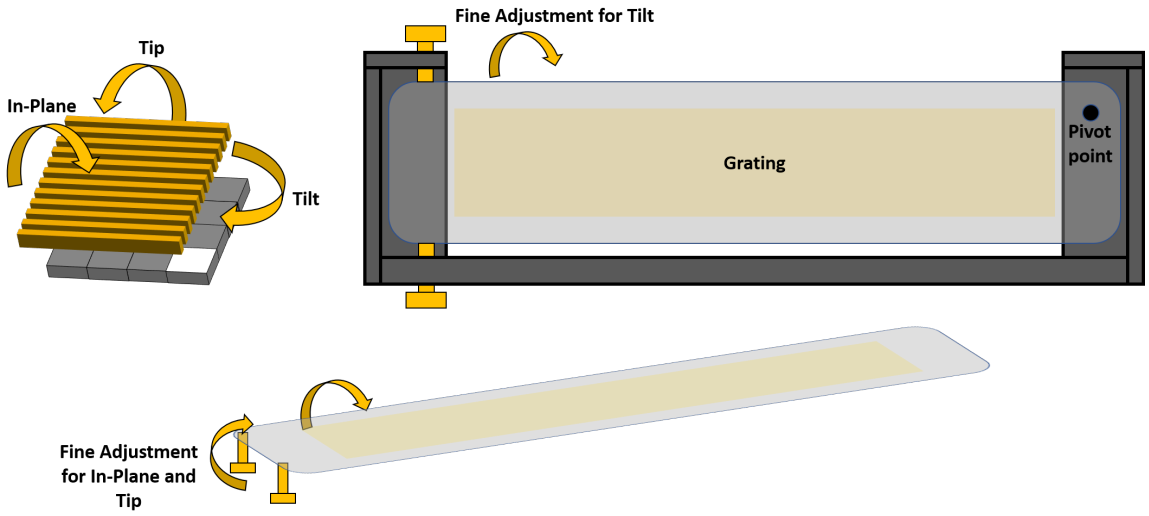

Figure 3.6: The three rotational orientations of tip, tilt, and in-plane rotation are illustrated for a single grating. Furthermore, the designed grating holders and the fine-adjustment screws for G_1 and G_2 are shown. Fine adjustment of the tilt is accomplished with two screws parallel to the gratings that allow the gratings to rotate about a pivot point. Fine adjustment of the in-plane rotation and tip are accomplished with two screws placed on the bottom of the gratings.

the bottom of the grating. These screws are placed on the end opposing the pivot point. In-plane adjustment is accomplished by raising or lowering both screws together, while tip rotation is enabled by raising or lowering only one of the screws. Figure 3.6 illustrates the working principles of the housing units.

3.3 Interferometer Alignment and Performance

3.3.1 Alignment

This section outlines the steps taken to align the grating interferometer such that a high visibility interference pattern can be achieved at the detector plane. This process is broken down into the following steps:

1. Alignment of G_0
2. Alignment of G_2
3. Rough Alignment of G_1
4. Fine alignment of G_1-G_2 distance to adjust moiré period

5. Fine alignment of G_1 in-plane rotation to adjust moiré orientation.

The G_0 grating was aligned by positioning its plane perpendicular to the incident X-ray beam. Initially, G_0 was placed in proximity to the X-ray tube's exit window. Although the G_0 grating is not sensitive to in-plane orientation, preliminary alignment was carried out by capturing projection images of G_0. The tilt and tip orientations were approximately aligned with a laser lever. Subsequently, fine alignment of both rotational directions was accomplished by acquiring projection images and analyzing profiles in the transverse and longitudinal directions. The alignment of the tip orientation was considered satisfactory when the profiles across the transverse direction were flat. For the tilt adjustments, fine-tuning was repeated until an intensity peak in the center of the field of view (FOV) was achieved in a profile across the longitudinal direction. A projection image of the aligned G_0 grating is illustrated in Figure 3.7. This alignment procedure was then repeated for the G_2 grating.

Initial alignment of the G_1 grating was performed by placing G_1 at the theoretically calculated distance from G_2. The inter-grating distance was then finely adjusted using the linear stage until the moiré pattern could be visualized in a projection image. An example of the initial moiré pattern generated at the detector plane is shown in Figure 3.7. From here the tip and tilt orientations are adjusted such that the intensity across the FOV is roughly uniform.

The next alignment step is to finely adjust the moiré period. The period of the fringes is adjusted by fine-tuning the inter-grating distance with the linear stage for G_1. The final alignment procedure is to make the orientation of the interference fringes perpendicular to the scanning, or longitudinal, direction. The in-plane orientation of G_1 must be finely adjusted to change the orientation of the moiré pattern. The gratings were aligned once the orientation of the moiré was perpendicular to the scanning direction with a sufficient period. The resulting moiré pattern for the aligned interferometer is shown in Figure 3.7.

3.3.2 Characterization of the Interferometric Performance

The performance of the interferometer was characterized by measuring the visibility of the interference pattern generated across the entire imaging FOV. The quantification of the visibility was performed through a phase-stepping acquisition with only the patient table in the FOV. The overall

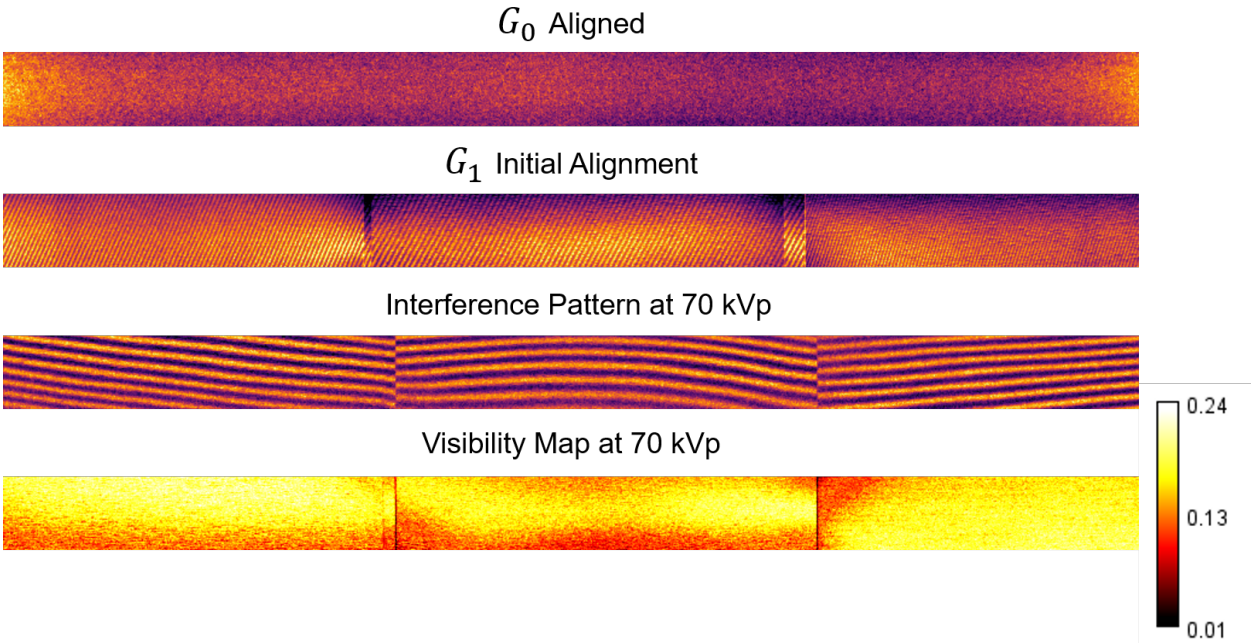

Figure 3.7: Projection images acquired of the scan FOV with (1) G_0 aligned (2) the initial interference pattern generated following the coarse alignment of the G_1 grating (3) the moiré pattern generated at 70 kVp (4) a map of the visibility at 70 kVp, demonstrating a high level of uniformity across the FOV.

Table 3.3: Mean Visibility

Peak Tube Potential	**Mean Visibility**
40 kVp	$29 \pm 7\%$
50 kVp	$28 \pm 5\%$
60 kVp	$24 \pm 4\%$
70 kVp	$19 \pm 3\%$
80 kVp	$15 \pm 2\%$
90 kVp	$13 \pm 2\%$
100 kVp	$13 \pm 2\%$
110 kVp	$12 \pm 2\%$
120 kVp	$12 \pm 2\%$

intensity $I_0(x,y)$ and the amplitude of the fringes $I_1(x,y)$ were calculated for each pixel using Equations 2.35 and 2.36. This process was repeated for peak tube potentials ranging from 40 kVp to 120 kVp. The visibility was then quantified as the mean of the visibility across the entire grating FOV. Table 3.3 summarizes the visibilities at each peak tube potential tested. For reference, a map of the visibility generated at 70 kVp is shown in 3.7. An overall high level of uniformity is achieved across all three grating tiles. Furthermore, the acquired images demonstrated no stability issues arising from mechanical disturbances.

3.4 Image Reconstruction

After constructing the prototype system and optimizing the grating interferometer, the next step was to implement the scanning acquisition scheme. In the phase stepping acquisition scheme, each point of the patient is mapped across the sinusoidal interference pattern by shifting the interference pattern across the patient through slight translations of one of the gratings. On the other hand, the scanning acquisition scheme performs this mapping by translating the patient across the interference pattern. Mathematically, this acquisition scheme is equivalent to scanning the grating interferometer across a stationary patient. To simplify the presentation of the algorithm, it is presented from this perspective. The signal model discussed in Chapter 2 can also be expressed in this manner.

$$I_{obj}(x,y) = I_0(x,y)T(x,y)\left(1 + v_{air}(x,y)d(x,y)\cos\left(\phi_0(x,y) + P(x,y)\right)\right] \tag{3.1}$$

where $T(x,y)$ is the transmission of through the object defined as $I_0^{(obj)}/I_0^{(air)}$ and $d(x,y)$ is the ratio defined as $I_1^{(obj)}/I_1^{(air)}$. If scanning is performed along the longitudinal, or y, axis then the intensity of the k-th frame is given as

$$I_{obj}^{(k)}(x,y) = I_0(x,y+\Delta y^{(k)})T(x,y)\left[1 + v_{air}(x,y+\Delta y^{(k)})d(x,y)\cos\left(\phi_0(x,y+\Delta y^{(k)}) + P(x,y)\right)\right] \tag{3.2}$$

where Δy is the distance the interference pattern has shifted between acquired frames. Since this algorithm is devised from the perspective of a stationary object, the three object-specific quantities $T(x,y)$, $d(x,y)$ and $\phi_{obj}(x,y)$ remain unchanged across the acquired frames. By performing the same analysis presented in Section 2.2.4, the quantities $I_0(x,y+\Delta y^{(k)})T(x,y)$, $v_{air}(x,y+\Delta y^{(k)})d(x,y)$,

and $\phi_0(x, y + \Delta y^{(k)}) + \phi_{obj}(x, y)$ can be extracted from the scan of the object. Therefore, to solve for $T(x, y)$, $d(x, y)$ and $P(x, y)$ one only needs the quantities $I_0(x, y + \Delta y^{(k)})$, $v_{air}(x, y + \Delta y^{(k)})$, and $\phi_0(x, y + \Delta y^{(k)})$.

To solve for $I_0(x, y + \Delta y^{(k)})$, $v_{air}(x, y + \Delta y^{(k)})$, and $\phi_0(x, y + \Delta y^{(k)})$ several assumptions can be made. First, it can be assumed that the overall mean intensity and the visibility of the interference pattern are roughly uniform across the entire FOV. As such, these two quantities can be assumed to be independent of spatial location such that $I_0(x, y + \Delta y^{(k)}) = I_0$ and $v_{air}(x, y + \Delta y^{(k)}) = v_{air}$. With these two assumptions, the three quantities I_0, v_{air}, and $\phi(x, y + \Delta y^{(k)})$ can be measured by performing a phase stepping scan in air such that $T(x, y)$, $d(x, y)$, and $P(x, y)$ can be recovered. From here $A(x, y)$ and $D(x, y)$ can be directly calculated as

$$A(x, y) = -\ln\left(T(x, y)\right) \tag{3.3}$$

$$D(x, y) = \ln\left(\frac{d(x, y)}{T(x, y)}\right) \tag{3.4}$$

This signal extraction framework replaces the M phase steps with M frames acquired from the image object at different spatial locations. The number of frames for a single reconstruction is defined by the width of the grating along the longitudinal direction (l_y), the speed of the object (v_y), and the frame rate fps. As such, multiple reconstructions are required to generate images of the entire thoracic cavity in a single scanning acquisition. The reconstructions are then tiled up in post-processing as shown in Figure 3.8.

3.5 Image Correction Framework

While the construction of a prototype system and the development of an image reconstruction algorithm are important steps toward realizing clinical multi-contrast imaging, the quality of the generated images may be degraded by the use of a flat panel detector and a fast scanning acquisition scheme. This section presents a correction framework to mitigate these potential degradations.

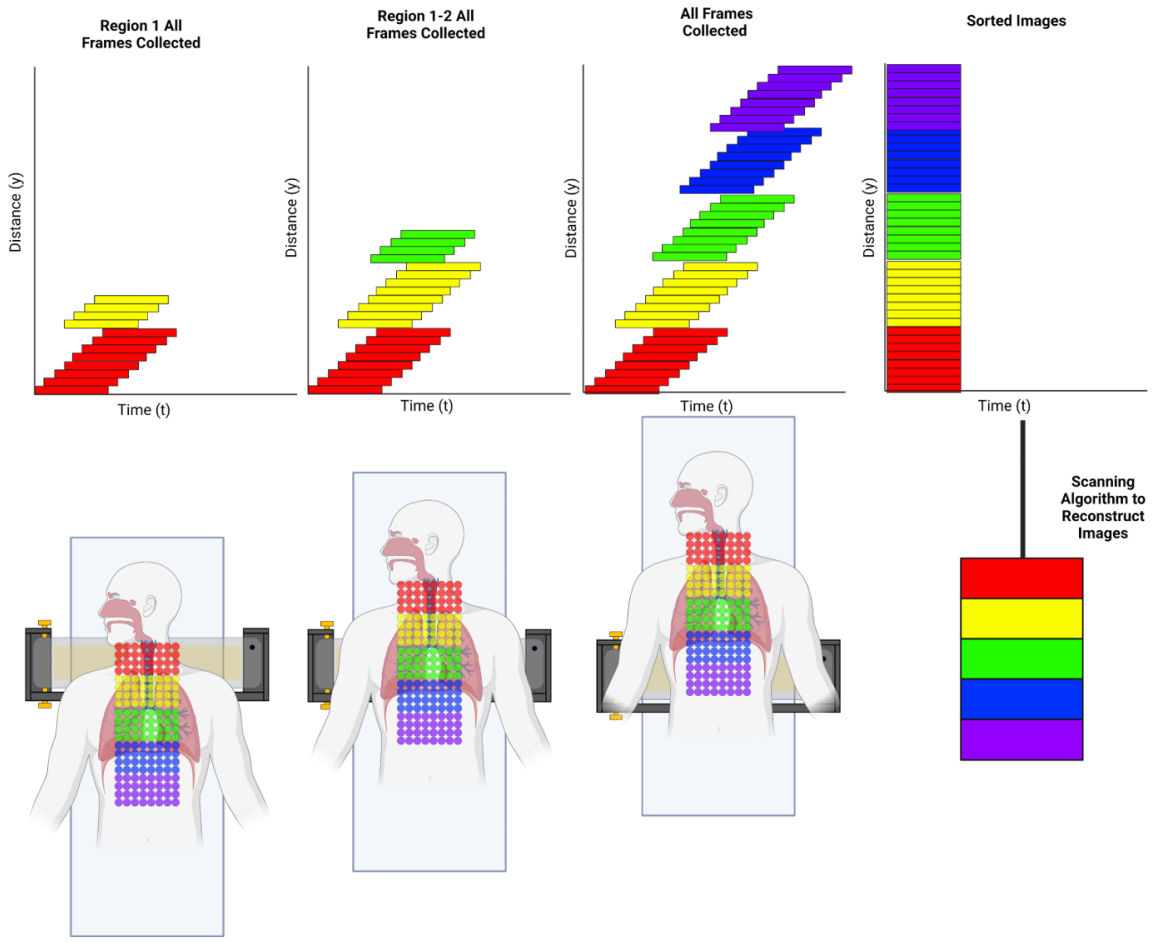

Figure 3.8: Illustration of the sorting and tiling of the acquired scanning frames to reconstruct the multi-contrast images. (Created in Biorender)

3.5.1 Detector Offset and Gain Corrections

Image uniformity of the entire scanning FOV is essential for accurate and high-quality multi-contrast imaging. However, image uniformity is a challenge in flat panel detectors unless appropriate corrections are applied. Dark current and non-uniform pixel sensitivity are among the predominant challenges in flat panel uniformity. Dark current refers to the electrical signal that is detected in the absence of interacting X-rays. This dark current arises from thermal energy and is non-uniform across the detector as demonstrated in Figure 3.9. Non-uniform pixel sensitivity is the result of discrepancies in the manufacturing of the detector elements, changes in detector response over time, and differences in the electronics between detector panels and elements.

The vendor provided dark offset, and detector gain corrections were employed to correct for the dark current and non-uniformity in the pixels respectively. Figure 3.9 depicts the images generated

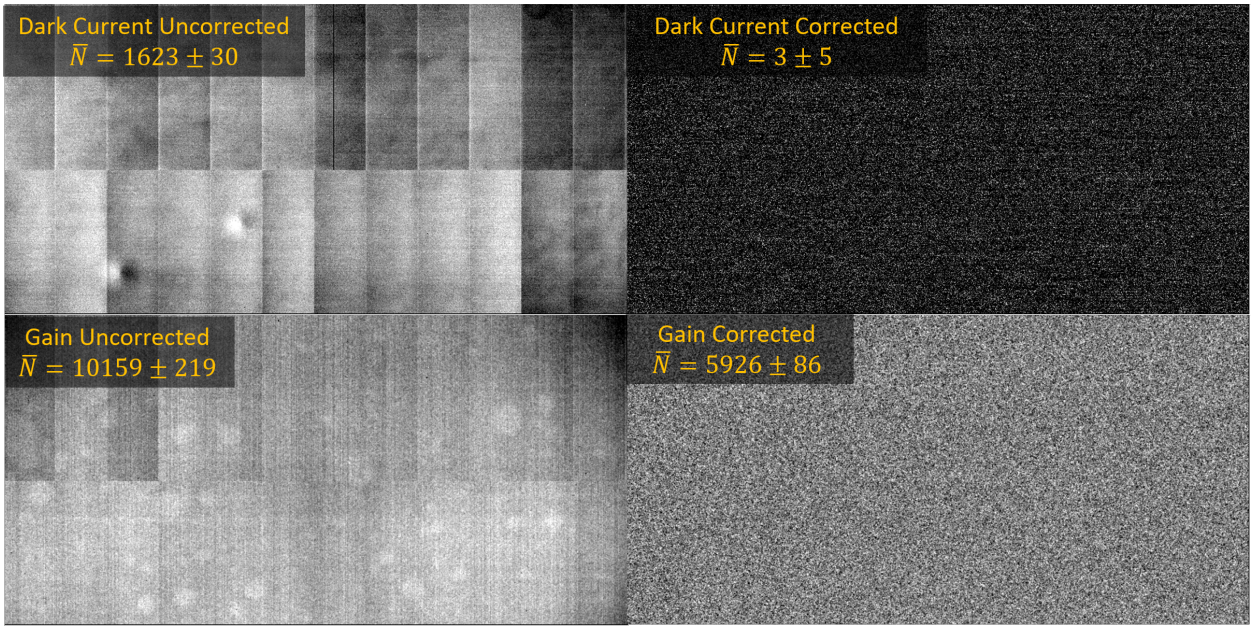

Figure 3.9: (Top) Demonstration of the detector non-uniformities arising from the presence of dark current and the utility of the offset correction. (Bottom) Projection images were acquired with and without the gain correction applied.

before and after the corrections were applied. For the dark offset correction, there are visible inter-panel and intra-panel discrepancies in the magnitude of the dark current. The mean of the dark current signal was 1623 ± 30 digital counts. Following the correction, a flat field image is produced with the mean digital counts being reduced to nearly 0. Similarly, when the X-ray beam is turned on, there are visual non-uniformities present across the flat panel detector. However, these non-uniformities are entirely mitigated following the application of the gain correction.

3.5.2 Detector Lag and Scanning Motion Blur Corrections

3.5.2.1 Method to Correct for Detector Lag

An inherent limitation of employing a flat panel detector and a rapid train of X-ray pulses is the impact of the detector lag effect. The lag effect is the contamination of a given image frame with residual signals generated in previous frames. Lag is predominantly the result of the scintillator afterglow and the charge-trapping effect in the amorphous silicon layer of the flat panel detector. In conventional projection imaging, lag causes temporal blurring. However, for the scanning acquisition scheme employed in this work, the temporal blurring associated with the lag effect is translated into a blurring of the spatial resolution along the scanning direction. Lag not only

degrades the spatial resolution of the imaging system along the scanning direction but may also result in artifacts in each of the three complementary images. Specifically, lag may result in the ghosting of highly attenuating objects. The severity of lag artifacts increases with increasing scanning speed, thus a correction framework must be established to enable fast and accurate MC-CXR imaging.

The impact of the lag effect for a given frame, k, can be modeled as a convolution of the true image signal with a detector lag kernel ($L(k)$) which is characterized by the detector's temporal impulse response function.

$$I_{measured}(k) = L(k) * I_{true}(k) \tag{3.5}$$

One model for the lag kernel is the multi-exponential model presented by Hsieh et al.[193], in which the impact of the detector lag effect is modeled to exponentially decay with time. The multi-exponential lag kernel is represented as

$$L(k) = \sum_{n=1}^{N} \frac{b_n}{1 - e^{-a_n}} e^{-a_n k}, \tag{3.6}$$

where N is the number of exponential terms used to fit the data, a_n, b_n are empirically determined parameters, and $u(k)$ is the unit step function. The two parameters a_n and b_n can be determined by measuring the residual signal in image frames acquired after the X-ray beam has been turned off. For this thesis work, this was done by exposing the detector for 350 frames at 70 kVp, 60 mA, and 30 frames per second. An additional 100 frames were then collected after the termination of the X-rays. The response function of the detector was then measured as the average residual signal intensity of a 200 $\times$ 60-pixel region of interest. Frames 1, 5, 10, and 25 following the termination of the X-rays are shown in Figure 3.10. The measured residual intensity was then fit with the lag kernel in Equation 3.6 such that a_n and b_n could be determined. A fourth-order lag kernel was found to demonstrate a good agreement with the empirical data. The measured data and associated fit are also shown in Figure 3.10. To correct for the lag signal, the computationally efficient recursive deconvolution algorithm presented by Hsieh et al. was employed.

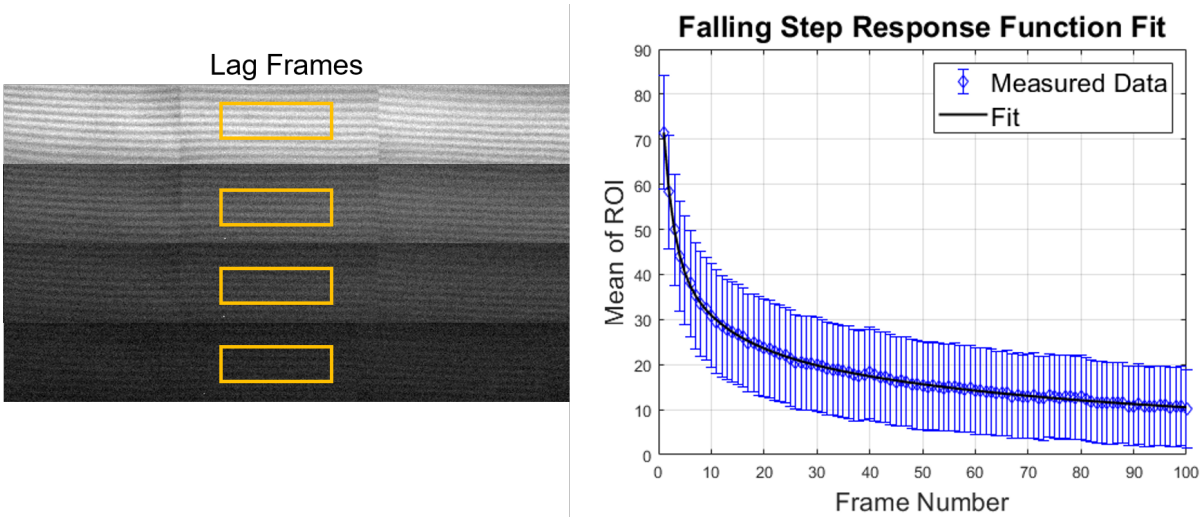

Figure 3.10: (Left) Residual signal generated from the detector lag effect for frames 1, 5, 10, and 25 following the termination of the X-rays. (Right) The plot of the average residual signal in the frames acquired after the termination of the X-rays and fit with the lag kernel described in Equation 3.6

3.5.3 Method to Correct for Scanning Motion Blur

The spatial resolution along the longitudinal axis will also be degraded by the object being in motion during the time in which the X-ray is on. The degree of blurring is dependent upon the speed of the table translation, the frame rate, the duty cycle, and the size of the detector pixels. At the detector plane, the distance the object travels in pixels is:

$$\Delta d = \frac{v\tau}{f}\frac{M}{p_y} \tag{3.7}$$

where v is the table translation speed, τ is the duty cycle, f is the frame rate, M is the magnification, and p_y is the pixel size along the y-dimension. The blurring process can be modeled as a convolution of the true image with a boxcar kernel that has a width equal to Δd. With the forward blur model known, a non-blind, total-variation regularized deconvolution was deployed to recover the lost spatial resolution[194]. The regularization problem is postulated as:

$$\hat{x} = \arg\min_x \frac{\lambda}{2}\|\mathbf{H}x - y\|_{l1}^2 + \|x\|_{\mathrm{TV}}. \tag{3.8}$$

Here, y is the acquired blurred image, $\mathbf{H}$ is the boxcar blur kernel with width Δd, x is the estimated deblurred image, $\|\cdot\|_{\mathrm{TV}}$ is the total variation norm, and λ is a regularization parameter.

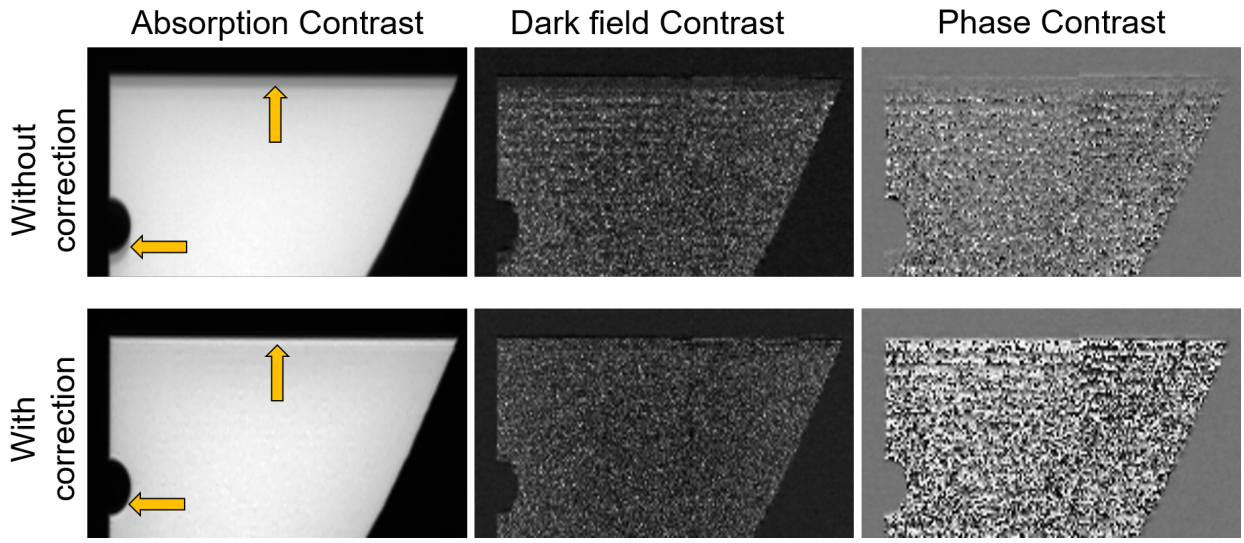

Figure 3.11: Demonstration of the utility of the lag and scanning motion correction algorithms. The presence of the ghosting signals in the uncorrected images of the metallic edge phantom at 45 mm/s is reduced by the application of the two algorithms.

3.5.4 Methods

A metallic edge phantom was scanned at speeds of 9 mm/s, 18 mm/s, 27 mm/s, 36 mm/s, and 45 mm/s to test the effectiveness of the detector lag correction and the scanning motion correction. For comparison, the three contrast images were first reconstructed with the algorithm discussed in Section 3.4 without either correction applied. The lag correction was then applied with the empirically determined coefficients from the previous section. Finally, the scanning motion deconvolution algorithm was applied to the lag corrected images. In this process, images were reconstructed with λ values ranging from 0.1 to 1000 to determine the optimal regularization parameter for each of the three contrast images. With the optimal λ values determined, the edge spread function of the three contrast images was measured for all scan speeds. The edge spread functions were normalized and plotted at each speed for the uncorrected, lag corrected, and motion + lag corrected images.

3.5.5 Results

The optimal values of λ were determined to be 5.5, 15, and 10 for the absorption, dark field, and phase images respectively. Figure 3.11 demonstrates the utility of the detector lag and scanning motion correction algorithms. The resulting absorption, dark field, and phase contrast images

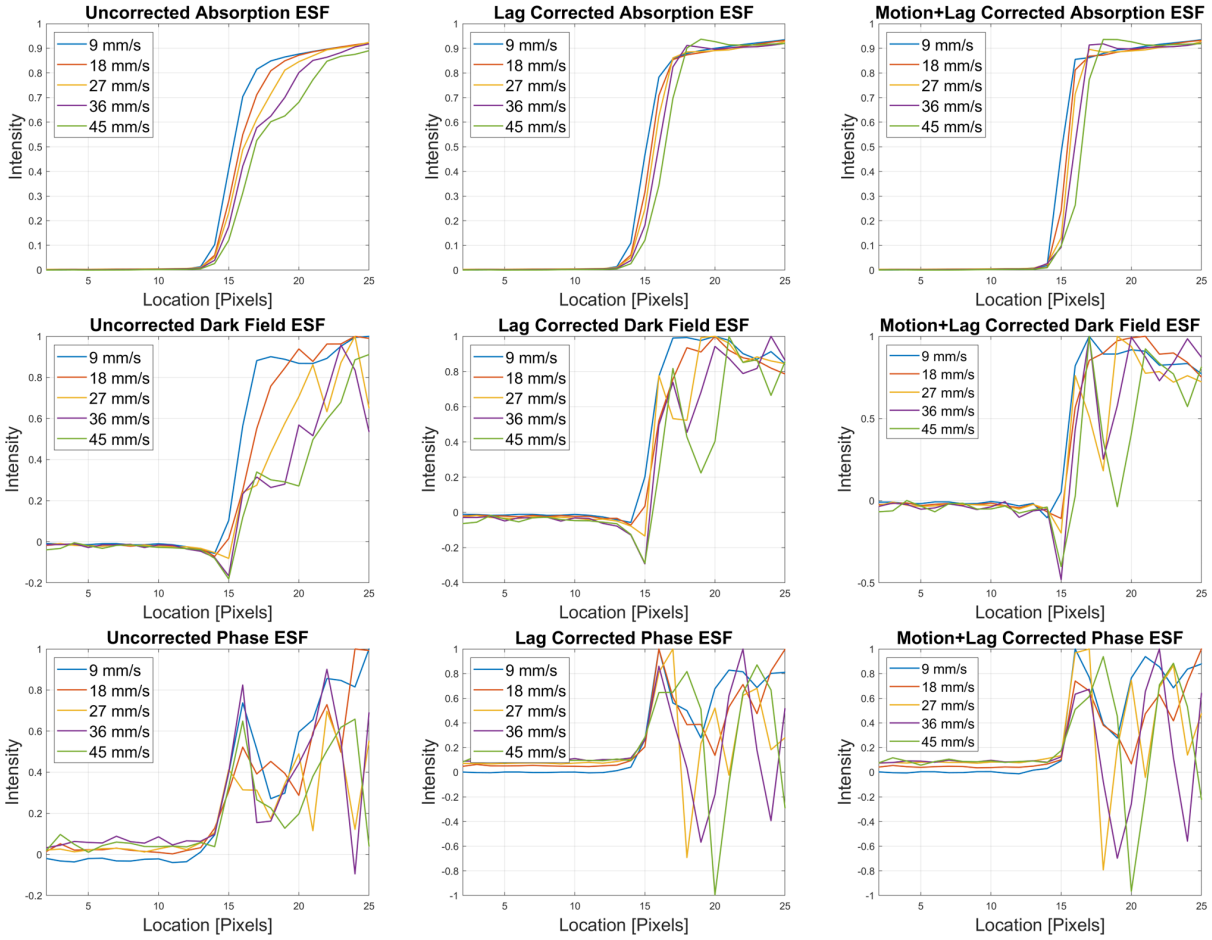

Figure 3.12: Edge spread functions for the uncorrected, lag corrected, and scanning motion + lag corrected acquisitions across all scan speeds and contrast mechanisms for the metallic edge phantom.

are depicted in Figures 3.13, 3.15, and 3.16 respectively. The detector lag correction was able to eliminate the ghosting of the metallic edge for all scan speeds and each of the contrast mechanisms. Based on the edge spread results, the majority of the spatial resolution recovery can be attributed to the detector lag correction. The edge spread functions for all scan speeds and contrast mechanisms are shown in Figure 3.12. The noise in the dark field images and the differential nature of the phase images make visualizing the edges challenging in the plots of the edge spread functions for these contrast mechanisms. This issue becomes increasingly challenging as the scan speed increases due to the increase in image noise. However, the edges were preserved when qualitatively assessing the images for the dark field and phase contrast images. Qualitatively, the difference between the lag corrected and motion plus lag corrected results is negligible. However, the edge spread functions of the lag + motion corrected images highlight the importance of the motion correction algorithm.

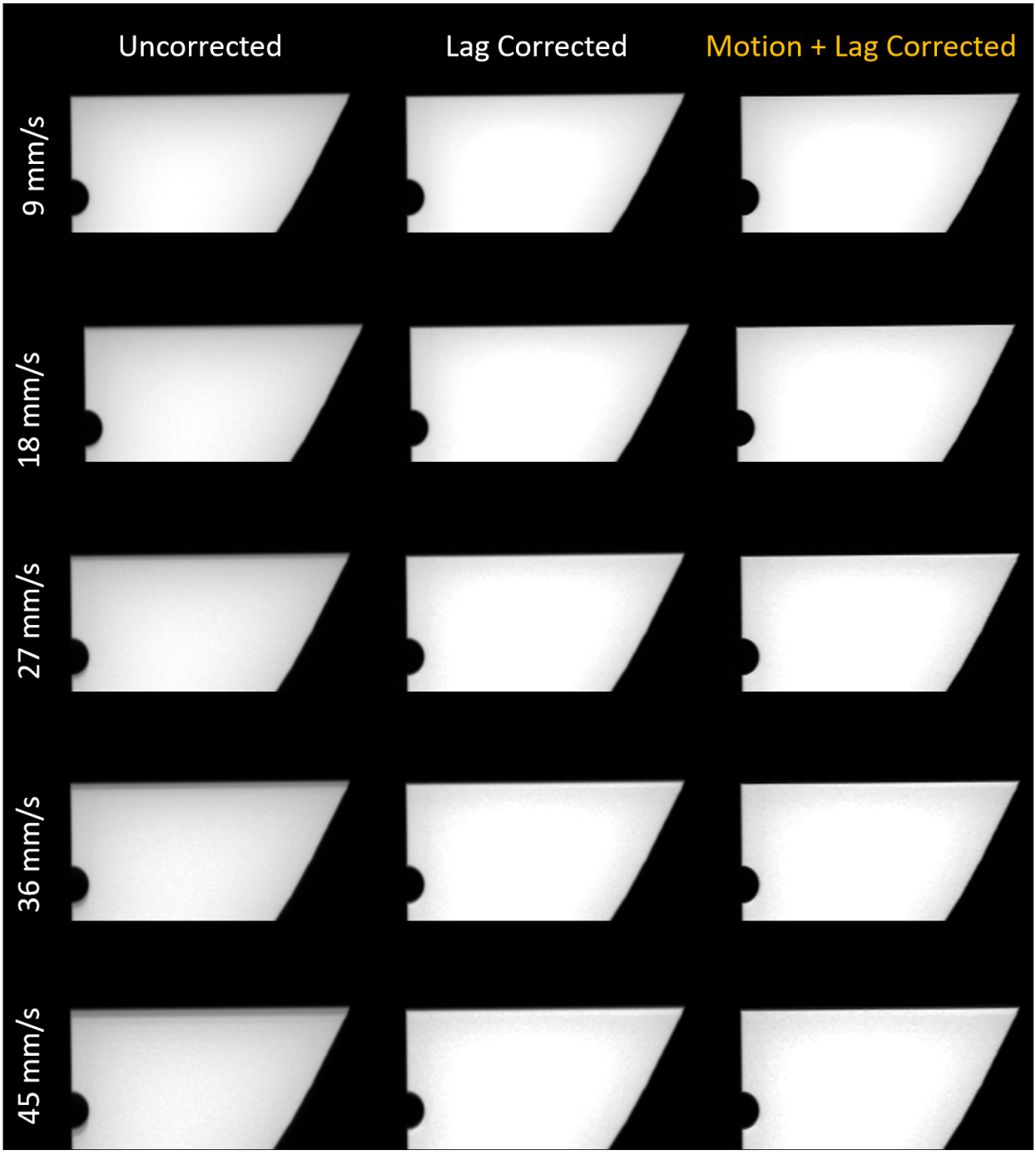

Figure 3.13: Comparison between the uncorrected, lag corrected, and scanning motion + lag corrected absorption images of the metallic edge phantom for each scan speed. The window/level was matched for all images.

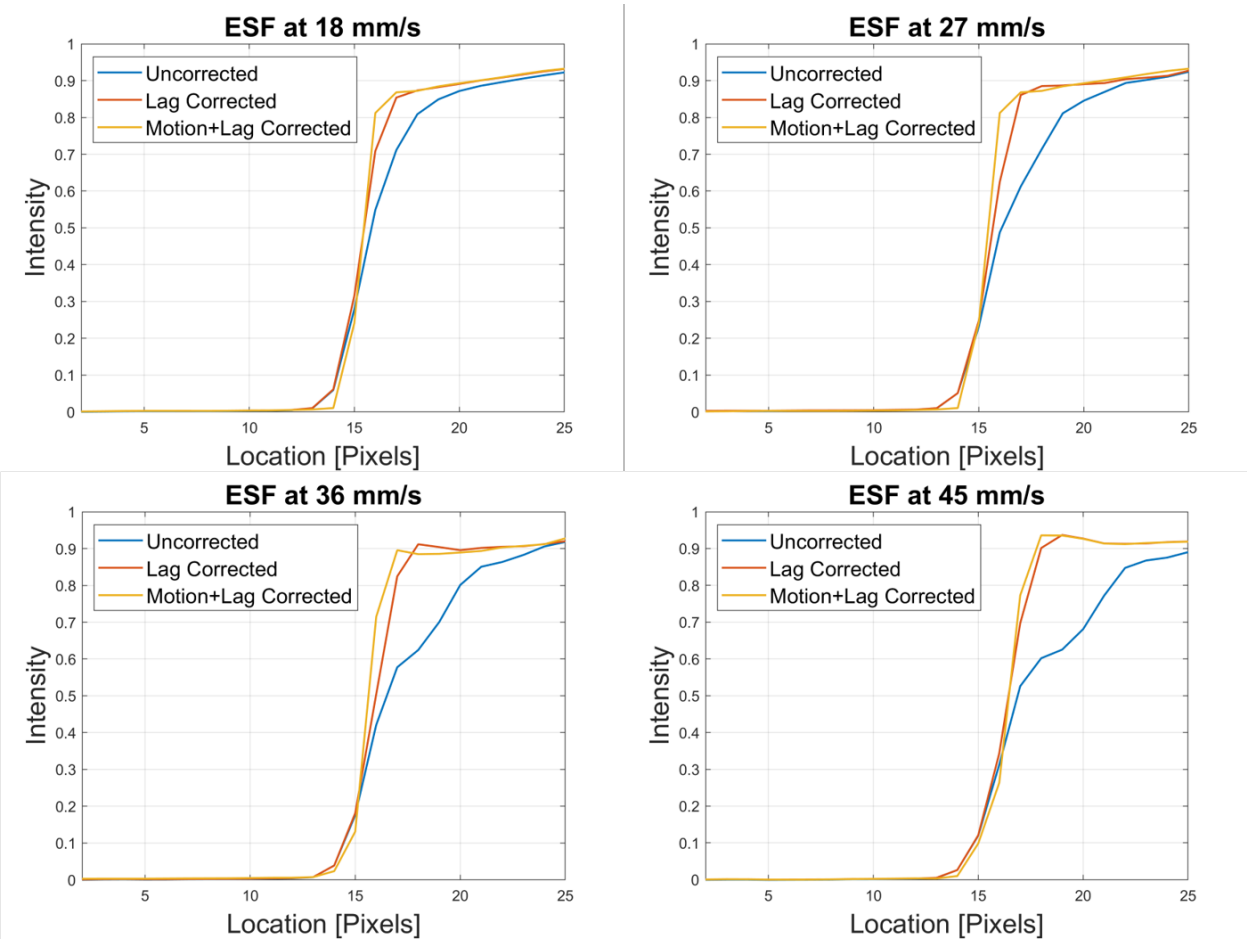

Figure 3.14: Direct comparison of the uncorrected, lag corrected, and scanning motion + lag corrected edge spread functions at scan speeds of 18 mm/s, 27 mm/s, 36 mm/s, and 45 mm/s for the uncorrected.

As demonstrated in Figure 3.14, the motion correction algorithm was able to improve the resolution across all scanning speeds for the absorption image.

The lag corrected and motion + lag corrected images do exhibit subtle qualitative differences when compared to the uncorrected images. At higher scan speeds, the lag corrected and lag + motion corrected absorption and dark field images begin to exhibit a subtle shading in the center of the phantom that is not present in the uncorrected dark field images. For the absorption contrast the center of the lag corrected images demonstrate an increased signal when compared to the uncorrected images. This suggests that the lag correction slightly overestimates the amount of residual signal for a given frame.

For the dark field images, the intensity at the center of the phantom for the lag corrected images is decreased when compared with the uncorrected images. This can be explained by recognizing

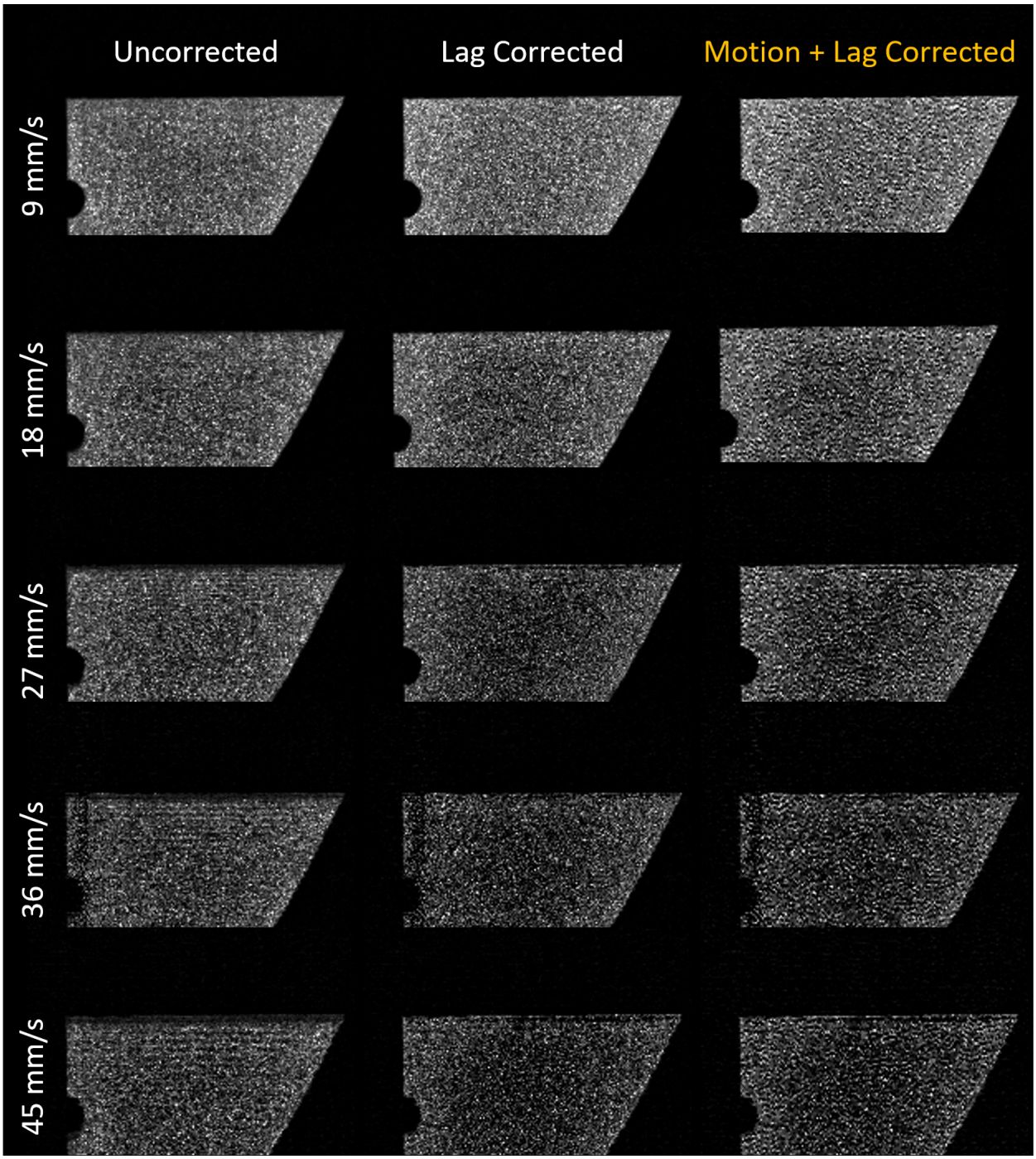

Figure 3.15: Comparison between the uncorrected, lag corrected, and scanning motion + lag corrected dark field images of the metallic edge phantom for each scan speed. The window/level was matched for all images.

that the dark field signal for the metallic edge phantom does not arise from small-angle scattering events. Rather, the dark field signal can be attributed to changes in the interference pattern from the hardening of the X-ray beam, a topic that is covered in greater detail in Chapter 5. As such, the shading in the dark field lag corrected images can be directly tied to the subtle shading in the absorption image. The overestimation of the residual lag signal also manifests as an overall increase in the intensity of the differential phase contrast images presented in Figure 3.16.

3.6 Summary

In this chapter, the design and construction of a novel prototype multi-contrast X-ray imaging system were presented. The prototype provides a compact, economical, and clinically compatible system that overcomes the limitations of grating interferometry through the introduction of a fast scanning acquisition scheme. Custom grating housing units were constructed to perform alignment of the grating interferometer for the G_1 and G_2 gratings. The alignment of the interferometer was outlined. The interferometric performance was optimized and an image reconstruction algorithm was introduced. Finally, a novel image correction framework was introduced to address the dark current, non-uniform pixel sensitivity, detector lag, and scanning motion blur phenomena associated with flat panel detectors and a scanning beam acquisition.

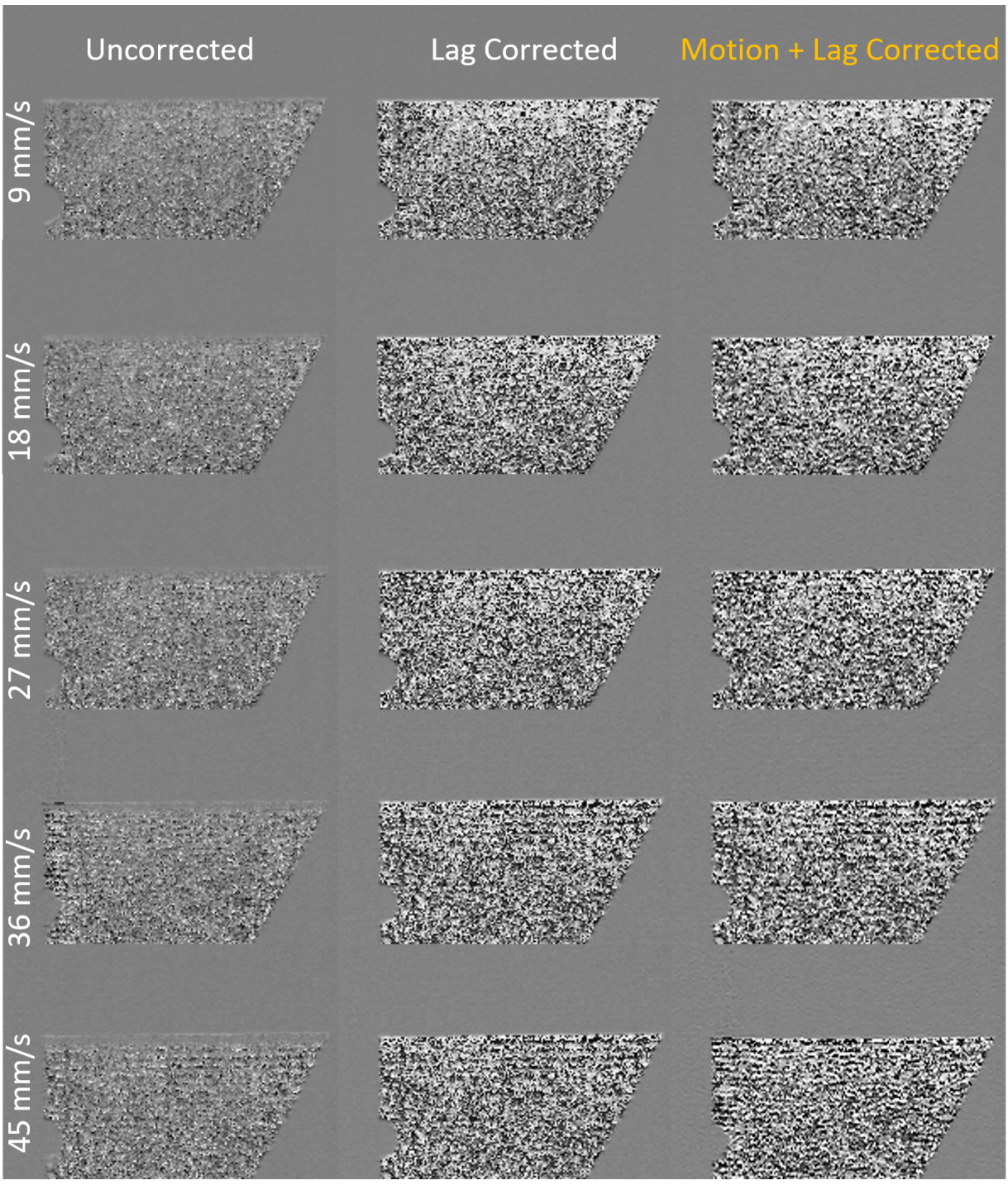

Figure 3.16: Comparison between the uncorrected, lag corrected, and scanning motion + lag corrected phase images of the metallic edge phantom for each scan speed. The window/level was matched for all images.

Chapter *4*

Optimization and Evaluation of Multi-Contrast X-ray Imaging Scan Protocols

4.1 Introduction

The successful clinical translation of a novel imaging system is contingent on the capacity of the system to effectively improve clinical outcomes. An essential step in improving clinical outcomes is the optimization of imaging protocols. Optimization of clinical imaging protocols allows clinicians to generate diagnostically useful information while reducing the potential risks associated with radiation exposure. In the previous chapter, the design and interferometric performance of the prototype multi-contrast X-ray imaging system developed in this thesis work was optimized. In this chapter, the focus is shifted to the optimization of clinical imaging parameters including peak tube potential (kVp) and tube current-time product (mAs). The dosimetric properties of the prototype system are first characterized to guide the optimization of these parameters and ensure patient safety. Optimization of the imaging parameters is then achieved for both the absorption and dark field contrast mechanisms through a novel phantom imaging study. The optimized imaging parameters are then evaluated for clinical imaging via an anthropomorphic chest phantom study.

4.2 Dosimetric Characterization of the Prototype System

The addition of three gratings to an X-ray imaging system has implications for the dosimetric properties of the system. The three absorption gratings reduce the number of X-rays used in the information encoding process, raising concerns about dose efficiency, particularly given the placement of the modulation and absorption gratings behind the patient. However, there are several

factors that counteract the potential degradations in dose efficiency associated with grating-based interferometry.

First, although the number of information carriers is reduced, the amount of information encoded in each X-ray is increased. The additional information encoded via the phase and dark field contrast mechanisms has the capacity to provide more comprehensive diagnostic information such that the diagnostic efficacy of X-ray imaging can be improved at a given dose level. Second, the source grating serves as a filter for the system, removing many of the low-energy X-rays that only contribute to the patient dose without contributing to the image encoding process. A final consideration with respect to dose efficiency is that the G_1 and G_2 gratings act as anti-scatter grids, which are widely used in current clinical practice. These gratings reduce the amount of scattered radiation that reaches the detector, improving image quality and enabling high-quality imaging to be achieved at reduced dose levels. Overall, while the addition of gratings to an X-ray imaging system may impact the dosimetric properties of the system, several factors inherent to grating-based interferometry serve to counteract potential degradations in dose efficiency.

Given the potential dosimetric implications associated with grating interferometry, it is important to perform a comprehensive characterization of the prototype system's radiation output. In this section, the quality of the X-ray beam is evaluated through half-value layer (HVL) measurements at different peak tube potentials. The radiation output is then measured to determine the effective dose to the patient for a given imaging exam.

4.2.1 Half-Value Layer

The half-value layer is defined as the thickness of a given material required to reduce the intensity of an incident radiation beam by one-half with the filtration that will be used for imaging. The method to measure the HVL was adapted from the American Association of Physicists in Medicine (AAPM) Report Number 25[195]. The only change to the HVL measurement outlined in the AAPM report is that the aluminum filtration was not added to the exit window of the collimator. Rather, the aluminum was added just behind the G_0 grating which is placed at the exit window of the collimator. In this sense, the G_0 grating was treated as if it was an inherent filter for the system. Exposure measurements were made with a general-purpose 6cc ion chamber and Radcal 9095 electrometer. The ion chamber was placed in the air at a height of 23 cm from the patient table.

An initial exposure measurement was made without the presence of aluminum filtration to establish a reference intensity. Different thicknesses of aluminum filtration were incrementally added behind the G_0 grating until the beam intensity was reduced to one-half the reference value. Logarithmic interpolation was then performed to calculate the HVL. This process was repeated for peak tube potentials ranging from 70 kVp to 120 kVp.

Table 4.1: Measured HVLs at each kVP with minimum HVLs from AAPM Report No. 25.

Peak Tube Potential	HVL [cm]	Minimum HVL [cm]
70 kVp	2.7	1.5
80 kVp	3.0	2.3
90 kVp	3.6	2.5
100 kVp	4.1	2.7
110 kVp	4.6	3.0
120 kVp	5.1	3.2

A summary of the measured HVLs for each peak tube potential is presented in Table 4.1. It should be noted that the HVL for each kVp exceeds the minimum HVL that has been defined in the AAPM Report No. 25.

4.2.2 Estimation of Entrance Skin Exposure, Kerma-Area Product, and Effective Dose

The three most important dosimetric quantities in diagnostic radiography are entrance skin exposure, kerma-area product, and effective dose. To effectively characterize and benchmark the performance of the multi-contrast X-ray imaging prototype relative to conventional chest radiography, it is necessary to develop a method for estimating these three quantities.

Entrance skin exposure (ESE) refers to the radiation output of the imaging system at the point of entry into the patient's skin. The kerma-area product (KAP) represents the product of the average air kerma and the cross-sectional area of the X-ray beam at the patient's entrance plane, typically measured in units of Gy·cm^2. The effective dose, typically reported in mSv, is the tissue-weighted sum of equivalent doses to the organs exposed to radiation during a given imaging exam.

ESE measurements for the prototype system were made following the recommendations established by the AAPM Report No. 31[196] for diagnostic X-ray imaging systems operated in manual mode. The general purpose 6cc ion chamber and Radcal 9095 electrometer were once again utilized to measure the exposure in air. The chamber was placed at a height of 23 cm above the

patient table. Five measurements of the free air exposure were then measured for tube potentials ranging from 70 to 120 kVp in 10 kVp intervals with all measurements being made at 40 mAs. The mean free ESE, the air kerma, and the air kerma per mAs are reported in Table 4.2 for a patient entrance skin plane of 23 cm above the patient table. An inverse square correction can be applied to estimate the ESE for patients with entrance skin planes at different distances from the patient table.

Table 4.2: Exposre and air kerma for each tube potential of the system.

Peak Tube Potential	ESE [mR]	Air Kerma [mGy]	Air Kerma per mAs [mGy/mAs]
70 kVp	19.37 ± 0.19	0.17 ± 0.0021	$0.0042 \pm 5.2 \times 10^{-5}$
80 kVp	26.56 ± 0.15	0.23 ± 0.0015	$0.0058 \pm 3.3 \times 10^{-5}$
90 kVp	35.09 ± 0.10	0.31 ± 0.0010	$0.0076 \pm 2.3 \times 10^{-5}$
100 kVp	43.60 ± 0.13	0.39 ± 0.0013	$0.0096 \pm 2.8 \times 10^{-5}$
110 kVp	49.45 ± 0.21	0.44 ± 0.0021	$0.0109 \pm 4.5 \times 10^{-5}$
120 kVp	57.97 ± 0.25	0.51 ± 0.0025	$0.0127 \pm 5.4 \times 10^{-5}$

For a given imaging exam, the tube current-time product can be calculated from the mA and the number of image frames acquired in the scan. Given the synchronization of the imaging system, the number of frames acquired also provides the number of X-ray pulses. With a pulse width of 5 ms and a frame rate of 30 fps, the tube current-time product can be calculated as:

$$\text{mAs} = (\#\text{ of Frames}) \times \text{mA} \times 0.005 \tag{4.1}$$

As a reference, a total of 1167 frames would need to be acquired to cover 35 cm along the longitudinal direction for a slow scan speed of 9 mm/s, while 234 frames would need to be acquired at a scan speed of 45 mm/s. The tube current time product for such acquisitions at 60 mA would be 350 mAs and 70 mAs respectively.

The next step was to establish a pathway for estimating the KAP for a given imaging exam. Assuming a full FOV of 35 cm $\times$ 28 cm at the reference patient skin entrance for a scanning acquisition, the cross-sectional area of the radiation field at the patient entrance plane is 980 cm^2. Table 4.3 summarizes the KAP per mAs for a full FOV scan. To estimate the effective dose in mSv from the measured KAP, a set of conversion coefficients established by Le Heron et al. were employed [197]. The HVL measurements from Section 4.2.1 were used in conjunction with the SPEKTR X-ray spectra computational toolkit to determine the equivalent thickness of inherent aluminum

Table 4.3: Kerma-area product per mAs at each tube potential.

Peak Tube Potential	KAP/mAs [mGy · cm^2/mAs]
70 kVp	4.16 ± 0.058
80 kVp	5.69 ± 0.037
90 kVp	7.48 ± 0.026
100 kVp	9.44 ± 0.031
110 kVp	10.65 ± 0.050
120 kVp	12.44 ± 0.060

filtration required to match the beam quality for the prototype system. The conversion coefficients for chest AP radiography were then determined from this approximation for an adult reference phantom. Table 4.4 tabulates the determined conversion coefficients and approximated effective dose per mAs for each peak tube potential.

Table 4.4: Exposre and air kerma for each tube potential of the system.

Peak Tube Potential	Conversion Coefficient [mSv/Gy·cm^2]	Effective Dose per mAs [μSv/mAs]
70 kVp	0.188	0.78
80 kVp	0.213	1.21
90 kVp	0.235	1.76
100 kVp	0.255	2.41
110 kVp	0.273	2.91
120 kVp	0.289	3.60

From Table 4.4 and Equation 4.1, the effective dose can be estimated for any given multi-contrast scanning acquisition. For example, the estimated effective dose to a reference patient for a scanning acquisition at 70 kVp, 60 mA, and 45 mm/s table translation would be 0.05 mSv. It is worth noting that 60 mA is the maximum tube current achievable. Compared to the average effective dose of 0.1 mSv associated with CXR, the prototype system offers comparable or even lower radiation doses to the patient. Furthermore, the effective dose from the prototype system developed in this thesis is significantly reduced when compared to prototype MC-CXR systems developed in other countries. For instance, the mean effective dose to a reference phantom for the prototype system developed by Pfeiffer et al. is 0.35 mSv [198].

4.3 Optimization of Clinical Imaging Parameters

The dosimetric properties characterized in the previous section can be leveraged to guide the optimization of clinical imaging parameters for the prototype system. The peak tube potential and tube current-time product have a direct impact on multi-contrast image quality and the radiation dose delivered to the patient.

In conventional absorption imaging, the selection of X-ray energy affects soft tissue contrast, contrast within osseous structures, and the suppression of the image signal from osseous structures. Although soft tissue contrast is generally improved at reduced X-ray energies, it remains relatively constant over the spectrum of energies used in chest radiography. Therefore, higher X-ray energies are typically used in chest radiography to suppress the signal from osseous structures[199]. The dark field and phase contrast mechanisms also depend strongly on X-ray energy. Visibility and phase sensitivity directly impact the contrast and noise for the dark field and phase images, respectively. As demonstrated in Chapters 2 and 3, visibility and sensitivity are significantly improved at reduced X-ray energies. For example, the visibility of the interferometer is $19 \pm 3\%$ at 70 kVp and $12 \pm 2\%$ at 120 kVp. Despite this, the image noise at 70 kVp may become an issue for larger patients. As such, the overall quality of the additional contrast mechanisms is not necessarily best at the lowest X-ray energies.

Optimizing the X-ray energy and dose level for multi-contrast imaging presents a unique challenge due to the complexities associated with X-ray energy and dose. However, in this thesis, a novel pathway and custom optimization phantom are presented to overcome these challenges and guide the optimization of the peak tube potential and tube current time product. The optimization approach taken in this work is empirical, where the entire clinical imaging parameter space is explored to determine the optimal parameters for a given patient thickness. Furthermore, the optimization process only considers the imaging performance for the dark field and absorption contrast mechanisms, as they are the most relevant contrast images for pulmonary imaging. This approach ensures that the resulting optimal imaging parameters provide the best possible dark field and absorption contrast images, which are crucial for accurate pulmonary imaging. By utilizing this approach, the optimization process can be tailored to individual patients, leading to improved diagnostic accuracy and patient outcomes.

4.3.1 Optimization Metric

The dose-normalized contrast to noise ratio (D-CNR) is the metric employed to guide the optimization of the peak tube potential and dose level in this thesis work. The rationale for selecting the D-CNR as the metric to optimize for is that the D-CNR encompasses dosimetric properties and the fundamental quantity utilized in diagnosis. The D-CNR is defined with the following formula:

$$\text{D-CNR} = \frac{\mu_{obj} - \mu_{bkg}}{\sigma_{bkg} \cdot \sqrt{ED}}, \tag{4.2}$$

where μ_{obj} is the mean intensity for an ROI with a contrast-generating object, μ_{bkg} is the mean intensity for an ROI without a contrast-generating object, σ_{bkg} is the standard deviation of that same ROI, and ED is the effective dose of the acquisition to a reference phantom in mSv.

4.3.2 Image Quality Phantom

A phantom with absorption and dark field contrast-generating objects and the capacity to simulate different patient thicknesses must be introduced to enable the measurement of the D-CNR and the optimization of scan parameters for a given patient. In this thesis work, this task is accomplished by creating a custom multi-contrast-specific chest phantom. The chest phantom is adapted from the American National Standards Institute (ANSI) chest phantom as defined in the AAPM Report No. 31[196]. A diagram and picture of the ANSI chest phantom are shown in Figure 4.1A. The ANSI phantom consists of two sets of two 30.5 cm $\times$ 30.5 cm $\times$ 2.5 cm acrylic, or polymethyl methacrylate (PMMA), slabs that are separated by a 19 cm air gap to simulate the thoracic cavity. Aluminum alloy sheets are then placed in between the two acrylic slabs on each side of the air gap to simulate the osseous structures in the thorax. Additional acrylic slabs were added to the conventional ANSI phantom to simulate patients of varying thicknesses in this work.

A custom insert was designed and inserted into the ANSI phantom to generate contrast in the absorption and dark field images. The custom insert (Figure 4.1B) consists of two components: an absorption contrast component and a dark field contrast component. The absorption contrast component consists of an acrylic slab with a total of 14 cylindrical contrast objects drilled into the acrylic. The 16 contrast objects have 4 different depths, or contrast levels, and range from 0.5 mm in diameter to 1.5 mm in diameter. The absorption D-CNR is measured from the 1.5 mm insert with

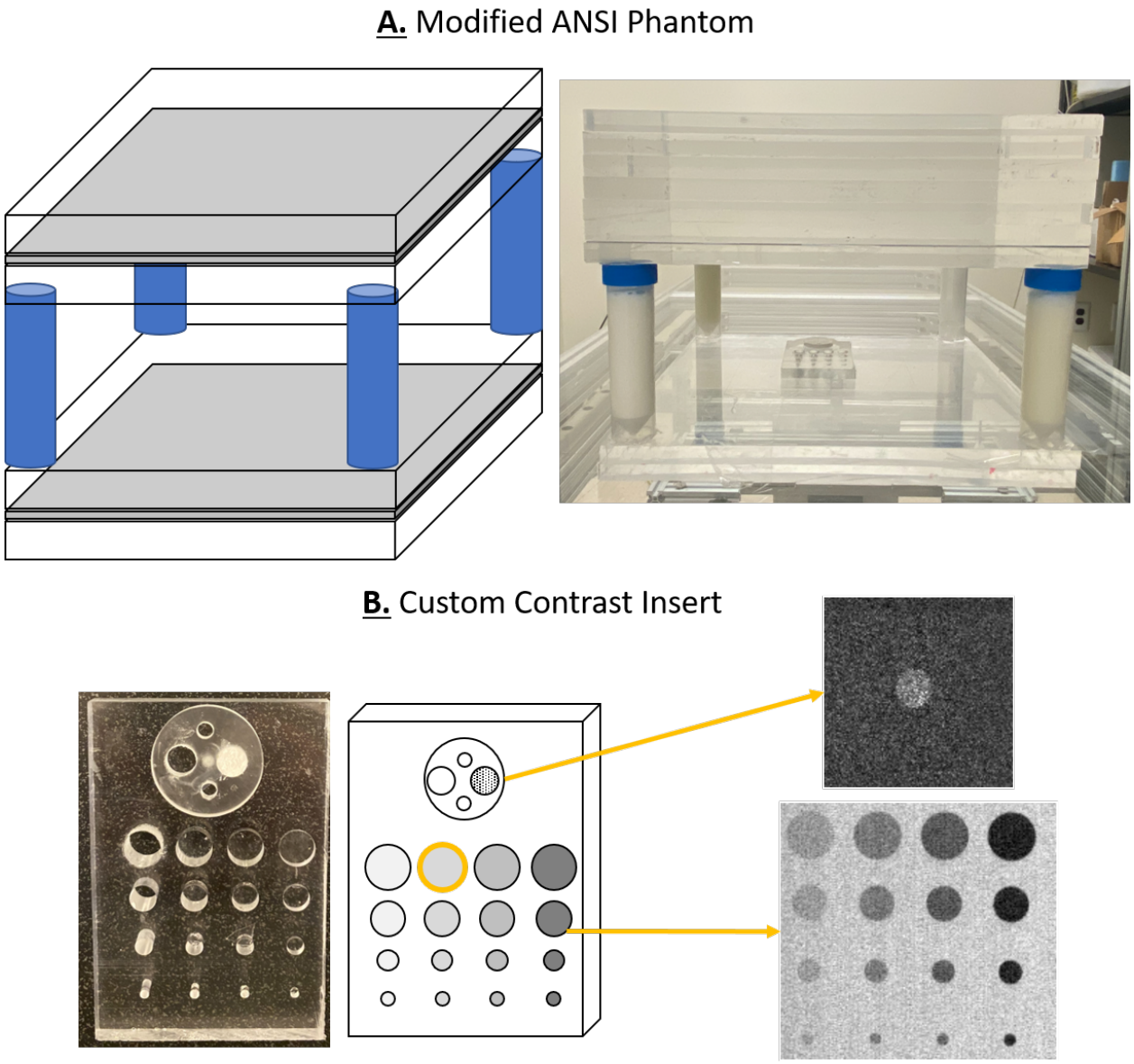

Figure 4.1: Illustration and pictures of the modified ANSI chest phantom and the custom contrast insert.

the second lowest contrast level (Row 1, Column 2), as highlighted in Figure 4.1B. The dark field D-CNR is measured from a 1.5 mm cylindrical object that contains a 5 μm microbubble powder that is designed to generate a strong small-angle scattering signal.

4.3.3 Imaging Methods

The total number of scanning acquisitions was 370. All imaging was performed at a fast scan speed of 36 mm/s with 250 frames collected. The peak tube potential was varied from 70 kVp to 120 kVp in 10 kVp intervals. The tube current was modulated from 5 mA to the maximal tube current achievable for a given peak tube potential. The effective dose for each peak tube potential and tube current are summarized in Table 4.6. The total number of acrylic slabs used for the ANSI phantom was varied from 3 to 12 (7.5 cm to 30 cm) for each peak tube potential and tube current investigated. The optimal tube potential for a given patient thickness and contrast mechanism was selected as

Table 4.5: Effective dose in mSv for each kVp and mA investigated.

kVp/mA	5 mA	10 mA	20 mA	30 mA	40 mA	50 mA	60 mA
70 kVp	0.00488	0.00977	0.0195	0.0293	0.0391	0.0488	0.0586
80 kVp	0.00757	0.0151	0.0303	0.0454	0.0605	0.0757	0.0908
90 kVp	0.0110	0.0220	0.0439	0.0659	0.0879	0.1099	0.132
100 kVp	0.0151	0.0301	0.0602	0.00903	0.0120	0.151	-
110 kVp	0.0182	0.0363	0.0726	0.109	0.145	-	-
120 kVp	0.0225	0.0449	0.0899	0.135	0.157*	-	-

Table 4.6: *this is the effective dose for the maximal tube current of 35 mA for 120 kVp.

the highest D-CNR at a dose level closest to 0.586 mSv, or that of the 70 kVp and 60 mA acquisition. Similarly, the optimal tube current was determined as the highest D-CNR achieved for a given patient thickness, contrast mechanism, and kVp.

4.3.4 Results

All reconstructed absorption and dark field images are displayed at the end of this chapter (Section 4.6). Table 4.7 summarizes the optimal peak tube potential for each contrast mechanism and given patient thickness. Plots of the D-CNR as a function of tube potential at four different patient thicknesses are shown in Figures 4.2 and 4.3. The optimized kVp values demonstrate a compromise between contrast and noise for both the absorption and dark field contrast mechanisms. Lower

Table 4.7: Optimal Peak Tube Potential for each Patient thickness.

# of Slabs	$\text{kVp}_{opt,absorp}$	$\text{kVp}_{opt,dark}$
3	70	70
4	70	70
5	70	70
6	70	80
7	70	70
8	70	70
9	100	70
10	100	80
11	100	70
12	100	70

tube potentials provide better performance for both mechanisms in smaller patients, in accordance with our understanding of the relationship between the effective energy of the X-ray beam and image contrast. In absorption imaging, lower X-ray energies enhance soft tissue contrast, while in dark field imaging, fringe visibility and overall image contrast increase at lower energies. Therefore, when noise is not significant, such as in smaller patients, the D-CNR is dominated by the increase in image contrast associated with lower tube potentials. However, as the patient's overall attenuation increases, image noise becomes a more prominent component of the D-CNR metric. For a given dose level, a greater proportion of X-rays from higher energy spectra can be used in the image encoding process. Consequently, the relative contribution of image noise is reduced for higher tube potentials. Furthermore, this improvement in X-ray statistics is more pronounced as patient attenuation increases. Although higher X-ray energies reduce the contrasts of both the absorption and dark field images, the reduction in noise at higher tube potentials results in a relative improvement in the D-CNR compared to lower tube potentials for larger patients. This tradeoff is best exhibited for the absorption D-CNR measurements, in which the optimal tube potential is increased to 100 kVp for simulated patient thicknesses of 9 acrylic slabs or greater. For dark field imaging, this tradeoff can be see as differences in D-CNR across peak tube potentials becomes more uniform as patient thickness is increased.

As the patient thickness increases, it becomes more challenging to determine the optimal kVp for dark field imaging due to uncertainties in the D-CNR measurement. Furthermore, the thickness of the patient has a more significant impact on the overall D-CNR for dark field imaging compared to absorption D-CNR. For instance, when comparing patient thicknesses of 3 and 12 acrylic slabs,

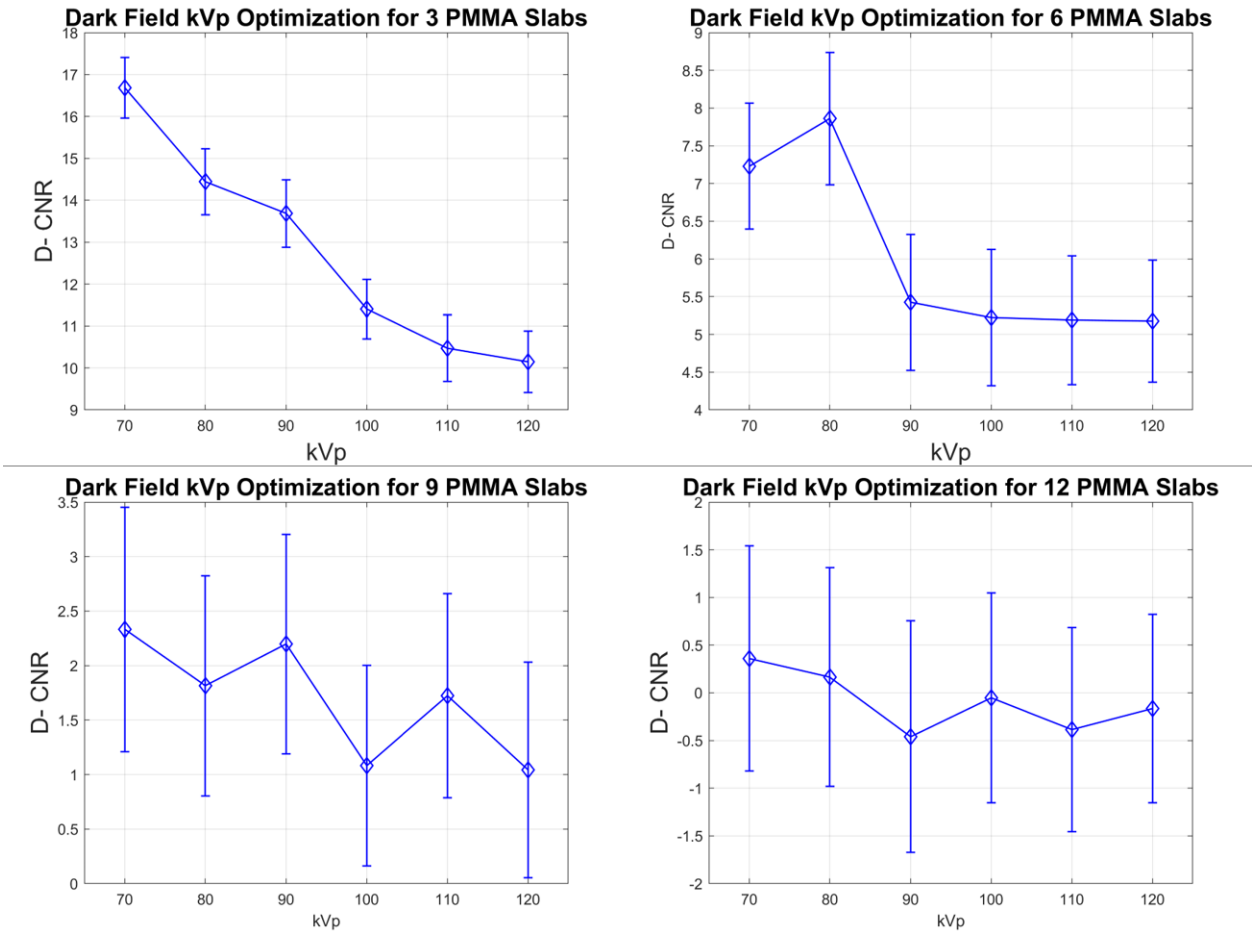

Figure 4.2: Dark field D-CNR as a function of kVp for patient thicknesses of 3, 6, 9, and 12 acrylic slabs.

there is a 92% decrease in the highest D-CNR for the dark field images, while the absorption D-CNR only shows a 59% decrease. These findings suggest that dark field imaging may not be well-suited for imaging larger patients.

Figures 4.4 and 4.5 provide surface plots of the D-CNR for each kVp, patient thickness, and dose level. These surface plots can be utilized as lookup tables in clinical settings to determine appropriate imaging parameters for a given multi-contrast acquisition.

Across all tube potentials, higher dose levels resulted in improved dark field D-CNR for moderate-to-high patient thicknesses. However, negative dark field D-CNR values were observed for low-dose acquisitions of highly attenuating patients at all tube potentials. The negative dark field contrast may result from statistical bias or spectral distortions caused by the beam hardening effect. In contrast, the absorption D-CNR remained relatively uniform across dose levels as patient thickness increased, and no negative absorption D-CNR measurements were recorded. In general,

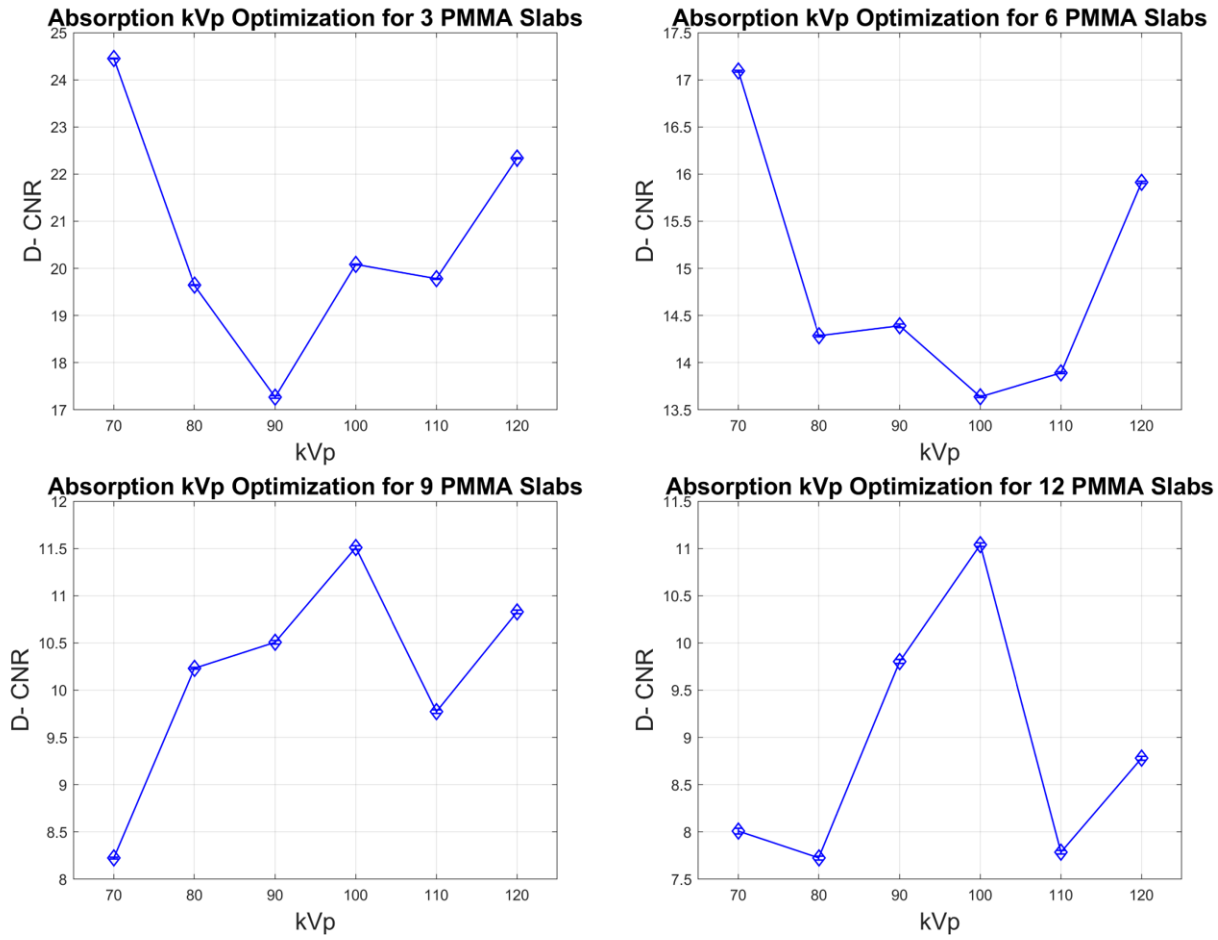

Figure 4.3: Absorption D-CNR as a function of kVp for patient thicknesses of 3, 6, 9, and 12 acrylic slabs.

the lower tube potentials demonstrated improved absorption and dark field imaging performance at the highest dose levels. In contrast, performance was found to be best at reduced dose levels when the tube potential was high and the patient thickness was low. Given the more consistent image performance associated with the absorption contrast mechanism, it is suggested that the kVp should be selected based on the optimal dark D-CNR for for a given patient exam.

4.4 Evaluation of Optimized Imaging Protocols

The final objective of this chapter is to evaluate the optimized imaging parameters in a simulated clinical scenario. While the ANSI phantom and custom contrast-generating insert are suitable for the purpose of parameter optimization, they do not fully replicate the heterogeneity and intricacies of the human thorax. Conversely, anthropomorphic phantoms have been extensively used in medical

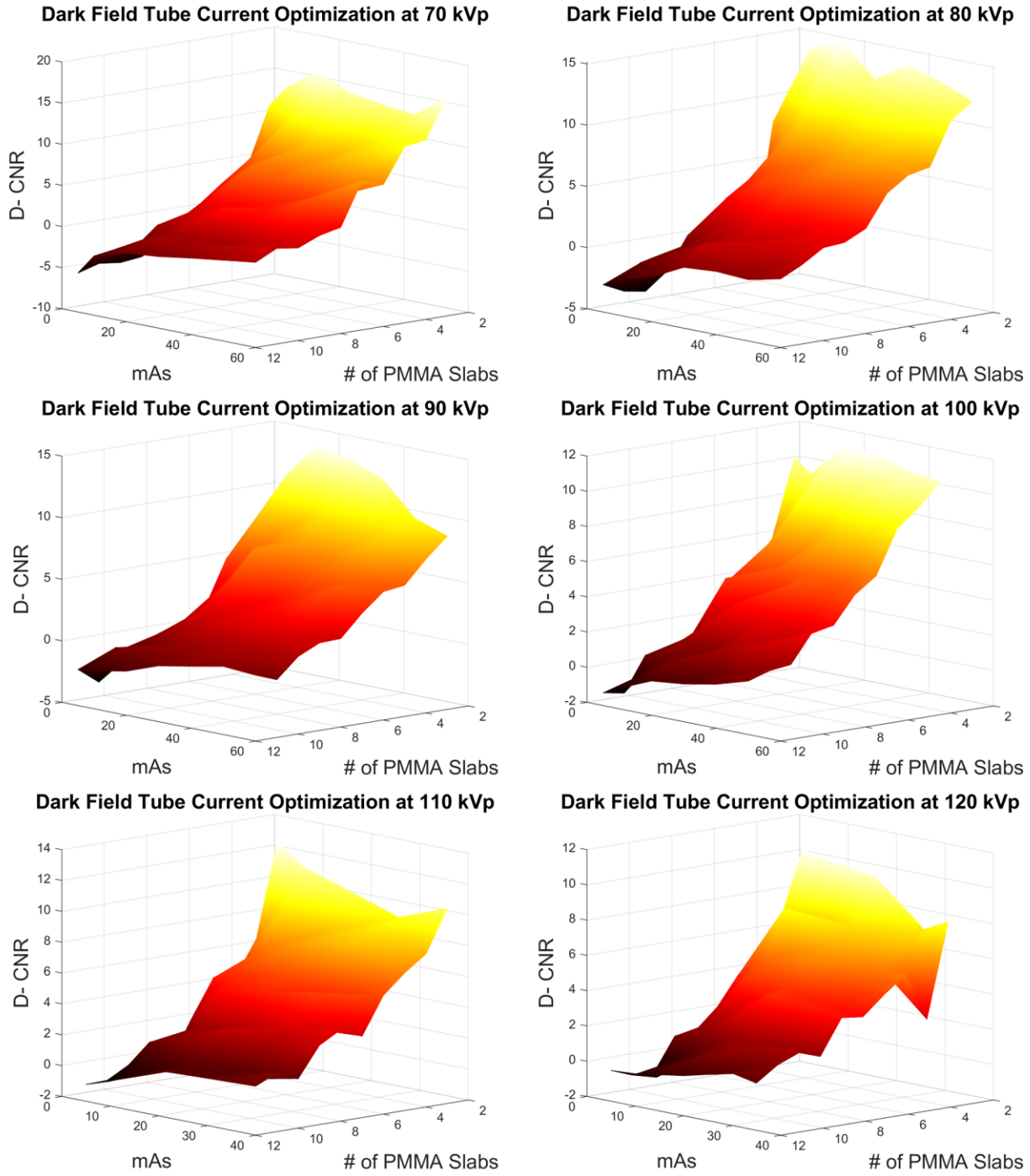

Figure 4.4: Surface plot of the dark field D-CNR to determine the optimal clinical imaging parameters for a given patient thickness.

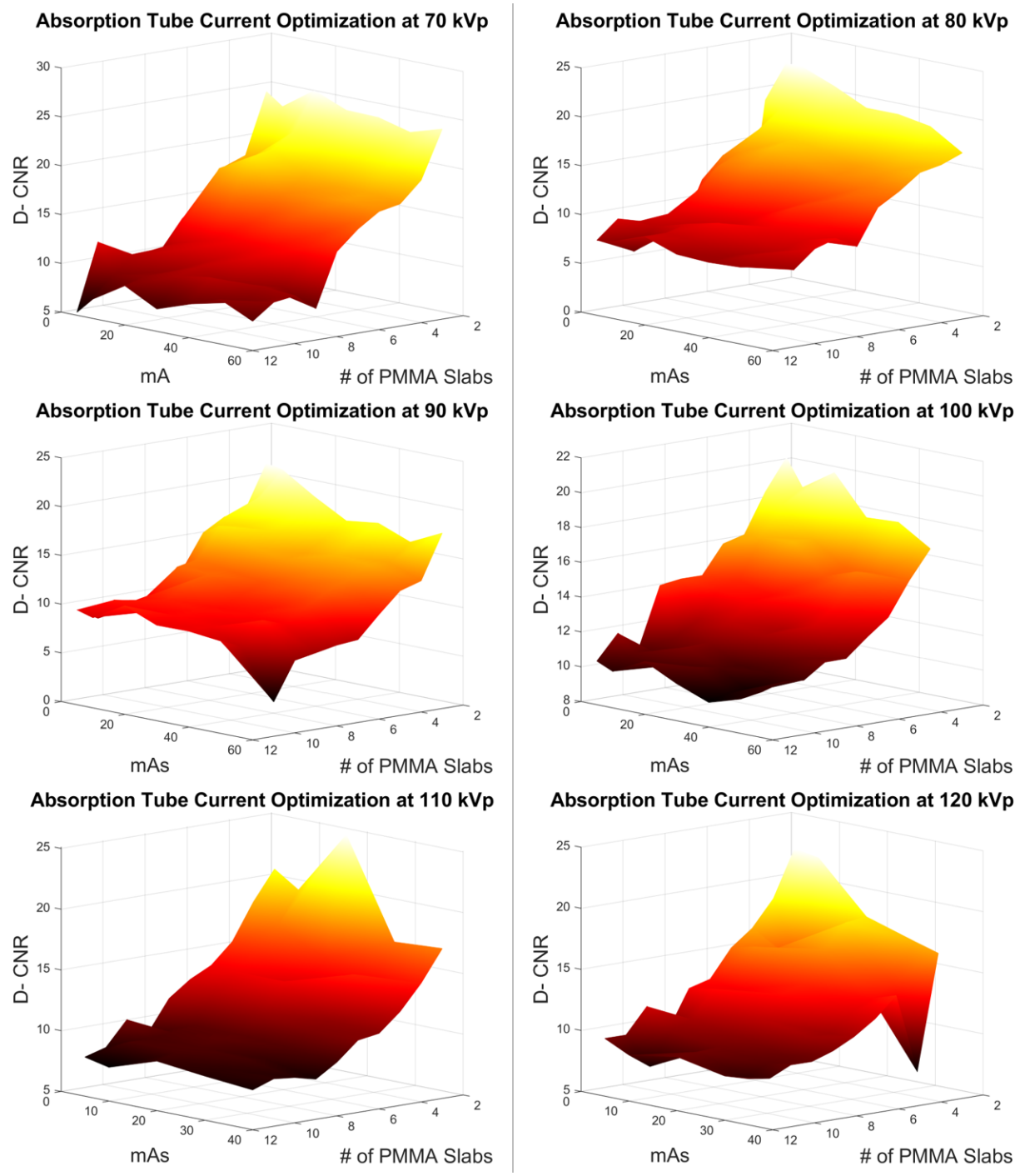

Figure 4.5: Surface plot of the dark field D-CNR to determine the optimal clinical imaging parameters for a given patient thickness.

imaging due to their ability to realistically simulate the properties and complexities of the various tissues and structures of the human body. Therefore, this section aims to evaluate the performance of the optimized scan protocols by conducting multi-contrast imaging of an anthropomorphic chest phantom that features a simulated disease model.

4.4.1 Methods

The optimized imaging parameters were tested on the LUNGMAN chest phantom (Kyoto Kagaku). The LUNGMAN phantom contains an outer torso consisting of a soft-tissue-equivalent outer layer, ribs, the spine, clavicles, and sternum. The other major component of the phantom is an insert that consists of the heart, bronchi, bronchioles, mediastinum, and pulmonary vasculature. For the purposes of this study, the components of the LUNGMAN insert mimic the complex anatomy of the lungs while the outer torso provides the attenuation and signal from osseous structures that are associated with chest X-ray imaging.

Although the LUNGMAN phantom provides many of the essential pulmonary structures of the human chest, it is incapable of providing the alveoli-air interface that the dark field image signal is intrinsically connected to. A cellulose lung phantom was therefore constructed to overcome this inherent limitation of the LUNGMAN phantom. The diameter of the pores in cellulose sponge closely resembles that of the human alveoli[200]. The cellulose lung phantom was constructed by cutting and stitching together Ocelo multi-purpose sponges (St. Paul, MN) into the shape of the right lung of the LUNGMAN phantom. To approximate the thoracic cavity of the LUNGMAN phantom, the total thickness of the cellulose sponge was made to be 9 cm. The sponge phantom was tapped above the right lung of the LUNGMAN phantom for imaging as insertion into the chest cavity was not feasible.

Two pulmonary edema lesions were simulated by injecting the cellulose lung phantom with water. Additionally, a total of three lung tumor nodules were inserted into the phantom, including two high-density nodules (CT Hounsfield Unit, or HU, of 100) with diameters of 1.0 and 0.8 cm, and one low-density nodule (630 HU) with a diameter of 0.8 cm. The 0.8 cm high-density nodule was placed directly into the sponge phantom, while the other nodules were placed into the pulmonary structures of the LUNGMAN insert. The LUNGMAN phantom, LUNGMAN insert, and multi-contrast images of the LUNGMAN insert and sponge phantom are displayed in Figure

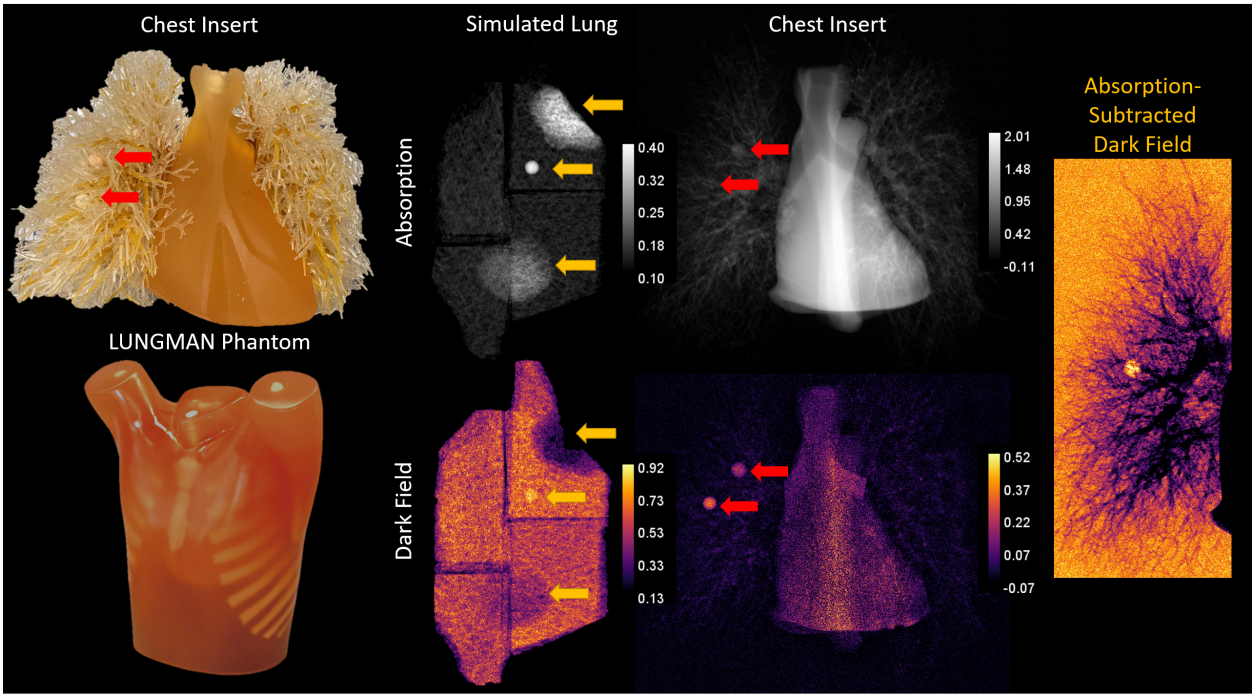

Figure 4.6: Photographs of the LUNGMAN anthropomorphic phantom, LUNGMAN insert with simulated lung tumor nodules (red arrows), and multi-contrast images of the cellulose sponge phantom with pulmonary edema and a lung tumor nodule (gold arrows) and the chest insert with the two lesion models.

4.6. The pulmonary edema and high-density nodules can be easily visualized in both the absorption and dark field images. However, the low-density lung cancer nodule is only detectable in the dark field image.

The material of the low-density lung nodule is styrofoam, a material that has many air-surface interfaces that may induce a strong small-angle scattering signal. However, the high-density nodules are made of epoxy, which in theory should not induce a strong dark field signal as a result of the material's uniform density. The presence of the dark field signal arising from the high-density nodules may be the result of a reduction in the fringe visibility arising from the attenuation of the image object or the hardening of the X-ray beam. To test this hypothesis, an absorption-subtracted dark field image was generated. As shown in Figure 4.6, the dark field signal arising from the high-density lung nodule is entirely eliminated in the absorption-subtracted dark field image.

The overall attenuation of the LUNGMAN phantom is comparable to the attenuation for the ANSI phantom with 5 acrylic slabs. Based on the results of the previous section, the LUNGMAN phantom was scanned with a kVp of 70 and an mA of 60. The table translation speed was set to 36 mm/s to enable coverage of the 30 cm chest within 10 s. The effective dose was estimated to be

0.0586 mSv, well below the average effective dose in conventional chest AP imaging. However, given the constraints of the tube output, this was the highest achievable dose level to enable a clinically compatible imaging time.

4.4.2 Results

Reconstructed multi-contrast images of the LUNGMAN phantom with the cellulose sponge phantom are shown in Figure 4.7. Despite being masked by the surrounding pulmonary tissues and ribs, the two high-density lung nodules are detectable in the absorption contrast image. The pulmonary edema lesions and low-density lung nodule are, however, not readily apparent in the absorption image.

Upon initial examination of the dark field image, an overall increase in the dark field signal of the right lung is demonstrated. However, the detection of the pulmonary disease models is challenging. The low-density and the 0.8 cm high-density lung nodules can be seen in the dark field images, however, the contrast is quite limited. Furthermore, the contrast of the pulmonary edema model in the sponge phantom is significantly reduced when compared to the dark field image presented in Figure 4.6. This obfuscation of image contrast can be partially attributed to the high dark field signal exhibited by the ribs, spine, mediastinum, and chest wall. For instance, the dark field signal is as large as 0.15 in-between the ribs of the left lung. In theory, these additional structures should not contribute to the dark field signal as there are no, or limited, small-angle scatterers present. It is for this reason that dark field imaging was hypothesized to mitigate the undesirable masking effect associated with projection imaging.

To potentially mitigate these effects, an absorption-subtracted dark field image was also generated, similar to that of the LUNGMAN insert in the previous subsection, to remove any dark field signals arising from attenuation. The pulmonary edema in the upper lobe of the right becomes more readily apparent in the absorption-subtracted dark field image, as indicated by the gold arrow. One major limitation of the absorption subtraction technique is that a false dark field signal is induced in the right lung, where no small-angle scattering events occur.

The poor performance of the dark field images in this anthropomorphic phantom study highlights the two major issues to be addressed throughout the remainder of this thesis work. First, the dark field signal arising from true small-angle scattering events is degraded by the high dark field signal

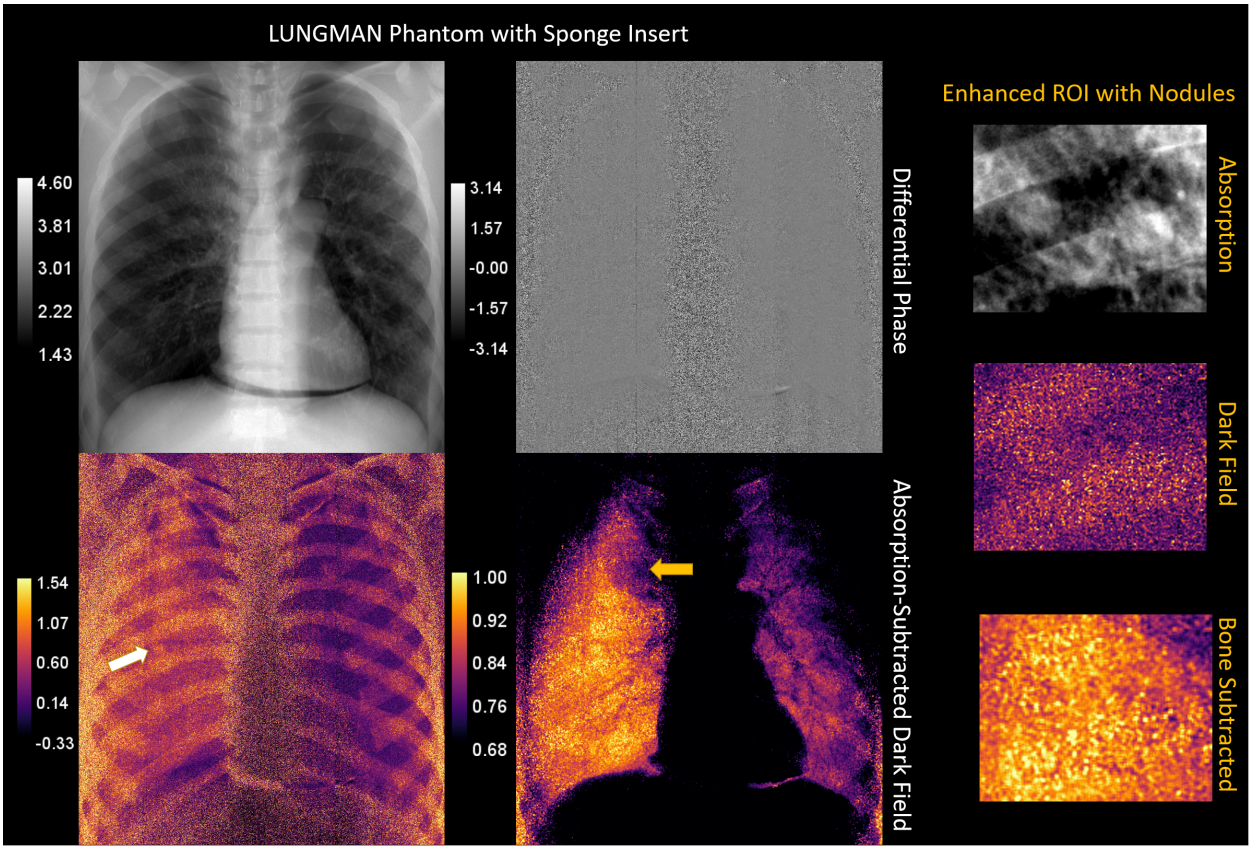

Figure 4.7: (Left) Reference dark field and absorption images of the sponge insert. (Center) Reconstructed absorption, phase, and dark field images of the LUNGMAN phantom with simulated disease models. A bone-subtracted dark field image is also provided, in which one of the pulmonary edema lesions is indicated by the gold arrow. (Right) Enhanced ROIs with the two high-density (100 HU) lung nodules

associated with the ribs, spine, mediastinum and chest wall. This phenomenon is a result of the beam hardening effect. In the beam hardening effect, a reduction of the fringe visibility is not induced by small-angle scattering. Rather, spectral discrepancies between the air and object scan generate a reduction in visibility as the attenuation through the object increases the effective energy of the X-rays.

In addition to beam hardening, it is clear that anthropomorphic phantoms can not sufficiently mimic the microscopic aspects of pulmonary anatomy. Accurate representation of the underlying pulmonary structures is essential to evaluate the potential for dark field imaging to enhance the detection of diseases. The disease models presented in this study provide some insight into the clinical utility of multi-contrast but cannot fully encapsulate the pathophysiological nature of lung diseases. For instance, several important aspects of dark field lung cancer detection could not be investigated through a phantom study. As lung cancer lesions develop, the tissue-to-air ratio of

the affected region decreases, causing an increase in the density homogeneity and reducing the intensity of the dark field signal. In certain types of lung cancer, such as invasive adenocarcinomas and squamous cell carcinomas, the alveolar air spaces may be directly filled, thus extinguishing the dark field signal. Additionally, as lung nodules grow, they displace the underlying pulmonary structures, including the alveoli, leading to a reduction in small-angle scattering events within the affected region. In conclusion, the results of this study have motivated further investigations into the beam hardening effect and more realistic pulmonary models.

4.5 Summary

Ensuring patient safety and achieving high image quality are essential to the successful clinical translation of the novel prototype system developed in this thesis. The dosimetric properties of the system were characterized in this chapter to ensure patient safety and provide a pathway to estimate the relevant radiation quantities. The dose-normalized contrast-to-noise ratio of the dark field and absorption contrast mechanisms was then quantified for different patient sizes to determine the optimal X-ray energies and dose levels that minimize potential risks to the patient while producing the best image quality. To gain a more comprehensive understanding of multi-contrast imaging, the complex relationship between image contrast and noise was discussed in the context of energy, dose, and patient size. These optimized clinical imaging parameters were evaluated in an anthropomorphic phantom imaging study, in which two disease models were assessed. The beam hardening effect and inadequate disease models were identified as the two major challenges that hindered the capacity of the dark field mechanism to generate contrast between diseased and healthy tissues. Therefore, the remainder of this thesis will be focused on addressing these two challenges.

4.6 Absorption and Dark Field Images for all Scan Parameters

The absorption and dark field images of the custom contrast phantom are shown in this section for every tube potential and tube current investigated for the optimization of the clinical imaging parameters. A consistent window and level could not be achieved for all images. As such, all

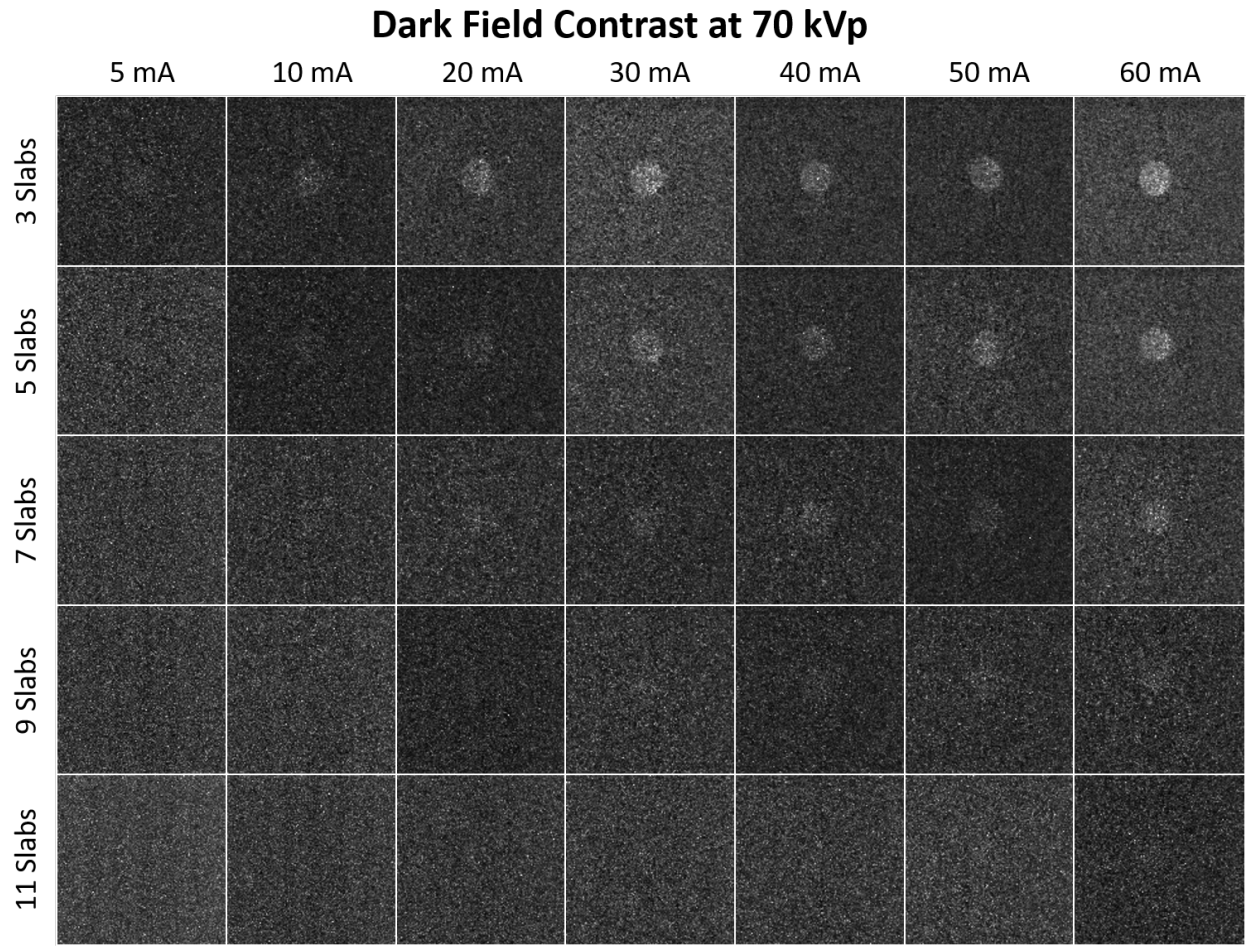

images were normalized such that the maximum pixel value was 1 and the minimum pixel value was 0. Images are then displayed with a window/level of [0.2, 0.8].

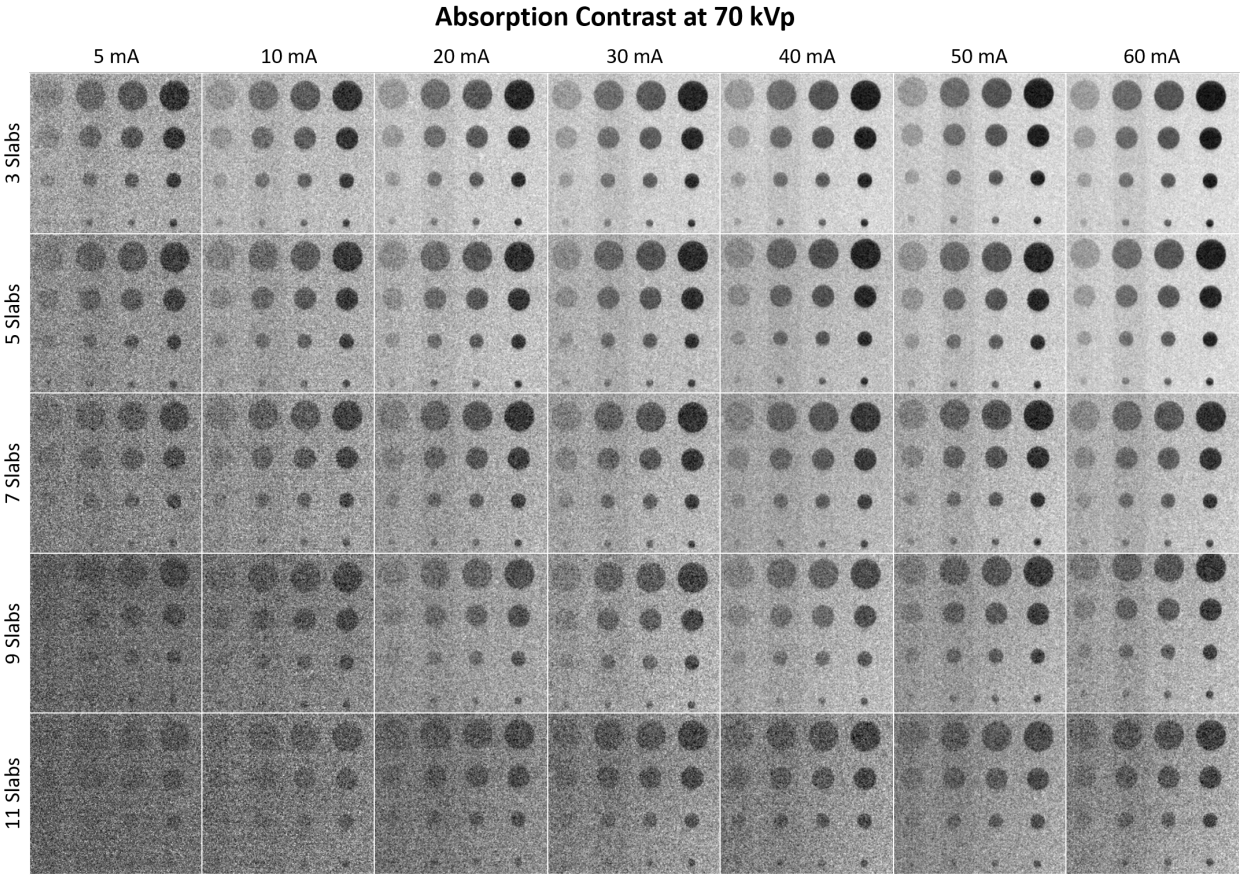
Absorption Contrast at 70 kVp
5 mA
10 mA
20 mA
30 mA
40 mA
50 mA
60 mA
3 Slabs
5 Slabs
7 Slabs
9 Slabs
11 Slabs

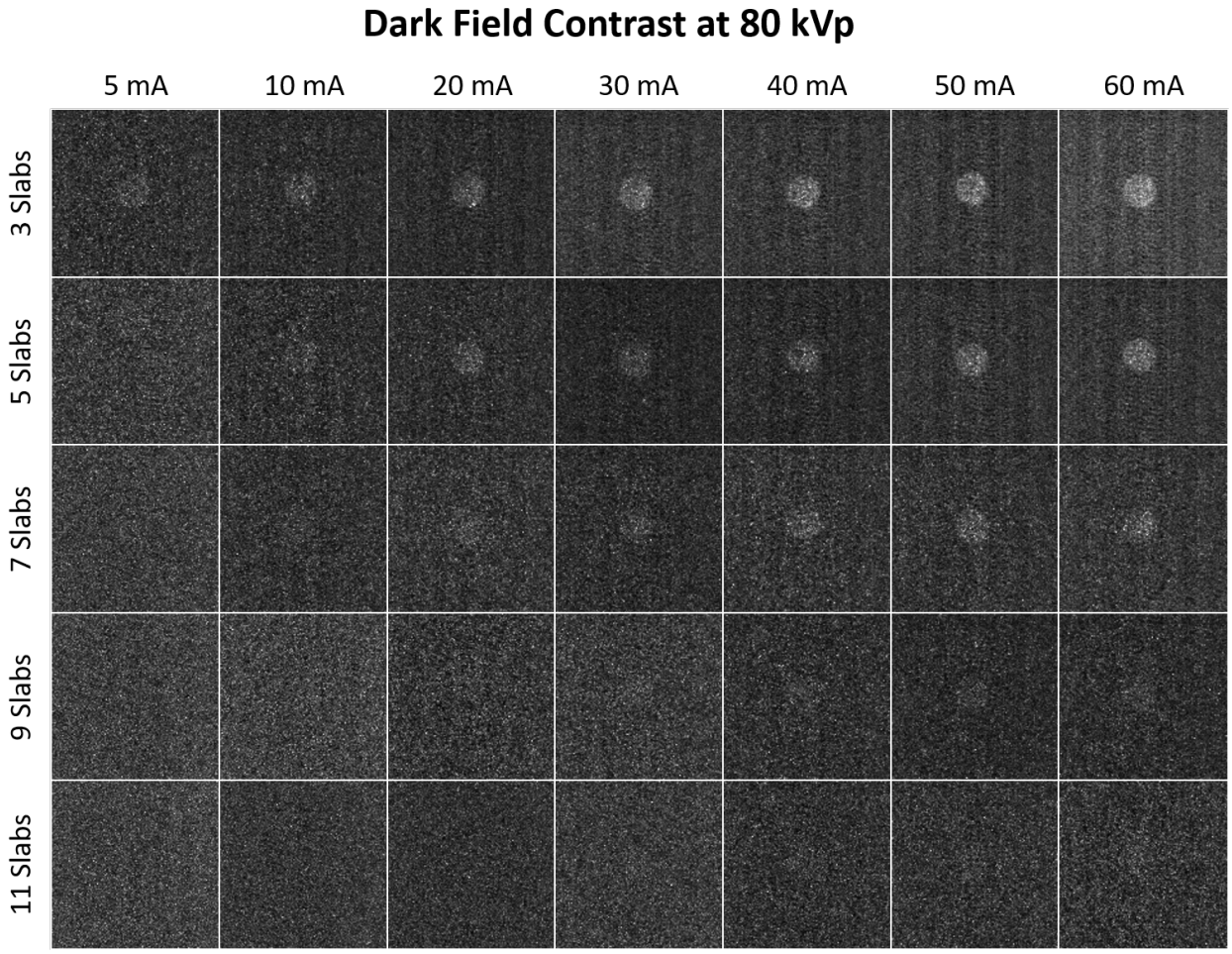
Dark Field Contrast at 80 kVp
5 mA
10 mA
20 mA
30 mA
40 mA
50 mA
60 mA
3 Slabs
5 Slabs
7 Slabs
9 Slabs
11 Slabs

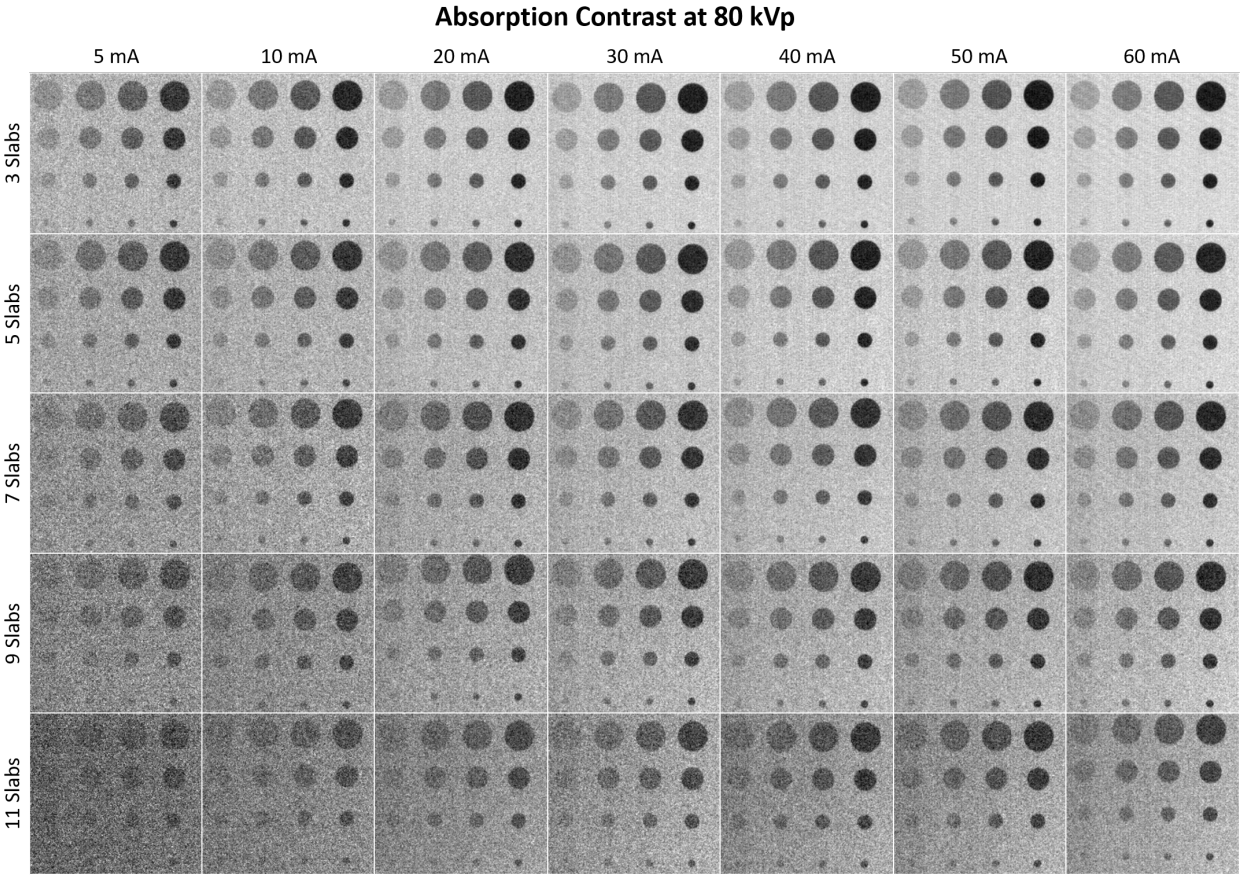
Absorption Contrast at 80 kVp
5 mA
10 mA
20 mA
30 mA
40 mA
50 mA
60 mA
3 Slabs
5 Slabs
7 Slabs
9 Slabs
11 Slabs

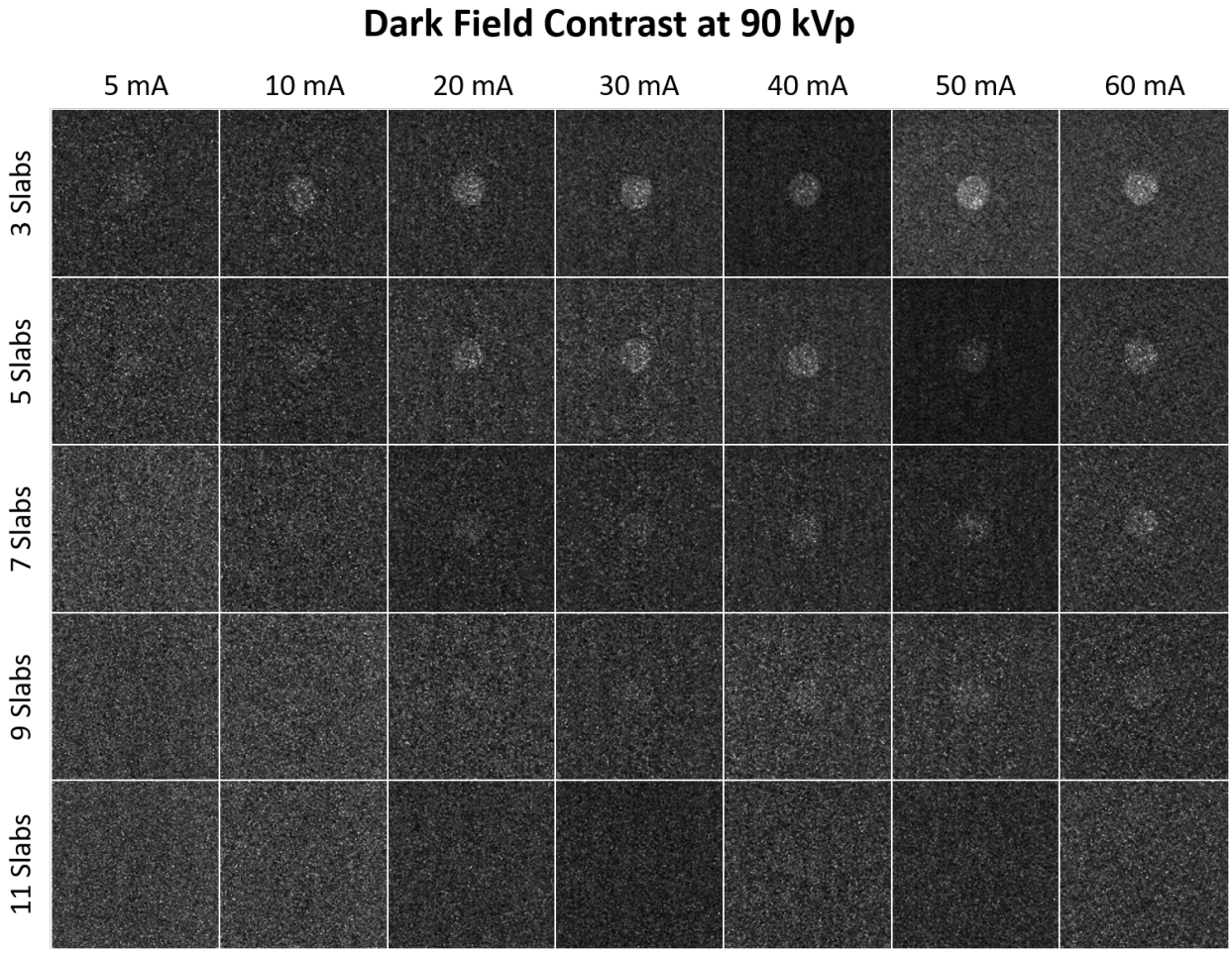
Dark Field Contrast at 90 kVp
5 mA
10 mA
20 mA
30 mA
40 mA
50 mA
60 mA
3 Slabs
5 Slabs
7 Slabs
9 Slabs
11 Slabs

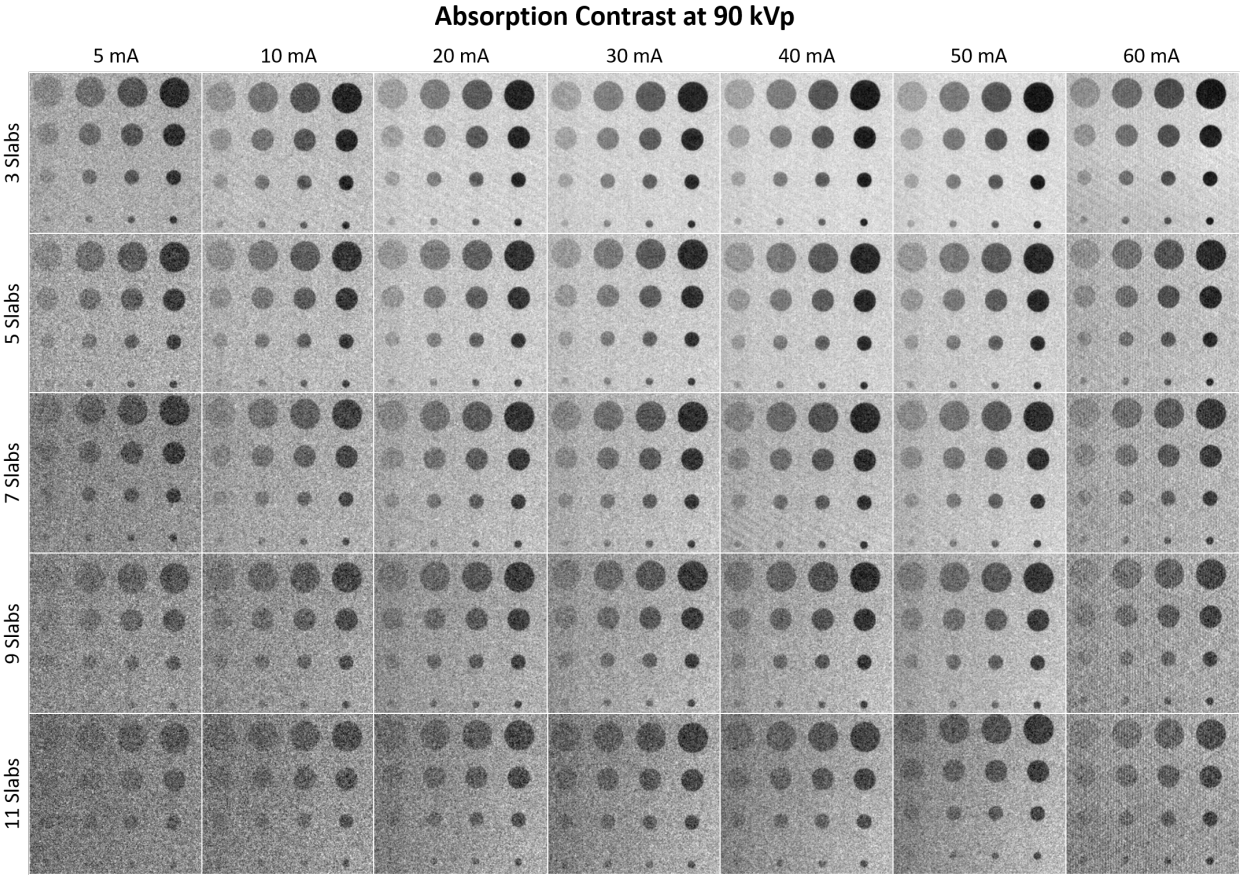
Absorption Contrast at 90 kVp
5 mA
10 mA
20 mA
30 mA
40 mA
50 mA
60 mA
3 Slabs
5 Slabs
7 Slabs
9 Slabs
11 Slabs

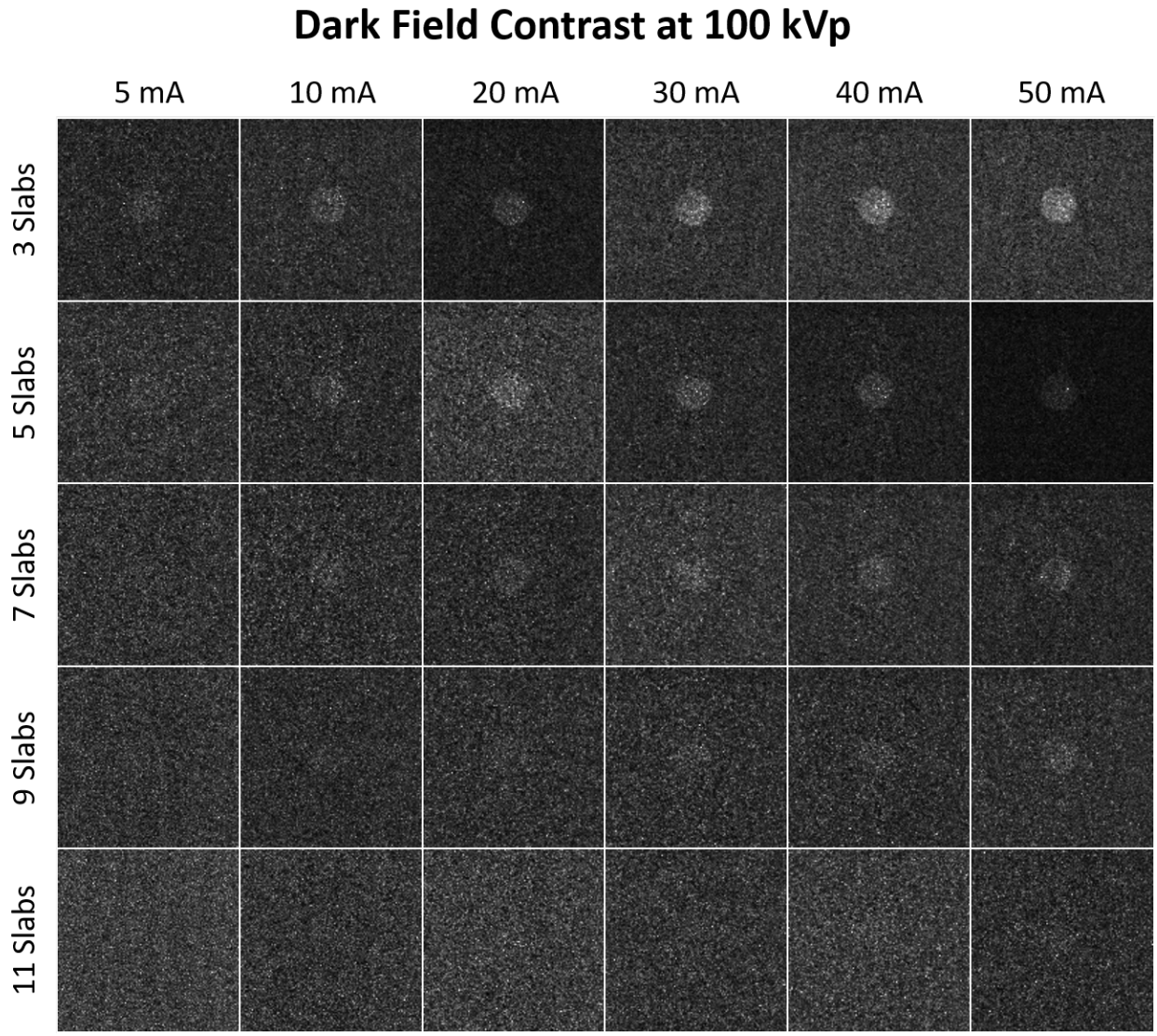
Dark Field Contrast at 100 kVp
5 mA
10 mA
20 mA
30 mA
40 mA
50 mA
3 Slabs
5 Slabs
7 Slabs
9 Slabs
11 Slabs

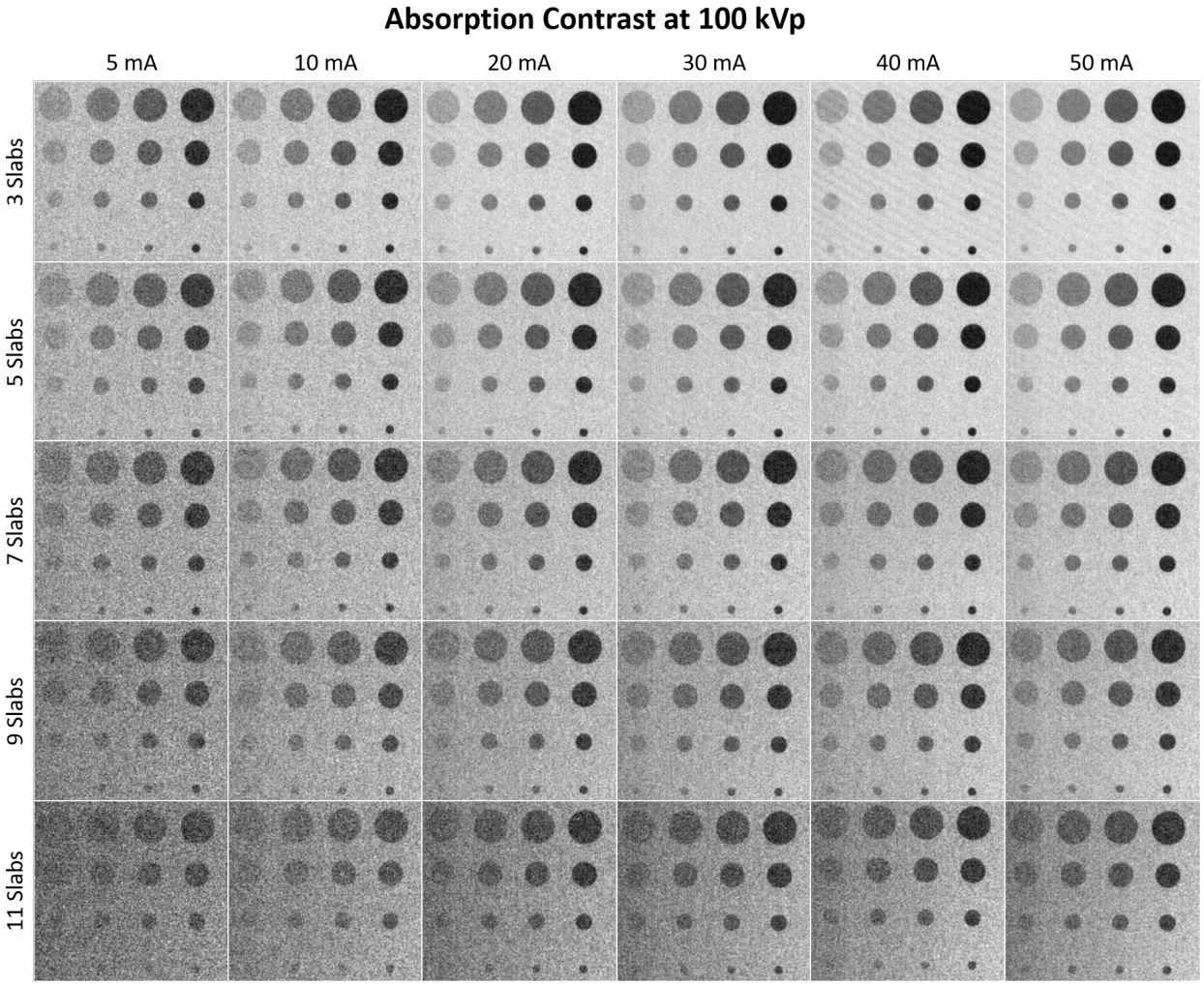
Absorption Contrast at 100 kVp
5 mA
10 mA
20 mA
30 mA
40 mA
50 mA
3 Slabs
5 Slabs
7 Slabs
9 Slabs
11 Slabs

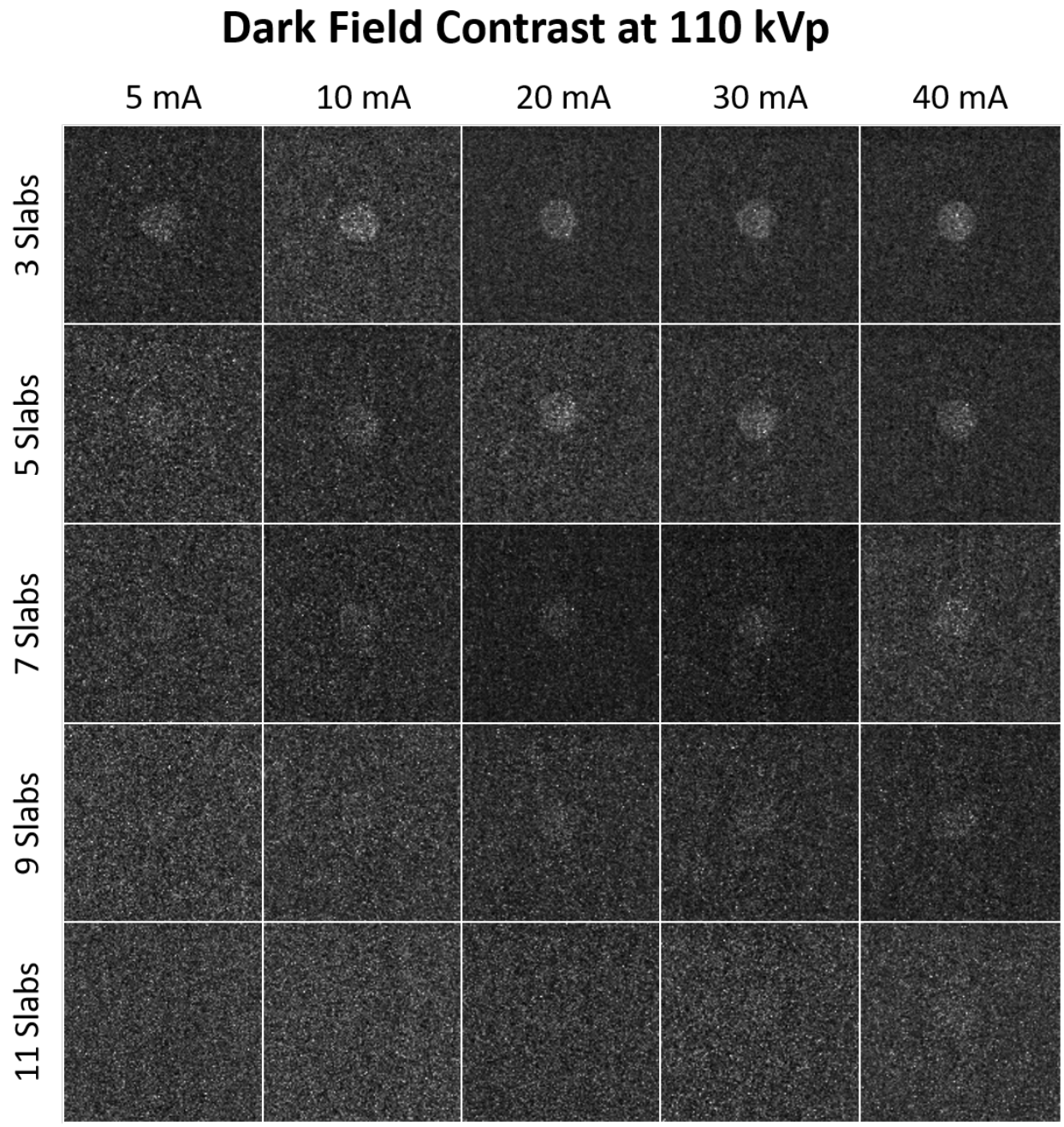
Dark Field Contrast at 110 kVp
5 mA
10 mA
20 mA
30 mA
40 mA
3 Slabs
5 Slabs
7 Slabs
9 Slabs
11 Slabs

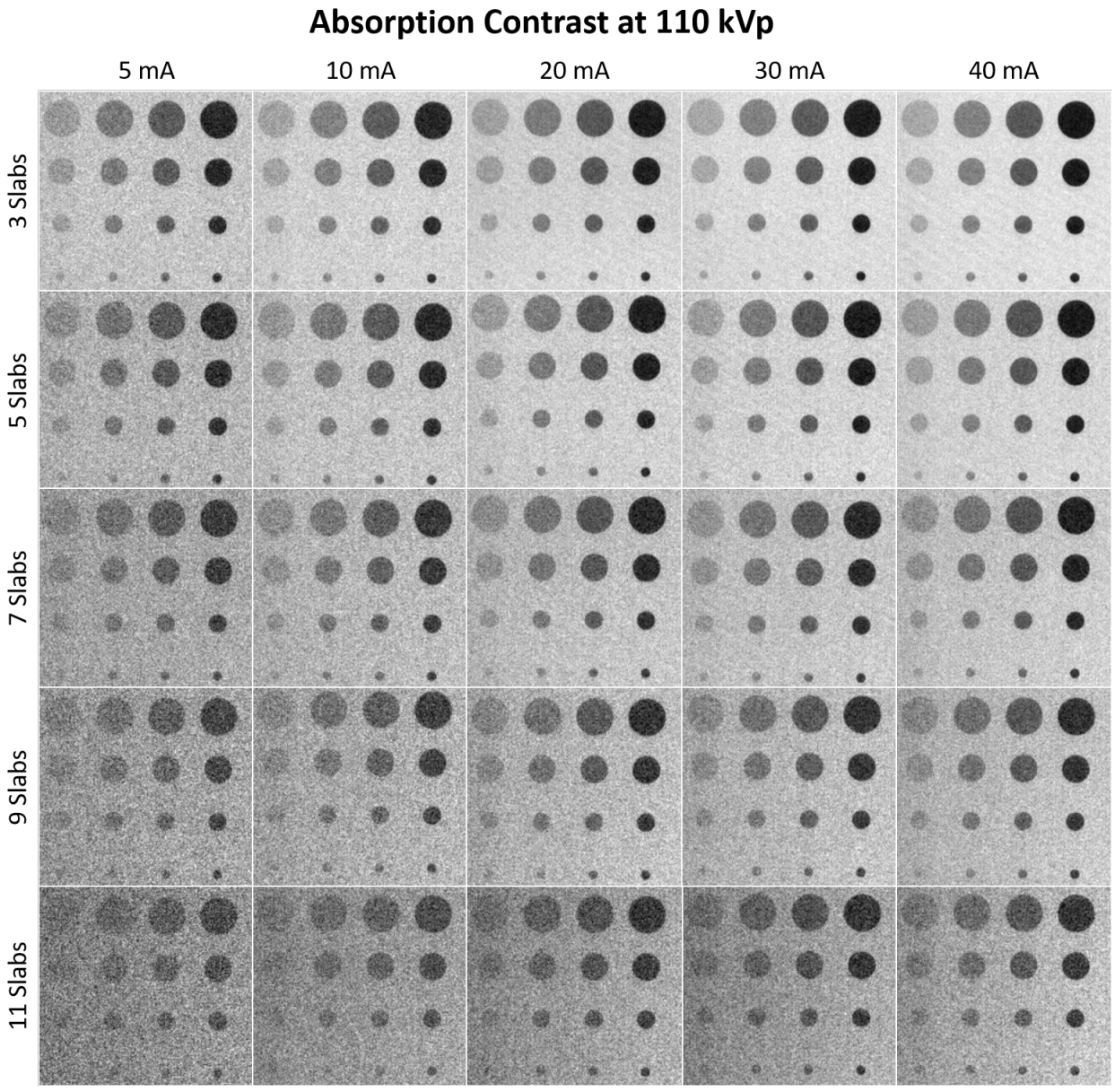
Absorption Contrast at 110 kVp
5 mA
10 mA
20 mA
30 mA
40 mA
3 Slabs
5 Slabs
7 Slabs
9 Slabs
11 Slabs

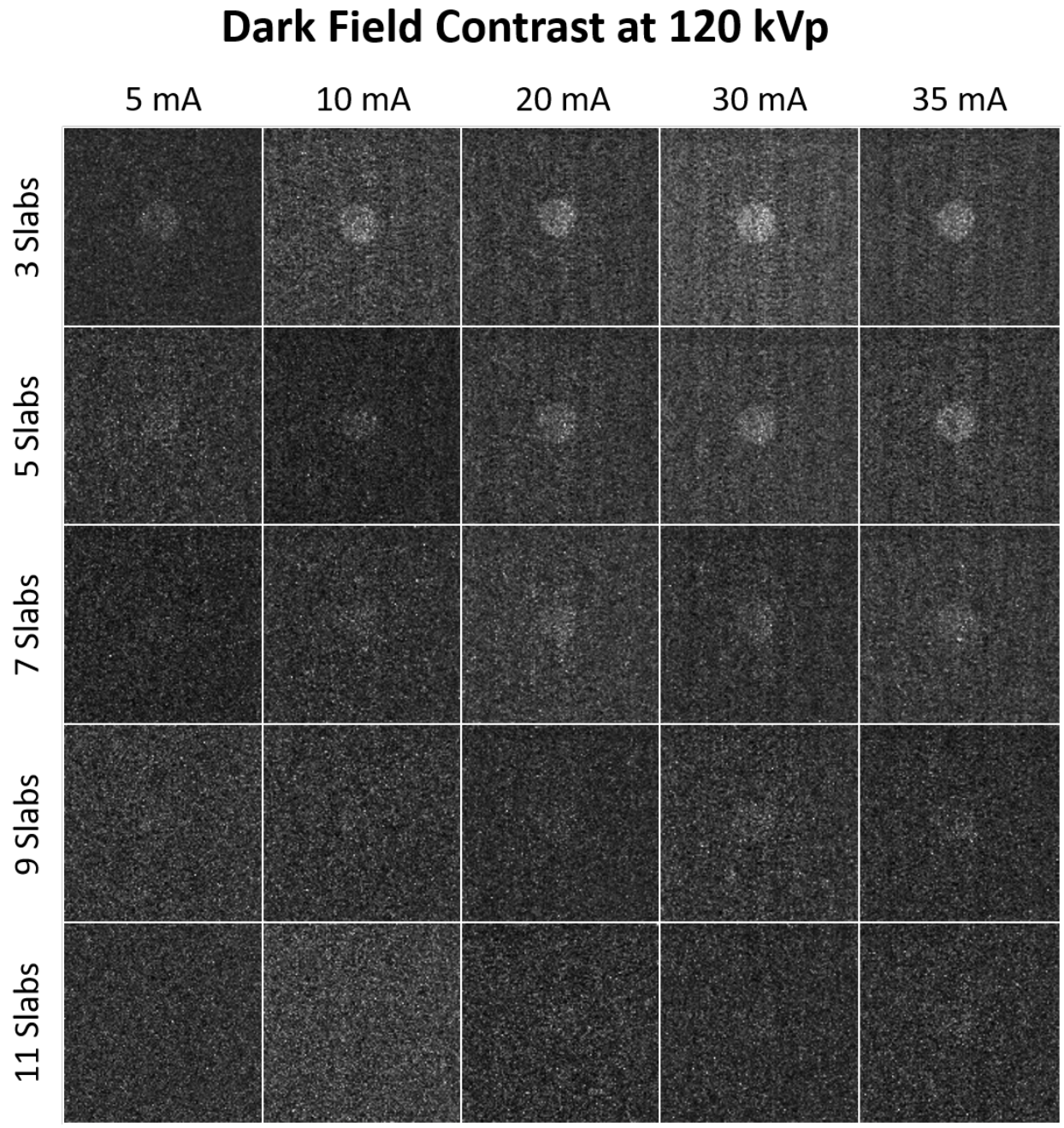
Dark Field Contrast at 120 kVp
5 mA
10 mA
20 mA
30 mA
35 mA
3 Slabs
5 Slabs
7 Slabs
9 Slabs
11 Slabs

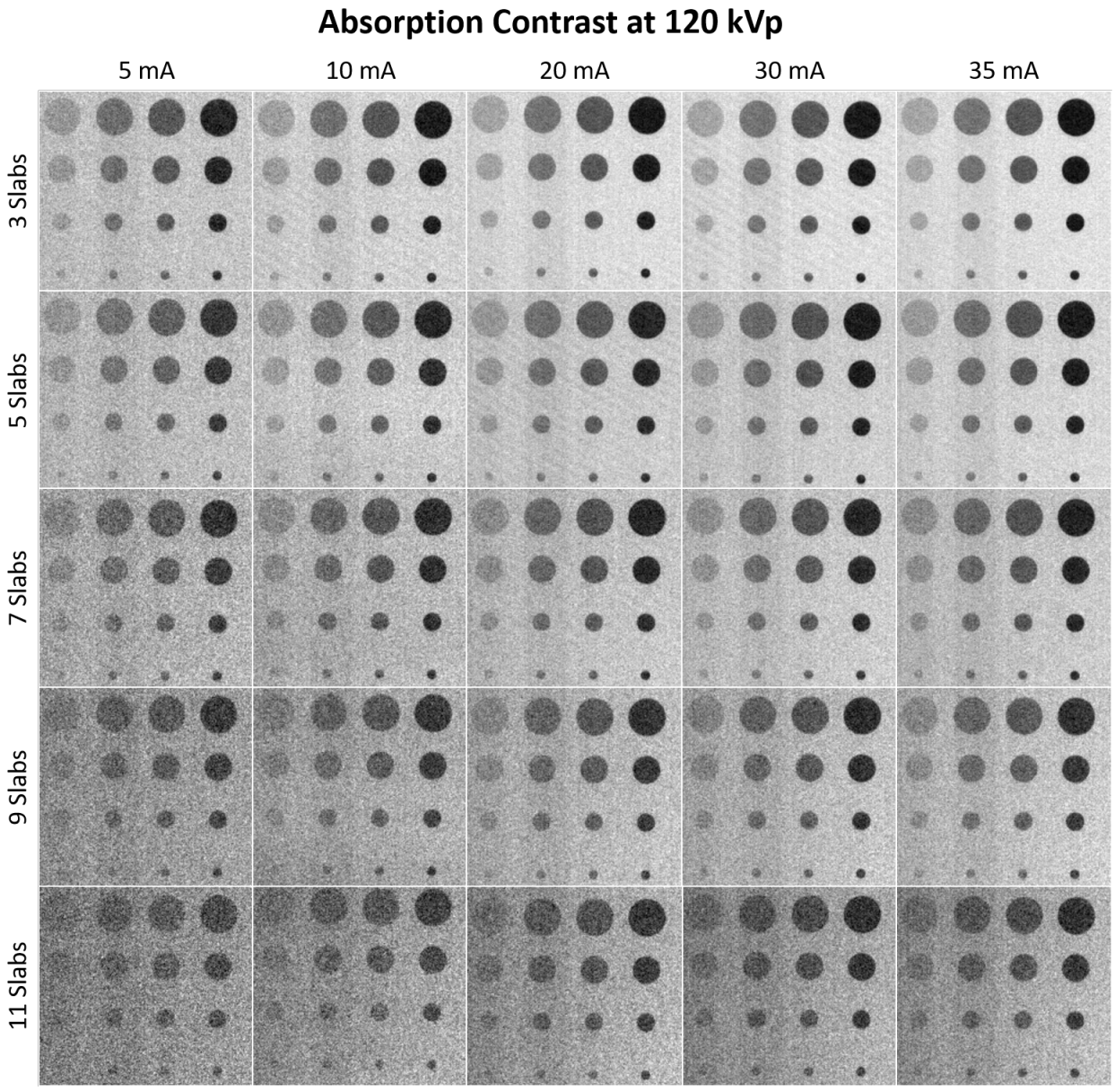
Absorption Contrast at 120 kVp
5 mA
10 mA
20 mA
30 mA
35 mA
3 Slabs
5 Slabs
7 Slabs
9 Slabs
11 Slabs

Chapter 5

The Beam Hardening Effect in X-ray Dark Field Imaging

5.1 Introduction

Motivated by the degradation of the image signal and contrast observed in the anthropomorphic phantom imaging study conducted in Chapter 4, the purpose of this chapter is to provide a more comprehensive investigation into the impact of spectral distortions on the dark field contrast mechanism. The beam hardening effect arises as a result of spectral inconsistencies between the interference patterns generated during the reference air scan and the patient scan. In Chapter 3, the intrinsic relationship between fringe visibility and the effective energy of the X-ray field was shown through the characterization of the interferometric performance at different peak tube potentials. For the energy range investigated, the visibility of the interference pattern was reduced as the effective energy of the X-ray field increased. As a result, the visibility of the detected X-ray spectrum for the object scan will be reduced when compared to the air scan as a result of the hardening of the X-ray spectrum by the image object. Since the dark field signal is a measure of the visibility reduction caused by the object, the reduction in the visibility arising from the change in the effective energy of the detected X-ray spectrum will generate a false or artificial dark field signal to be detected that is independent of any small-angle scattering interactions.

Figure 5.1 demonstrates the artificial dark field signal that is generated by the reduction in fringe visibility from the beam hardening effect for an object with no small-angle scatterers. Multi-contrast images were acquired with different thicknesses of acrylic in the image FOV. Acrylic provides a uniform material that will cause the hardening of the X-ray spectrum without introducing any small-angle scattering interactions. As such, the dark field signal is solely a measure of the spectral

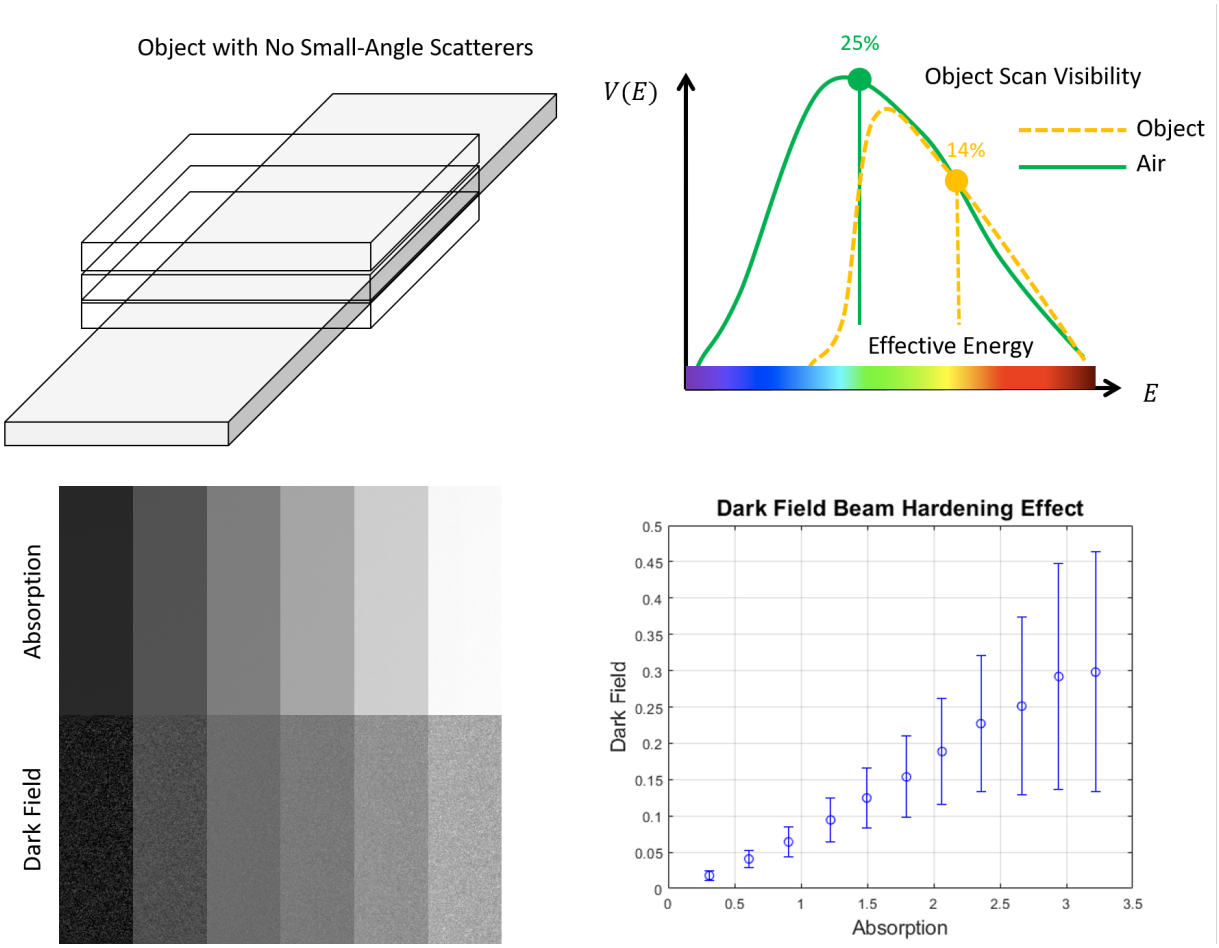

Figure 5.1: Demonstration of the beam hardening effect in X-ray dark field imaging. Discrepancies in the effective energies of the detected X-ray spectrums between the air and patient scans result in the generation of a dark field signal even when small-angle scatterers are not present. The relationship between the spectral component of the dark field signal and the attenuation of the image object is presented in the plot to the bottom right of the figure.

component of the visibility reduction. It can be seen from the plot in Figure 5.1, that the dark field intensity has an approximately linear relationship with the overall attenuation by the acrylic.

The results of this study clearly indicate that the visibility reduction observed in a given imaging exam is composed of two distinct components: a spectral component and a small-angle scattering component. Correcting the spectral component of the dark field signal is essential, as the small-angle scattering component is the only component relevant for diagnostic imaging. This chapter presents two strategies to correct the spectral component of the dark field signal. The first method is a calibration approach, where the spectral component of the dark field signal is modeled as a function of attenuation to restore the true visibility reduction caused by small-angle scattering events. While the calibration method offers a simplified model to correct the beam hardening effect in dark field

imaging, it is incapable of incorporating spectral information into the correction framework due to the energy-integrating nature of flat panel detectors. To address this limitation, the second correction method employs an energy-resolving photon counting detector (PCD).

5.2 Beam Hardening Calibration Correction

5.2.1 Theory and Methods

A model for the measured visibility reduction in the presence of beam hardening is necessary to construct a correction framework. The measured visibility reduction can be modeled as the product of the visibility reduction generated by the spectral and small-angle scattering (SAS) components[201].

$$V^r(T)_{\text{measured}} = V^r_{\text{SAS}} \cdot V^r(T)_{\text{spectral}} \tag{5.1}$$

Here, V^r is the visibility reduction which is the ratio of the air and image object scan visibilities, such that $D = -ln(V^r)$. Furthermore, the measured visibility reduction and the spectral component of the visibility reduction are dependent on the object's transmission function, T, which was defined in Chapter 3 of this thesis. If $V_{\text{spectral}}(T)$ can be determined, then the small-angle scattering component of the visibility reduction can be recovered.

$$V^r_{\text{SAS}} = \frac{V^r(T)_{\text{measured}}}{V^r(T)_{\text{spectral}}} \tag{5.2}$$

In the absence of small-angle scatterers, the measured visibility reduction is directly equal to the spectral component of the visibility reduction, $V^r(T)_{\text{measured}} = V_{\text{spectral}}(T)$, as $V^r_{\text{SAS}} = 1$. Therefore, $V_{\text{spectral}}(T)$ can be measured by imaging an object that is absent of small-angle scatterers at various thicknesses. In this thesis work, a calibration process is performed to empirically determine $V_{\text{spectral}}(T)$ from measurements of the visibility reduction at different thicknesses of acrylic, or polymethyl methacrylate (PMMA), as was done in the Introduction section of this chapter. As mentioned in the Introduction, acrylic does not generate a small-angle scattering

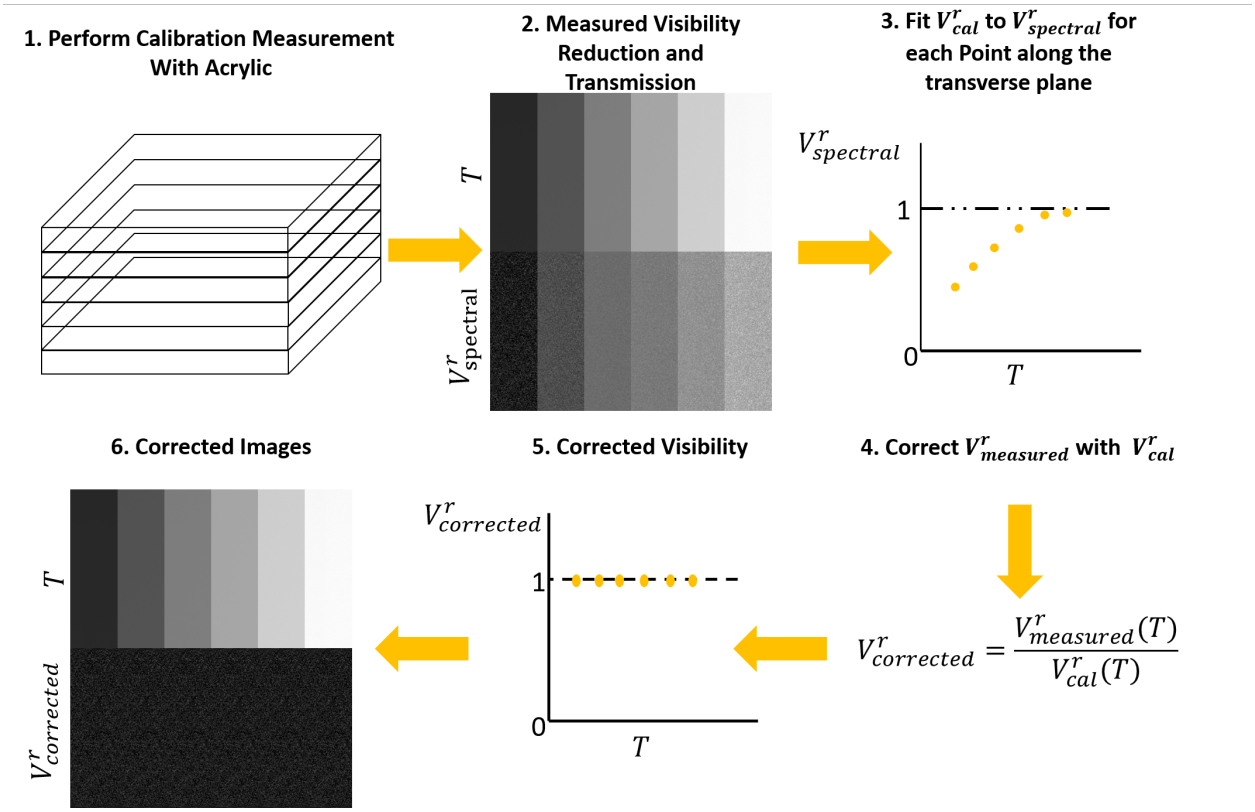

Figure 5.2: Illustration of the calibration beam hardening correction method. Multi-contrast images of acrylic are acquired at different thicknesses to cause hardening of the X-ray beam in the absence of small-angle scattering contrast mechanisms. The measured visibility reduction is then fit with a second-order exponential function for each point along the transverse plane of the interference pattern. The fitting function is then used to correct for the measured visibility reduction caused by spectral effects.

signal. Furthermore, acrylic provides comparable properties to human tissue with respect to X-ray interactions in the diagnostic energy range.

Figure 5.2 illustrates the calibration process employed in this work. Scanning acquisitions were performed at 70 kVp, 60 mA, and a slow scan speed of 9 mm/s. Acquisitions were repeated for acrylic thicknesses ranging from 2.5 cm to 27.5 cm in 2.5 cm intervals. To account for potential discrepancies in the visibility across the transverse direction, measurements of $V_{\text{spectral}}(T)$ and T were made for each image pixel in the FOV and then averaged along the scanning beam direction. To fit the measured values of V_{spectral} as a function of T for each point along the transverse plane of the image field of view (FOV), an exponential fitting function with the following form was employed.

$$V_{\text{cal}}(T) = a \cdot \exp(b \cdot T) + c \cdot \exp(d \cdot T) \tag{5.3}$$

Here, a, b, c, and d are empirically determined fit parameters. Non-linear least squares fitting of Equation 5.3 to $V_{\text{spectral}}(T)$ was carried out to estimate a, b, c, and d for each point along the transverse plane. The corrected visibility reduction was then defined as:

$$V^r_{\text{SAS}} \approxeq V^r_{\text{corrected}} = \frac{V^r(T)_{\text{measured}}}{V^r(T)_{\text{cal}}} \tag{5.4}$$

The beam hardening calibration correction was applied to the dark field images acquired for the optimization of the clinical imaging parameters at 70 kVp and 60 mA in Chapter 4 to evaluate the efficacy of the method. Performance was evaluated by quantifying the correction scheme's impact on noise, contrast, and CNR.

5.2.2 Results

Figure 5.3 shows a comparison of the beam hardening-corrected and uncorrected dark field signal intensity as a function of acrylic absorption. The proposed correction effectively reduces the spectral component of the dark field signal, as demonstrated by the results. The largest residual dark field signal measured was 0.052 ± 0.161 after the beam hardening correction, whereas the uncorrected dark field signal at the same absorption level was measured to be 0.292 ± 0.233. This indicates an 82% decrease in the spectral component of the dark field signal. In addition, Figure 5.3 also shows a demonstration of the measured V_{spectral} as a function of object transmission, along with the exponential fit using Equation 5.3.

Table 5.1 presents the noise standard deviation, dark field contrast, and dark field CNR for the beam hardening corrected and uncorrected images generated from the parameter optimization study in Chapter 4. The results show that the beam hardening correction led to an increase in contrast and CNR across all levels of attenuation, with a greater performance improvement observed at higher levels of attenuation. Furthermore, the noise level was relatively unaffected by the beam hardening correction. This result is unexpected since a division operation is performed in the correction algorithm. However, since the noise magnitude in the dark field image is significantly greater than that in the absorption image, the division operation may not significantly impact the overall noise in the corrected image. It should be noted that the dark field signal contrast is still reduced at high levels of object attenuation. This may be due to statistical bias, which can occur

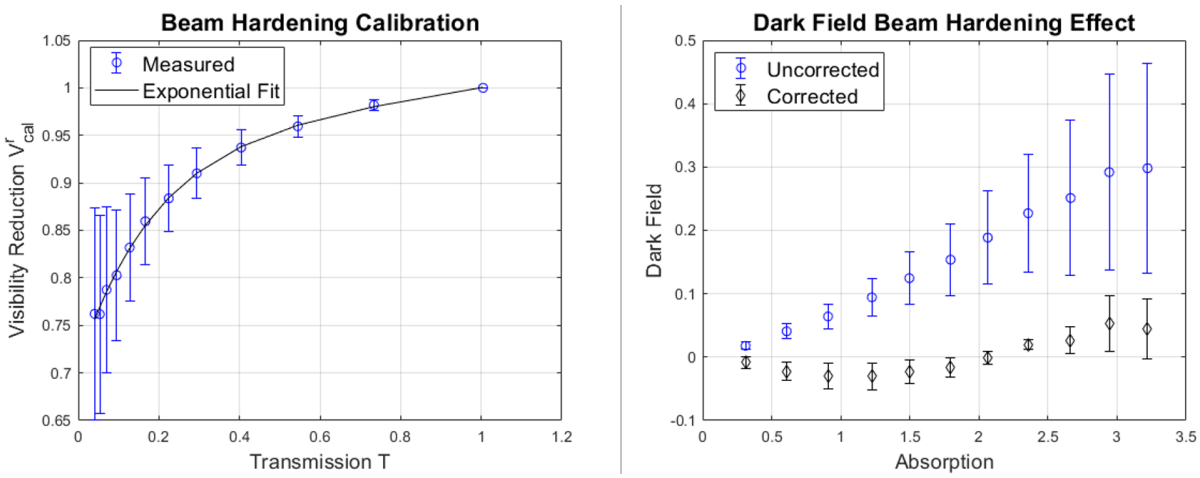

Figure 5.3: (Left) Measured spectral component of the visibility reduction as a function of the object transmission for the entire image FOV with the exponential fitting from Equation 5.3. (Right) Comparison of the beam hardening corrected and uncorrected measured dark field intensity as a function of total attenuation for the acrylic acquisitions. The impact of the spectral component of the dark field signal is significantly reduced when the beam hardening correction is applied.

when the number of X-rays reaching the detector is significantly reduced.

Table 5.1: Beam hardening calibration correction impact on noise, contrast, and CNR

Acrylic Slabs	σ Uncorr.	σ Corr.	Contrast Uncorr.	Contrast Corr.	CNR Uncorr.	CNR Corr
3	0.09	0.09	0.44	0.47	4.64	4.98
4	0.12	0.12	0.39	0.43	3.30	3.64
5	0.14	0.14	0.41	0.45	2.84	3.17
6	0.17	0.17	0.41	0.46	2.35	2.65
7	0.21	0.21	0.36	0.42	1.73	2.02
8	0.26	0.26	0.28	0.34	1.09	1.32
9	0.32	0.32	0.29	0.35	0.91	1.12
10	0.40	0.40	0.19	0.26	0.48	0.65
11	0.48	0.48	0.18	0.25	0.38	0.53
12	0.52	0.53	0	0.07	0	0.14

Although the dark field beam hardening calibration correction was useful in reducing the spectral component of the dark field signal, there are still significant limitations associated with this method. First, this calibration method is only expected to be effective on materials that are similar to the calibration material used. Similar to the effects of beam hardening in CT imaging, the extent of the spectral shift in the X-ray energy is dependent upon the interacting material that is causing the hardening of the beam. For instance, soft tissue and bone will result in significantly different changes in the effective energy for the same level of attenuation. Therefore, the calibration method presented in this work will not sufficiently generalize to all anatomical structures, such as

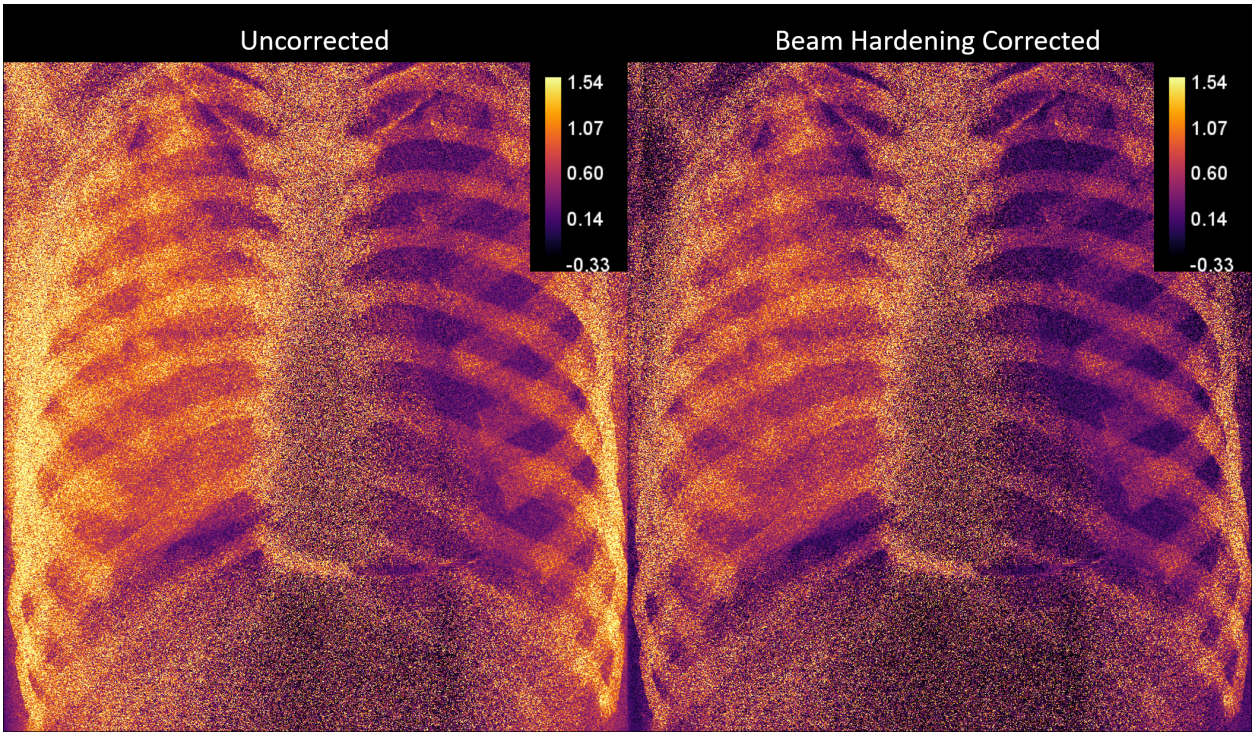

Figure 5.4: Uncorrected and beam hardening corrected dark field images of the LUNGMAN phantom with the custom lung insert at a matching W/L. The calibration correction method successfully reduces the dark field signal associated with the soft tissue components of the LUNGMAN phantom but is incapable of mitigating the dark field signal associated with the osseous structures.

the osseous structures in the chest. To validate this proposition, the beam hardening correction was applied to the LUNGMAN phantom images from Chapter 4. As shown in Figure 5.4, the correction algorithm was incapable of suppressing the dark field signal from the bony structures. However, the dark field signal from the soft tissue components of the LUNGMAN phantom was successfully reduced.

The results of the LUNGMAN study demonstrate the need for a more comprehensive beam hardening correction. The beam hardening correction method does not truly address the spectral inconsistencies caused by the beam hardening effect, but rather calibrates the measured data to some reference scan to reduce the impact of the spectral inconsistencies. In the next section of this chapter, the energy-resolving capabilities of photon counting detectors is leveraged in an attempt to provide a more comprehensive dark field beam hardening correction.

5.3 Photon-Counting Detector Multi-Contrast Imaging

5.3.1 Introduction

Promising results from semi-conductor-based photon counting detectors (PCDs) have sparked interest in the scientific community regarding the potential for PCDs to offer a new paradigm in medical X-ray imaging[202–207]. The underlying design and physical principles governing PCD technology provide inherent advantages when compared to conventional energy-integrating X-ray detectors. Among the prominent attributes that make PCDs alluring for medical imaging are their energy-resolving capabilities, capacity for increased spatial resolution, and improved detective quantum efficiency.

Most modern PCDs are comprised of a semi-conductor sensor material sandwiched between two electrodes, along with a dedicated readout circuit. When a voltage is applied, an electric field is generated across the semi-conductor material. As X-rays interact with the sensor material, they deposit energy that can excite electrons in the valence band, causing them to move to the conduction band and generate free electron-hole pairs. The electrons and holes then travel to their respective electrodes due to the applied electric field, inducing a current pulse in the electrodes. The induced pulse height is proportional to the energy of the interacting X-ray, enabling signals to be distinguished by energy such that detected X-rays can be sorted into different energy bins.

The capacity to select the energy threshold for which X-rays are sorted provides a unique opportunity for multi-contrast X-ray imaging. In theory, a quasi-monochromatic low-energy bin with high visibility and a polychromatic high-energy bin can be created by implementing a narrow low-energy bin and a wide high-energy bin. For instance, a low energy bin of 20-40 keV should theoretically provide the visibility of a 40 kVp spectrum. As demonstrated in Chapter 3, the visibility at 40 kVp is significantly higher than the visibility generated at 70 kVp. However, the 70 kVp or higher spectra must be employed to generate enough transmission through the patient such that image noise is not too substantial.

Although the quasi-monochromatic bin will suffer from poor photon statistics, the high-energy and total-energy bin data will not. Therefore, there is potential to leverage the preferred photon statistics from the high-energy and total-energy bins to improve the photon statistics from the low-energy bin, while still benefiting from the enhanced dark field imaging associated with low-

energy X-rays. Additionally, the use of a quasi-monochromatic low-energy bin has the potential to mitigate the impact of the beam hardening effect. If higher-energy X-rays can be excluded from the low-energy bin image formation, then the reduction in visibility resulting from increases in the effective energy of the X-ray field can be eliminated. As such, material-independent beam hardening corrections could theoretically be made to overcome the challenges associated with the calibration method presented in Section 5.2. Furthermore, the high- and low-energy bins can also be leveraged to perform material decomposition with the absorption images, such that bone-subtracted images can be generated.

In this section, two studies are conducted to investigate the potential for a quasi-monochromatic low-energy bin and a polychromatic high-energy bin to improve multi-contrast imaging performance. The purpose of the first study was to test the hypothesis that a quasi-monochromatic low-energy bin can enable multi-contrast imaging at higher fringe visibilities when compared to the use of the total-energy bin. In the second study, the potential for a quasi-monochromatic low-energy bin to mitigate the impact of beam hardening in dark field imaging was investigated.

5.3.2 Fringe Visibility of Quasi-Monochromatic Low-Energy Bin

5.3.2.1 Methods

The prototype system's flat panel detector was substituted with the XC-Thor photon counting detector from Varex Imaging (Salt Lake City, Utah). The XC-Thor is a cadmium telluride-based (CdTe) detector composed of 1024 $\times$ 512 elements, each measuring 100 μm $\times$ 100 μm in size. Two energy thresholds can be adjusted on the detector, with the low threshold typically set at 24 keV or higher to eliminate electronic noise. It is important to note that the PCD employed in the subsequent studies does not provide sufficient lateral coverage for chest imaging. Therefore, the studies presented in this chapter are meant to serve as a proof-of-concept study.

For the two studies presented in this chapter, the PCD was operated in the anti-coincidence mode. The anti-coincidence mode was implemented by the PCD manufacturer to address the charge-sharing effect, in which a single interacting photon may induce pulses to be counted for more than one detector element. This mode is designed to detect coincident count events within a given detector element, and its adjacent detector elements. For each detected coincident event, the

total induced charges within a given pixel block are assigned to a single detector element.

To benchmark the performance of the quasi-monochromatic low-energy bin, the total-energy (TE) bin fringe visibility was quantified at peak tube potentials ranging from 40 kVp to 120 kVp in 10 kVp step intervals. However, the focus of this study will be on imaging with the 70 and 120 kVp spectra. The quantification of the visibility was performed through a phase-stepping acquisition with only the patient table in the FOV. The overall intensity $I_0(x, y)$ and the amplitude of the fringes $I_1(x, y)$ were calculated for each pixel. The visibility was then reported as the mean of the visibility across the entire grating FOV.

After establishing a baseline reference using the total-energy bin, the next step was to determine the optimal energy thresholds for the quasi-monochromatic low-energy bin acquisition scheme. To accomplish this task, two energy threshold methods were investigated:

- **Fixed Low Threshold, Low-Energy (LE) Bin:** In this method, the low energy threshold remains fixed at 24 keV, while the high energy threshold is varied from 29-69 for the 70 kVp acquisitions and 29-117 keV for the 120 kVp acquisitions in 5-11 keV step intervals. This method allows for the direct investigation of the impact of higher-energy X-rays as the energy window width is increased. Throughout this thesis, this method will be referred to as the fixed low threshold scheme.

- **Variable Low Threshold, Low-Energy (LE) Bin:** In this method, both the low energy threshold and high energy threshold are varied from 24-69 for the 70 kVp acquisitions and 24-117 keV for the 120 kVp acquisitions, while maintaining an energy window width between 5-11 keV. This method may be preferable for mitigating the beam hardening effect due to the consistent use of a narrow energy window. Throughout this thesis, this method will be referred to as the variable low threshold scheme.

The visibility of the low-energy bin with a 70 kVp spectrum was quantified for a total of 7 fixed low threshold acquisitions and 7 variable low threshold acquisitions. Similarly, a total of 12 fixed low threshold acquisitions and 12 variable low threshold acquisitions were employed for the 120 kVp spectrum.

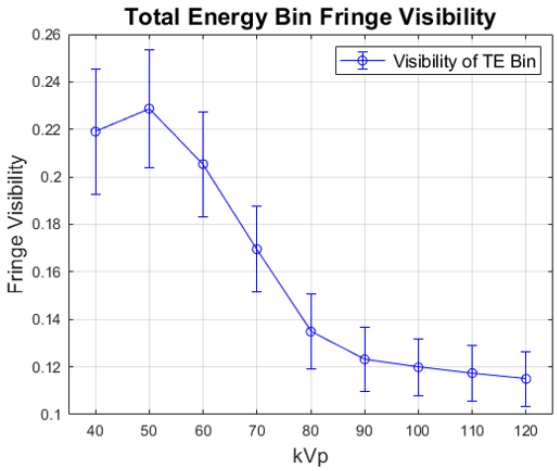

Figure 5.5: Measured fringe visibility for the total-energy bin across each peak tube potential from 40 kVp to 120 kVp.

5.3.2.2 Results

The measured total-energy bin visibility for each peak tube potential is plotted in Figure 5.5. At 70 and 120 kVp, the total-energy bin visibility across the FOV was measured to be 17% $\pm$ 2% and 11% $\pm$ 2%.

The measured visibility for each fixed and variable low threshold acquisition at 70 and 120 kVp are plotted in Figure 5.6. The highest measured visibility for the 70 kVp spectrum was 17% $\pm$ 2% at the 24-29 keV threshold for both acquisition schemes. This result matches the visibility of the total energy bin. All other energy thresholds either matched or had worse performance when compared to the total-energy bin visibility. For the fixed low threshold acquisitions, the visibility remained relatively unchanged as the energy window width was increased and the TE visibility was well within the error bars for each measurement. However, as expected, the measured visibility decreased for the 70 kVp variable low threshold acquisition scheme as the narrow energy window was pushed to higher energies. This further confirms the idea that the high visibility information is carried by lower energy X-rays.

Similar results were demonstrated for the 120 kVp spectrum. The total-energy bin visibility was also within the error bars for all fixed low threshold visibility measurements. In contrast to the results obtained at 70 kVp, an increasing trend in the variable low energy results at a high energy window was exhibited. Potential explanations for this phenomenon include statistical bias of the visibility or that the uncertainty associated with the measurements at higher energy windows is too

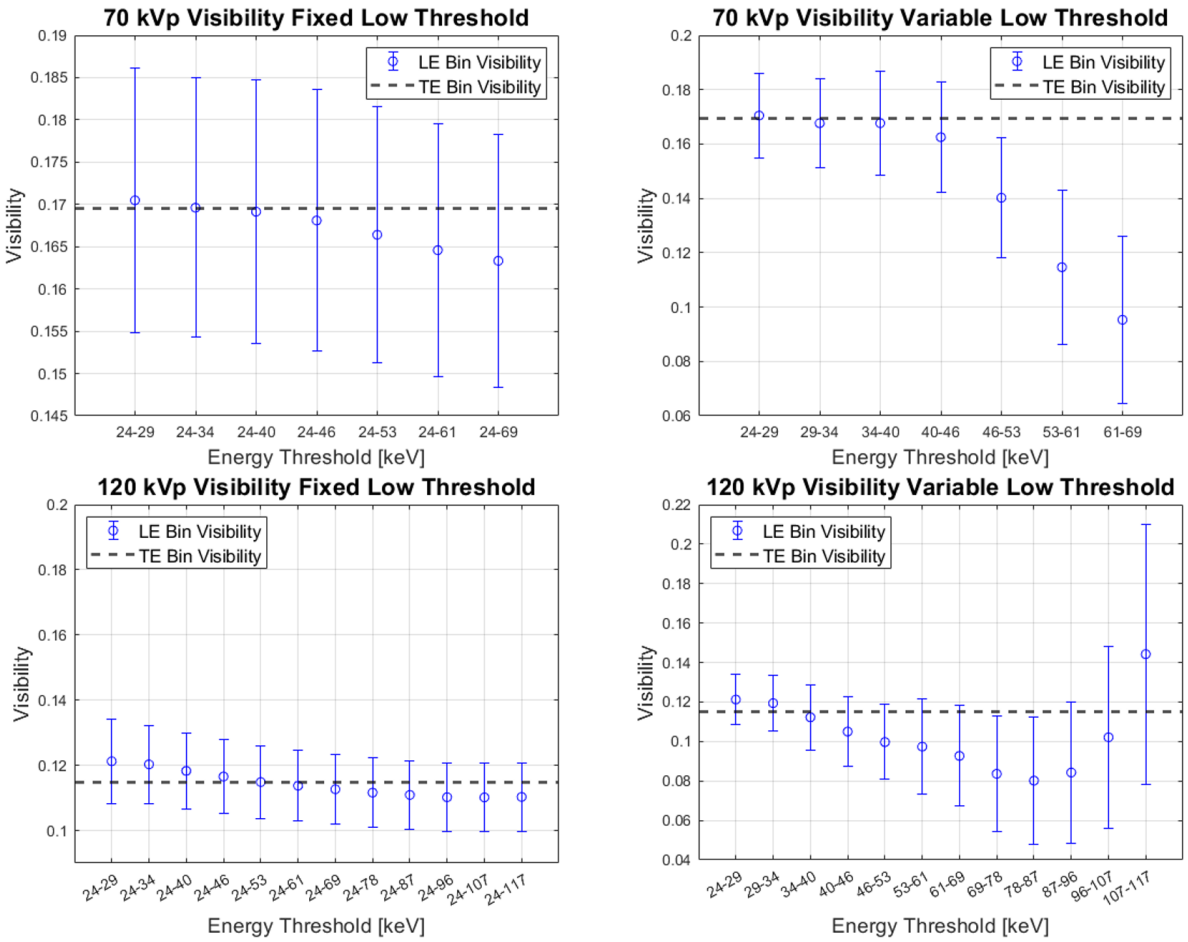

Figure 5.6: Fringe visibility for each fixed and variable low threshold, low-energy bin at 70 and 120 kVp. The measured total-energy bin visibility is plotted as the dashed black line.

large to draw conclusions regarding the trends in the visibility.

In summary, the use of a quasi-monochromatic low-energy bin did not demonstrate a significant improvement in the measured fringe visibility. One potential explanation for the lack of improvement in visibility is that higher energy X-rays are contributing to the lower energy bin counts as a result of the poor energy resolution of the detector. Furthermore, spectral distortions arising from the charge-sharing effect or Compton scattering may also impact the measured visibility even with the use of the anti-coincidence mode. Discrepancies between the total energy bin visibility and the energy threshold of 24-69 keV, which should be equivalent to the total energy bin, may also be the result of the poor energy resolution of the PCD or poor calibration of the PCD energy thresholds. These concepts will be further evaluated in the beam hardening study presented in the next section.

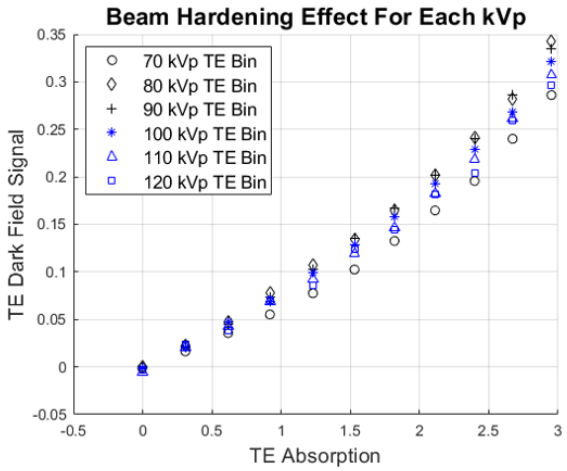

Figure 5.7: Plot of the dark field signal intensity as a function of acrylic absorption for peak tube potentials ranging from 70 kVp to 120 kVp. The energy of the X-rays has a negligible impact on the intensity of the spectral component of the dark field signal.

5.3.3 Beam Hardening Correction with a Quasi-Monochromatic Low-Energy Bin

5.3.3.1 Methods

Although the visibility of the multi-contrast images could not be improved, there is still potential for the quasi-monochromatic low-energy bin to mitigate the impact of the beam hardening effect. To evaluate this potential, multi-contrast images were acquired with various simulated patient thicknesses and a dark field contrast-generating object in the imaging field, following the methodology used in Section 4.3. In this experiment, a cylindrical phantom filled with cotton was used as the image object. The acquisitions were repeated at 70 kVp and 120 kVp for each of the quasi-monoenergetic low-energy bin energy thresholding schemes introduced in the previous section and for 0, 5, and 10 acrylic slabs (2.5 cm thick).

To quantify the effectiveness of the quasi-monochromatic low-energy bin, the dark field background signal intensity was measured and compared it to the total energy bin background intensity. These measures of background intensity directly relate to the extent of spectral distortion induced by beam hardening. Additionally, the contrast and CNR of the cylindrical cotton phantom were measured.

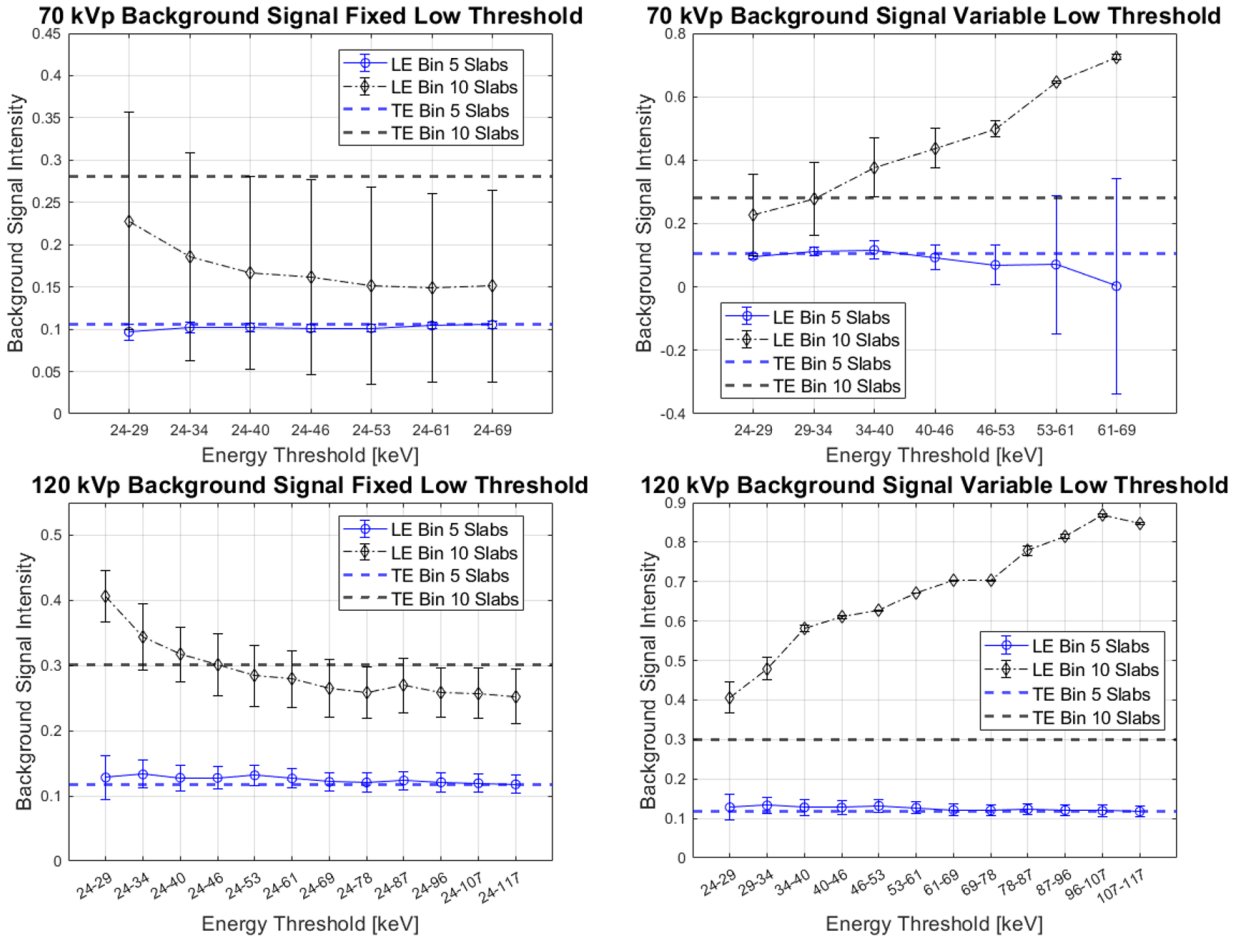

Figure 5.8: Each sub-plot presents the quantification of the background dark field signal intensity in the quasi-monochromatic low energy bins for 5 and 10 acrylic slabs. The top row of the figure displays the results for the 70 kVp spectrum with the fixed (left) and variable (right) low threshold acquisition schemes. The bottom row presents the results from the 120 kVp acquisition.

5.3.4 Results

The plot in Figure 5.7 displays the measured total-energy bin dark field signal intensity as a function of acrylic attenuation. The relationship between the spectral component of the dark field signal demonstrates an approximately linear correlation with acrylic attenuation. Moreover, the energy does not seem to have a notable impact on the manifestation of the beam hardening effect within the diagnostic energy range.

The first quantitative measure of interest for the quasi-monochromatic low-energy bin dark field images was the background signal intensity. Figure 5.8 displays the background dark field signal for each investigated energy thresholding scheme and for simulated patient thicknesses of 5 and 10 acrylic slabs. For reference, the total energy bin background signal intensity is also plotted.

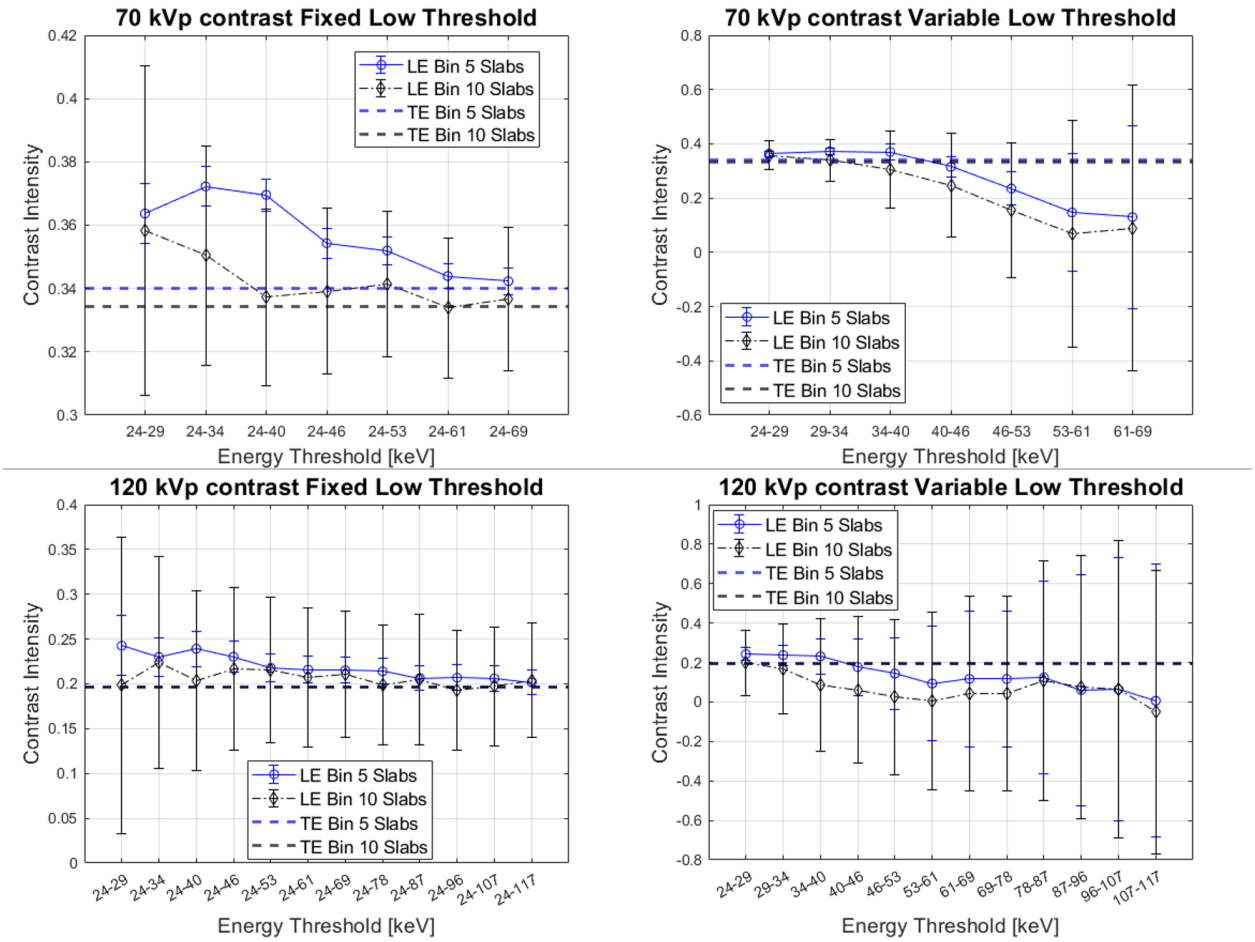

Figure 5.9: Dark field contrast of the cotton phantom in the quasi-monochromatic low energy bins for 5 and 10 acrylic slabs. The top row of the figure displays the results for the 70 kVp spectrum with the fixed (left) and variable (right) low threshold acquisition schemes. The bottom row presents the results from the 120 kVp acquisition.

Ideally, the background signal would be close to zero if the low-energy bin is quasi-monoenergetic. However, the results do not demonstrate this.

For the case of 5 PMMA slabs, the background signal remains relatively unchanged compared to the total-energy bin background signal for both peak tube potentials and all energy thresholds. When a fixed low energy threshold was used, there was some reduction in the background signal for a simulated patient thickness of 10 acrylic slabs, compared to the total energy bin. However, the background signal still remained high (>0.15). On the other hand, the variable low energy threshold with a narrow energy bin showed an increase in background signal for energy bins with higher energies than the 29-34 keV and a simulated patient thickness of 10 acrylic slabs.

Figures 5.9 and 5.10 display plots of the dark field contrast and CNR of the cotton phantom.

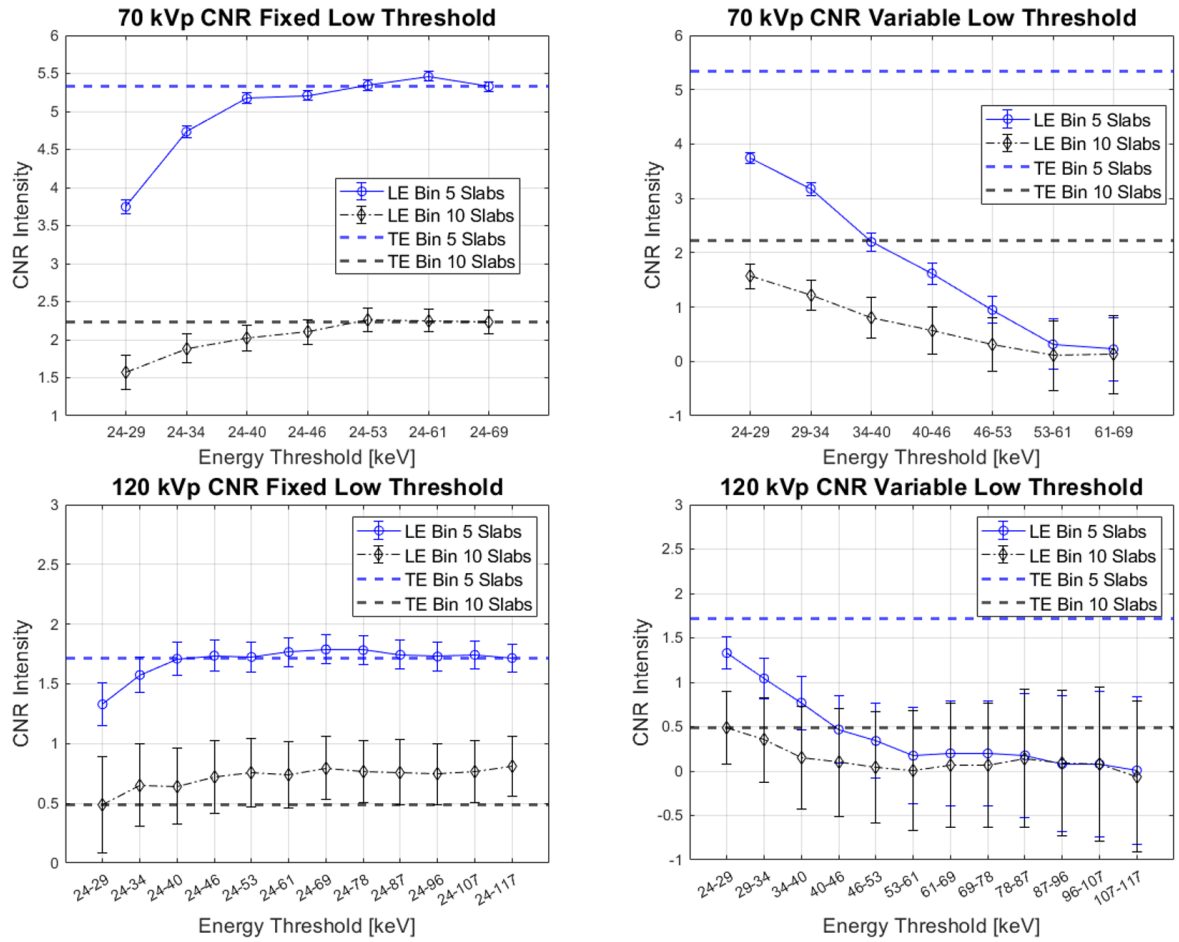

Figure 5.10: Quantification of the CNR for the cotton phantom in the quasi-monochromatic low energy bins for 5 and 10 acrylic slabs. The top row of the figure displays the results for the 70 kVp spectrum with the fixed (left) and variable (right) low threshold acquisition schemes. The bottom row presents the results from the 120 kVp acquisition.

The fixed low threshold quasi-monoenergetic bin demonstrated an improvement in the dark field contrast for both spectra investigated. The contrast increase was most significant for the case of 5 acrylic slabs and at lower energy bins. Conversely, the variable low threshold acquisition scheme led to a considerable reduction in the dark field signal contrast at higher energy bins, consistent with our understanding of the relationship between dark field contrast and X-ray energy.

Regarding CNR, wider energy bins showed better performance, achieving CNRs comparable or slightly greater than those of the total-energy bin. However, narrow energy bins, such as those used in the variable low energy threshold acquisition scheme, resulted in significant degradation of the CNR when compared to the total-energy bin. This degradation is partially due to a decrease in image contrast and the considerable noise associated with narrow energy bins.

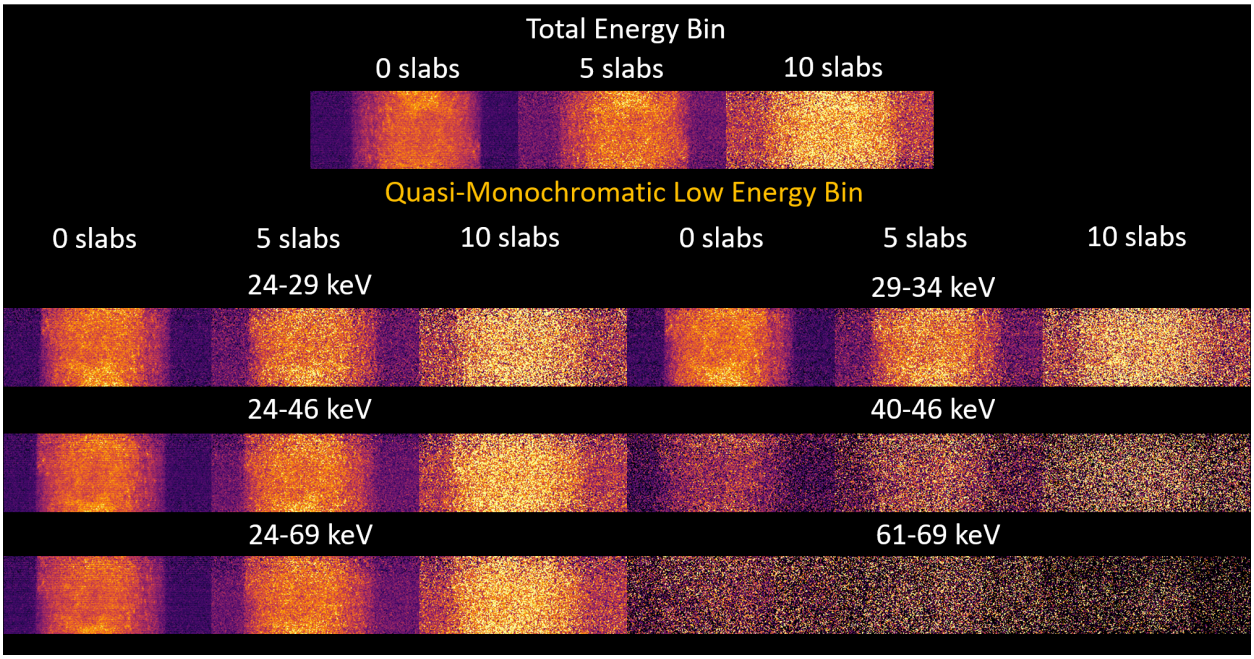

Figure 5.11: Dark field images of the cylindrical cotton phantom with 5 and 10 acrylic slabs placed in the beam path. The top row shows the acquired total energy bin images of the cotton phantom at each attenuation level. The remainder of the presented images are of the quasi-monochromatic low-energy bin with various energy thresholds.

Sample dark field images of the cylindrical cotton phantom are provided in Figure 5.11. Qualitative assessment of the generated dark field images further validates the inability of the proposed quasi-monochromatic low-energy bin scheme to address the beam hardening issue.

The results of the two studies conducted in this section make it evident that the PCD employed in this work does not provide sufficient energy-resolving capabilities to enable a quasi-monochromatic low-energy bin. The contamination of the low-energy bin with high energy X-rays negates the hypothesized benefits of PCDs for multi-contrast imaging. Despite marginal improvements when compared to the total-energy bin, the background signal associated with the spectral component of the dark field signal could not be substantially reduced with the energy thresholds investigated. In comparison, the calibration method outlined in Section 5.2 outperformed the quasi-monochromatic low-energy bin correction scheme. Although the same calibration can be applied to the PCD dark field images, the challenge of correcting for more than a single material is still present. Given the high cost associated with PCDs, the flat panel detector remains the preferred detector for the prototype system.

5.4 Summary

This chapter delved into the impact of the beam-hardening effect in dark field imaging and explored various remedies for its mitigation. An in-depth discussion on the origin and manifestation of the beam hardening effect was presented. A theoretical model for the spectral component of the visibility reduction was then introduced to create a beam hardening calibration correction method. The calibration method was proven highly effective in reducing the spectral component of the dark field signal for soft-tissue equivalent materials. However, the major limitation of the calibration method was realized when the correction was applied to non-soft-tissue materials, such as the osseous structures of an anthropomorphic phantom. To address this limitation, a photon counting detector was introduced to the prototype system. Spectral PCD imaging was extensively studied with the goal of creating a quasi-monoenergtic low-energy bin that would be free of the impact of beam hardening. However, the results of the investigations indicated that the PCD could not provide sufficient spectral imaging to warrant the detector's added cost to the prototype system. Overall, the findings of this chapter contribute to our understanding of the complexities involved in addressing the beam-hardening effect in X-ray dark field imaging.

Chapter *6*

In-Vivo and *Ex-Vivo* Animal Imaging

6.1 Introduction

The alveolar-air interface plays an essential role in the clinical potential of X-ray dark field imaging. While anthropomorphic phantoms are useful in optimizing and testing clinical imaging systems, they fail to sufficiently model the microstructure of the lungs. Thus, more comprehensive models are necessary to assess the clinical viability of the multi-contrast prototype system developed in this thesis.

Animal imaging trials have long served an important role in the field of medical imaging. Large animal models offer the closest approximation to clinical imaging scenarios due to their anatomical and physiological similarities to human subjects. Crucially, animal imaging models offer the alveolar-air interface required to test the clinical potential of the dark field contrast mechanism. This chapter presents a series of *ex-vivo* and *in-vivo* large animal imaging trials conducted to test the clinical utility of the multi-contrast prototype system developed in this thesis.

Two *ex-vivo* animal imaging studies will be presented in this chapter. The rationale for conducting *ex-vivo* imaging studies is that they provide a controlled environment to isolate multi-contrast image signals, without the influence of confounding factors. In the first study, the dark field image signal of healthy lungs was characterized at various dose levels and in the presence of different levels of beam hardening. Following this characterization, a lung cancer disease model was studied to evaluate the potential for multi-contrast imaging to enhance the detection of pulmonary abnormalities. Finally, a preliminary *in-vivo* swine study was conducted. These studies aim to provide a more comprehensive understanding of the system's performance and limitations in the context of clinical

imaging scenarios.

6.2 *Ex-Vivo* Swine Lung Study: Analysis of Dark Field Signal in Healthy Lungs

There were several purposes for conducting the studies presented in this section. The first major goal was to characterize how the dark field signal of healthy lungs changes with dose level and to determine the impact of noise and statistical bias. The next goal of this section was to characterize the impact of the beam hardening effect on the dark field signal of healthy lungs. The final objective of the studies conducted in this section was to evaluate the beam hardening calibration correction introduced in Chapter 4 on more realistic dark field signals.

6.2.1 Methods

A set of *Ex-vivo* swine lungs with the heart and trachea attached, were obtained from the Cardiovascular Physiology Core Facility at the University of Wisconsin-Madison. Approval from the University of Wisconsin-Madison Research Animal Resources Center (RARC) was not required as the swine subject had been euthanized for a different research study. Upon receiving the specimen, a baseline multi-contrast imaging was performed at a high effective dose of 0.234 mSv to determine the mean dark field intensity for each lung. The lungs remained in the resting, or deflated state, for all imaging studies conducted in this section.

The first study evaluated the dark field image signal of the healthy lungs at different dose levels. Scanning acquisitions were performed at 70 kVp with a table translation speed of 9 mm/s. The tube current was varied from 5 (0.0195 mSv) to 60 mA (0.234 mSv). An estimate of the image noise was obtained by measuring the standard deviation of the dark field signal in a uniform region of the heart for each acquisition. The mean dark field signal of the healthy lungs was also quantified at each dose level to test for potential statistical bias.

Subsequently, a second imaging series was conducted to evaluate the impact of beam hardening on the dark field signal. Acrylic thicknesses ranging from 0 cm to 15 cm were placed above the lungs to simulate patients of varying thickness, while all other imaging parameters were set to match the reference baseline multi-contrast acquisition. Dark field images were reconstructed with

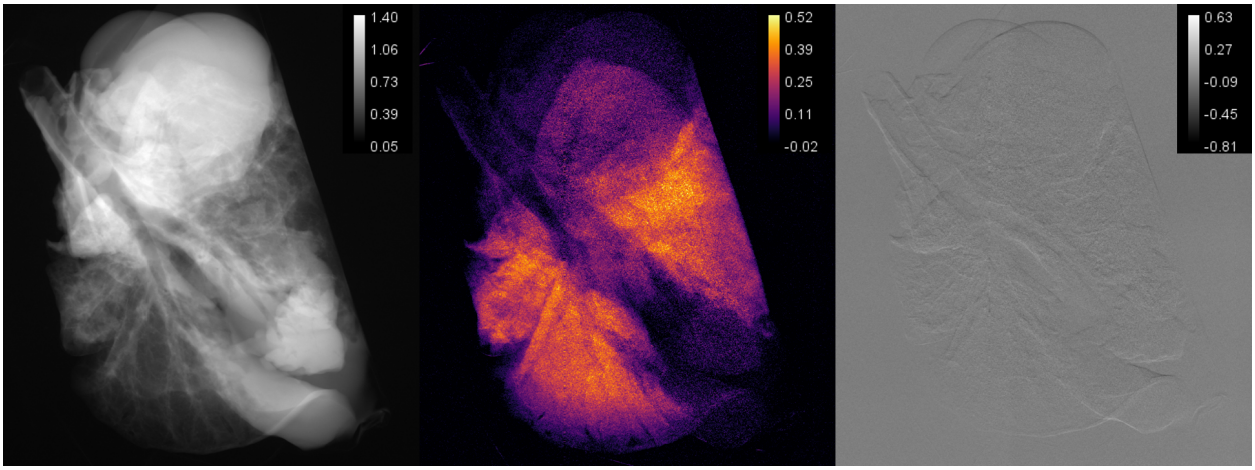

Figure 6.1: Reference high dose images of the *ex-vivo* swine lungs employed in the noise, bias, and beam hardening study.

and without the beam hardening calibration correction developed in Chapter 5. The dark field CNR of the lungs was compared for each image reconstruction.

6.2.2 Results

As demonstrated in Figure 6.1, the healthy lungs generate a strong dark field contrast within the alveoli. In addition, the edge-enhancing nature of the differential phase contrast signal allows for visualization of the blood vessels and airways pertaining to the lungs. The mean intensity of the dark field signal in the right and left lungs was measured to be 0.365 ± 0.05 and 0.376 ± 0.081, respectively. The dark field beam hardening correction was not applied on the dark field image shown in Figure 6.1. As a result, a beam hardening induced dark field signal can be seen in the heart.

The noise standard deviation measured in the heart and the mean intensity of the dark field signal in the right lung at various dose levels are tabulated in Table 6.1. Based on the quantitative results, no significant statistical bias was demonstrated for the dose levels investigated. This conclusion is further confirmed by qualitative assessment of the multi-contrast images displayed in Figure 6.2. Aside from increases in image noise, the overall intensity of the displayed dark field images remains relatively unchanged with dose level.

The impact of image noise is more drastic at reduced dose levels for the phase and dark field contrast images when compared to the absorption images. One interesting finding from this study

Table 6.1: Mean Intensity and Noise Standard Deviation for different dose levels.

Dose Level [mSv]	Noise Standard Deviation	Mean Dark Field Intensity in the Right Lung
0.020	0.179	0.273
0.039	0.120	0.260
0.078	0.085	0.264
0.117	0.073	0.262
0.156	0.065	0.267
0.195	0.057	0.268
0.234	0.054	0.267

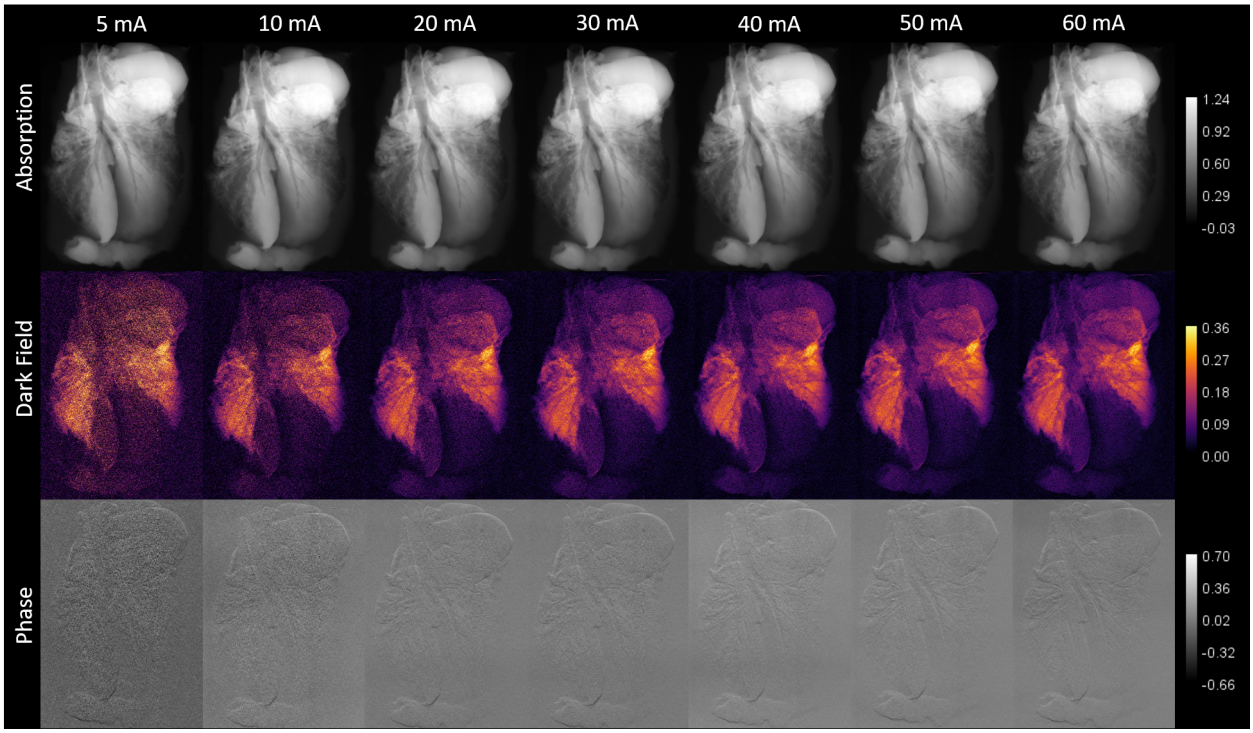

Figure 6.2: Multi-contrast images of the *ex-vivo* swine lungs at increasing dose level from left to right. A significant increase in image noise is demonstrated at reduced dose levels for the dark field and phase contrast images. The window/level is matched for all contrast images.

was the manifestation of shading artifacts in the differential phase contrast images. Non-linear shadings can be seen in different spatial locations across all of the investigated dose levels. Further investigations into this phenomenon are warranted, although outside of the scope of this thesis chapter.

Beam hardening corrected and uncorrected images of the healthy lung specimen are shown in Figure 6.3. In the presence of no additional attenuation, the beam hardening correction successfully suppresses the dark field image signal arising from the heart. As the amount of attenuation increases,

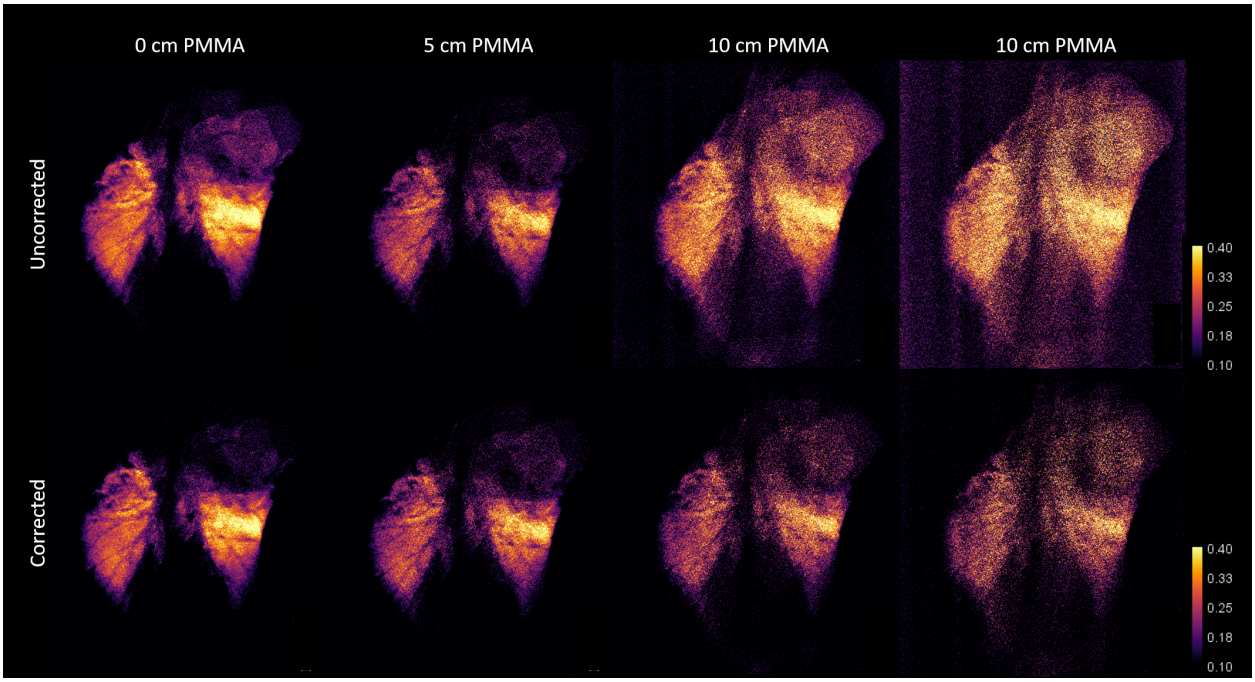

Figure 6.3: Comparison of the beam hardening corrected and uncorrected dark field images of the *ex-vivo* swine lungs at different patient thicknesses. A significant reduction in the dark field of non-alveolar anatomical structures is exhibited when the calibration beam hardening correction is applied.

the contrast between the lungs and surrounding tissues becomes significantly reduced when a beam hardening correction is not applied. For instance, the heart and lungs have similar dark field signal intensities at 15 cm of acrylic. Although this reduction in contrast is mitigated by the beam hardening correction, it should be noted that a residual dark field signal is still present in the hearts for all corrected images. This may be the result of material differences between the heart tissue and the acrylic used in the calibration process.

As reported in Table 6.2, the CNR between the lung and heart was improved by the beam hardening correction for all patient thicknesses tested. Furthermore, the estimated image noise was not increased by the application of the beam hardening correction and was in fact decreased for the 15 cm of acrylic case.

Table 6.2: Evaluation of the beam hardening correction on the dark field signal from the *ex-vivo* swine lungs.

Acrylic [cm]	$\sigma_{\text{uncorrected}}$	$\sigma_{\text{corrected}}$	CNR Uncorrected	CNR Corrected
0	0.053	0.053	5.00	5.75
5	0.074	0.074	3.15	3.58
10	0.103	0.103	1.76	2.04
15	0.159	0.159	0.99	1.14

In summary, the studies presented in this section established a baseline for the dark field signal characteristics in healthy lungs. The investigations assessed changes in the intensity, image noise, and contrast of the dark field signal at varying dose levels and simulated patient thicknesses. The beam hardening calibration correction method proposed in Chapter 5 was implemented on the acquired dark field images to evaluate its generalizability to real tissues, which proved to be useful in mitigating the degradation of the dark field images by the beam hardening effect. With this developed understanding regarding the multi-contrast image signals in healthy lungs, the next step was to evaluate the prototype system's potential for disease detection.

6.3 *Ex-vivo* Swine Lung Study: Lung Cancer Disease Model

One of the primary objectives of this thesis is to assess the capacity for a novel multi-contrast prototype system to enhance the diagnosis of pulmonary diseases. In this thesis, the efficacy of multi-contrast X-ray imaging for diagnosing lung diseases was evaluated through an *ex-vivo* swine lung study using an inserted disease model. The disease model studied in this thesis is lung cancer, which is the leading cause of global cancer-related deaths[14,15]. With a 5-year survival rate of just 21%, lung cancer prognosis remains among the worst of all cancers. The challenges in diagnosing early-stage lung cancers are among the prominent factors contributing to the high mortality associated with lung cancers. As mentioned in Chapter 1, lung cancers often present as small, low-density nodules with ill-defined margins during their early manifestations, resulting in poor contrast with conventional radiographic imaging[29,87,89,92,93].

In contrast to conventional absorption imaging, the dark field image signal has demonstrated the capacity to detect small, low-density lung cancer nodules in small animals[208]. There are several distinct features of dark field imaging that make it well-suited to the diagnosis of lung cancers. First, the tissue-to-air ratio of a region impacted by lung cancer is decreased as the nodules develop, resulting in an overall increase in the density homogeneity of the impacted region, and thus reducing the overall intensity of the dark field signal. Similarly, some histological classifications of lung cancer, including invasive adenocarcinomas and squamous cell carcinomas, have demonstrated direct filling of the alveolar air spaces. A final consideration is that lung nodules begin to displace the underlying pulmonary structures as they begin to develop. The displacement of the alveoli

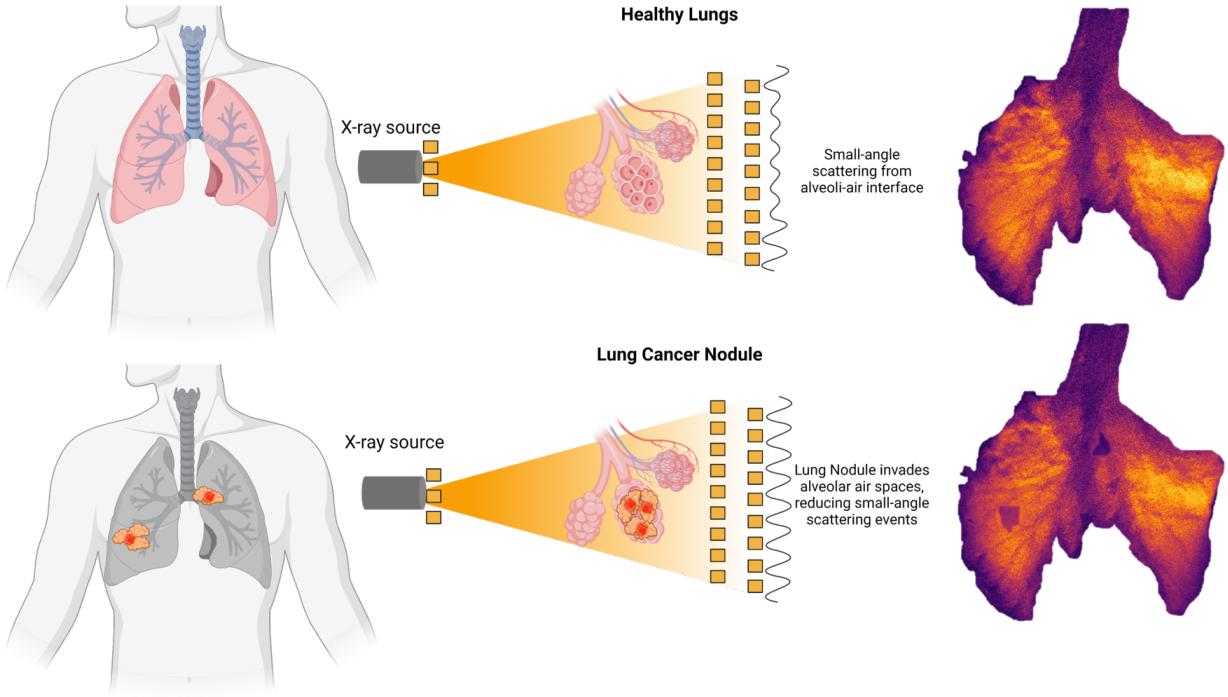

Figure 6.4: Illustration of the underlying mechanism to enable lung cancer nodule detection in dark field images. (Created in Biorender)

may also result in a reduction of the small-angle scattering events that occur for a region impacted by lung cancer. In conjunction with the dark field image, the differential phase contrast image may also provide clinically valuable information. Phase imaging has also demonstrated utility in detecting cancers through improved soft tissue contrast in mammographic and tomographic applications[38,117,120–123,157,158,169–174]. If the phase signal can be accurately retrieved from the acquired differential phase contrast images, this may provide yet another pathway for lung cancer diagnosis.

6.3.1 Methods

6.3.1.1 Baseline Reference Imaging

A set of *ex-vivo* swine lungs, with the heart and trachea still intact, were harvested from an adult swine at a local slaughterhouse (UW Provision Company, Middleton, WI). Approval from the University of Wisconsin-Madison RARC was not required as the swine subject was not euthanized for the purposes of this study. Upon arrival at the Wisconsin Institute for Medical Research, the lung samples received imaging on the multi-contrast prototype system and on a clinical multi-detector row CT (MDCT) system (GE Discovery CT750 HD). For the prototype system, a reference high

dose scan (0.234 μSv) was acquired at 70 kVp, 60 mA, and a low scan speed of 9 mm/s. MDCT imaging was performed in the high-resolution mode at 100 kV. Images were reconstructed with a 30.5 cm FOV using the commercially available high definition lung kernel. The purpose of these initial imaging sessions is to ensure that no disease is present in the samples prior to the insertion of the disease models and to establish baseline reference images of the healthy lung samples.

6.3.1.2 Lung Nodule Model Preparation and Insertion

The lung nodule model and insertion technique are adapted from the works of Bolte et al. and Burgard et al[209]. The artificial lung nodules were generated from a solution consisting of 97% water and 3% agar. The agar-water solution was heated to a temperature of 90 C and left to cool until an internal temperature of 35 C was reached. The agar solution was then injected via syringe and cannula into the *ex-vivo* swine lungs in the resting state. The total number of lung nodules injected was five, with four nodules in the right lung and one in the left lung. The amount of solution injected at each site ranged from 0.5 mL to 1 mL. The depth of insertion ranged from 1-3 cm.

6.3.1.3 Imaging with Disease Model Inserted

All imaging in this section was performed with the swine lungs in the rested state. Inflation was not feasible following the disease model insertion as a result of the puncturing of the visceral pleura. Following a 10-minute rest period, the lung samples were imaged on the MDCT scanner with the same scan protocols outlined previously. The MDCT images were then analyzed to confirm the number and location of lung nodules that formed. Measurement of the mean Hounsfield unit (HU) of each formed lung nodule was performed by measuring the HU value of the entire nodule across all image slices for which the nodule was detectable. The sample was then transferred back to the MC-CXR imaging suite for a series of MC-CXR scanning acquisitions. MC-CXR scanning was repeated at 70 kVp, 60 mA, with a slow table translation speed of 9 mm/s with the disease model inserted. Following the reconstruction of the multi-contrast images, the dark field and absorption CNR were quantified by placing ROIs over the formed nodules and in an unimpacted, homogeneous region of the lung.

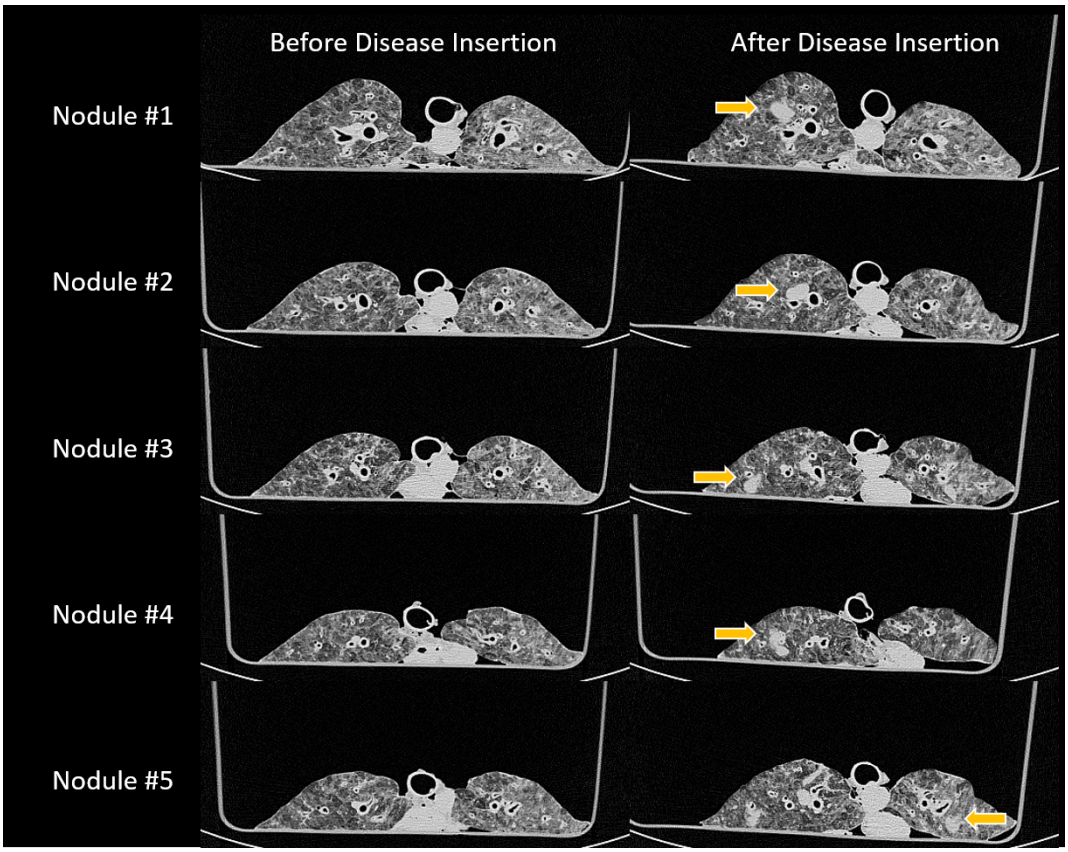

Figure 6.5: CT images of the *ex-vivo* lungs before and after disease model insertion. All five of the inserted lung nodules were successfully formed, with four in the right lung and one in the left lung. The mean HU values for the five nodules were -9 HU $\pm$ 18 HU, 24 HU $\pm$ 48, -19 HU $\pm$ 23, -18 HU $\pm$ 49 HU, and -14 HU $\pm$ 8.

6.3.2 Results

Figure 6.5 displays CT images of the *ex-vivo* lungs before and after disease insertion. The CT images confirmed the uptake and formation of all five inserted lung nodules and the absence of any detectable pre-existing diseases. The nodules, as indicated by the golden arrows in Figure 6.5, are labeled 1-5 for future reference. The mean Hounsfield unit (HU) values were -9 HU $\pm$ 18 HU, 24 HU $\pm$ 48, -19 HU $\pm$ 23, -18 HU $\pm$ 49 HU, and -14 HU $\pm$ 8 HU for nodules 1-5 respectively. The maximum HU value for a given image slice in which the nodule was detectable, was determined to be 18 HU, 48 HU, 23 HU, 49 HU, and 8 HU for nodules 1-5 respectively.

Reconstructed multi-contrast images of the healthy and diseased lung specimen are presented in Figure 6.6. The five nodules are readily apparent when comparing the healthy lungs to the lungs after disease model insertion. The lung nodules present as low-density opacities in the absorption contrast image. In contrast, the nodules present as a reduction of the dark field image signal for the

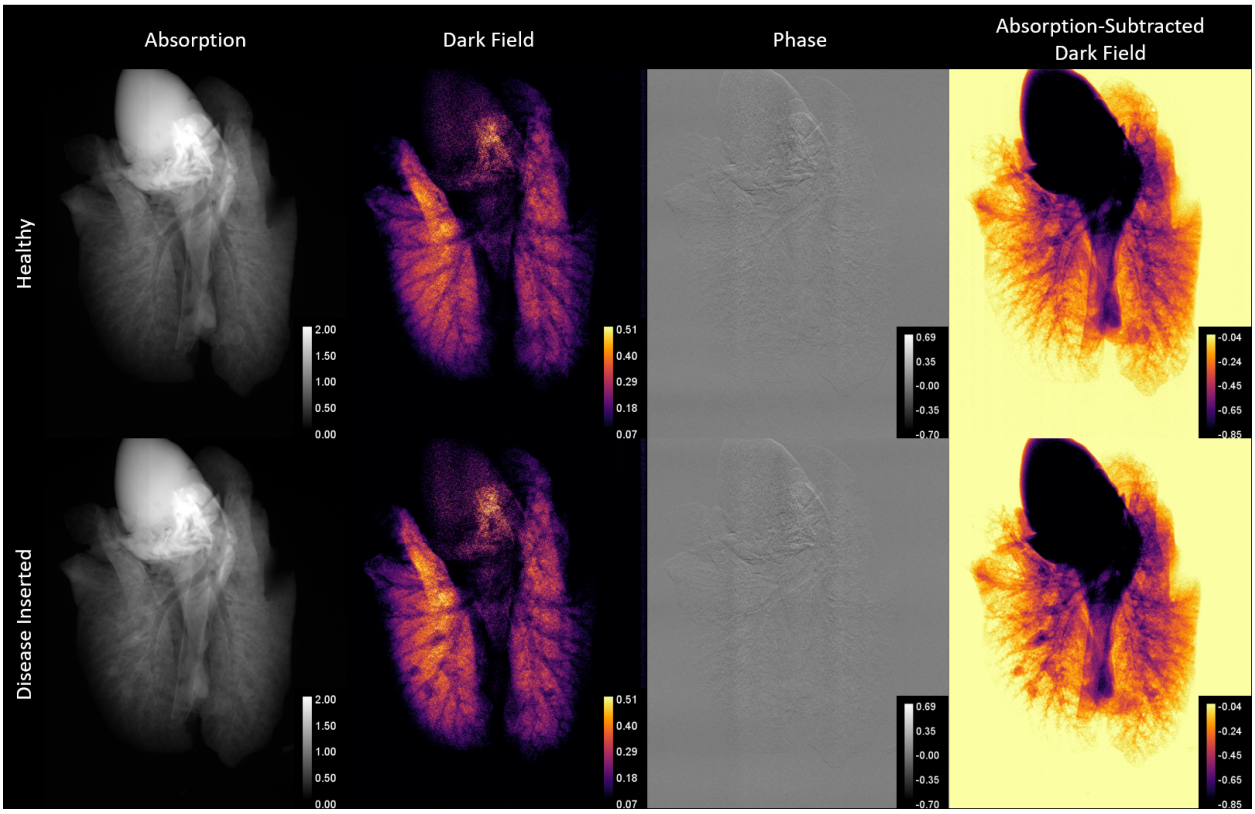

Figure 6.6: (Top) Absorption, dark field, phase, and absorption-subtracted dark field images of the healthy lungs prior to the insertion of the lung cancer disease model. (Bottom) Absorption, dark field, phase, and absorption-subtracted dark field images of the *ex-vivo* lungs with the inserted disease model.

reasons discussed earlier in this section. In addition to the absorption, phase, and dark field images, absorption-subtracted dark field images are also presented. The polarity of the disease model signal is opposite in the absorption and dark field images when compared to the surrounding tissues. As such, subtraction has the potential to enhance the contrast of lung nodules.

The combination of the absorption and dark field contrast mechanisms also motivated the exploration of other contrast fusion techniques. In addition to subtraction, division is another operation that can be investigated. As discussed in Chapter 2, the absorption and dark field projection images are measures of the line integrals of the linear attenuation coefficient and the density spatial correlation function respectively. Therefore, dividing the two images eliminates the path-length dependence of the signal. Figure 6.7 displays the absorption-normalized dark field and dark field-normalized absorption image signals for the diseased and healthy lungs. No weighting coefficients were applied for either image. For better comparison, Figure 6.8 shows ROIs of the five lesions in the absorption, dark field, absorption-subtracted dark field, absorption-normalized dark

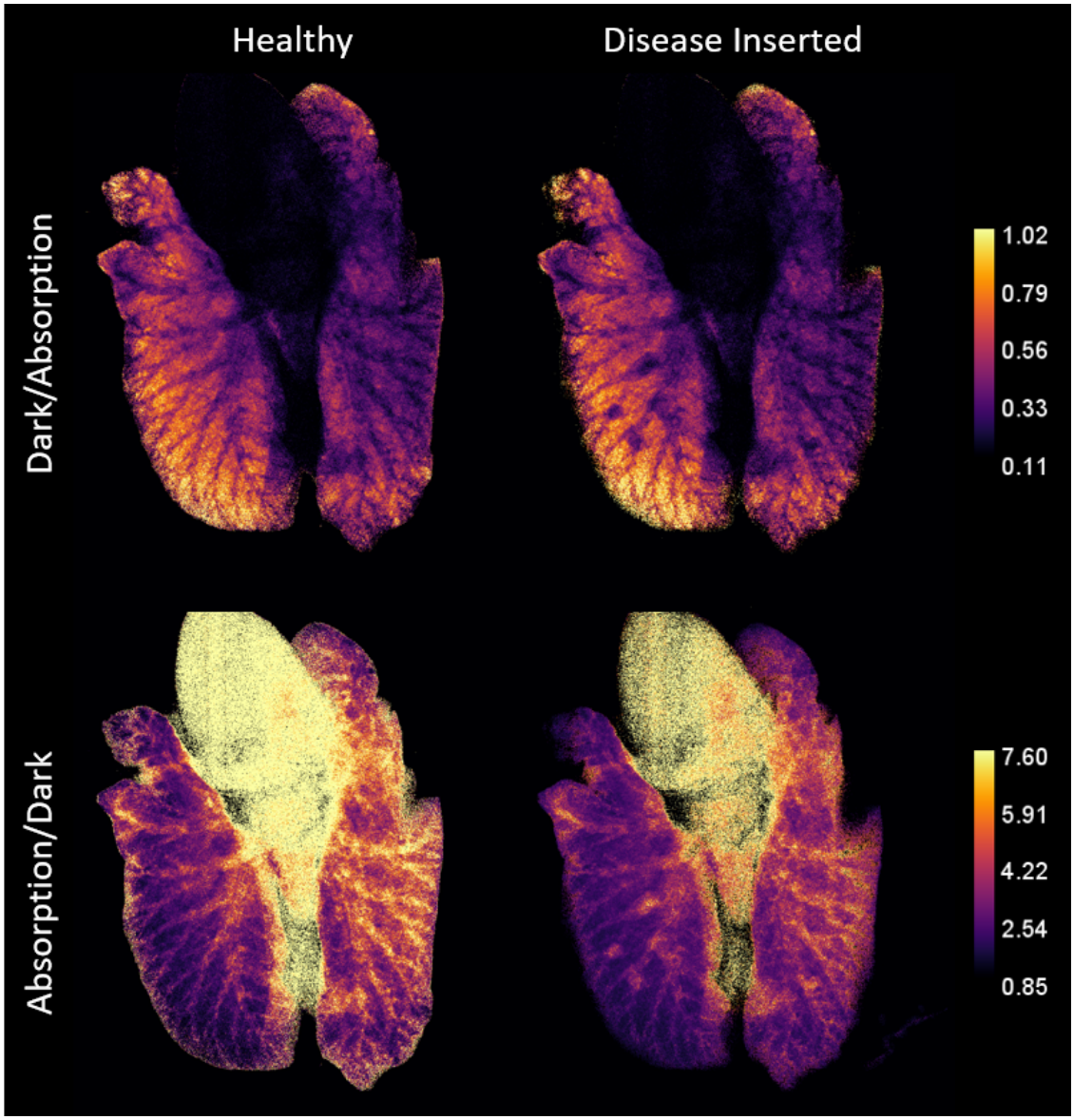

Figure 6.7: (Top) Absorption-normalized dark field images for the diseased and healthy lungs. (Bottom) Dark field-normalized absorption images for the diseased and healthy lungs.

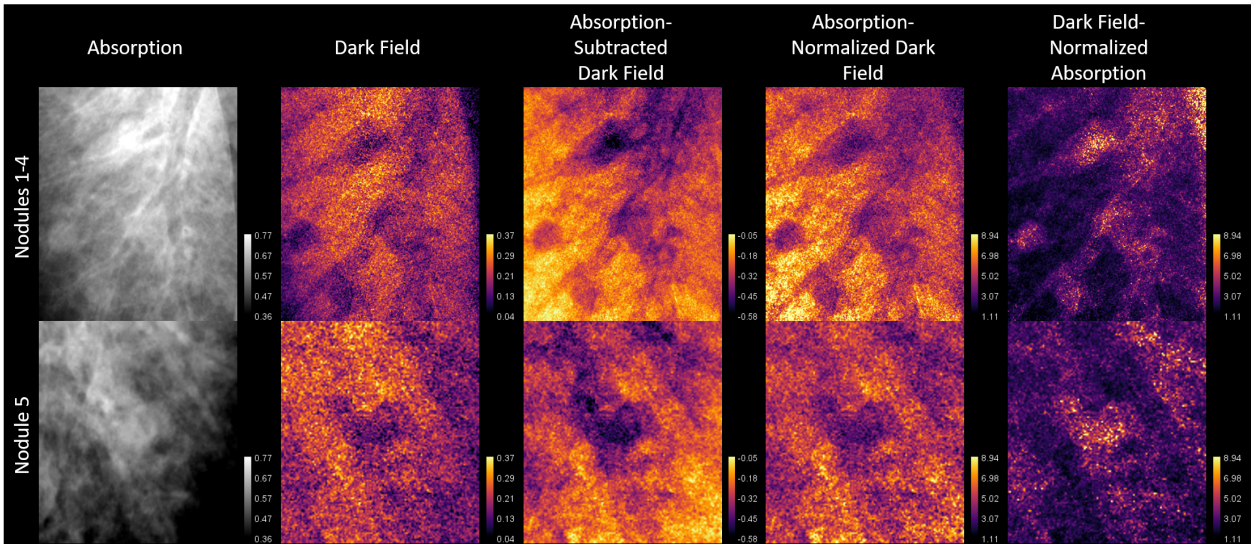

Figure 6.8: (Top) ROI with nodules 1-4

field, and dark field-normalized absorption images.

Table 6.3 summarizes the absorption and dark field CNR for each of the five nodules. The dark field imaging provided a higher CNR for 4 out of the 5 nodules, with the exception being nodule 3. The percent increase in the dark field CNR relative to the absorption CNR was 24.3% for nodule 1, 11.8% for nodule 2, - 1.8% for nodule 3, 195.6% for nodule 4, and 373.1% for nodule 5. The absolute value of the CNR is reported for all measurements.

Table 6.3: Dark field and absorption CNR for each formed lung nodule.

Nodule #	Absorption	Dark Field
Nodule 1	1.42	1.77
Nodule 2	2.03	2.27
Nodule 3	2.01	1.97
Nodule 4	0.82	2.42
Nodule 5	0.28	1.34

The findings of this study underscore the potential of multi-contrast imaging to improve the detection of pulmonary abnormalities, particularly in the context of lung cancer diagnosis. The dark field image provided enhanced lesion CNR for four out of the five inserted lung nodules. Furthermore, this study demonstrated that the fusion of the absorption and dark field images can provide potentially clinically relevant information. However, the major limitation of an *ex-vivo* study is that the beam hardening effect cannot be adequately modeled. As shown in Chapters 4

and 5, the overlapping osseous structures can significantly degrade the dark field image signal as a result of the beam hardening effect. Therefore, the next logical step in the development of the prototype system is to conduct *in-vivo* animal imaging studies to provide a more clinically relevant assessment of the prototype system.

6.4 Pilot *In-Vivo* Animal Imaging Study

The final objective of this thesis was to investigate the feasibility of performing *in-vivo* animal imaging. The purpose for conducting *in-vivo* animal imaging studies is to identify the potential limitations, pitfalls, and strengths of the prototype system in an environment similar to that of the clinic.

Before delving into the animal subject and multi-contrast scanning protocols, it is important to highlight several significant limitations of the study presented in this section. First, the study was conducted during the early stages of the prototype's development. Thus, the clinical imaging parameters had not yet been optimized and the beam hardening correction framework had not been developed. Consequently, optimized scan protocols and the beam hardening correction were not employed during this study. Moreover, the disease model used in this study was not expected to produce any significant contrast in the absorption or dark field images. Due to the unavailability of additional large animals, this study could not be replicated more recently. Given these limitations, this study merely serves as a pilot or proof of concept for *in-vivo* multi-contrast imaging using the prototype system.

6.4.1 Methods

The image subject for this pilot *in-vivo* study was a 40 kg female swine subject from the Cardiovascular Physiology Core Facility at the University of Wisconsin-Madison. The subject was inserted with a pulmonary embolism model for the purposes of a perfusion imaging trial. Due to the physiological nature of pulmonary embolisms, no disease-related contrast is expected to be generated in any of the three contrast mechanisms..

To allow for breath-holding, the subject was anesthetized and mechanically ventilated. Multi-contrast scanning was performed with a tube potential of 70 kVp, a scan speed of 9 mm/s, and a

tube current of 60 mA. The estimated effective dose to a reference patient was 0.234 mSv for the imaging exam. The total scan time required to cover the entirety of the lungs was 34 seconds. In addition to the three contrast mechanisms, an absorption-subtracted dark field image was also generated.

6.4.2 Results

The resulting absorption, dark field, and absorption-subtracted dark field images of the swine subject are shown in Figure 6.9. However, the quality of the raw dark field image was severely degraded due to the high noise level and the effects of beam hardening. The swine subject caused a substantial attenuation of the X-ray field, resulting in the high noise level. The measured line integral of the linear attenuation coefficient through the center of the subject was 4.098 ± 0.062, which is notably higher than the linear attenuation coefficient for the ANSI chest phantom with 30 cm of acrylic at 70 kVp and 60 mA, which was only 3.208. One potential explanation for the high attenuation measured in this study is that the thickest portion of the swine is along the X-ray beam axis during AP imaging. Another explanation is that the subject may have had some residual iodine signal from the pulmonary embolism insertion and confirmation processes.

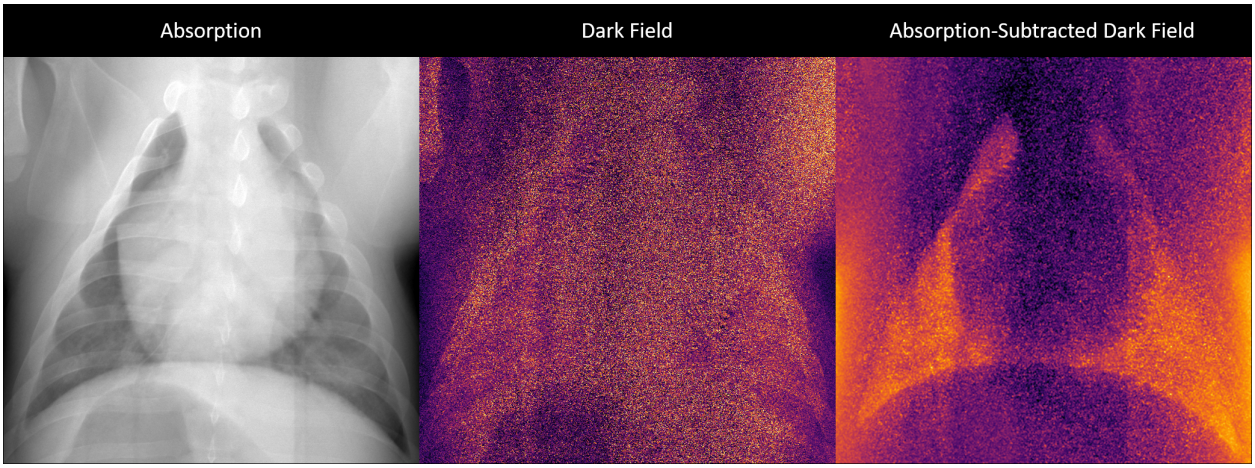

Figure 6.9: (Left) Absorption image of the swine subject. (Center) Dark field image (Right) Absorption-subtracted dark field image.

From a qualitative standpoint, the raw dark field image did not generate any discernible dark field contrast in the pulmonary structures of the chest cavity. However, a strong contrast in the pulmonary structures was recovered after subtracting the absorption image from the raw dark

field measurement. In addition to the recovered contrast, the absorption-subtraction technique eliminated the dark field signal arising from the ribs, clavicles, and spine. It is worth noting that the absorption-subtracted dark field image displayed in Figure 6.9 was filtered with a 3×3 neighborhood mean operation to reduce the impact of image noise.

One limitation of the absorption-subtraction technique is that the image object's periphery also demonstrates a high-intensity signal, which may obscure the contrast generated in the lungs. Furthermore, the absorption-subtracted image clearly shows the three grating panels, each demonstrating a different overall intensity. This phenomenon can be overcome with the beam hardening calibration correction because the correction is designed to address visibility inconsistencies along the transverse plane. A final qualitative observation is the presence of motion artifacts at the boundaries of the heart in the raw and absorption-subtracted dark field images. Motion artifacts manifest from spatial inconsistencies in the mapping of the object across the interference pattern. It is expected that motion artifacts will become more severe when the image subject is not anesthetized.

The results of this pilot study highlight several important considerations for future *in-vivo* imaging studies. First, swine subjects may not be well-suited for projection-based AP or PA X-ray imaging. In contrast to human subjects, swine are thickest along the imaging axis for chest AP/PA imaging. Therefore, lateral-view swine imaging or the use of other animal subjects may provide more clinically applicable imaging results in the future. Second, absorption-subtracted dark field images have demonstrated great utility in reducing the dark field signal associated with the osseous structures of the chest cavity. However, limitations including the high signal at the periphery of the imaging FOV must be addressed to enable more robust and impactful multi-contrast imaging.

The final major consideration is that the scan speed must be significantly increased for future *in-vivo* imaging acquisitions. In this study, the use of a slow scan speed was necessary in order to get a sufficient X-ray dose to the detector. At this time, the limiting factor governing the use of slow acquisition speeds is the X-ray tube output. For instance, the maximum achievable estimated effective dose to a reference patient for a 45 mm/s scan is only 0.047 mSv, well below the average effective dose reported in chest radiography.

6.5 Summary

In this chapter, the clinical potential of the prototype multi-contrast imaging system was evaluated through a series of animal imaging studies. To begin, a baseline for the dark field image signal of healthy lungs was established for several dose levels and different simulated patient thicknesses. In addition to the dark field signal characterization, the generalizability of the beam hardening calibration correction to tissue samples was also investigated. Once the dark field image signal was characterized for healthy lungs, the next step was to evaluate the prototype imaging system's potential to enhance the diagnosis of lung disease. This objective was carried out through the study of a lung cancer disease model in *ex-vivo* lungs. The dark field image contrast and the fusion of the dark field and absorption mechanisms demonstrated the potential to improve the diagnosis of lung nodules. To conclude this chapter, a pilot *in-vivo* imaging trial was conducted. The goal of this study was to assess potential limitations, shortcomings, or strengths associated with the prototype system in order to guide future *in-vivo* and clinical imaging trials. At the conclusion of this chapter, the major objectives of this thesis work have been achieved. In summary, a prototype multi-contrast imaging system has been designed, constructed, optimized, and evaluated for its potential clinical application.

Chapter 7

Conclusion and Future Works

7.1 Discussion

The objective of this thesis was to develop, optimize and evaluate the potential clinical utility of a novel prototype system for multi-contrast chest X-ray radiography. Chapter 3 describes the construction of a compact, cost-effective, and clinically viable prototype system that overcomes the limitations associated with traditional grating-based X-ray imaging methods. To enable a seamless clinical translation, a fast scanning acquisition scheme was introduced and implemented through the creation of a novel correction framework. Chapter 4 reports the dosimetric properties of the imaging system to ensure patient safety and inform the optimization of clinical imaging parameters. A novel optimization framework was introduced to identify the optimal X-ray energy and dose level to achieve high-quality multi-contrast imaging while minimizing radiation-induced risks to the patient. The imaging performance of the prototype system was first evaluated via an anthropomorphic phantom imaging study, in which, the beam hardening effect was identified as a potential obstacle to clinical translation. In Chapter 5, the origin of the beam-hardening effect was discussed and two potential remedies were investigated. The clinical potential of the prototype system was assessed by examining its ability to detect simulated lung cancer nodules and generate a robust signal in healthy *ex-vivo* animal lung samples. The investigation was concluded with a pilot *in-vivo* animal imaging study to identify any potential limitations, pitfalls, and strengths of the prototype system in an environment similar to that of a clinical setting.

In the following several sections, the key results of this thesis work are summarized and discussed.

7.1.1 Key Result #1: Construction of a Novel Prototype System

One of the major accomplishments of the thesis work was the construction of a novel human-compatible prototype system from scratch. To begin, the unified optimization framework presented in Chapter 2 was used to guide the design of the grating interferometer employed in the prototype system. Once the design of the grating interferometer was established, two seperate gantries and a patient table were constructed. By constructing all components of the system in-house, the system was able to be custom designed to enable the highest achievable imaging performance while adhering to the constraints imposed by a clinical setting.

7.1.2 Key Result #2: Fast Scanning Acquisition Scheme and Scanning Correction Framework

The fast scanning acquisition scheme developed in this work is crucial for ensuring that the developed prototype system is compatible with clinical practice. The acquisition process involves mapping each point on the image object across multiple positions on the sinusoidal interference pattern as the patient table is moved longitudinally. By using the continuous translation of the image object instead of phase stepping, the fast scanning acquisition enables imaging of the entire chest within a single breath-hold. Moreover, this acquisition scheme reduces the need for large FOV gratings to a single dimension, thereby significantly lowering the overall cost of the prototype system.

As with any method, there are inherent limitations associated with the scanning acquisition method. A scanning correction framework was introduced to address the two major limitations of the scanning beam acquisition strategy, namely, the detector lag effect and scanning motion blur. The detector lag correction was found to have the greatest impact on preserving the spatial resolution of the imaging system. Throughout this thesis work, the fast scanning acquisition scheme and scanning correction framework enabled accurate and robust multi-contrast X-ray imaging.

7.1.3 Key Result #3: Framework to Optimize Multi-Contrast Clinical Imaging Parameters

A major component of this thesis work was the development of a framework to empirically determine the optimal multi-contrast imaging scan protocols. The optimization process presented in this work incorporates information regarding the absorption and dark field contrast mechanisms. Custom absorption and dark field contrast-generating inserts were introduced to the ANSI chest phantom to measure the dose-normalized contrast-to-noise ratio for a range of X-ray energies, dose levels, and simulated patient thicknesses.

The optimization process not only guided the selection of clinical imaging parameters, but also provided insight into the relationship between image contrast, energy, and noise for the absorption and dark field contrast mechanisms. Based on the results of the optimization process, it was suggested that the scan protocols should be optimized with respect to the dark field contrast because the absorption contrast mechanism provided more consistent image performance over the range of parameters investigated.

7.1.4 Key Result #4: The Beam Hardening Effect in Dark Field Imaging

Throughout this thesis, one of the major challenges encountered was the impact of beam hardening on the dark field image signal. In dark field imaging, beam hardening occurs due to spectral inconsistencies between the interference patterns generated during the reference air scan and the object scan. As demonstrated in Chapter 3, the visibility of the interference pattern typically decreases with increasing X-ray energy, across the diagnostic energy range. Therefore, the hardening of the X-ray spectra during the object scan can lead to a perceived reduction of the fringe visibility, inducing a false dark field signal to be measured even in the absence of small-angle scatterers.

To address the beam hardening effect, the concept of the spectral component of the visibility reduction was introduced. This concept was then leveraged to construct a beam hardening correction method. In this correction method, the relationship between the object's transmission function and the spectral component of the visibility reduction was learned empirically through a series of calibration measurements. The learned relationship was then used to mitigate the impact of the spectral component of the visibility reduction.

The correction method demonstrated success when it was applied to materials that were similar to the material used in the calibration process. However, the generalization of the method to dissimilar materials was poor.

7.1.5 Key Result #5: Potential for Enhanced Lung Cancer Detection

One of the major findings of this thesis work was the potential for multi-contrast imaging to improve the detection of lung cancer nodules. The dark field signal has demonstrated utility for the diagnosis of lung cancers in small-animal imaging studies. However, the results presented in this thesis are the first known investigation into the use of multi-contrast X-ray imaging for the detection of lung cancers in a large animal model.

The results of the artificial lung nodule study were exciting for several reasons. First, the dark field image signal demonstrated an increased CNR in four out of the five formed nodules. Furthermore, the combination of the absorption and dark field contrast mechanisms provided interesting imaging results that may generate clinically valuable information. However, there are several obvious limitations associated with this study. First, only a single lung specimen was investigated. Furthermore, the study was an *ex-vivo* in nature, and therefore many potential confounding factors were not included in the study. Nevertheless, further investigations into the potential for multi-contrast imaging in lung cancer diagnosis are warranted.

7.2 Future Works

This thesis work was focused on the design, construction, and initial evaluation of the developed prototype multi-contrast imaging system. However, additional work is needed to fully realize the potential of multi-contrast imaging for the diagnosis of lung disease. In this section, several projects are suggested as future works worth investigating.

7.2.1 Comprehensive Lung Cancer Animal Imaging Study

A logical next step for the development of the prototype system is to conduct a more comprehensive investigation into the potential of multi-contrast imaging for the diagnosis of lung cancers. To begin, more *ex-vivo* swine lung studies can be conducted to determine the minimal size and density of

lesions that can be detected with each contrast mechanism. Further *ex-vivo* studies would also allow for statistical testing to be performed. Depending on the findings of the *ex-vivo* studies, the next step could be to conduct an *in-vivo* large animal imaging trial with more accurate disease models.

7.2.2 Development of a More Comprehensive Beam Hardening Correction

There is a need for a beam hardening correction method that can simultaneously correct for dark field signals arising from beam hardening both soft tissues and bones. One potential avenue to pursue is a thresholding approach in which the beam hardening-induced soft tissue and bone dark field signals are separated by thresholding the dark field based on pixel intensity. If this can be accomplished, then two separate calibration corrections can be applied to correct for the dark field signal arising from both materials.

7.2.3 Multi-Contrast Fusion Imaging

Fusion of the different contrast mechanisms could have the potential to generate diagnostically useful information. This concept was demonstrated briefly in Chapter 6 with the introduction of the absorption-normalized dark field image and dark field-normalized absorption images. However, a thorough investigation into various techniques to enhance the information provided by the individual contrast mechanisms could prove fruitful.

7.2.4 Leveraging the Differential Phase Contrast Information

Throughout this thesis, the focus was on the dark field and absorption contrast mechanisms. However, the differential phase signal also contains valuable information regarding the electron density of the image object. A future project could examine pathways to improve the differential phase contrast signal and develop robust methods to leverage the encoded electron density information for material-specific imaging. Additionally, the differential nature of the phase image has the potential to provide information regarding pulmonary diseases that manifest along the major airways.

7.2.5 Increasing the X-ray Tube Output to Enable Faster Scanning Speeds

The output of the X-ray tube is a major limitation of the prototype system at this time. As mentioned in Chapter 6, the highest achievable effective dose at a high scan speed of 45 mm/s with a 70 kVp spectrum is only 0.047 mSv. It is not expected that this effective dose level will provide sufficient multi-contrast imaging results for larger image subjects. To enable the use of higher scanning speeds, modifications must be made to the system. Modifications can include the replacement of the X-ray tube with a more powerful tube or adjustments to the system to enable a greater tube output.

References

[1] S. Levine and D. Marciniuk, "Global impact of respiratory disease – what can we do, together, to make a difference?," *Chest*, 01 2022.

[2] "The top 10 causes of death," *World Health Organization*, 2023.

[3] M. Montero-Fernandez and R. Pardo, "Histopathology features of the lung in covid-19 patients," *Diagnostic Histopathology*, vol. 27, 12 2020.

[4] "The nobel prize in physics 1901."

[5] W. C. Röntgen, "On a new kind of rays," *Science*, vol. 3, no. 59, pp. 227–231, 1896.

[6] "James clerk maxwell," Apr 2023.

[7] X. Li, X. Cao, M. Guo, M. Xie, and X. Liu, "Trends and risk factors of mortality and disability adjusted life years for chronic respiratory diseases from 1990 to 2017: Systematic analysis for the global burden of disease study 2017," *BMJ*, vol. 368, p. m234, 02 2020.

[8] P. F. F. J. B. Soriano, M.D., P. Kendrick, K. Paulson, V. Gupta, E. Abrams, R. Adedoyin, T. Adhikari, S. Advani, A. Agrawal, E. Ahmadian, F. Alahdab, S. Aljunid, K. Altirkawi, N. Alvis Guzmán, N. Anber, C. Andrei, M. Anjomshoa, F. Ansari, J. Antó, and T. Vos, "Prevalence and attributable health burden of chronic respiratory diseases, 1990–2017: a systematic analysis for the global burden of disease study 2017," *The Lancet Respiratory Medicine*, vol. 8, pp. 585–596, 06 2020.

[9] J. Meghji, K. Mortimer, A. Agusti, B. Allwood, I. Asher, E. Bateman, K. Bissell, C. Bolton, A. Bush, B. Celli, C.-Y. Chiang, A. Cruz, A. T. Dinh-Xuan, A. Elsony, K. Fong, P. Fujiwara, M. Gaga, L. Garcia-Marcos, D. Halpin, and G. Marks, "Improving lung health in low-income and middle-income countries: from challenges to solutions," *The Lancet*, vol. 397, 02 2021.

[10] N. Kosacz, T. Croxton, M. Ndenecho, J. Kiley, G. Weinmann, A. Wheaton, E. Ford, L. Presley-Cantrell, J. Croft, and W. Giles, "Chronic obstructive pulmonary disease among adults — united states, 2011," *MMWR. Morbidity and mortality weekly report*, vol. 61, pp. 938–943, 11 2012.

[11] D. Singh, A. Agusti, A. Anzueto, P. Barnes, J. Bourbeau, B. Celli, G. Criner, P. Frith, D. Halpin, M. Han, M. Varela, F. Martinez, M. Oca, A. Papi, I. Pavord, N. Roche, D. Sin, R. Stockley, J. Vestbo, and C. Vogelmeier, "Global strategy for the diagnosis, management, and prevention of chronic obstructive lung disease: The gold science committee report 2019," *European Respiratory Journal*, vol. 53, p. 1900164, 03 2019.

[12] P. Pahal, A. Avula, and S. Sharma, "Emphysema," 2018.

[13] D. E. Niewoehner, R. A. Stockley, S. I. Rennard, K. Rabe, and B. Celli, *CHAPTER 1 Structure–Function Relationships: The Pathophysiology of Airflow Obstruction*, p. 3–5. Blackwell Pub., 2007.

[14] J. Ferlay, M. Colombet, I. Soerjomataram, C. Mathers, D. Parkin, M. Piñeros, A. Znaor, and F. Bray, "Global and regional estimates of the incidence and mortality for 38 cancers: Globocan 2018. lyon: International agency for research on cancer," *World Health Organization*, pp. 394–424, 2018.

[15] H. Sung, J. Ferlay, R. Siegel, M. Laversanne, I. Soerjomataram, A. Jemal, and F. Bray, "Global cancer statistics 2020: Globocan estimates of incidence and mortality worldwide for 36 cancers in 185 countries," *CA: a cancer journal for clinicians*, vol. 71, 02 2021.

[16] R. Siegel, K. Miller, H. Fuchs, and A. Jemal, "Cancer statistics, 2021," *CA: A Cancer Journal for Clinicians*, vol. 71, 01 2021.

[17] A. Casal, A. Ruano-Ravina, M. Lorenzo-González, n. Rodríguez-Martínez, A. Giraldo-Osorio, L. Varela-Lema, T. Pereiro-Brea, J. Barros-Dios, L. Valdés, and M. Pérez-Rios, "Epidemiology of stage iii lung cancer: Frequency, diagnostic characteristics, and survival," *Translational Lung Cancer Research*, vol. 10, pp. 506–518, 01 2021.

[18] S. Birring and M. Peake, "Symptoms and the early diagnosis of lung cancer," *Thorax*, vol. 60, pp. 268–9, 05 2005.

[19] B. Parris, H. O'Farrell, K. Fong, and I. Yang, "Chronic obstructive pulmonary disease (copd) and lung cancer: common pathways for pathogenesis," *Journal of Thoracic Disease*, vol. 11, pp. S2155–S2172, 10 2019.

[20] P. Jänne, B. Freidlin, S. Saxman, D. Johnson, R. Livingston, F. Shepherd, and B. Johnson, "Twenty-five years of clinical research for patients with limited-stage small cell lung carcinoma in north america: Meaningful improvements in survival," *Cancer*, vol. 95, pp. 1528–38, 11 2002.

[21] M. Riihimäki, A. Hemminki, M. Fallah, H. Thomsen, K. Sundquist, J. Sundquist, and K. Hemminki, "Metastatic sites and survival in lung cancer," *Lung Cancer*, vol. 86, pp. 78–84, 08 2014.

[22] C. Rudin, E. Brambilla, C. Faivre-Finn, and J. Sage, "Small-cell lung cancer," *Nature Reviews Disease Primers*, vol. 7, 12 2021.

[23] K.-S. Park, M.-C. Liang, D. Raiser, R. Zamponi, R. Roach, S. Curtis, Z. Walton, B. Schaffer, C. Roake, A.-F. Hämmerli, C. Kriegel, K.-K. Wong, J. Sage, and C. Kim, "Characterization of the cell of origin for small cell lung cancer," *Cell cycle (Georgetown, Tex.)*, vol. 10, pp. 2806–15, 08 2011.

[24] B. Oronsky, T. Reid, A. Oronsky, and C. Carter, "What's new in sclc? a review," *Neoplasia (New York, N.Y.)*, vol. 19, pp. 842–847, 09 2017.

[25] S. Wang, J. Tang, T. Sun, X. Zheng, J. Li, H. Sun, X. Zhou, C. Zhou, H. Zhang, Z. Cheng, H. Ma, and H. Sun, "Survival changes in patients with small cell lung cancer and disparities between different sexes, socioeconomic statuses and ages," *Scientific Reports*, vol. 7, 12 2017.

[26] M. Zheng, "Classification and pathology of lung cancer," *Surgical Oncology Clinics of North America*, vol. 25, pp. 447–468, 07 2016.

[27] W. Travis, "Pathology of lung cancer," *Clinics in chest medicine*, vol. 32, pp. 669–92, 12 2011.

[28] Z. Chen, C. Fillmore, P. Hammerman, C. Kim, and K.-K. Wong, "Non-small-cell lung cancers: A heterogeneous set of diseases," *Nature reviews. Cancer*, vol. 14, pp. 535–46, 07 2014.

[29] H. Soda, H. Tomita, S. Kohno, and M. Oka, "Limitation of annual screening chest radiography for the diagnosis of lung cancer. a retrospective study," *Cancer*, vol. 72, pp. 2341–6, 11 1993.

[30] N. Knechel, "Tuberculosis: Pathophysiology, clinical features, and diagnosis," *Critical care nurse*, vol. 29, pp. 34–43; quiz 44, 05 2009.

[31] E. Morales, *The Global Asthma Report 2018*. 09 2018.

[32] G. Pavón-Romero, N. Serrano-Pérez, L. García-Sánchez, F. Ramírez Jiménez, and L. Teran, "Neuroimmune pathophysiology in asthma," *Frontiers in Cell and Developmental Biology*, vol. 9, 05 2021.

[33] N. Zhu, D. Zhang, W. Wang, X. Li, B. Yang, J. Song, X. Zhao, B. Huang, W. Shi, R. Lu, P. Niu, F. Zhan, X. Ma, D. Wang, W. Xu, G. Wu, and G. Gao, "A novel coronavirus from patients with pneumonia in china, 2019," *New England Journal of Medicine*, vol. 382, 01 2020.

[34] "Who coronavirus (covid-19) dashboard," *World Health Organization*.

[35] "Cdc covid data tracker," *Centers for Disease Control and Prevention*.

[36] B. Alexis, C. Austyn, J. Max, B. Domnique, A. Tamara, and G. Sandusky, "A post-mortem examination of covid-19 pulmonary pathology in 9 cases," *Archives of Pulmonology and Respiratory Care*, vol. 6, pp. 045–047, 06 2020.

[37] S. Lukassen, R. L. Chua, T. Trefzer, N. Kahn, M. Schneider, T. Muley, H. Winter, M. Meister, C. Veith, A. Boots, B. Hennig, M. Kreuter, C. Conrad, and R. Eils, "Sars-cov-2 receptor ace2 and tmprss2 are primarily expressed in bronchial transient secretory cells," *The EMBO journal*, p. e105114, 04 2020.

[38] H. Zhang, J. Penninger, Y. Li, N. Zhong, and A. Slutsky, "Angiotensin-converting enzyme 2 (ace2) as a sars-cov-2 receptor: molecular mechanisms and potential therapeutic target," *Intensive Care Medicine*, vol. 46, 03 2020.

[39] A. Rendeiro, H. Ravichandran, Y. Bram, V. Chandar, J. Kim, C. Meydan, J. Park, J. Foox, T. Hether, S. Warren, Y. Kim, J. Reeves, S. Salvatore, C. Mason, E. Swanson, A. Borczuk, O. Elemento, and R. Schwartz

[40] A. Rabaan, S. Al-Ahmed, S. Haque, R. Sah, R. Tiwari, Y. Malik, K. Dhama, D. M. Yatoo, D. Bonilla-Aldana, and A. Rodriguez-Morales, "Sars-cov-2, sars-cov, and mers-cov: a comparative overview," *Le infezioni in medicina: rivista periodica di eziologia, epidemiologia, diagnostica, clinica e terapia delle patologie infettive*, vol. 28, pp. 174–184, 04 2020.

[41] Y. Yan, W. Shin, Y. Pang, Y. Meng, J. Lai, C. You, H. Zhao, E. Lester, T. Wu, and C. H. Pang, "The first 75 days of novel coronavirus (sars-cov-2) outbreak: Recent advances, prevention, and treatment," *International Journal of Environmental Research and Public Health*, vol. 17, p. 2323, 03 2020.

[42] A. Borczuk, S. Salvatore, S. Seshan, S. Patel, J. Bussel, M. Mostyka, S. Elsoukkary, B. He, C. Del Vecchio, F. Fortarezza, F. Pezzuto, P. Navalesi, A. Crisanti, M. Fowkes, C. Bryce, F. Calabrese, and M. Beasley, "Covid-19 pulmonary pathology: a multi-institutional autopsy cohort from italy and new york city," *Modern Pathology*, vol. 33, pp. 1–13, 09 2020.

[43] S. Tian, W. Hu, L. Niu, H. Liu, H. Xu, and X. Yuan, "Pulmonary pathology of early-phase 2019 novel coronavirus (covid-19) pneumonia in two patients with lung cancer," *Journal of Thoracic Oncology*, vol. 15, 02 2020.

[44] B. Bikdeli, M. Madhavan, D. Jiménez, T. Chuich, I. Dreyfus, E. Driggin, C. der nigoghossian, W. Ageno, M. Madjid, Y. Guo, L. Tang, Y. Hu, J. Giri, M. Cushman, I. Quéré, E. Dimakakos, M. Gibson, G. Lippi, E. Favaloro, and G. Lip, "Covid-19 and thrombotic or thromboembolic disease: Implications for prevention, antithrombotic therapy, and follow-up," *Journal of the American College of Cardiology*, 04 2020.

[45] L. Bos, F. Paulus, A. Vlaar, L. Beenen, and M. Schultz, "Subphenotyping ards in covid-19 patients: Consequences for ventilator management," *Annals of the American Thoracic Society*, vol. 17, 05 2020.

[46] A. Laing, A. Lorenc, I. Barrio, A. Das, M. Fish, L. Monin, M. Muñoz-Ruiz, D. McKenzie, T. Hayday, I. Francos-Quijorna, S. Kamdar, M. Joseph, D. Davies, R. Davis, A. Jennings, I. Zlatareva, P. Vantourout, Y. Wu, V. Sofra, and A. Hayday, "A dynamic covid-19 immune signature includes associations with poor prognosis," *Nature Medicine*, vol. 26, pp. 1–13, 10 2020.

[47] C. Lucas, P. Wong, J. Klein, T. B. De Castro, J. Silva, M. Sundaram, M. Ellingson, T. Mao, J. Oh, B. Israelow, T. Takahashi, M. Tokuyama, P. Lu, A. Venkataraman, A. Park, S. Mohanty, H. Wang, A. Wyllie, C. Vogels, and A. Iwasaki, "Longitudinal analyses reveal immunological misfiring in severe covid-19," *Nature*, 08 2020.

[48] D. Mathew, J. Giles, A. Baxter, D. Oldridge, A. Greenplate, J. Wu, C. Alanio, L. Kuri-Cervantes, M. Pampena, K. D'Andrea, S. Manne, Z. Chen, Y. Huang, J. Reilly, A. Weisman, C. Ittner, O. Kuthuru, J. Dougherty, K. Nzingha, and E. J. Wherry, "Deep immune profiling of covid-19 patients reveals distinct immunotypes with therapeutic implications," *Science*, vol. 369, p. eabc8511, 07 2020.

[49] R. Nienhold, Y. Ciani, V. Koelzer, A. Tzankov, J. Haslbauer, T. Menter, N. Schwab, M. Henkel, A. Frank, V. Zsikla, N. Willi, W. Kempf, T. Hoyler, M. Barbareschi, H. Moch, M. Tolnay, G. Cathomas, F. Demichelis, T. Junt, and K. Mertz, "Two distinct immunopathological profiles in autopsy lungs of covid-19," *Nature Communications*, vol. 11, 10 2020.

[50] W. Wang, B. Su, L. Pang, L. Qiao, Y. Feng, Y. Ouyang, X. Guo, H. Shi, F. Wei, X. Su, J. Yin, R. Jin, and D. Chen, "High-dimensional immune profiling by mass cytometry revealed immunosuppression and dysfunction of immunity in covid-19 patients," *Cellular & Molecular Immunology*, vol. 17, 04 2020.

[51] G. Zhao, Y. Xu, J. Li, X. Cui, X. Tan, H. Zhang, and L. Dang, "Sex differences in immune responses to sars-cov-2 in patients with covid-19," *Bioscience Reports*, vol. 41, 12 2020.

[52] J. Hadjadj, N. Yatim, L. Barnabei, A. Corneau, J. Boussier, N. Smith, P. Helene, B. Charbit, B. Vincent, C. Chenevier-Gobeaux, B. Paul, N. Carlier, R. Gauzit, C. Morbieu, F. Pène, N. Marin,

N. Roche, T.-A. Szwebel, S. Merkling, and B. Terrier, "Impaired type i interferon activity and inflammatory responses in severe covid-19 patients," *Science*, vol. 369, p. eabc6027, 07 2020.

[53] J. Chan, S. Yuan, K.-H. Kok, K. To, H. Chu, J. Yang, F. Xing, J. Liu, C. Yip, R. Poon, H.-W. Tsoi, S. Lo, K.-H. Chan, V. Poon, W.-M. Chan, J. Ip, J.-P. Cai, V. Cheng, H. Chen, and K.-Y. Yuen, "A familial cluster of pneumonia associated with the 2019 novel coronavirus indicating person-to-person transmission: a study of a family cluster," *The Lancet*, vol. 395, 01 2020.

[54] G. Washko, "Diagnostic imaging in copd," *Seminars in respiratory and critical care medicine*, vol. 31, pp. 276–85, 06 2010.

[55] E. Pudney and M. Doherty, "Plain chest x-ray (cxr) in the diagnosis of chronic obstructive pulmonary disease (copd)," *European Respiratory Journal*, vol. 48, p. PA3936, 09 2016.

[56] C. Miller, K. Lönnroth, G. Sotgiu, and G. B. Migliori, "The long and winding road of chest radiography for tuberculosis detection," *European Respiratory Journal*, vol. 49, p. 1700364, 05 2017.

[57] A. Speets, A. Hoes, Y. Graaf, S. Kalmijn, A. Sachs, and W. Mali, "Chest radiography and pneumonia in primary care: Diagnostic yield and consequences for patient management," *The European respiratory journal : official journal of the European Society for Clinical Respiratory Physiology*, vol. 28, pp. 933–8, 11 2006.

[58] "Acr recommendations for the use of chest radiography and computed tomography (ct) for suspected covid-19 infection."

[59] G. Rubin, L. Haramati, J. Kanne, N. Schluger, J.-J. Yim, D. Anderson, T. Altes, S. Desai, J. M. Goo, Y. Inoue, F. Luo, M. Prokop, L. Richeldi, N. Tomiyama, A. Leung, C. Ryerson, N. Sverzellati, S. Raoof, A. Volpi, and A. Wells, "The role of chest imaging in patient management during the covid-19 pandemic: A multinational consensus statement from the fleischner society," *Radiology*, vol. 296, p. 201365, 04 2020.

[60] A. M. Thomas and A. K. Banerjee, *The history of radiology*. OUP Oxford, 2013.

[61] K. Sansare, V. Khanna, and F. Karjodkar, "Early victims of x-rays: a tribute and current perception," *Dentomaxillofacial Radiology*, vol. 40, no. 2, pp. 123–125, 2011.

[62] L. I. Grossman, "A brief history of endodontics," *Journal of endodontics*, vol. 8, pp. S36–S40, 1982.

[63] R. Breeches and E. Breeches, "The rays—history of radiology in us and canada," *Baltimore: Williams and Wilkins Co*, vol. 71, 1969.

[64] W. D. Coolidge, "A powerful röntgen ray tube with a pure electron discharge," *Physical Review*, vol. 2, no. 6, p. 409, 1913.

[65] F. E. Linder, T. D. Woolsey, O. Sagen, A. M. Waterhouse, J. E. Kelly, W. R. Simmons, A. J. McDowell, P. S. Lawerence, and R. T. Little, "Health statistics from the u.s. national health survery: Volume of x-rays, united states july 1960-june 1961," *U.S. National Health Survery*, vol. B, no. 38, 1962.

[66] A. Lilienfeld, P. Archer, C. Burnett, E. Chamberlain, B. Chazin, D. Davies, R. Davis, P. Haber, F. Hodges, I. Koprowska, B. Kordan, J. Lane, A. Lawton, L. Lee, D. MacCallum, J. McDonald, J. Milder, B. Naylor, G. Papanicolaou, and W. Umiker, "An evaluation of radiologic and cytologic screening for the early detection of lung cancer: A cooperative pilot study of the american cancer society and the veterans administration," *Cancer Research*, vol. 26, 10 1966.

[67] F. Nash, J. Morgan, and J. Tomkins, "South london lung cancer study.," *British medical journal*, vol. 2, no. 5607, p. 715, 1968.

[68] W. Weiss and K. Boucot, "The philadelphia pulmonary neoplasm research project. early roentgenographic appearance of bronchogenic carcinoma," *Archives of internal medicine*, vol. 134, pp. 306–11, 08 1974.

[69] G. Brett, "The value of lung cancer detection by 6 monthly chest radiographs," *Thorax*, vol. 23, pp. 414–20, 08 1968.

[70] S. H. Yoon, K. Lee, J. Kim, Y. Lee, H. Ko, K. Kim, C. M. Park, and Y.-H. Kim, "Chest radiographic and ct findings of the 2019 novel coronavirus disease (covid-19): Analysis of nine patients treated in korea," *Korean Journal of Radiology*, vol. 21, 02 2020.

[71] H. Y. F. Wong, H. Lam, A. H.-T. Fong, B. S. T. Leung, T. Chin, C. Lo, M. Lui, J. Lee, W. H. Chiu, T. Chung, E. Lee, E. Wan, F. Hung, T. Lam, M. Kuo, and M.-Y. Ng, "Frequency and distribution of chest radiographic findings in covid-19 positive patients," *Radiology*, p. 201160, 03 2020.

[72] A. Borakati, A. Perera, J. Johnson, and T. Sood, "Diagnostic accuracy of x-ray versus ct in covid-19: A propensity-matched database study," *BMJ Open*, 11 2020.

[73] S. Stephanie, T. Shum, H. Cleveland, S. Challa, A. Herring, F. Jacobson, H. Hatabu, S. Byrne, K. Shashi, T. Araki, J. Hernandez, C. White, R. Hossain, A. Hunsaker, and M. Hammer, "Determinants of chest x-ray sensitivity for covid- 19: A multi-institutional study in the united states," *Radiology: Cardiothoracic Imaging*, vol. 2, p. e200337, 10 2020.

[74] J. Frost, W. Ball, M. Levin, M. Tockman, R. Baker, D. Carter, J. Eggleston, Y. Erozan, P. Gupta, and N. Khouri, "Early lung cancer detection: Results of the initial (prevalence) radiologic and cytologic screening in the johns hopkins study," *The American review of respiratory disease*, vol. 130, pp. 549–54, 11 1984.

[75] S. Fontana, D. Sanderson, W. Taylor, L. Woolner, W. Miller, J. Muhm, and M. Uhlenhopp, "Early lung cancer detection: Results of the initial (prevalence) radiologic and cytologic screening in the mayo clinic study," *The American review of respiratory disease*, vol. 130, pp. 561–5, 11 1984.

[76] B. Flehinger, M. Melamed, M. Zaman, R. Heelan, W. Perchick, and N. Martini, "Early lung cancer detection: Results of the initial (prevalence) radiologic and cytologic screening in he memorial sloan-kettering study," *The American review of respiratory disease*, vol. 130, pp. 555–60, 11 1984.

[77] N. Berlin, R. Buncher, R. Fontana, J. Frost, and M. Melamed, "The national cancer institute cooperative early lung cancer detection program," *The American review of respiratory disease*, vol. 130, pp. 545–9, 11 1984.

[78] M. Tockman, "Survival and mortality from lung cancer in a screened population: The johns hopkins study," *Chest*, vol. 89, 04 1986.

[79] D. Sanderson, "Lung cancer screening: The mayo study," *Chest*, vol. 89, 04 1986.

[80] N. Martini, "Results of the memorial sloan-kettering study in screening for early lung cancer," *Chest*, vol. 89, 04 1986.

[81] R. Sanderson, D. Woolner, L. Taylor, W. Miller, William Muhm, J. Bernatz, P. Payne, W. Pairolero, P. Bergstralh, and E. Fontana, "Screening for lung cancer. a critique of the mayo lung project," *Cancer*, vol. 67, pp. 1155 – 1164, 02 1991.

[82] G. M. Strauss, R. E. Gleason, and D. J. Sugarbaker, "Chest x-ray screening improves outcome in lung cancer: a reappraisal of randomized trials on lung cancer screening," *Chest*, vol. 107, no. 6, pp. 270S–279S, 1995.

[83] M. M. Oken, W. G. Hocking, P. A. Kvale, G. L. Andriole, S. S. Buys, T. R. Church, E. D. Crawford, M. N. Fouad, C. Isaacs, D. J. Reding, *et al.*, "Screening by chest radiograph and lung cancer mortality: the prostate, lung, colorectal, and ovarian (plco) randomized trial," *Jama*, vol. 306, no. 17, pp. 1865–1873, 2011.

[84] J. Austin, B. Romney, and L. Goldsmith, "Missed bronchogenic carcinoma: Radiographic findings in 27 patients with a potentially resectable lesion evident in retrospect," *Radiology*, vol. 182, pp. 115–22, 02 1992.

[85] P. Shah, J. Austin, C. White, P. Patel, L. Haramati, G. Pearson, M. Shiau, and Y. Berkmen, "Missed non–small cell lung cancer: Radiographic findings of potentially resectable lesions evident only in retrospect1," *Radiology*, vol. 226, pp. 235–41, 02 2003.

[86] T. Byers, J. Vena, and T. Rzepka, "Predilection of lung cancer for the upper lobes: An epidemiologic inquiry," *Journal of the National Cancer Institute*, vol. 72, pp. 1271–5, 07 1984.

[87] L. Quekel, A. Kessels, R. Goei, and J. van Engelshoven, "Miss rate of lung cancer on the chest radiograph in clinical practice," *Chest*, vol. 115, pp. 720–4, 04 1999.

[88] L. Monnier-cholley, L. Arrivé, A. Porcel, K. Shehata, H. Dahan, T. Urban, M. Febvre, B. Lebeau, and J. Tubiana, "Characteristics of missed lung cancer on chest radiographs: A french experience," *European radiology*, vol. 11, pp. 597–605, 02 2001.

[89] M.-H. Wu, M. Gotway, T. Lee, M.-S. Chern, H.-C. Cheng, J.-C. Ko, M. Sheu, and C.-Y. Chang, "Features of non-small cell lung carcinomas overlooked at digital chest radiography," *Clinical radiology*, vol. 63, pp. 518–28, 06 2008.

[90] J. Muhm, W. Miller, S. Fontana, D. Sanderson, and M. Uhlenhopp, "Lung cancer detected during a screening program using four-month chest radiographs," *Radiology*, vol. 148, pp. 609–15, 10 1983.

[91] T. Sobue, T. Suzuki, M. Matsuda, T. Horai, A. Kajita, K. Kuriyama, M. Fukuoka, Y. Kusunoki, M. Kikui, S.-e. Ryu, and I. Isaburo, "Sensitivity and specificity of lung cancer screening in osaka, japan," *Cancer Science*, vol. 82, pp. 1069 – 1076, 10 1991.

[92] R. Heelan, B. Flehinger, M. Melamed, M. Zaman, W. Perchick, J. Caravelli, and N. Martini, "Non-small-cell lung cancer: Results of the new york screening program," *Radiology*, vol. 151, pp. 289–93, 06 1984.

[93] S. Sone, F. Li, Z. Yang, S. Takashima, Y. Maruyama, M. Hasegawa, J. Wang, S. Kawakami, and T. Honda, "Characteristics of small lung cancers invisible on conventional chest radiography and detected by population based screening using spiral ct," *The British journal of radiology*, vol. 73, pp. 137–45, 03 2000.

[94] A. Guinier and G. Fournet, "Small angle scattering of x-rays,"

[95] U. Bonse and M. Hart, "An x-ray interferometer," *Applied Physics Letters*, vol. 6, pp. 155–156, 04 1965.

[96] O. Glatter and O. Kratky, *In Small Angle X-ray Scattering*. 01 1982.

[97] G.-H. Chen, N. Bevins, J. Zambelli, and Z. Qi, "Small-angle scattering computed tomography (sas-ct) using a talbot-lau interferometer and a rotating anode x-ray tube: Theory and experiments," *Optics express*, vol. 18, pp. 12960–70, 06 2010.

[98] M. Bech, O. Bunk, T. Donath, R. Feidenhans'l, C. David, and F. Pfeiffer, "Quantitative x-ray dark-field computed tomography," *Physics in medicine and biology*, vol. 55, pp. 5529–39, 09 2010.

[99] T. Davis, D. Gao, T. E. Gureyev, A. W. Stevenson, and S. W. Wilkins, "Phase-contrast imaging of weakly absorbing materials using hard x-rays," *Nature*, vol. 373, pp. 595–598, 1995.

[100] S. Wilkins, T. E. Gureyev, D. Gao, A. Pogany, and A. Stevenson, "Phase-contrast imaging using polychromatic hard x-rays," *Nature*, vol. 384, no. 6607, pp. 335–338, 1996.

[101] A. Momose, T. Takeda, and Y. e. a. Itai, "Phase–contrast x–ray computed tomography for observing biological soft tissues," *Nat. Med.*, vol. 2, pp. 473–475, 1996.

[102] F. A. Dilmanian, Z. Zhong, B. Ren, X. Y. Wu, L. D. Chapman, I. Orion, and W. C. Thomlinson, "Computed tomography of x-ray index of refraction using the diffraction enhanced imaging method," *Physics in Medicine and Biology*, vol. 45, pp. 933–946, mar 2000.

[103] A. Momose, S. Kawamoto, I. Koyama, Y. Hamaishi, K. Takai, and Y. Suzuki, "Demonstration of x-ray talbot interferometry," *Japanese Journal of Applied Physics*, vol. 42, pp. L866–L868, jul 2003.

[104] T. Weitkamp, A. Diaz, C. David, F. Pfeiffer, M. Stampanoni, P. Cloetens, and et al, ""phase retrieval and differential phase-contrast imaging with low-brilliance x-ray sources," *Nat. Phys.*, vol. vol. 12, no. 16, pp. 6296–6304, 2005.

[105] C. Kottler, F. Pfeiffer, O. Bunk, C. Grünzweig, J. Bruder, R. Kaufmann, T. Tlustos, H. Walt, I. Briod, T. Weitkamp, and C. David, "Phase contrast x-ray imaging of large samples using an incoherent laboratory source," *physica status solidi (a)*, vol. 204, p. 2728, 08 2007.

[106] F. Pfeiffer, M. Bech, O. Bunk, P. Kraft, E. Eikenberry, C. Brönnimann, C. Grünzweig, and C. David, "Hard-x-ray dark-field imaging using a grating interferometer," *Nature materials*, vol. 7, pp. 134–7, 03 2008.

[107] F. Pfeiffer, J. Herzen, M. Willner, M. Chabior, S. Auweter, M. Reiser, and F. Bamberg, "Grating-based x-ray phase contrast for biomedical imaging applications," *Zeitschrift für Medizinische Physik*, vol. 23, no. 3, pp. 176–185, 2013.

[108] A. Bravin, P. Coan, and P. Suortti, "X-ray phase-contrast imaging: from pre-clinical applications towards clinics," *Phys. Med Biol.*, vol. 58, no. 1, pp. R1–35, 2013.

[109] R. Han, H.and Hu, F. Wali, Z. Wu, K. Gao, S. Wang, Y. Gu, Y. Jin, and C. Zhai, "Phase-contrast imaging for body composition measurement," *Physica Medica*, vol. 43, pp. 25–33, 2017.

[110] H. Han, Y. Sharma, G. Zan, Z. Wu, S. Wang, Y. Wu, A. Momose, and C. Zhai, "Preliminary research on body composition measurement using x-ray phase contrast imaging," *Phys Med*, vol. 52, pp. 1–8, 2018.

[111] D. M. Connor, Z. Zhong, H. D. Foda, S. Wiebe, C. A. Parham, F. A. Dilmanian, E. B. Cole, and E. D. Pisano, "Diffraction enhanced imaging of a rat model of gastric acid aspiration pneumonitis," *Academic radiology*, vol. 18, no. 12, pp. 1515–1521, 2011.

[112] L. Dong, J. Li, W. Jian, L. Zhang, M. Wu, H. Shi, and S. Luo, "Emphysema early diagnosis using x-ray diffraction enhanced imaging at synchrotron light source," *BioMedical Engineering OnLine*, vol. 13, pp. 1–11, 2014.

[113] k. Li, Y. Ge, J. Garrett, N. Bevins, J. Zambelli, and G.-H. Chen, "Grating-based phase contrast tomosynthesis imaging: Proof-of-concept experimental studies," *Medical physics*, vol. 41, p. 011903, 01 2014.

[114] J. Garrett, Y. Ge, k. li, and G.-H. Chen, "Anatomical background noise power spectrum in differential phase contrast and dark field contrast mammograms," *Medical physics*, vol. 41, p. 120701, 12 2014.

[115] K. Li, J. Garrett, Y. Ge, X. Ji, and G.-H. Chen, "Design, construction, and initial results of a prototype multi-contrast x-ray breast imaging system," *Proceedings of SPIE–the International Society for Optical Engineering*, p. 105730W, 2018.

[116] E.-M. Braig, N. Roiser, M. Kimm, M. Busse, J. Andrejewski, J. Scholz, C. Petrich, A. Gustschin, A. Sauter, J. Bodden, F. Meurer, R. Korbel, F. Pfeiffer, J. Herzen, and D. Pfeiffer, "X-ray dark-field radiography: Potential for visualization of monosodium urate deposition," *Investigative Radiology*, vol. Publish Ahead of Print, p. 1, 04 2020.

[117] X. Ji, R. Zhang, K. Li, and G. H. Chen, "Dual energy differential phase contrast ct (de-dpc-ct) imaging," *IEEE Transactions on Medical Imaging*, vol. 39, no. 11, pp. 3278–3289, 2020.

[118] R. Zhang, A. Fowler, L. Wilke, F. Kelcz, J. Garrett, G. Chen, and k. li, "Fast acquisition with seamless stage translation (fasst) for a trimodal x-ray breast imaging system," *Medical Physics*, vol. 47, 05 2020.

[119] K. Willer, A. A. Fingerle, W. Noichl, F. De Marco, M. Frank, T. Urban, R. Schick, A. Gustschin, B. Gleich, J. Herzen, *et al.*, "X-ray dark-field chest imaging for detection and quantification of emphysema in patients with chronic obstructive pulmonary disease: a diagnostic accuracy study," *The Lancet Digital Health*, vol. 3, no. 11, pp. e733–e744, 2021.

[120] R. Longo, M. Tonutti, L. Rigon, F. Arfelli, D. Dreossi, E. Quai, F. Zanconati, E. Castelli, G. Tromba, and M. A. Cova, "Clinical study in phase-contrast mammography: image-quality analysis," *Philosophical Transactions of the Royal Society A: Mathematical, physical and engineering sciences*, vol. 372, no. 2010, p. 20130025, 2014.

[121] S. Pacile, F. Brun, C. Dullin, Y. Nesterets, D. Dreossi, S. Mohammadi, M. Tonutti, F. Stacul, D. Lockie, F. Zanconati, *et al.*, "Clinical application of low-dose phase contrast breast ct: methods for the optimization of the reconstruction workflow," *Biomedical optics express*, vol. 6, no. 8, pp. 3099–3112, 2015.

[122] A. Sarno, G. Mettivier, B. Golosio, P. Oliva, G. Spandre, F. Di Lillo, C. Fedon, R. Longo, and P. Russo, "Imaging performance of phase-contrast breast computed tomography with synchrotron radiation and a cdte photon-counting detector," *Physica Medica*, vol. 32, no. 5, pp. 681–690, 2016.

[123] T. Gureyev, Y. I. Nesterets, P. Baran, S. Taba, S. Mayo, D. Thompson, B. Arhatari, A. Mihocic, B. Abbey, D. Lockie, *et al.*, "Propagation-based x-ray phase-contrast tomography of mastectomy samples using synchrotron radiation," *Medical physics*, vol. 46, no. 12, pp. 5478–5487, 2019.

[124] R. P. Murrie, A. W. Stevenson, K. S. Morgan, A. Fouras, D. M. Paganin, and K. K. Siu, "Feasibility study of propagation-based phase-contrast x-ray lung imaging on the imaging and medical beamline at the australian synchrotron," *Journal of Synchrotron Radiation*, vol. 21, no. 2, pp. 430–445, 2014.

[125] R. Gradl, M. Dierolf, L. Hehn, B. Günther, A. Ö. Yildirim, B. Gleich, K. Achterhold, F. Pfeiffer, and K. S. Morgan, "Propagation-based phase-contrast x-ray imaging at a compact light source," *Scientific reports*, vol. 7, no. 1, p. 4908, 2017.

[126] K. Shaker, I. Häggmark, J. Reichmann, M. Arsenian-Henriksson, and H. M. Hertz, "Phase-contrast x-ray tomography resolves the terminal bronchioles in free-breathing mice," *Communications Physics*, vol. 4, no. 1, p. 259, 2021.

[127] J. Albers, W. L. Wagner, M. O. Fiedler, A. Rothermel, F. Wünnemann, F. Di Lillo, D. Dreossi, N. Sodini, E. Baratella, M. Confalonieri, *et al.*, "High resolution propagation-based lung imaging at clinically relevant x-ray dose levels," *Scientific Reports*, vol. 13, no. 1, p. 4788, 2023.

[128] I. Häggmark, K. Shaker, S. Nyrén, B. Al-Amiry, E. Abadi, W. P. Segars, E. Samei, and H. M. Hertz, "Phase-contrast virtual chest radiography," *Proceedings of the National Academy of Sciences*, vol. 120, no. 1, p. e2210214120, 2023.

[129] S. Schleede, F. Meinel, M. Bech, J. Herzen, K. Achterhold, G. Potdevin, A. Malecki, S. Adam-Neumair, S. Thieme, F. Bamberg, K. Nikolaou, A. Bohla, A. Yildirim, R. Loewen, M. Gifford, R. Ruth, O. Eickelberg, M. Reiser, and F. Pfeiffer, "Emphysema diagnosis using x-ray dark-field imaging at a laser-driven compact synchrotron light source," *Proceedings of the National Academy of Sciences of the United States of America*, vol. 109, 10 2012.

[130] A. Yaroshenko, F. Meinel, M. Bech, A. Tapfer, A. Velroyen, S. Schleede, S. Auweter, A. Bohla, A. Yildirim, K. Nikolaou, F. Bamberg, O. Eickelberg, M. Reiser, and F. Pfeiffer, "Pulmonary emphysema diagnosis with a preclinical small-animal x-ray dark-field scatter-contrast scanner," *Radiology*, vol. 269, 05 2013.

[131] A. Yaroshenko, K. Hellbach, M. Bech, S. Grandl, M. Reiser, F. Pfeiffer, and F. Meinel, "Grating-based x-ray dark-field imaging: a new paradigm in radiography," *Current Radiology Reports*, vol. 2, 07 2014.

[132] F. Meinel, A. Yaroshenko, K. Hellbach, M. Bech, K. Nikolaou, O. Eickelberg, M. Reiser, F. Pfeiffer, and A. Yildirim, "Improved diagnosis of pulmonary emphysema using in vivo dark-field radiography," *Pneumologie*, vol. 68, 06 2014.

[133] A. Yaroshenko, K. Hellbach, A. Yildirim, T. Conlon, I. Fernandez, M. Bech, A. Velroyen, F. Meinel, S. Auweter, M. Reiser, O. Eickelberg, and F. Pfeiffer, "Improved in vivo assessment of pulmonary fibrosis in mice using x-ray dark-field radiography," *Scientific Reports*, vol. 5, p. 17492, 12 2015.

[134] A. Yaroshenko, T. Pritzke, M. Koschlig, N. Kamgari, K. Willer, L. Gromann, S. Auweter, K. Hellbach, M. Reiser, O. Eickelberg, F. Pfeiffer, and A. Hilgendorff, "Visualization of neonatal lung injury associated with mechanical ventilation using x-ray dark-field radiography," *Scientific Reports*, vol. 6, p. 24269, 04 2016.

[135] K. Hellbach, A. Yaroshenko, F. Meinel, A. Yildirim, T. Conlon, M. Bech, M. Müller, A. Velroyen, M. Notohamiprodjo, S. Auweter, M. Reiser, O. Eickelberg, and F. Pfeiffer, "In vivo dark-field radiography for early diagnosis and staging of pulmonary emphysema," *Investigative radiology*, vol. 50, 03 2015.

[136] K. Hellbach, A. Yaroshenko, K. Willer, T. Pritzke, A. Baumann, N. Hesse, S. Auweter, M. Reiser, O. Eickelberg, F. Pfeiffer, A. Hilgendorff, and F. Meinel, "Facilitated diagnosis of pneumothoraces in newborn mice using x-ray dark-field radiography," *Investigative Radiology*, vol. 51, p. 1, 05 2016.

[137] K. Hellbach, F. Meinel, T. Conlon, K. Willer, A. Yaroshenko, A. Velroyen, M. Braunagel, S. Auweter, M. Reiser, O. Eickelberg, F. Pfeiffer, and A. Yildirim, "X-ray dark-field imaging to depict acute lung inflammation in mice," *Scientific Reports*, vol. 8, 02 2018.

[138] K. Hellbach, A. Baehr, F. De Marco, K. Willer, L. Gromann, J. Herzen, M. Dmochewitz, S. Auweter, A. Fingerle, P. Noël, E. Rummeny, A. Yaroshenko, I. Maack, T. Pralow, H. Heijden, N. Wieberneit, R. Proksa, T. Koehler, K. Rindt, and M. Reiser, "Depiction of pneumothoraces in a large animal model using x-ray dark-field radiography," *Scientific Reports*, vol. 8, 02 2018.

[139] K. Scherer, A. Yaroshenko, D. Bölükbas, L. Gromann, K. Hellbach, F. Meinel, M. Braunagel, J. Berg, O. Eickelberg, M. Reiser, F. Pfeiffer, S. Meiners, and J. Herzen, "X-ray dark-field radiography - in-vivo diagnosis of lung cancer in mice," *Scientific Reports*, vol. 7, 12 2016.

[140] K. Willer, A. Fingerle, L. Gromann, F. De Marco, J. Herzen, K. Achterhold, B. Gleich, D. Pfeiffer, K. Scherer, M. Renz, B. Renger, F. Kopp, F. Kriner, F. Fischer, C. Braun, S. Auweter, K. Hellbach, M. Reiser, T. Schröter, and P. Noël, "X-ray dark-field imaging of the human lung - a feasibility study on a deceased body," *PLOS ONE*, vol. 13, p. e0204565, 09 2018.

[141] C. Hauke, P. Bartl, M. Leghissa, L. Ritschl, S. Sutter, T. Weber, J. Zeidler, J. Freudenberger, T. Mertelmeier, M. Radicke, T. Michel, G. Anton, F. Meinel, A. Baehr, S. Auweter, D. Bondesson, T. Gaass, J. Dinkel, M. Reiser, and K. Hellbach, "A pre-clinical talbot-lau prototype for x-ray dark-field imaging of human-sized objects," *Medical Physics*, vol. 45, 03 2018.

[142] A. Fingerle, F. De Marco, J. Andrejewski, K. Willer, L. Gromann, W. Noichl, F. Kriner, F. Fischer, C. Braun, I. Maack, T. Pralow, T. Koehler, P. Noël, F. Meurer, D. Deniffel, A. Sauter, B. Haller, D. Pfeiffer, E. Rummeny, and F. Pfeiffer, "Imaging features in post-mortem x-ray dark-field chest radiographs and correlation with conventional x-ray and ct," *European Radiology Experimental*, vol. 3, p. 25, 07 2019.

[143] A. Momose and J. Fukuda, "Phase-contrast radiographs of nonstained rat cerebellar specimen," *Medical physics*, vol. 22, no. 4, pp. 375–379, 1995.

[144] A. Snigirev, I. Snigireva, V. Kohn, S. Kuznetsov, and I. Schelokov, "On the possibilities of x-ray phase contrast microimaging by coherent high-energy synchrotron radiation," *Review of scientific instruments*, vol. 66, no. 12, pp. 5486–5492, 1995.

[145] D. Bushe, R. Zhang, X. Ji, M. Feng, G.-H. Chen, and K. Li, "Single-kv multi-contrast x-ray imaging for gout detection and gout-pseudogout differentiation," p. 59, 02 2021.

[146] J. Kuhlman, J. Collins, G. Brooks, D. Yandow, and L. Broderick, "Dual-energy subtraction chest radiography: What to look for beyond calcified nodules1," *Radiographics : a review publication of the Radiological Society of North America, Inc*, vol. 26, pp. 79–92, 01 2006.

[147] R. Gilkeson and P. Sachs, "Dual energy subtraction digital radiography," *Journal of thoracic imaging*, vol. 21, pp. 303–13, 12 2006.

[148] L. Lehmann, R. Alvarez, A. Macovski, W. Brody, N. Pelc, S. Riederer, and A. Hall, "Generalized image combinations in dual kvp digital radiography," *Medical physics*, vol. 8, pp. 659–67, 09 1981.

[149] T. Takeda, A. Momose, J. Wu, Q. Yu, T. Zeniya, T.-T. Lwin, A. Yoneyama, and Y. Itai, "Vessel imaging by interferometric phase-contrast x-ray technique," *Circulation*, vol. 105, no. 14, pp. 1708–1712, 2002.

[150] A. Yoneyama, T. Takeda, Y. Tsuchiya, J. Wu, A. Koizumi, K. Hyodo, Y. Itai, *et al.*, "A phase-contrast x-ray imaging system—with a 60× 30 mm field of view—based on a skew-symmetric two-crystal x-ray interferometer," *Nuclear Instruments and Methods in Physics Research Section A: Accelerators, Spectrometers, Detectors and Associated Equipment*, vol. 523, no. 1-2, pp. 217–222, 2004.

[151] A. Momose, W. Yashiro, Y. Takeda, Y. Suzuki, and T. Hattori, "Phase tomography by x-ray talbot interferometry for biological imaging," *Japanese journal of applied physics*, vol. 45, no. 6R, p. 5254, 2006.

[152] T. Takeda, A. Yoneyama, J. Wu, A. Momose, K. Hyodo, *et al.*, "In vivo physiological saline-infused hepatic vessel imaging using a two-crystal-interferometer-based phase-contrast x-ray technique," *Journal of Synchrotron Radiation*, vol. 19, no. 2, pp. 252–256, 2012.

[153] D. Chapman, W. Thomlinson, F. Arfelli, N. Gmür, Z. Zhong, R. Menk, R. Johnson, D. Washburn, E. Pisano, and D. Sayers, "Mammography imaging studies using a laue crystal analyzer," *Review of Scientific Instruments*, vol. 67, no. 9, pp. 3360–3360, 1996.

[154] "Diffraction enchanced x-ray imaging," nov 1997.

[155] O. Oltulu, Z. Zhong, M. Hasnah, M. N. Wernick, and D. Chapman, "Extraction of extinction, refraction and absorption properties in diffraction enhanced imaging," *Journal of Physics D: Applied Physics*, vol. 36, no. 17, p. 2152, 2003.

[156] D. M. Connor and Z. Zhong, "Diffraction-enhanced imaging," *Current Radiology Reports*, vol. 2, pp. 1–11, 2014.

[157] E. D. Pisano, R. E. Johnston, D. Chapman, J. Geradts, M. V. Iacocca, C. A. Livasy, D. B. Washburn, D. E. Sayers, Z. Zhong, M. Z. Kiss, *et al.*, "Human breast cancer specimens: diffraction-enhanced imaging with histologic correlation—improved conspicuity of lesion detail compared with digital radiography," *Radiology*, vol. 214, no. 3, pp. 895–901, 2000.

[158] T. Kao, D. Connor, F. Dilmanian, L. Faulconer, T. Liu, C. Parham, E. D. Pisano, and Z. Zhong, "Characterization of diffraction-enhanced imaging contrast in breast cancer," *Physics in Medicine & Biology*, vol. 54, no. 10, p. 3247, 2009.

[159] J. Mollenhauer, M. Aurich, Z. Zhong, C. Muehleman, A. Cole, M. Hasnah, O. Oltulu, K. Kuettner, A. Margulis, and L. Chapman, "Diffraction-enhanced x-ray imaging of articular cartilage," *Osteoarthritis and cartilage*, vol. 10, no. 3, pp. 163–171, 2002.

[160] J. Li, Z. Zhong, D. Connor, J. Mollenhauer, and C. Muehleman, "Phase-sensitive x-ray imaging of synovial joints," *Osteoarthritis and cartilage*, vol. 17, no. 9, pp. 1193–1196, 2009.

[161] P. Diemoz, A. Bravin, and P. Coan, "Theoretical comparison of three x-ray phase-contrast imaging techniques: propagation-based imaging, analyzer-based imaging and grating interferometry," *Optics express*, vol. 20, no. 3, pp. 2789–2805, 2012.

[162] K. Nugent, T. Gureyev, D. Cookson, D. Paganin, and Z. Barnea, "Quantitative phase imaging using hard x rays," *Physical review letters*, vol. 77, no. 14, p. 2961, 1996.

[163] T. Gureyev and S. Wilkins, "On x-ray phase imaging with a point source," *JOSA A*, vol. 15, no. 3, pp. 579–585, 1998.

[164] T. E. Gureyev, S. C. Mayo, D. E. Myers, Y. Nesterets, D. Paganin, A. Pogany, A. W. Stevenson, and S. Wilkins, "Refracting röntgen's rays: propagation-based x-ray phase contrast for biomedical imaging," *Journal of Applied Physics*, vol. 105, no. 10, p. 102005, 2009.

[165] T. Gureyev, D. Paganin, B. Arhatari, S. Taba, S. Lewis, P. Brennan, and H. Quiney, "Dark-field signal extraction in propagation-based phase-contrast imaging," *Physics in Medicine & Biology*, vol. 65, no. 21, p. 215029, 2020.

[166] P. Cloetens, J. Guigay, C. De Martino, J. Baruchel, and M. Schlenker, "Fractional talbot imaging of phase gratings with hard x rays," *Optics letters*, vol. 22, no. 14, pp. 1059–1061, 1997.

[167] C. David, B. Nöhammer, H. Solak, and E. Ziegler, "Differential x-ray phase contrast imaging using a shearing interferometer," *Applied physics letters*, vol. 81, no. 17, pp. 3287–3289, 2002.

[168] T. Weitkamp, A. Diaz, C. David, F. Pfeiffer, M. Stampanoni, P. Cloetens, and E. Ziegler, "X-ray phase imaging with a grating interferometer," *Opt. Express*, vol. 13, pp. 6296–6304, Aug 2005.

[169] Z. Qi, N. Bevins, J. Zambelli, K. Li, and G.-H. Chen, "Quantitative imaging of electron density and effective atomic number using phase contrast ct," *Institute of Physics and Engineering in Medicine*, vol. 55, no. 9, pp. 2669–2677, 2010.

[170] N. Bevins, J. Zambelli, k. li, Z. Qi, and G.-H. Chen, "Multicontrast x-ray computed tomography imaging using talbot-lau interferometry without phase stepping," *Medical physics*, vol. 39, pp. 424–8, 01 2012.

[171] B. Lorenz, D. Pfeiffer, F. Pfeiffer, and H. Julia, "Quantitative x-ray phase contrast computed tomography with grating interferometry," *European Journal of Nuclear Medicine and Molecular Imaging*, vol. 48, no. 13, pp. 4171–4188, 2021.

[172] M. Stampanoni, Z. Wang, T. Thüring, C. David, E. Roessl, M. Trippel, R. A. Kubik-Huch, G. Singer, M. K. Hohl, and N. Hauser, "The first analysis and clinical evaluation of native breast tissue using differential phase-contrast mammography," *Investigative radiology*, vol. 46, no. 12, pp. 801–806, 2011.

[173] T. Michel, J. Rieger, G. Anton, F. Bayer, M. W. Beckmann, J. Durst, P. A. Fasching, W. Haas, A. Hartmann, G. Pelzer, *et al.*, "On a dark-field signal generated by micrometer-sized calcifications in phase-contrast mammography," *Physics in Medicine & Biology*, vol. 58, no. 8, p. 2713, 2013.

[174] K. Scherer, K. Willer, L. Gromann, L. Birnbacher, E. Braig, S. Grandl, A. Sztrókay-Gaul, J. Herzen, D. Mayr, K. Hellerhoff, *et al.*, "Toward clinically compatible phase-contrast mammography," *PloS one*, vol. 10, no. 6, p. e0130776, 2015.

[175] F. T. Gassert, T. Urban, M. Frank, K. Willer, W. Noichl, P. Buchberger, R. Schick, T. Koehler, J. von Berg, A. A. Fingerle, *et al.*, "X-ray dark-field chest imaging: qualitative and quantitative results in healthy humans," *Radiology*, vol. 301, no. 2, pp. 389–395, 2021.

[176] M. Frank, F. T. Gassert, T. Urban, K. Willer, W. Noichl, R. Schick, M. Schultheiss, M. Viermetz, B. Gleich, F. De Marco, *et al.*, "Dark-field chest x-ray imaging for the assessment of covid-19-pneumonia," *Communications Medicine*, vol. 2, no. 1, pp. 1–9, 2022.

[177] J. C. Maxwell, "Viii. a dynamical theory of the electromagnetic field," *Philosophical transactions of the Royal Society of London*, no. 155, pp. 459–512, 1865.

[178] E. Lau, "Beugungserscheinungen an doppelrastern," *Annalen der Physik*, vol. 437, no. 7-8, pp. 417–423, 1948.

[179] F. Pfeiffer, T. Weitkamp, O. Bunk, and C. David, "Phase retrieval and differential phase-contrast imaging with low-brilliance X-ray sources," *Nat. Phys.*, vol. 2, pp. 258–261, mar 2006.

[180] J. W. Goodman, *Introduction to Fourier optics*. Roberts and Company Publishers, 2005.

[181] D. Paganin, *Coherent X-ray optics*. No. 6, Oxford University Press on Demand, 2006.

[182] A. Momose, H. Kuwabara, and W. Yashiro, "X-ray Phase Imaging Using Lau Effect," *Appl. Phys. Express*, vol. 4, p. 066603, may 2011.

[183] T. Donath, M. Chabior, F. Pfeiffer, O. Bunk, E. Reznikova, J. Mohr, E. Hempel, S. Popescu, M. Hoheisel, M. Schuster, J. Baumann, and C. David, "Inverse geometry for grating-based x-ray phase-contrast imaging," *Journal of Applied Physics*, vol. 106, no. 5, p. 054703, 2009.

[184] D. Williams, J. Siewerdsen, D. Tward, N. Paul, A. Dhanantwari, N. Shkumat, S. Richard, J. Yorkston, and R. Van Metter, "Optimal kvp selection for dual-energy imaging of the chest: Evaluation by task-specific observer preference tests," *Medical physics*, vol. 34, no. 10, pp. 3916–3925, 2007.

[185] W. Muhogora, A. Trianni, F. Toso, A. Devetti, R. Padovani, P. Msaki, and R. Kazema, "Comparison of image quality and patient dose for chest x-ray examinations on conventional and low cost computed radiography systems," *Radiography*, vol. 18, no. 4, pp. 275–278, 2012.

[186] S. Gay, C. Sistrom, C. Holder, and P. Suratt, "Breath-holding capability of adults," *Investigative Radiology*, vol. 29, pp. 848–851, 09 1994.

[187] T. Koehler, H. Daerr, G. Martens, N. Kuhn, S. Löscher, U. van Stevendaal, and E. Roessl, "Slit-scanning differential x-ray phase-contrast mammography: Proof-of-concept experimental studies," *Medical physics*, vol. 42, p. 1959, 04 2015.

[188] C. Arboleda, Z. Wang, K. Jefimovs, T. Koehler, U. Stevendaal, N. Kuhn, B. David, S. Prevrhal, K. Lång, S. Forte, R. Kubik-Huch, C. Leo, G. Singer, M. Marcon, A. Boss, E. Roessl, and M. Stampanoni, "Towards clinical grating-interferometry mammography," *European Radiology*, vol. 30, 08 2019.

[189] E. Bennett, R. Kopace, A. Stein, and H. Wen, "A grating-based single-shot x-ray phase contrast and diffraction method for in vivo imaging," *Medical physics*, vol. 37, pp. 6047–54, 11 2010.

[190] Y. Ge, k. li, J. Garrett, and G.-H. Chen, "Grating based x-ray differential phase contrast imaging without mechanical phase stepping," *Optics express*, vol. 22, pp. 14246–14252, 06 2014.

[191] C. Kottler, F. Pfeiffer, O. Bunk, C. Grünzweig, and C. David, "Grating interferometer based scanning setup for hard x-ray phase contrast imaging," *The Review of scientific instruments*, vol. 78, p. 043710, 05 2007.

[192] M. Seifert, V. Ludwig, S. Kaeppler, F. Horn, P. Meyer, G. Pelzer, J. Rieger, D. Sand, T. Michel, J. Mohr, C. Riess, and G. Anton, "Talbot-lau x-ray phase-contrast setup for fast scanning of large samples," *Scientific Reports*, vol. 9, p. 4199, 03 2019.

[193] J. Hsieh, O. Gurmen, and K. King, "Recursive correction algorithm for detector decay characteristics in ct," *Proceedings of SPIE - The International Society for Optical Engineering*, 04 2000.

[194] S. H. Chan, R. Khoshabeh, K. B. Gibson, P. E. Gill, and T. Q. Nguyen, "An augmented lagrangian method for total variation video restoration," *IEEE Transactions on Image Processing*, vol. 20, no. 11, pp. 3097–3111, 2011.

[195] A. A. of Physicists in Medicine *et al.*, "Protocols for the radiation safety surveys of diagnostic radiological equipment," *AAPM Report*, vol. 25, 1988.

[196] R. Y. Chu, J. Fisher, B. R. Archer, B. J. Conway, M. M. Goodsitt, S. Glaze, J. E. Gray, and K. J. Strauss, "Standardized methods for measuring diagnostic x-ray exposures," *American Association of Physicists in Medicine*, vol. 31, 1990.

[197] J. Heron, "Estimation of effective dose to the patient during medical x-ray examinations from measurements of the dose-area product," *Physics in medicine and biology*, vol. 37, pp. 2117–26, 12 1992.

[198] M. Frank, T. Urban, K. Willer, W. Noichl, F. De Marco, R. Schick, B. Gleich, A. Schegerer, U. Lechel, P. Meyer, *et al.*, "Dosimetry on first clinical dark-field chest radiography," *Medical physics*, vol. 48, no. 10, pp. 6152–6159, 2021.

[199] N. E. Peacock, A. L. Steward, and P. J. Riley, "An evaluation of the effect of tube potential on clinical image quality using direct digital detectors for pelvis and lumbar spine radiographs," *Journal of medical radiation sciences*, vol. 67, no. 4, pp. 260–268, 2020.

[200] J. Zhou and X. Zhang, "A lung phantom model to study pulmonary edema using lung ultrasound surface wave elastography," *Ultrasound in Medicine & Biology*, vol. 44, 08 2018.

[201] F. De Marco, K. Willer, L. B. Gromann, J. Andrejewski, K. Hellbach, A. Bähr, M. Dmochewitz, T. Koehler, H.-I. Maack, F. Pfeiffer, *et al.*, "Contrast-to-noise ratios and thickness-normalized, ventilation-dependent signal levels in dark-field and conventional in vivo thorax radiographs of two pigs," *PLoS One*, vol. 14, no. 6, p. e0217858, 2019.

[202] X. Ji, M. Feng, K. Treb, R. Zhang, S. Schafer, and K. Li, "Development of an integrated c-arm interventional imaging system with a strip photon counting detector and a flat panel detector," *IEEE transactions on medical imaging*, vol. PP, 07 2021.

[203] K. Treb, X. Ji, M. Feng, R. Zhang, S. Periyasamy, P. Laeseke, and K. Li, "Enlarging the longitudinal coverage of a prototype c-arm photon counting ct system for image-guided interventions," *Proc. SPIE*, 04 2022.

[204] S. Leng, M. Bruesewitz, S. Tao, K. Rajendran, A. Halaweish, N. Campeau, J. Fletcher, and C. McCollough, "Photon-counting detector ct: System design and clinical applications of an emerging technology," *Radiographics*, vol. 39, p. 729, 05 2019.

[205] K. Rajendran, M. Petersilka, A. Henning, E. Shanblatt, B. Schmidt, T. Flohr, A. Ferrero, F. Baffour, F. Diehn, L. Yu, P. Rajiah, J. Fletcher, S. Leng, and C. McCollough, "First clinical photon-counting detector ct system: Technical evaluation," *Radiology*, vol. 303, 12 2021.

[206] K. Taguchi, R. Ballabriga, M. Campbell, and D. Darambara, "Photon counting detector computed tomography," *IEEE Transactions on Radiation and Plasma Medical Sciences*, vol. PP, pp. 1–1, 12 2021.

[207] K. Stephens, "Fda approves siemens healthineers' naeotom alpha ct scanner," *AXIS Imaging News*, Oct 01 2021. Name - Siemens Healthineers; Food & Drug Administration–FDA; Copyright - Copyright Anthem Media Group Oct 1, 2021; Last updated - 2021-12-10.

[208] K. Scherer, A. Yaroshenko, D. A. Bölükbas, L. B. Gromann, K. Hellbach, F. G. Meinel, M. Braunagel, J. v. Berg, O. Eickelberg, M. F. Reiser, *et al.*, "X-ray dark-field radiography-in-vivo diagnosis of lung cancer in mice," *Scientific reports*, vol. 7, no. 1, p. 402, 2017.

[209] C. A. Burgard, T. Gaass, M. Bonert, D. Bondesson, N. Thaens, M. F. Reiser, and J. Dinkel, "Detection of artificial pulmonary lung nodules in ultralow-dose ct using an ex vivo lung phantom," *Plos one*, vol. 13, no. 1, p. e0190501, 2018.